**ABSTRACT**

Smith, Nicholas Andrew. Novel Approaches to Nitride Film Growth: Seeded Supersonic Molecular Beam Methods (under the direction of Dr. H. Henry Lamb).

Seeded supersonic molecular beams can provide high-intensity sources of precursor molecules with tunable translational energies for III-nitride film growth; however, non-equilibrium (kinetic) phenomena associated with supersonic free jet expansions can affect the translational energy, intensity, and energy resolution of the resulting molecular beams. Time-of-flight (TOF) methods are used herein to measure the translational energies, flux intensities, and parallel speed ratios of species in seeded supersonic molecular beams generated from binary gas mixtures containing He, $N_2$, Ar, and Kr. Aerodynamic focusing of heavy molecules along the centerline of the free jet was found to result in mass separation (*i.e.,* heavy species enrichment). The enrichment data scale to a common dimensionless parameter, the Stokes number at the nozzle throat. An empirical correlation is provided that allows enrichment ratios to be calculated for binary mixtures using only the species mass ratio, the Schmidt number, and the nozzle Reynolds number (calculated using the nozzle stagnation conditions and the physical properties of the carrier gas). The enrichment correlation was found to predict with reasonable accuracy the relative flux intensities of triethylgallium (TEG)/He and TEG/$N_2$ supersonic molecular beams. Optical emission spectroscopy (OES) and a novel TOF-appearance potential mass spectrometry (APMS) technique were used to characterize the active nitrogen species generated by a radio-frequency discharge supersonic jet (RFD-SSJ) source. The results indicate that the RFD-SSJ source yields supersonic beams

containing primarily ground-state ($^4S$) atomic nitrogen. Homoepitaxial GaN(0001) films were grown by supersonic jet epitaxy (SJE) and characterized by reflection high-energy electron diffraction (RHEED), scanning electron microscopy (SEM) and atomic force microscopy (AFM). Topological scaling analysis applied to the AFM data indicated that surface diffusion is the dominant surface transport mechanism in the growth of GaN films by SJE.

# Novel Approaches to Nitride Film Growth: Seeded Supersonic Molecular Beam Methods

By

**Nicholas A. Smith**

A dissertation submitted to the Graduate Faculty of

North Carolina State University

in partial fulfillment of the

requirements for the Degree of

Doctor of Philosophy

**Chemical Engineering**

Raleigh, North Carolina

2003

**Approved by:**

| ______________________________ | ______________________________ |
| --- | --- |
| Dr. David F. Ollis | Dr. Gregory N. Parsons |
| ______________________________ | ______________________________ |
| Dr. Robert F. Davis | Dr. H. Henry Lamb<br>Chair of Advisory Committee |

To my Dad, whose guidance and support I am always in debt.

## BIOGRAPHY

Nicholas Andrew Smith was born on April 11, 1975, in Cincinnati, Ohio. He grew up in his formative years in Circleville, Ohio and then moved to Columbus, Ohio to attend Bishop Watterson High School, graduating in 1993. He didn't leave Columbus for a while, until he earned a Bachelors of Science in Chemical Engineering from The Ohio State University in 1997. After a quick tour of Europe in the summer of 1997, he arrived at North Carolina State University in the fall of 1997 to begin his graduate education.

## ACKNOWLEDGEMENTS

I would like to thank Dr. H. Henry Lamb for his guidance, knowledge, advice, support, time, effort, encouragement and sense of humor throughout my graduate education. I will be forever in debt to him for his mentorship, and I am grateful for that. Most would agree with me that his "hands on" approach is invaluable in our field. I would also like to thank present and past group members for their assistance and advice: Arthur McGinnis for his training me in supersonic jet epitaxy and providing thoughtful discussions, and Bryan Silleti, Susan Sigmon, Brock Harris and Amit Khandelwal for their hands on help in equipment issues. I am thankful to Kevin Bray for his assistance and advice with AFM. Special thanks goes to Kit Yeung to his creative and resourceful approaches to solving many research equipment issues.

First and foremost I would like to thank my wife Kristen for her support and encouragement. I would also like to thank my entire family and extended family for their support and always providing a healthy environment where one is hungry to learn.

**TABLE OF CONTENTS**


List of Tables vi
List of Figures vii
1. Introduction 1
- 1.1 Background of GaN 1
- 1.2 Growth methods 2
  - 1.2.1 Chemical vapor deposition 2
  - 1.2.2 Molecular beam epitaxy 4
  - 1.2.3 Supersonic jet epitaxy 8
  - 1.2.4 Seeded supersonic jets[44,45] 9
  - 1.2.5 Applications of supersonic jet epitaxy 11
- 1.3 Homoepitaxial growth of GaN 12
- 1.4 Growth of GaN vs. V/III ratio and surface morphology 13
- 1.5 GaN reaction chemistry[16] 15
- 1.6 Experimental methods 17
  - 1.6.1 SJE/XPS System 17
  - 1.6.2 Film characterization 18
    - 1.6.2.1 Surface analysis 19
- 1.7 Species segregation in seeded molecular beams 20
- 1.8 RF supersonic plasma source characterization via APMS and OES to determine dissociation fraction 22
- 1.9 Dissertation outline 25
- 1.10 References 31

2. Heavy species enrichment due to aerodynamic focusing in seeded supersonic jets 37
3. Surface roughness correlations in homoepitaxial growth of GaN(0001) films by $NH_3$ supersonic jet epitaxy 74
4. GaN growth using seeded supersonic jets: Effects of aerodynamic focusing on triethylgallium flux and surface morphology 106
5. Time-of-flight appearance potential mass spectrometry of an radio-frequency -discharge supersonic jet nitrogen source 136
6. Appendices 183
- 6.1 Chemical beam epitaxy of indium nitride using seeded supersonic beams of ammonia and trimethyl-indium 184
- 6.2 Si-H (100) Nitridation via an atomic N RF-discharge supersonic molecular beam 194
- 6.3 Converting time-of-flight spectra to velocity distributions 206

7. Future Work 211

## LIST OF TABLES

**Chapter 1.**

**Table 1:** Properties of possible nitride substrates. 27

**Chapter 2.**

**Table 1:** Estimated values of $m_p/m$, $N_{Sc}$ and $N_F$ for several gas mixtures. 73

**Chapter 3.**

**Table 1:** Theoretically predicted values of static scaling exponent $\alpha$ and dynamic scaling exponent $\beta$ 94

**Table 2:** Conditions and roughness parameters for GaN(0001) growth. 95

**Chapter 4.**

**Table 1:** Growth conditions for GaN and TEG beam. 127

**Table 2:** TEG beam conditions and corresponding roughness parameters determined by AFM images. 128

**Chapter 5.**

**Table 1:** Appearance potential mass spectrometry 180

**Table 2:** Energy balance table. 181

**Table 3:** Energy analysis of $N_2$/Ar beam expansions. 182

**LIST OF FIGURES**

**Chapter 1**.

**Figure 1:** Energy level diagram of nitrogen showing N, $N_2$ and $N_2^+$, and GaN reaction 28

**Figure 2:** Continuum free-jet expansion 29

**Figure 3**: Top view of SJE/XPS growth and analysis chamber 30


**Chapter 2.**

**Figure 1:** Schematic of two-stage TOF apparatus. 60

**Figure 2:** TOF spectra for 5 sccm $N_2$ in (a) 95 sccm He ($P_o$ = 240 Torr) and (b) 95 sccm Ar ($P_o$ = 429 Torr). 61

**Figure 3:** $\Phi_{exp}$ vs. $P_o$ (Torr). 5% mole fraction seed gas in carrier gas. 62

**Figure 4:** $\Phi_{exp}$ vs. molar flow ratio. 63

**Figure 5(a):** Relative intensity of seeded beam vs. carrier flow rate ($Q_C$) for constant $Q_S$ = 10 sccm. 64

**Figure 5(b):** $\Phi_{exp}$ vs. carrier flow rate ($Q_C$) for constant $Q_S$ = 10 sccm. 64

**Figure 6(a):** $S$ vs. $P_o$, 5%$N_2$ in He. 65

**Figure 6(b):** $S$ vs. $P_o$, 5%$N_2$ in Ar. 65

**Figure 7(a)**: $T_{ll}$ vs. $P_o$ for 5% $N_2$ in He. 66

**Figure 7(b)**: $T_{ll}$ vs. $P_o$ for 5% $N_2$ in Ar. 66

**Figure 8:** $\Phi_{exp}$ vs. $\Phi_{S2}$, a prediction based off of measured speed ratios. 67

**Figure 9:** Mass-weighted speed ratio vs. TSP. 68

**Figure 10:** Speed ratio vs. $P_o$. 69

**Figure 11:** Energy correction factor ($\xi$) vs. VSP. 71

**Figure 12:** $\Phi_{exp}$ versus $N_{Re}/N_F$. 72

**Chapter 3.**

**Figure 1:** Growth rate of GaN with $NH_3$ (0.2 eV to 0.4 eV) in He, vs. %$NH_3$ in He. 96

**Figure 2:** AFM topographs of GaN(0001) grown with $NH_3$ in He. 97

**Figure 3**: RHEED patterns of GaN(0001). 98

**Figure 4**: SEM of GaN grown with 20% $NH_3$ seeded in Ar. 99

**Figure 5:** AFM topographs of GaN(0001) grown with $NH_3$ in $H_2$. 100

**Figure 6**: Roughness vs. surface coverage of Ga and growth rate. 101

**Figure 7**: A log-log plot of roughness versus length scale. 102

**Figure 8**: Scaling analysis of GaN(0001) films. 103

**Figure 9:** (a) Scaling analysis of non-faceted GaN(0001) (b) Scaling analysis of faceted GaN(0001). 104

**Figure 10:** Critical length to the scaling exponent vs. saturation roughness value. 105

**Chapter 4.**

**Figure 1:** QMS intensity of TEG seeded in 100 sccm He and 50 sccm $N_2$. 129

**Figure 2:** RHEED Patterns for clean substrate (top), 0.70 sccm TEG in $N_2$ beam (middle), 0.78 sccm TEG in He beam (bottom). 130

**Figure 3:** 750°C growth runs, low-energy ($N_2$ seeded) growth runs. 131

**Figure 4:** AFM topographs of GaN(0001) grown with TEG-seeded beams. 132

**Figure 5:** AFM topographs of GaN(0001) grown with TEG-seeded 133

beams for different growth times.

**Figure 6:** Roughness plot of GaN(0001) grown with TEG-seeded beams. 134

**Figure 7:** Plot of roughness vs. length, GaN(0001). 135

**Chapter 5.**

**Figure 1:** Schematic diagram of supersonic plasma jet nozzle. 161

**Figure 2:** TOF-APMS system with attached supersonic jet RF plasma source. 162

**Figure 3(a):** TOF spectrum for m/e = 28; 1.5 sccm $N_2$ in 2.5 sccm Ar and 41.2 sccm He. 163

F**igure 3(b):** TOF spectrum for m/e= 14; 1.5 sccm $N_2$ in 2.5 sccm Ar and 41.2 sccm He. 164

**Figure 4(a):** OES spectra of 1.5 sccm $N_2$ in 23 sccm Ar and Ar only gas flow (~150 Torr). 165

**Figure 4(b):** OES spectra of 1.5 sccm $N_2$ in He/Ar and He/Ar only gas flow (~150 Torr). 166

**Figure 5**: TOF-APMS curves for (a) m/e = 40 and (b) m/e = 4 for 1.5 sccm $N_2$ in 2.5 sccm Ar and 41.2 sccm He. 167

**Figure 6(a):** TOF-APMS of 1.5 sccm $N_2$ in 23 sccm Ar, m/e=28. **(b)** TOF-APMS of 1.5 sccm $N_2$ in 23 sccm Ar, m/e=14. 168

**Figure 7(a):** TOF-APMS of 1.5 sccm $N_2$ in 2.5 sccm Ar and 41.2 sccm He, m/e=28. **(b)** TOF-APMS of 1.5 sccm $N_2$ in He/Ar, m/e=14. 169

**Figure 8:** TOF-APMS of 1.5 sccm $N_2$ in He/Ar, m/e= 28. Data is fit to cross sections for $N_2$(A) to determine the percentage concentration. 170

**Figure 9:** Calculation of $\eta$ and $\alpha$ for 6.7% $N_2$ in Ar and 4% $N_2$ in He/Ar vs. electron energy (eV). 171

**Figure 10:** Dissociation fraction vs. %$N_2$. 172

**Figure 11(a)**: TOF of an 80 W, 1.5 sccm $N_2$ in 23 sccm Ar expanision; m/e=40 signal at 70 eV. 173

**Figure 11(b)**: TOF of an 80 W, 1.5 sccm $N_2$ in 23 sccm Ar expanision; m/e=28 signal at 23 eV. 173

**Figure 11(c)**: TOF of an 80 W, 1.5 sccm $N_2$ in 23 sccm Ar expanision; m/e=14 signal at 23 eV. 174

**Figure 12(a):** TOF data from a 80-W, 1.5 sccm $N_2$ in 2.5 sccm Ar and 41.2 sccm He plasma supersonic jet. m/e=28 and at 70 eV electron impact energy. 175

**Figure 12(b)**: TOF data from a 80-W, 1.5 sccm $N_2$ in 2.5 sccm Ar and 41.2 sccm He plasma supersonic jet. m/e=14 and at 23 eV electron impact energy. 176

**Figure 12(c)**: TOF data from a 80-W, 1.5 sccm $N_2$ in 2.5 sccm Ar and 41.2 sccm He plasma supersonic jet. m/e=4 and at 70 eV electron impact energy. 177

**Figure 12(d)**: TOF data from a 80-W, 1.5 sccm $N_2$ in 2.5 sccm Ar and 41.2 sccm He plasma supersonic jet. m/e=40 and at 178

70 eV electron impact energy.

**Figure 13:** $T_o$ vs. $N_2$ flow rate. 179

# 1. Introduction

## 1.1 Background of GaN

Group III nitrides (AlN, GaN, InN and mixed alloys) provide many opportunities for high power, high temperature devices. These materials allow the possibility of blue light emiiting diodes (LEDs) and laser diodes. Applications can be found in the areas of optics, data storage, solar power and military equipment.[1] Key advantages to these materials are their high thermal conductivities, resistance to radiation, low chemical reactivity, large avalanche breakdown fields and large high-field electron drift velocities. GaN (bandgap of 3.34 eV) forms a continuous range of solid solutions with AlN (6.28 eV) and InN (1.95 eV), allowing production of laser diodes with tunable emission frequencies covering the visible and ultraviolet (UV) region.[1] Nichia Chemical Industries of Japan and Cree Research of Research Triangle Park (RTP) have developed commercial high-efficiency blue and green LEDs consisting of GaN. Full-color flat panel and television displays, indicator lights, and traffic signals can incorporate these devices. Blue GaN/InGaN multiquantum-well, continuous-wave laser diodes with an estimated 10,000 h lifetime have been achieved by Nichia Chemical.[2] Significant gains in optical-storage density of compact disks will be effected with employment of blue lasers (380-450 nm) as opposed to current technologies using red or infrared (680-780 nm) laser diodes.

Optimal GaN growth is hampered by the lack of bulk GaN single crystals or a suitable substrate for heteroepitaxial growth. Key properties involved finding a suitable substrate for heteroepitaxial growth of GaN films are lattice mismatch, differences in coefficients of thermal expansion and the structure of the substrate, which should match GaN's wurtzite (or cubic) structure. Sapphire is the most common used substrate because of

its abundance. Adversly, it has a 14% lattice mismatch with GaN at the $GaN(0001)/\alpha Al_2O_3(0001)$ interface and possesses a higher thermal coefficient of expansion. Other materials, such as hexagonal SiC, have been investigated due to their closer lattice match. Table 1 lists the properties of potential substrate materials.[3] Buffer layers of AlN and GaN attempt to relax strains due to lattice mismatch and thermal expansion.

High-quality GaN films employ sapphire as the substrate of choice using metal-organic chemical vapor deposition (MOCVD) at a substrate temperature above 1000ºC. Deposition of a typical buffer layer occurs at 450-600ºC.[4] Crystallization of the amorphous buffer layer commences during annealing, allowing GaN films to be grown with a reduced number of defect densities ($\sim 10^8$ $cm^{-2}$). A recent development bringing about low-density GaN films is lateral epitaxial overgrowth (LEO). A MOCVD-grown GaN substrate is patterned with $SiO_2$. GaN selectively deposits vertically to the top of the mask and then begins a lateral growth over the mask. Transmission electron microscopy (TEM) demonstrates the lack of threading dislocations in the laterally overgrown material.[2,5] MOVCD suffers from the problem of high substrate temperature, leading to material incompatibilities, so alternate procedures are investigated to grow at lower temperatures.

## 1.2 Growth Methods

### 1.2.1 Chemical Vapor Deposition

Reactions of gaseous precursors on a solid substrate resulting in the formation of a thin film define chemical vapor deposition (CVD). Typically, precursors are transported laminarly to the substrate surface. The heated substrate surface provides the energy necessary to decompose the precursor in a cold-wall CVD reactor. Atmospheric CVD (ACVD) involves pressures from 100 - 1000 Torr, while low-pressure CVD (LPCVD)

involves pressures from 0.1 Torr to 1 Torr. Plasma-assisted CVD (PACVD) employs an external energy source to generate plasma and hence allow the reaction to proceed on the substrate. The first epitaxial GaN film was grown by Maruska and Tietjen[6] by flowing HCl vapor over metallic Ga, producing GaCl, which reacted downstream on the substrate with $NH_3$. Gallium precursors such as GaCl, $GaCl_2$, $GaCl_3$, Ga $(C_2H_5)Cl$, and $GaCl_2NH_3$ have been used to grow GaN;[1] however, metal-organic CVD (MOCVD) has been the most useful growth technique for producing device-quality GaN films. In MOCVD, a metal-organic gallium precursor, such as triethylgallium (TEG) or trimethylgallium (TMG) reacts with $NH_3$ on the substrate to produce high-quality GaN films.

High growth rates, good compositional control, uniformity and high crystal quality can be achieved by MOCVD of GaN. At substrate temperatures exceeding 1000ºC,[7] ample thermal energy is available to overcome activation barriers for precursor decomposition and to provide high adatom surface migration. While producing device-quality GaN films, MOCVD growth at high temperatures has some drawbacks. Disadvantages associated with high growth temperatures and post-annealing steps include thermal stresses in the film, poor compatibility with existing integrated circuit technology, and difficulty of indium alloy formation.[8] The high bond energy of $N_2$ (9.5 eV) prevents its use and necessitates the use of $NH_3$ as the nitrogen precursor in MOCVD. Hydrogen from $NH_3$ has been found to compensate p-type dopants, such as Mg; thus, a high-temperature anneal is required for dopant activation.[7]

### 1.2.2 Molecular Beam Epitaxy

Molecular beam epitaxy (MBE) provides a low temperature alternative for growth and doping of GaN using active N species. MBE involves the impingement of thermal-energy beams of atoms or molecules onto a heated substrate under high vacuum or better conditions. As a process, MBE inherently offers the following benefits over CVD for thin film growth, including a) low growth temperatures, b) abrupt material interfaces due to negligible bulk diffusion at low temperatures and automated shutter control, and c) facility for in-situ surface analysis, typically reflection high energy electron diffraction (RHEED), to maintain desired surface reactions, as well as examining crystal growth.[9] A reduction in growth temperature is achieved by providing highly reactive species (e.g., atoms, radicals, excited state molecules) for growth. MBE growth of GaN using active N species (e.g., N, $N_2^+$) is advantageous because as-deposited Mg-doped films show p-type conductance without a post anneal, a step necessary for $NH_3$ MOCVD-grown GaN films.[10-12]

Active nitrogen species for the growth of III-V semiconductors can be generated by plasma sources. Broad ranges of plasma sources have produced GaN. These plasma sources segregate into two categories: ones that produce primarily active molecular nitrogen and ones that produce primarily atomic nitrogen. Electron cyclotron resonance (ECR), compact coaxial magnetrons (CCM), and hollow-anode nitrogen plasmas activate nitrogen into mostly molecular nitrogen states, while inductively coupled radio frequency plasmas typically convert nitrogen into atomic nitrogen species.

ECR nitrogen sources produce mainly 2$^{nd}$-positive series excited molecular nitrogen ($N_2^*$) and nitrogen molecular ions ($N_2^+$), with little atomic nitrogen. ECR produces GaN at a rates of 40 nm/h with conditions of 50-150 W, nitrogen pressures of $5\times10^{-5}$ to $3\times10^{-4}$ Torr, and sapphire (0001) substrate temperatures of 550-700ºC. ECR grown films are rougher

with higher plasma power, due to damage from high-energy ions, although they are quite stoichiometric in nature. Lower power ECR produces structurally smooth films, but they are nonstoichiometric. The belief is that the higher power ECR produces a higher flux of atomic nitrogen.[12] In some cases, a grid voltage can be applied to a substrate to drive away the impinging nitrogen ions. Photoluminescence (PL) measurements indicate that midgap state defects (yellow band) are greatly reduced when high-energy nitrogen ions are involved in the growth process.[13] However, the overall growth rate improves when the ions are driven away by the grid bias.

Compact coaxial magnetron (CCM) active nitrogen sources produce primarily excited nitrogen molecules instead of atomic nitrogen. CCM activators employ both radio frequency power and a magnetic field to produce a plasma. Preliminary results for CCM activators indicate a growth rate of 0.5 μm/h on GaAs(113) can be achieved with a power level of 250 W. No degradation of luminescence quality of the GaN epilayers has been observed with this method.[14] In addition, a CCM activator has produced GaN at a growth rate of 0.5 μm/h on $Al_2O_3$ (0001) and also $NdGaO_3$ (101), yielding similar crystal quality.[15]

The hollow-anode plasma source operates in a manner that produces activated nitrogen molecules, but at low kinetic energies (~ 1 eV).[16] Very little atomic nitrogen is yielded from this source. GaN grown at 600-800ºC on SiC(0001) or $Al_2O_3$(0001) exhibits a x-ray diffraction (XRD) rocking curve full width half-maximum (FWHM) of 5 arcmin.[17] Gassmann achieves homoepitaxial growth of GaN (0001) with a hollow anode source, yielding a high quality film as shown by transmission electron microscopy (TEM) and PL.[18] However, the small thickness of the grown film (~0.5 μm in 8 hrs) limits analysis via XRD.

Atomic nitrogen has a higher potential energy than excited molecular nitrogen (Fig. 1). Inductively coupled radio frequency plasmas (ICP) are efficient generators of atomic nitrogen and 1$^{st}$-positive excited nitrogen molecules. A number of ICPs have been applied to grow GaN, including the Oxford Applied Research CAR25, SVTA ICP and the Pollard source.

Ptak and coworkers have produced GaN using an Oxford source (atomic nitrogen) and also using an EPI Unibulb source (significant flux of $N_2^*$)[19] at a temperature range of 700-770ºC. Growth rates of GaN using the Oxford source are 0.25 μm/h at 700ºC and declines logarithmically up to about 770ºC. However, the EPI source produces a fairly constant growth rate of 1μm/h. They propose that the atomic N has too much excess energy to contribute to the surface growth, so that although it can drive the forward reaction, it also raises the temperature of the substrate enough to also drive the decomposition reaction. Activated molecular nitrogen is suspected to provide a mechanism for energy dissipation away from the surface: one N atom is incorporated into the surface while the other carries away the excess energy.

Shokhovets and coworkers grow GaN on GaAs(001) at 700-710ºC with an Oxford nitrogen plasma source at a rate of 0.3 μm/h.[20] Tarsa et al., growing GaN(0001) homoepitaxially on MOCVD grown GaN (to avoid lattice mismatch issues), yield a growth rate of 0.5μm/h with an Oxford plasma source at 650ºC.[21] Tarsa et al. find a strong morphological dependence of the III/V ratio, as N-stable conditions display films with rough surface morphology with columnar structure brought about by stacking faults. Ga-stable conditions bring structure quality comparable to MOCVD-grown GaN. Myers et al. demonstrated similar growth, except at 730ºC and on sapphire (0001),[22] finding the same

structural dependence of the III/V ratio. Zhao and coworkers employ As as a surfactant and grow homoepitaxial GaN with the Oxford source. Increased temperature of the surface improves surface morphology.[23]

The SVTA™ source primarily provides atomic nitrogen as opposed to activated molecular nitrogen. Piquette grows on sapphire(0001) showing that Ga-rich conditions yield a less rough surface.[24] SVTA™ grown cubic (In,Ga)N shows promise with regular patterns. Johnson produces high quality GaN at 0.4 μm/h for SVTA and Oxford sources.[25]

The EPI source generally produces activated molecular nitrogen. Reifsnider has grown reasonable GaN for MBE on sapphire (0002), while Johnson produces high quality GaN at 800ºC with a growth rate of 1μm/h for the EPI source.[26] Kushi and coworkers achieved a high growth rate of 1.2-1.4 μm/h on top of a GaN buffer layer. The buffer layer was grown via migration enhanced epitaxy (MEE), where the source of Ga involves 2 s growth interruptions to assist Ga adatom migration. The buffer layer is only produced at 0.3μm/h.[27] Beresford concludes that the III/V ratio is the key factor in growth of GaN, as he uses an EPI source of atomic nitrogen.[28]

The RF nitrogen source has produced the higher homoepitaxial GaN films grown at 0.25-0.30 μm/h and 800ºC substrate temperature.[29] Using sapphire as the substrate, GaN growth achieves rates of 0.8-1.0 mm/h at 730ºC-780ºC using RF nitrogen sources.[22,26] Ions produced by the ECR plasma sources damage GaN films in the growth regime of 0.3-0.4 μm/h at 650ºC-850ºC. A bias voltage on a grid installed between the substrate and holder can steer away ions.[12,13,30,31] Reactive ion MBE (RIMBE) using $NH_4^+$ ions has also been investigated, but the films contained high concentrations of ion-induced defects.[32]

Gas source MBE (GSMBE) growth using $NH_3$ obtains growth rates between 0.5-2.0 μm/h at 700ºC-850ºC.[33,34] GSMBE employs thermal energy $NH_3$ molecules and avoids ion damage associated with N plasma sources. H production, due to $NH_3$ decomposition, may induce higher growth rates of GaN, as it is found in PAMBE.[22] The downside is that H containing films limit chances of active p-type doping.

### 1.2.3 Supersonic Jet Epitaxy

Supersonic jet epitaxy (SJE) refers to the use of neutral beams of atoms or molecules with precisely controlled translational energies for epitaxial crystal growth. SJE makes use of seeded supersonic jets to impart directed kinetic energy to precursor molecules that can greatly exceed the average thermal energy of the source. Commonly, the energy required to overcome barriers to precursor chemisorption and adatom surface diffusion is supplied by high substrate temperatures. Ceyer and coworkers illustrated, in their investigation of $CH_4$ adsorption on Ni(111), that the energy at which a molecule collides with a surface can be the key factor in determining its reactivity with or on the surface.[35] Following a Lennard-Jones potential energy diagram model, direct dissociative chemisorption can only occur for molecules incident on the surface with energies higher than the energy of the barrier. Mullins and coworkers studied dissociative chemisorption of oxygen on Ru(0001) and ethane on Ir(111) and describe two reaction mechanisms for dissociative chemisorption.[36,37] When a molecule with low kinetic energy strikes the surface, it becomes trapped in a physisorbed precursor state, where there is competition between desorption to the gas phase and dissociative chemisorption. As the kinetic energy of the incident molecule increases, the energy must be dissipated by the surface for physisorption (trapping) to occur; thus, increased kinetic energy decreases adsorption probability. The adsorption probability is also

temperature dependent, since the energy to surmount the barrier to dissociative chemisorption comes from the thermal energy of the substrate. In the high kinetic energy limit, molecules overcome the chemisorption barrier through a direct adsorption mechanism. In this regime, the adsorption probability increases with increasing kinetic energy and is independent of substrate temperature. By fine-tuning the incident kinetic energy of precursor molecules, through the use of supersonic molecular beams, an increase in the dissociation probability of precursors such as $Si_2H_6$, triethylaluminum (TEA), TEG, and $NH_3$ has enabled growth of Si, AlN and GaN films at higher rates.[38-43]

### 1.2.4 Seeded Supersonic Jets[44,45]

Free jet expansion, or continuum jet expansion from a high-pressure ($P_o$) gas source into a low-pressure background ($P_b$), produces a higher intensity beam with a tighter velocity distribution of exiting gas molecules than an effusive source. Fig. 2 illustrates the features of a free jet expansion. In the nozzle, the gas at $P$ and $T_o$ has negligible velocity and is accelerated due to a pressure difference ($P_o$-$P_b$) towards the source exit. If the ratio $P_o/P_b$ is > 2.1, the gas mean velocity equals the local speed of sound, Mach number equal to one, at the nozzle exit. As seen in Fig. 2, the under-expanded, supersonic flow expands on exiting the nozzle in order to meet the boundary conditions imposed by the background pressure. The region of expansion before the Mach disk shock is termed the zone of silence and is a region of free isentropic expansion. A conical skimmer is usually place within this zone in order to form a molecular beam. Assuming the expanding gas to be ideal with constant specific heat and neglecting viscous and heat conduction effects, the energy balance can be used to determine the terminal velocity of the gas:

$$V_\infty = \sqrt{\frac{2R}{W}\left(\frac{\gamma}{\gamma - 1}\right)T_o} \tag{1}$$

where $R$, $W$, $T_o$ and $\gamma$ are the gas constant, species molecular weight, gas stagnation temperature and molar heat capacity ratio $C_p/C_v$, respectively. For gas mixtures, diluting a heavy molecule in a light gas will accelerate the heavy species; this technique is termed molecular seeding. The energy of an individual species in a seeded molecular beam is:

$$E_i = \left(\frac{W_i}{W}\right)\frac{\gamma R T_o}{(\gamma - 1)} \tag{2}$$

assuming ideal gas behavior which includes zero velocity slip and infinite terminal Mach number. Velocity slip quantifies the difference of velocities between two species with different masses.

If the background pressure is sufficiently low (<$10^{-3}$ Torr), at some point in the expansion, the flow will enter the molecular flow regime with a concomitant reduction in the collision frequency. This transition usually occurs beyond the point where $V=0.98V_x$. The product of the stagnation pressure and orifice diameter divided by temperature, $P_o d/T_o$ represents the total number of two body collisions undergone during the expansion process, and characterizes the degree of cooling for a molecule. Adjustments made to $P_o d/T_o$ through system design can produce supersonic molecular beams with very low velocity spreads. Precursor molecules can obtain a specific mean kinetic energy by seeding in a light carrier gas and adjusting the seeding ratio and nozzle temperature.

While most motion of molecules streamlined from a skimmer is directed parallel to the centerline of the orifice, some perpendicular motion remains. This motion is characterized as perpendicular temperature ($T_\perp$). The downstream perpendicular velocity

distribution is typically not Gaussian, however. Using beam intensity measurements, Beijerinck and Verster were able to correlate this $T_{\perp}$ for some singular monoatomic and diatomic beams using a quitting surface model.[46] Poulsen and Miller measure the $T_{\perp}$ ,$T_{ll}$ and $T_r$ of pure $N_2$ and also for $N_2$/Ar and $N_2$/He mixtures.[47]

#### 1.2.5 Applications of Supersonic Jet Epitaxy (SJE)

SJE, the use of controlled energy precursors, is a relatively new technology, but it has been successful in the growth of AlN, GaN and Si. Seeded SJE has allowed for the low-temperature growth of Group IV and III-nitride semiconductors by providing high intensity, high energy precursors for thin film growth.[48] Engstrom et al. have deposited Si films using supersonic beams of $Si_2H_6$ and reported an increase in the dissociative adsorption probability with increasing incident translational energy,[38,49,50] leading to higher Si epitaxial growth rates result under low hydrogen coverage conditions.[39,51] SJE has been used in order to lower the substrate temperature and grow epitaxial SiC. [52]

Group III-N films have also been grown with SJE in order to lower the growth temperature,[40,53] applying to both group III (metal-organic compounds) and group V compounds ($NH_3$ and $N_2$ plasmas). Growth rates of AlN by Brown et al.[40] were reported to increase greatly when TEA was seeded in either He or $H_2$. They concluded hyperthermal kinetic energy of AlN allowed an activation barrier for dissociative chemisorption to be surmounted. McGinnis et al. grew GaN(0001) with high energy (~2.1 eV) and low energy (~0.5 eV) TEG - seeded supersonic molecular beams, formed by using He and $N_2$, respectively.[54] By measuring GaN(0001) growth rates at 750°C under $NH_3$-rich conditions and using quadrupole mass spectrometer (QMS) data, they determined Ga incorporation efficiencies to be higher for TEG seeded in $N_2$, indicating a precursor-mediated process.

Previous studies of group III metal-organic compounds on semiconductor surfaces are shown to be unactivated, thus going through a precursor-mediated reaction pathway.[55]

SJE of GaN has been accomplished using hyperthermal $NH_3$ beams and TEG jets,[42,49,54] as well as with a supersonic jet of nitrogen atoms and a Ga effusion source.[41] GaN was also grown on sapphire (0001) using a supersonic jet of N atoms (in He) at a rate of 0.65 μm/h at 750ºC. Single crystal films were grown, as evidenced by XRD, but the surface was rough, as indicated by a spotty RHEED pattern. Sellidj et al. suggested the crystal quality of the films was degraded because of energetic ion bombardment from the N plasma. It was suggested that the kinetic energy of N atoms from the plasma source might hinder growth because it must be dissipated by the surface for the N atom to stick.[41] Jordan et al. use a corona discharge supersonic jet of $N_2$(A) to grown GaN(0001) on buffer layers of AlN deposited in situ on 6H-SiC(0001), citing a 100% N incorporation efficiency.[56] Seeded supersonic jets of $NH_3$ have been employed to grow GaN and AlN on SiC(0001).[57] McGinnis et al. grew GaN(0001) homoepitaxially on MOCVD grown GaN(0001) on 6H-SiC(0001) with a seeded supersonic jet of $NH_3$ and consequently proposed $NH_3$ chemisorption to be precursor-mediated. Work in SJE provides the opportunity to determine the effects of precursor kinetic energy on thin film growth.

### 1.3 Homoepitaxial Growth of GaN

The quality of heteroepitaxial GaN films is as dependent on substrate quality and growth of high quality buffer layers as it is on the actual growth method. Slight differences in the buffer layer can play a dominant role in determining the properties of subsequently gown films. The development of device-quality GaN films on sapphire hinged on the use of low-temperature AlN[58,59] and GaN[9,60] buffer layers. While these buffer layers have been

studied extensively and are used routinely, fundamental studies of GaN epitaxial growth are more successfully accomplished on monocrystalline GaN substrates, thereby avoiding lattice mismatch problems.

Homoepitaxial growth studies have been hampered by the slow development of bulk single-crystal GaN growth methods. Only a few successful attempts to grow bulk crystals of GaN have been reported. Porowski et al. grew crystal plates 8 mm square x 0.2 mm thick from a Ga melt under nitrogen hydrostatic pressure.[61,62] Davis and coworkers report the highest quality GaN crystals to date, as evidenced by optical microscopy, Raman spectroscopy and photoluminescence.[63,64] Bulk crystals, 0.2-0.3 mm wide and 0.7-1.0 mm long, were grown from GaN powder sublimed in an $NH_3$ atmosphere and condensed on a 6H-SiC(0001) substrate. Thick (1-2mm) MOCVD-grown GaN epilayers have been employed, in lieu of bulk GaN crystals, as substrates for homoepitaxial growth and for surface science studies.[21,23,65]

### 1.4 Growth of GaN vs. V/III ratio and Surface Morphology

Gassmann et al. reported MBE homoepitaxial growth on bulk GaN crystals yielding a GaN epilayer with one of the lowest reported defect densities;[18] however, this film does exhibit high dislocation densities near the film/substrate interface. Gassmann et al. suggests that three-dimensional growth with subsequent coalescence of the islands is the most likely source of the dislocations. Tarsa et al. illustrate how changes in the V/III ratio can produce a transition between three-dimensional and two-dimensional growth during PAMBE using a RF nitrogen source.[21]

Tarsa et al. examined surface structure and morphology using in-situ RHEED, ex-situ TEM, and ex-situ atomic force microscopy (AFM) for films grown at 650ºC using various

Ga fluxes. As the epilayers were grown under progressively lower Ga fluxes, RHEED patterns along the [2110] zone axis changed from truncated streaks to spots indicating a transition to three-dimensional growth under high V/III ratio conditions. Films grown under a high Ga flux exhibited a high density of spiral growth features with hexagonal boundaries, as evidenced by AFM. Films display coarse grainy features with a Ga flux of $6.2 \times 10^{-7}$ Torr BEP.[21] Feenstra et al., examined GaN surface reconstructions during homoepitaxy on GaN/sapphire substrates using RHEED and found N-rich growth conditions produced a spotty RHEED pattern indicating three-dimensional growth. They also noted the appearance of a streaky $1 \times 1$ RHEED pattern if Ga-rich conditions were maintained. The resulting film surface was characterized by large, atomically flat terraces and growth spirals.[66] Other investigators looking at MBE heteroepitaxial growth have also reported a similar dependence of growth morphology on V/III ratio.[22,67] The V/III ratio can affect the properties of the film grown irrespective of the active nitrogen source, as an ECR grown GaN film exhibits inversion domains with higher Ga to N ratios.[31] Pavloska, *et al.* grew homoepitaxial GaN(0001) by supersonic jet epitaxy (SJE) using $NH_3$-seeded beams at substrate temperatures of 655-710°C and reported a similar 3D to 2D transition.[68] Pavloska, *et al.* monitored the growth surface by in situ low energy electron microscopy (LEEM) and low energy electron diffraction (LEED) to gain insight into which growth mode prevails during $NH_3$-SJE of homoepitaxial GaN(0001) films.[69] Low V/III flux ratios yielded films with non-faceted surfaces resulting from quasi-two-dimensional growth, while high V/III flux ratios produced films with faceted surfaces. The literature seem to indicate that a V/III flux ratio-dependent faceted to non-faceted growth transition is a general phenomenon in GaN MBE

regardless of the substrate, GaN polarity, choice of nitrogen precursor, and the substrate temperature.

Previous investigators[21,22] have ascribed faceted GaN growth to a stochastic (statistical) roughening mechanism. Tarsa, *et al.* hypothesized that the interfacial roughness arises from a restricted Ga diffusion length under N-rich growth conditions.[21] For homoepitaxial films grown under N-rich conditions, Myers, *et al.* show XTEM results with inversion domain boundaries (IDBs) at the center of pyramidal hillocks.[22] The XTEM results of Liliental-Weber, *et al.* suggest that pinholes (growth pits) and nanotube defects in GaN films arise from differences in growth rates for GaN(0001) and GaN($000\bar{1}$) (Ga- and N-polar surfaces, respectively).[69] Daudin, *et al.* determined by convergent beam electron diffraction (CBED) that non-faceted GaN films had Ga-termination whereas pyramidal hillock formations (faceted GaN) had tiny columnar inversion domains (with Ga polarity) imbedded in a matrix exhibiting an N polarity.[70]

### 1.5 GaN Reaction Chemistry[16]

The central consideration in GaN growth is that the molecular $N_2$ species alone does not have enough energy to overcome the kinetic barrier. Providing high energy $NH_3$ is one alternative, but another effective alternative is to use active nitrogen sources produced from a plasma. Fig. 1 demonstrates that any of the activated nitrogen species has plenty of energy to overcome the kinetic barrier associated with GaN growth. The kinetic barrier displayed is for a typical substrate temperature and nitrogen flux. The following reactions can occur to produce GaN:

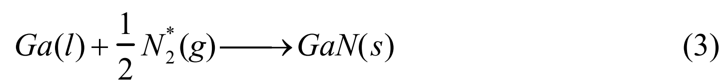

$$Ga(l) + \frac{1}{2}N_2^*(g) \longrightarrow GaN(s) \qquad (3)$$

where $N_2^* = A^3\Sigma_u^+, B^3\Pi_g, a^1\Pi_g, C^3\Pi_u$,

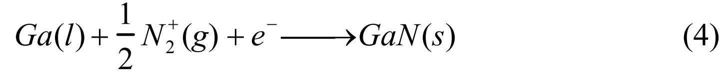

$$Ga(l) + \frac{1}{2}N_2^+(g) + e^- \longrightarrow GaN(s) \quad (4)$$

where $N_2^+ = {}^2\Sigma_g^+$,

$$Ga(l) + N(g) \longrightarrow GaN(s) \quad (5)$$

where $N = {}^4S$,

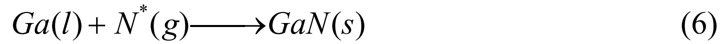

$$Ga(l) + N^*(g) \longrightarrow GaN(s) \quad (6)$$

where $N^* = {}^2P, {}^2D$.

While all of the following N precursors are candidates for growth, the exact effect of ion damage and accomodation of excess energy is unclear. A competing reaction exists, specifically decomposition:

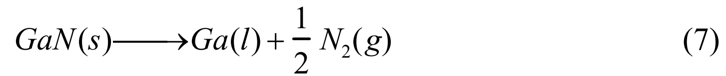

$$GaN(s) \longrightarrow Ga(l) + \frac{1}{2}N_2(g) \quad (7)$$

Although this is a thermodynamically favorable reaction, there exists a rather large kinetic barrier opposing its occurrence.[71] There is not enough kinetic energy available to have this reaction proceed at normal MBE temperatures (<850ºC). Fig. 1 indicates that there is plenty of excess energy available in the impinging active nitrogen species, which becomes accommodated in the GaN surface. Unfortunately, this accommodated energy might allow the kinetic barrier of the undesired decomposition reaction to be surpassed. Consequently, Ga droplets, formed on this surface, catalytically enhance the decomposition rate, hence worsening the situation.[72] Hence, as thus seen so far, PAMBE has lower growth rates than expected. Mullins and coworkers have demonstrated that they can achieve a growth rate of

0.65 μm/h with an inductively coupled plasma source.[41] The kinetic energy of the impinging active nitrogen species will greatly affect the growth rate of the GaN film.

The energy of the impinging active nitrogen species affects the quality of the film. It can alter the structure of the GaN film. Excess energy combined with ion bombardment can create undesired nitrogen vacancies, ruining the device characteristics of the film. Another undesired reverse reaction involves GaN evaporation:

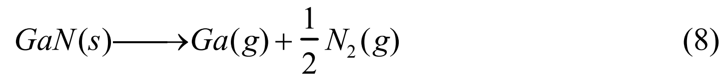

$$GaN(s) \longrightarrow Ga(g) + \frac{1}{2} N_2(g) \quad (8)$$

The kinetic barrier associated with this reaction is even higher. The evaporation coefficient, $\alpha$, defines the ratio of the observed evaporation rate compared to the thermodynamically predicted value. GaN possess an $\alpha$ of $< 1\times 10^{-3}$ - $6 \times 10^{-3}$. This high kinetic barrier allows the possibility of meta-stable growth.[71]

## 1.6 Experimental Methods

### 1.6.1 SJE/XPS System

The multi-chamber SJE/XPS system is shown in Fig. 3. The source chamber is pumped with an 8000 l/s diffusion pump (Varian VHS-400) connected to a Roots blower (Leybold WKP 250AS) and a two-stage mechanical pump (Leybold DUO 065DC) in series. The second differential pumping stage employs a 2000 l/s diffusion pump (Varian VHS-6) with a fluid-cooled baffle (Varian 0336-F8277), which is backed with a mechanical pump (Alcatel 2033A). The two nozzles, $NH_3$ and TEG, have replaceable laser-drilled orifices (Energy Beam Sciences) of 140 and 82 μm, respectively, and can be heated to 800ºC by 240W cable heaters (Watlow). Both nozzles are mounted to allow xyz adjustment for nozzle-skimmer alignment. The $NH_3$ nozzle body is made from titanium to inhibit $NH_3$

decomposition at high temperatures,[73] and the TEG nozzle is made from stainless steel. A skimmer mounting plate separates the first and second pumping stages. Two conical skimmers (Beam Dynamics), each having a 1-mm aperture and a 20-mm base, are used to extract the supersonic molecular beams. The skimmers have an included angle of 25 at the top section and 70 at the base. The second pumping stage and the growth chamber are separated by a plate containing two collimation apertures of $5 \times 5$ mm$^2$. The two molecular beams are incident onto the substrate at 6° with respect to the surface normal, and the deposition area on the substrate is $15 \times 15$ mm$^2$.

The sample is placed in the loadlock, pumped to $10^{-4}$ Torr by an Alcatel Drytel pump, and transferred to the growth chamber via an APD cryo-pumped transfer line (base pressure $6\times10^{-9}$ Torr). The growth chamber is equipped with a turbomolecular drag pump (Balzers, TMU 520) backed by a mechanical pump (Alcatel), which provides a $3\times10^{-9}$ Torr base pressure. The Mo substrate heater assembly is mounted on a magnetically coupled rotary-linear transfer rod that is attached to a bellows for tilt motion. The solid Mo sample holder is heated by radiation from a pyrolytic boron nitride (PBN)-coated graphite heating element (Advanced Ceramics). The power is supplied by a 2000W DC power supply (Hewlett Packard, 6269B), which is connected via two copper electrical feedthroughs. A hot-lip Ga K-cell (SVTS-450-20HL) and cold-lip Al K-cell (EPI) provide Ga and Al fluxes. The lip of each K-cell is about 5" from the substrate and a shutter turns off the flux.

### 1.6.2 Film Characterization

On-line surface characterization is provided by x-ray photoelectron spectroscopy (XPS) in a UHV surface analysis chamber. The XPS instrument (Physical Electronics, PHI 3057) is equipped with a dual anode (Al/Mg) x-ray source, 15-kV x-ray generator, spherical

capacitor analyzer (SCA), Omni Focus III small area lens, 16-element multichannel detector, and amplifier/discriminator. The sample is mounted on a rotary-tilt stage controlled by a xyz manipulator (Thermionics). The analysis chamber is pumped by a Perkin-Elmer TNBXion pump-TSP combination to a base pressure of 7 X $10^{-11}$ Torr.

#### 1.6.2.1 Surface Analysis

XP spectra were taken with both Mg Ka (1253.6 eV) and Al Ka (1486.6 eV) anodes to isolate N(1s),O(1s),C(1s) and Ga($2p_{3/2}$) photoelectron peaks from other interfering signals. Photons from x-ray penetrate the solid, interact with atoms and cause electrons to be emitted from the near-surface region. The measured kinetic energy of the emitted electrons yields information about elemental composition because each element has a unique set of binding energies.

$$KE = h\nu - BE - \Phi \quad (9)$$

where $h\nu$ is the photon energy, $BE$ is the binding energy of the core level from which the electron originates, and $\Phi$ is the spectrometer work function. Auger electrons can also be emitted due to relaxation of the atoms after photoemission. Because the kinetic energies of Auger electrons do not change with the photon energy, Auger peaks shift to higher apparent binding energy positions as x-ray energy is increased. As a result of overlap with Ga Auger peaks, N(1s) and O(1s) photoemission peaks can only be seen clearly in Mg Kα spectra, and C(1s) is only seen in Al Kα XP spectra. The Ga($2p_{3/2}$) peak ($BE$=1117.0 eV) due to the large thermal electron background using the Mg anode (1200eV) is best measured with the Al Kα anode (1400eV). The Ga(3d) peak has a binding energy of 19.5 eV. The low binding

energy, corresponding to high kinetic energy of the photoelectron, makes the Ga(3d) peak the least surface sensitive. Thus, the XP spectra are normalized to the Ga(3d) peak area.

In-situ reflection high-energy electron diffraction (RHEED) measurements were made using a Fisons LEG 110 15-kV electron gun and 100-mm Al-coated phosphor screen. Monoenergetic electrons are elastically scattered from the surface at glancing incidence, and the diffraction pattern is imaged on a phosphor screen. Smooth single crystal films exhibit sharp streaks that represent rods in the 2D reciprocal lattice net. The emergence of a spotty RHEED pattern indicates that the surface is rough and the diffracted electron beam is being transmitted through 3D surface features. RHEED patterns of the GaN substrate before and after in-situ cleaning, and after GaN growth were taken at 15kV. Scanning electron microscope (SEM) images of GaN films are obtained using a JEOL 6400FE SEM with a 5-kV cold field emission electron gun. Both surface and cross sectional images are taken. The atomic force microscopy (AFM) images were obtained using a Digital Instruments Dimension 300 Scanning Probe Microscope with a Nonoscope IIIa Controller. A silicon tip with a nominal tip radius of curvature of 5-10 nm was used. Depth profiles of GaN films are recorded using a Cameca IMS-6f secondary-ion mass spectroscopy (SIMS) instrument. Elemental composition can be determined with a detection limit of approximately $10^{15}$ $cm^{-3}$ throughout the film thickness. The facility features $O_2^+$, $O^-$ and $Cs^+$ sputtering beams and a mass resolution of 25000M/dM. The GaN films were typically sputtered by $Cs^+$ ions.

### 1.7 Species Segregation in Seeded Molecular Beams

Characterization of supersonic molecular beams has been accomplished by many previous investigators.[46,74-76] Single species supersonic molecular beams have been well characterized in centerline intensity,[46] parallel speed ratio (parallel velocity distribution) and

energy. Binary supersonic molecular beams properties are not as easy to characterize. Predictions have been made for energy and speed ratio of binary supersonic molecular beams,[74-76] but there has been little experimental conformation of these predictions. Particular interest is in aerodynamic focusing, a phenomenon segregating the lighter gas away from the centerline of the beam and concentrating the heavier gas towards the centerline.[46] In general, aerodynamic focusing is not as well quantified as the energetic effects of seeded SJE in the thin film growth literature. Accurately determining the intensities (fluxes) of reactant molecules at the growth surface is essential in any thin film growth process. For seeded supersonic molecular beams, the enrichment of the beam with respect to the seeded species is defined by an enrichment ratio,

$$\Phi = \frac{(J_S / J_C)_d}{(Q_S / Q_C)} \tag{10}$$

where $Q_S$ and $Q_C$ are the gas flow rates of seed and carrier gas to the nozzle, respectively, while $J_{S,d}$ and $J_{C,d}$ are the fluxes of the seed and carrier gas at the detector (or thin film surface), respectively. Eres, et al. first noted focusing phenomena in growth of GaAs using seeded supersonic beams, where growth profiles had a $cos^{22}\ \theta$ dependence,[77] as opposed to the standard $cos^4\ \theta$ dependence found in single component supersonic jet expansions.[78] Also, Pacheco, et al. noted focusing phenomena in Si epitaxial growth using disilane seeded in $H_2$.[39] Fernandez de la Mora et al.[79] provides experimental data for heavy gas expansion radial distributions for largely disparate gas mixtures at short axial distances away from the nozzle and correlates them to stagnation fluid properties, namely a dimensionless group, the Stokes number, $N_S$, (a Knudsen number governing translational nonequilibrium of the mixture), where

$$N_S = N_F / N_{Re} \tag{11}$$

The Fenn number, $N_F$, Schmidt number, $N_{Sc}$, and Reynolds number, $N_{Re}$, are defined as

$$N_F = \gamma m_S/(mN_{Sc}) \quad (12)$$

$$N_{Sc} = \mu/\rho D \quad (13)$$

$$N_{Re} = \gamma P_o d/\mu_o c_o \quad (14)$$

where $\mu_o$ is the viscoscity coefficient, $c_o$ is the sound speed, and $D$ is diffusivity.

### 1.8 RF Supersonic Plasma Source Characterization via APMS and OES to determine dissociation fraction

Determining concentrations of active species [for example, $N_2$, $N_2^+$, $N_2(A)$ and N] from sources in vacuum-based systems has long been an issue of interest and debate. Analysis of plasma molecular beams has been assisted by appearance potential mass spectrometry (APMS), where the electron impact energy is varied and subsequently QMS signals are analyzed, typically placed in line-of-sight of where materials processing would occur. QMS can only determine the mass-to-charge ratio of species detected. Thus, difficulty arises as species with the same mass to charge ratio are ionized (i.e., $C_2H_4$ vs. $N_2$ vs. $N_2^*$ or $N_2^{++}$ vs. $N^+$.) For example, $N_2(A)$ and $N_2(X)$ both contribute signal to the QMS, and thus the deconvolution between the two species signals is not trivial. Appearance potential mass spectrometry (APMS) is a method which can bypass this problem, and it is generated by varying the electron impact energy (E) and measuring the corresponding signal from the QMS for a single mass.[56,80-81] Each species' (active or ground) ionization would have a required $E$ for ionization, called the threshold voltage ($E_i$). A signal collected from a high $E$ would yield a combination of signals from multiple ionization processes. To accurately assess and identify active species concentrations, one must have accurate cross sectional data describing probability of ionization for electron impact ionization versus

energy. Singh et al. employ APMS to characterize a parallel-plate inductively-coupled $O_2$ plasma in a triply differentially pumped system.[80] They were able to detect O atom ionization for the discharge on condition. Jordan et al. employ APMS on a corona discharge supersonic free-jet of $N_2$ and determine the primary active species emitted is $N_2$ $A_3\Sigma_u^+$.[56]

Pollard developed a RF supersonic jet of $N_2$ and characterized the dissociation fraction with a QMS downstream at one electron impact energy, 70 eV.[82] He determined his source to have high dissociation fractions (~%60) for both $N_2$ and $O_2$ beams. As in the inductively coupled source in Anders,[17] we expect that an increase in power should enhance the dissociation fraction for atomic nitrogen, and perhaps increase the production of excited molecular nitrogen. Also, there have been reports that using Ar as the diluent instead of He would produce a higher gas temperature, and hence a higher fraction of energized nitrogen species.[83-85] Ar is much heavier than $N_2$, so it would lower nitrogen's parallel velocity. It would make the lateral speed of $N_2$ and other N species quite a bit larger, lowering the centerline flux of active species. Neon could be considered as an alternate diluent. Pollard determined the composition of the centerline beam of the plasma source will be determined by measuring intensities of N and $N_2$. In order to resolve mass spectrometer data with respect to concentrations of the species N, $N_2$ and $N_2^+$, knowledge of the cross sections ($\sigma_1$, $\sigma_2$, $\sigma_3$) of electron-impact ionization is required.[86-89]

$$\sigma_1 : N \rightarrow N^+ \quad (15)$$

$$\sigma_2 : N_2 \rightarrow N_2^+ \quad (16)$$

$$\sigma_3 : N_2 \rightarrow N^+ + N \quad (17)$$

Knowledge of mass spectrometer transmission probabilities ($\tau_1$, $\tau_2$, $\tau_3$ refers to mass spectrometer's efficiency of transmitting a signal for processes in eq. 15-17) and measuring ion intensity ratios

$$\eta \equiv N^+ / N_2^+ \quad \text{intensity ratio with plasma power off} \tag{18}$$

$$\rho \equiv N^+ / N_2^+ \quad \text{intensity ratio with plasma power on} \tag{19}$$

can yield the dissociation fraction $\alpha$, where

$$R \equiv [N]/[N_2] \tag{20}$$

$$R = (\tau_2 / \tau_1)(\sigma_2 / \sigma_1)(\rho - \eta) \tag{21}$$

$$\alpha = R/(R+2) \tag{22}$$

OES detects transmission of photons which are emitted when electrons descend from a higher to lower energy level (Fig. 1). Performing OES on the plasma for different conditions yields relative occupancy rates of species at different energy levels. Molecular nitrogen can undergo a number of electronic transitions while in a plasma. The 1$^{st}$ -positive series indicates molecular nitrogen going from $B^3\Pi_g$ to $A^3\Sigma_u^+$. Emissions of 540, 590, 660, 760 and 820 are characteristic of this series. The 2$^{nd}$-positive molecular nitrogen series ($C^3\Pi_u \rightarrow B^3\Pi_g$) occurs at shorter wavelengths, typically 316, 337, 357, 380 and 400 nm. Intensities of these peaks correlate with the concentration of excited molecular nitrogen produced by the RF nitrogen source. The 1$^{st}$ –negative series of $N_2^+$ ($B^2\Sigma_u^+ \rightarrow X^2\Sigma_g^+$), found at wavelengths of 391 and 428 nm, indicate a relaxation of ionized molecular nitrogen. Atomic nitrogen can undergo transitions from $3s^4P - 3p^4S^0$ showing peaks at 742.3, 744.2 and 746.8 nm. Also, a strong 7-line multiplet of peaks between 818.5 and 824.2 nm show

atomic nitrogen going from $3s^4P$ to $3p^4P^0$. Relative intensities of these peaks will indicate the composition of the RF plasma source, indicating knowledge of ions, atoms, and activated neutrals.[29,90]

### 1.9 Dissertation Outline

Chapter 2 describes our analysis and experimentation of aerodynamic focusing for mixed inert gases in seeded supersonic molecular beams using TOF methods with a QMS. TOF spectra are converted into intensity, energy and speed ratio data for seed and carrier gases.

Chapter 3 describes homepitaxial GaN(0001) films grown on MOCVD GaN/6H-SiC substrates using $NH_3$-seeded supersonic beams and Ga from an effusion cell. These films are characterized using AFM, reflection high-energy electron diffraction (RHEED), and scanning electron microscopy (SEM). Roughness scaling analysis using the AFM data is used to elucidate the dominant smoothening (or roughening) processes during growth. Growth rates acquired from cross-sectional SEM are applied to understand the relationship between kinetics and surface roughness.

Chapter 4 describes growth of GaN(0001) homoepitaxially on MOCVD grown GaN(0001)/6H-SiC with TEG-seeded in $N_2$ and He supersonic beams. Scanning electron microscopy (SEM) is used for surface analysis and growth rate measurement (cross section). Atomic force microscopy (AFM) measurements are used for mapping the growth surface to determine film morphology. A roughness scaling analysis is applied to AFM data.

Chapter 5 describes the construct and operation of $N_2$ RF-discharge supersonic jet source. A combination of APMS and TOF methods is employed to determine the relative fluxes of various N species (N, $N_2$, $N_2(A)$ and $N_2^+$) emitted from the source, as well as energy

and energy resolution of beam species. OES acquires information on radiative transmissions in the plume of the jet.

Appendix A describes a summary of growth of InN(0001) on GaN(0001)/6H-SiC with a seeded supersonic jet of trimethylindium (TMI) and leak valve $NH_3$. SEM images and energy-dispersive x-ray (EDX) analysis are employed on the films grown. *In situ* XPS is also employed on the films.

Appendix B entails nitridation of Si(100) at 300°C using the $N_2$ RF-discharge supersonic jet source in chapter 5. Angle resolved XPS is employed to get depth profile of N, C, O and Si as well as atomic concentration.

Appendix C describes the details of TOF characterization. Relevant equations using applications of our system geometries are included.

**Table 1:** Properties of possible nitride substrates

| Substrate Material | Symmetry | Lattice parameters | Coefficient of Thermal Expansion |
|---|---|---|---|
| Wurtzite GaN | Hexagonal | a=3.189Å | $5.59 \times 10^{-6}$/K |
| | | c=5.185Å | $3.17 \times 10^{-6}$/K |
| Wurtzite AlN | Hexagonal | a=3.112Å | $4.2 \times 10^{-6}$/K |
| | | c=4.982Å | $5.3 \times 10^{-6}$/K |
| $\alpha$-$Al_2O_3$ | Hexagonal | a=4.758Å | $7.5 \times 10^{-6}$/K |
| | | c=12.991Å | $8.5 \times 10^{-6}$/K |
| Si | Cubic | A=5.4301Å | $3.59 \times 10^{-6}$/K |
| GaAs | Cubic | A=5.6533Å | $6 \times 10^{-6}$/K |
| 6H-SiC | Hexagonal | a-3.08Å | |
| | | c=15.12Å | |
| 3C-SiC | Cubic | a=4.36Å | |
| InP | Cubic | A=5.8693Å | $4.5 \times 10^{-6}$/K |
| GaP | Cubic | A=5.4512Å | $4.65 \times 10^{-6}$/K |
| MgO | Cubic | a=4.216Å | $10.5 \times 10^{-6}$/K |
| ZnO | Hexagonal | a=3.252Å | $2.9 \times 10^{-6}$/K |
| | | c=5.213Å | $4.75 \times 10^{-6}$/K |
| $MgAl_2O_4$ | Cubic | a=8.083Å | $7.45 \times 10^{-6}$/K |

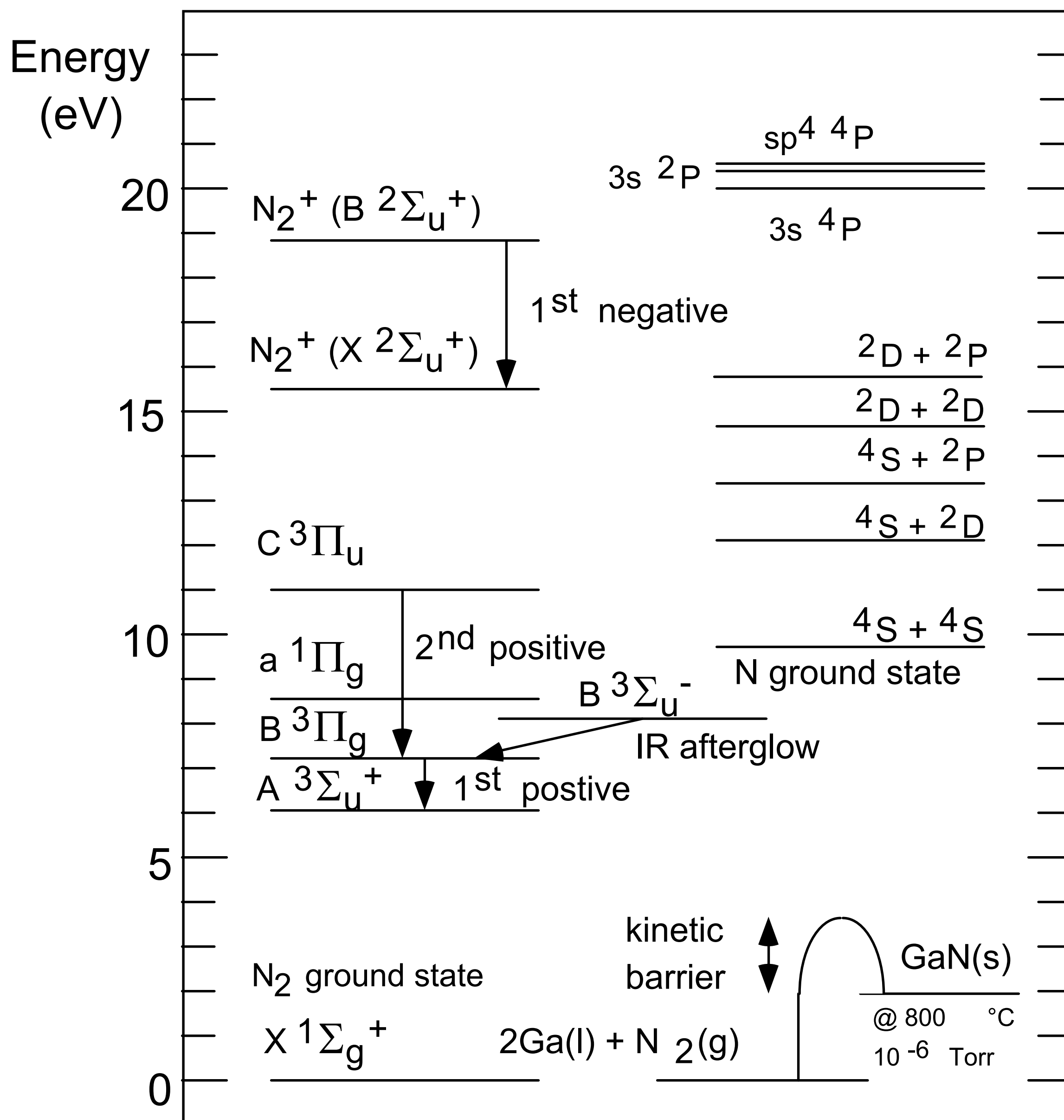


**Figure 1:** Energy Level Diagram of Nitrogen showing N, $N_2$ and $N_2^+$, and GaN reaction

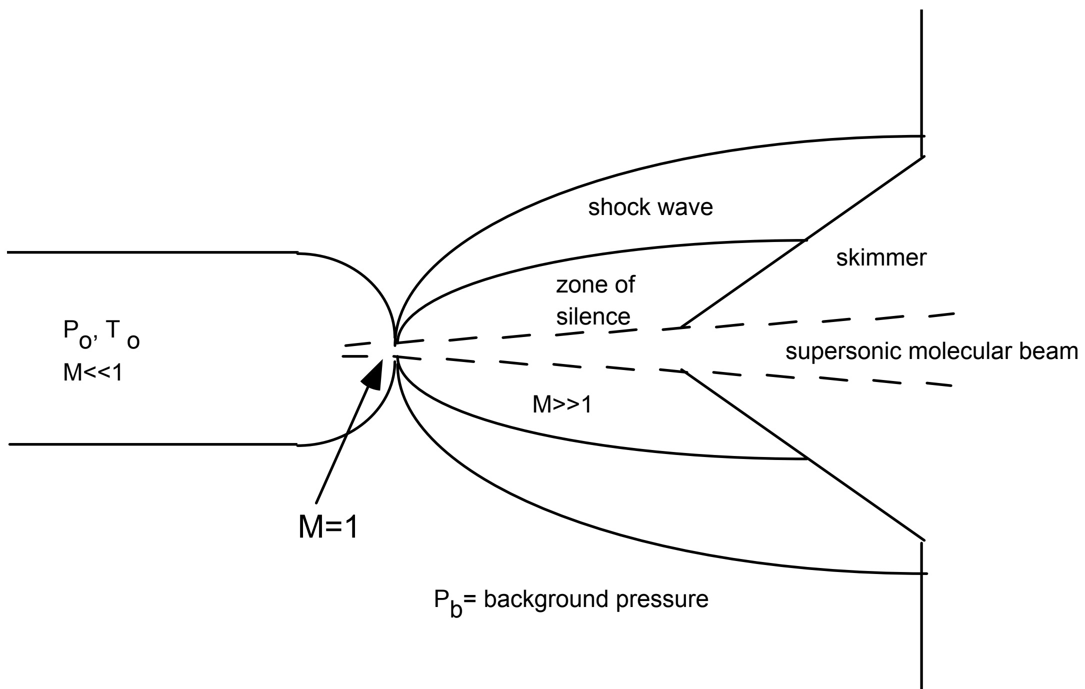


**Figure 2:** Continuum Free-Jet Expansion

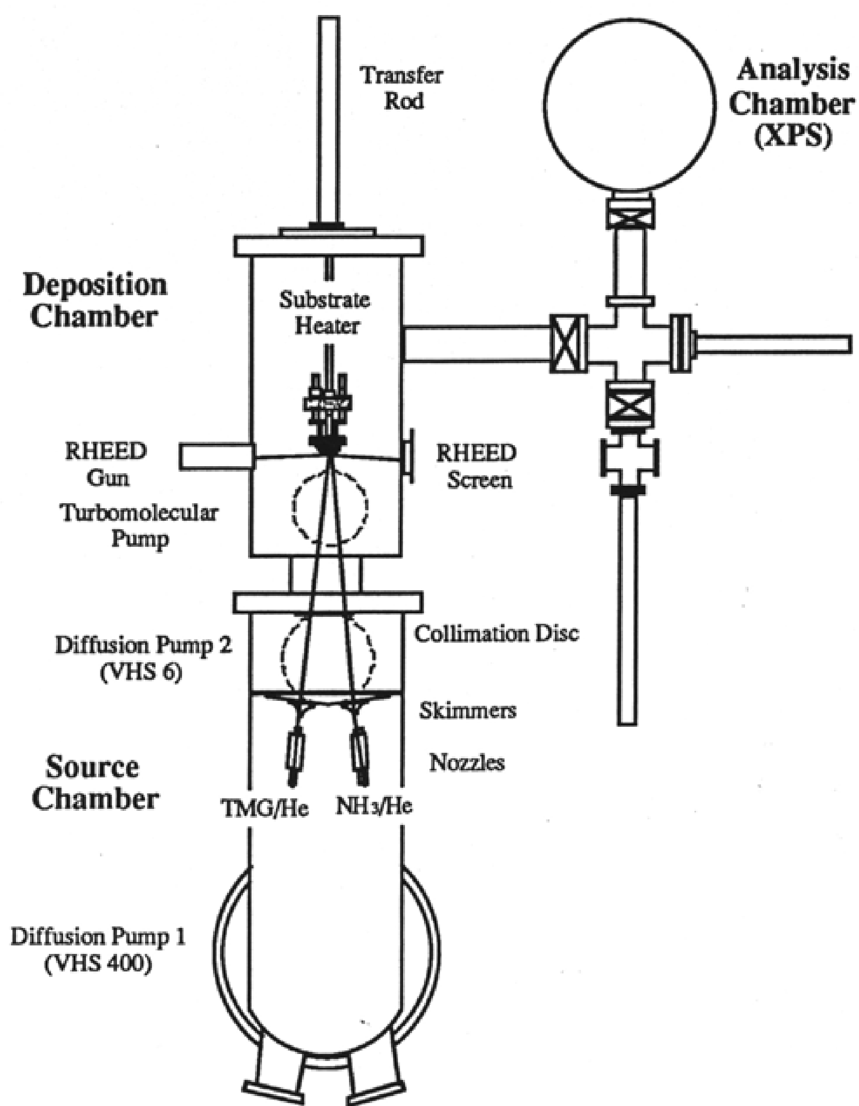


**Figure 3**: Top View of SJE/XPS Growth and Analysis Chamber

## 1.10 References

[1]S. N. Mohammad and H. Morkoc, Prog. Quan. Electron. **20**, 361 (1996).

[2]S. Nakamura, MRS Bulletin, **23**, 37 (1998).

[3]S. Strite and H. Morkoc, J. Vac. Sci. Technol. B **10**, 1237 (1992).

[4]S. Nakamura, N. Iwasa, M. Senoh, and T. Mukai, Jap. J. of Appl. Phys. **31**, 1258 (1992).

[5]O.H. Nam, M. D. Bremser, T. S. Zheleva and R. F. Davis, Appl. Phys. Lett., **71**, 2638 (1997).

[6]J.J. Tietjen, Appl. Phys. Lett. **15**, 327 (1969).

[7]S. Nakamura, S., Jap. J. Appl. Phys. **30**, L1705 (1991).

[8]D. A. Neumayer and J.G. Ekerdt, Chem. Mater. **8**, 9 (1996).

[9]K. Ploog, *Atomic and Molecular Beam Methods* Vol. **1**., edited by G. Scoles., (Oxford, New York, 1988), p. 417.

[10]R.P. Vaudo, D. Goepfert, T. D. Moustakas, D. M. Beyea, T. J. Frey and K. Meehan, J. Appl. Phys. **79**, 2779 (1996).

[11]W. Cheng, and R.F. Davis, Appl. Phys. Lett., **63**, 990 (1993).

[12]M.E. Lin, B.N. Sverdlov and H. Morkoc, J. of Appl. Phys. **74**, 5038 (1993).

[13]A. Botchkarev, A. Salvador, B. Sverdlov, J. Myong and H. Morkoc, J. Appl. Phys. **77**, 4455 (1995).

[14]V. N. Jmerik, V. V. Mamutin, V. A. Vekshin, T. V. Shubina, S. V. Ivanov and V. S. Kop'ev, Mater. Sci. Eng. B **59**, 60 (1999).

[15]V. V. Mamutin, A. A. Toropov, N. F. Kartenko, S. V. Ivanov, A. Wagner and B. Monemar, Mater. Sci. Eng. B **59**, 56 (1999).

[16]N. Newman, J. Crystal Growth **178**, 102 (1997).

[17]A. Anders, N. Newman, R. Rubin, M. Dickinson, E. Jones, P. Phatak and A. Gassman, Rev. Sci. Instr. **67**, 905 (1996).

[18]A. Gassmann, T. Suski, N. Newman, C. Kisielowski, E. Jones, E. R. Weber, Z. Liliental-Weber, M. D. Rubin, H. I. Helava, I. Grzegory, M. Bockowski, J. Jun and S. Poworski, J. Appl. Phys. **80**, 2195 (1996).

[19]A. J. Ptak, M. R. Millecchia, T. H. Myers, K. S. Ziemer and C. D. Stinespring, Appl. Phys. Lett. **74**, 3836 (1999).

[20]S. Shokhovets, R. Goldhahn, G. Gobsch, T. S. Cheng and C. T. Foxon, Mater. Sci. Eng. B **59**, 69 (1999).

[21]E. J. Tarsa, B. Heying, X. H. Wu, P. Fini, S. P. DenBaars and J. S. Speck, J. Appl. Phys. **82**, 5472 (1997).

[22]T. H. Myers, L. S. Hirsch, L. T. Romano and M. R. Richards-Babb, J. Vac. Sci. Technol. B **16**, 2261 (1998).

[23]Y. Zhao, F. Deng, S. S. Lau and C. W. Tu, J. of Vac. Sci. Technol. B **16**, 1297 (1998).

[24]E. C. Piquette, P. M. Bridger, Z. Z. Bandic and T. C. McGill, J. Vac. Sci. Technol. B **17**, 1241 (1999).

[25]M. A. L. Johnson, J. D. Brown, N. A. El-Masry, J. W. Cook, J. F. Schetzina, H. S. Kong and J. A. Edmond, J. Vac. Sci. Technol. B **16**, 1282 (1998).

[26]J. M. Reifsnider, D. W. Gotthold, A. L. Holmes and B. G. Streetman, J.M., J. Vac. Sci. Technol. B **16**, 1278 (1998).

[27]K. Kushi, H. Sasamoto, D. Sugihara, S. Nakamura, A. Kikuchi, and K. Kishino, Mater. Sci. Eng. B **59**, 65 (1999).

[28]R. Beresford, K. S. Stevens, Q. Cui, A. Schwartman and H. Cheng, Mater. Res. Soc. Symp. (1997). --??need vol #??

[29]W. C. Hughes, W. H. Rowland, M. A. L. Johnson, S. Fujita, J. W. Cook, J. F. Schetzina, J. Ren and J. A. Edmond, J. Vac. Sci. Technol. B **13**, 1571 (1995).

[30]C. R. Eddy, T. D. Moustakas and J. Scanlon, J. Appl. Phys. **73**, 448 (1993).

[31]L. T. Romano, B. S. Krusor, R. Singh and T. D. Moustakas, J. Elec. Mater. **26**, 285 (1997).

[32]N. E. Lee, R. C. Powell, Y. W. Kim and J. W. Greene, J. of Vac. Sci. Technol. A **13**, 2293 (1995).

[33]Z. Yang, L.K. Li, and W.I. Wang, J. Vac. Sci. Technol. B **14**, 2354 (1996).

[34]W. Kim, O. Atkas, A. E. Botchkarev, A. Salvador, S. N. Mohammad and H. Morkoc, J. Appl. Phys. **79**, 7657 (1996).

[35]S. T. Ceyer, Science, **249**, 133 (1990).

[36]C. B. Mullins and W.H. Weinberg, J. Vac. Sci. Technol. A **8**, 2458 (1990).

[37]C. B. Mullins and W.H. Weinberg, J. Chem. Phys. **92**, 4508 (1990).

[38]J. R. Engstrom, D. A. Hansen, M. J. Furjanic and L. Q. Xia, J. Chem. Phys. **99**, 4051 (1993).

[39]K. A. Pacheco, B. A. Ferguson, C. Li, S. John, S. Banerjee, and C. B. Mullins, Appl. Phys. Lett. **67**, 2951 (1995).

[40]K. A. Brown, S. A. Ustin, L. Lauhon, and W. Ho, J. Appl. Phys. **79**, 7667 (1996).

[41]B. A. Ferguson, A. Sellidj, B. B. Doris and C. B. Mullins, J. Vac. Sci. Technol A **14**, 825 (1996).

[42]H. H. Lamb, K. K. Lai, V. Torres and R. F. Davis, in Mater. Res. Soc. Symp., 1995.

[43]V. M. Torres, M. Stevens, J. L. Edwards, D. J. Smith, R. B. Doak and I. S. T. Tsong, Appl. Phys. Lett. **71**, 1365 (1997).

[44]D. R. Miller, in *Atomic and Molecular Beam Methods*, edited by G. Scoles (Oxford, New York, 1988), Vol. **1**., pp. 14-53.

[45]R Campargue, J. Phys. Chem. **88**, 4466 (1984).

[46]H. C. W. Beijerinck, N. F. Verster, Physica C, **111**, 327 (1981).

[47]P. Poulsen, and D.R. Miler. 10th Rar. Gas Dyn. (1977).

[48]B. A. Ferguson and C. B. Mullins, J. Cryst. Growth **178**, 134 (1997).

[49]J. R. Engstrom, L. Q. Xia, M. J. Furjanic and D. A. Hansen, J.R., App. Phys. Lett. **63**, 1821 (1993).

[50]L.-Q. Xia, M. E. Jones, N. Maity, and J. R. Engstrom, J. Vac. Sci. Technol. A **13**, 2651 (1995).

[51]K. A. Pacheco, B. A. Ferguson, and C. B. Mullins, J. Vac. Sci. Technol. A **14**, 2190 (1997).

[52]S. A. Ustin, K. A. Brown, and W. Ho, Rev. Sci. Instrum. **71**, 1479 (2000).

[53]J. J. Sumakeris, R. K. Chilukuri, R. F. Davis and H. H. Lamb in Mater. Res. Soc. Symp. (1996).

[54]A. J. McGinnis, D. Thomson, A. Banks, E. Preble, R. F. Davis, and H. H. Lamb, J. Vac. Sci. Technol. A **21**, 294 (2003).

[55]M. L. Yu and L. A. Delouise, Surf. Sci. Rep. **19**, 286 (1994).

[56]D. C. Jordan, I. S. T. Tsong, David J. Smith, B. J. Wilkens, and R. B. Doak, Appl. Phys. Lett. **77**, 3030 (2000).

[57]V. M. Torres, R. B. Doak, B. J. Wilkens, D. J. Smith and I. S. T. Tsong, J. Vac. Sci. Technol. A **17**, 1570 (1999).

[58]M. A. Khan, J. N. Kuznia, D. T. Olson and R. Kaplan, J. Appl. Phys. **73**, 3108 (1993).

[59]W. Qian, M. Skowronski, M. Degraef, K. Doverspike, L. B. Rowland and D. K. Gaskill, Appl. Phys. Lett. **66**, 1252 (1995).

[60]A. E. Wickenden, D.K. Wickenden, and T.J. Kistenmacher, J. Appl. Phys. **75**, 5367 (1994).

[61]Z. Liliental-Weber, C. Kisielowski, S. Ruvimov, Y. Chen, J. Washburn, I. Grzegory, M. Bockowski, J. Jun and S. Porowski, J. Elec. Mater. **25**, 1545 (1996).

[62]Z. Liliental-Weber, C. Kisielowski, S. Ruvimov, Y. Chen, W. Swider, N. Newman, A. Gassman, X. Liu, L. Schloss, E. R. Weber, T. Suski, K. Pakula, J. Baranowski, J. Washburn, I. Grzegory, M. Bockowski, J. Jun, S. Porowski, H. Amano and I. Akasaki, in Mater. Res. Soc. Symp. (1996).--??need vol #??

[63]C. M. Balkas, Z. Sitar, T. Zheleva, L. Bergman, I. K. Shmagin, R. Muth, R. Kolbas, R. Nemanich and R. F. Davis, in Mater. Res. Soc. Symp. (1996)--???need vol. #???.

[64]I. K. Shmagin, J. F. Muth, J. H. Lee, R. M. Kolbas, C. M. Balkas, Z. Sitar and R. F. Davis, Appl. Phys. Lett. **71**, 455 (1997).

[65]V. M. Bermudez, J. Appl. Phys. **80**, 1190 (1996).

[66]A. R. Smith, R. M. Feenstra, G. W. Greve, M. S. Shin, M. Skowronski, J. Neugebauer and J. E. Northrup, Appl. Phys. Lett. **72**, 2114 (1998).

[67]R. Held, D. E. Crawford, A. M. Johnston, A. M. Dabiran and P. I. Cohen, J. Elec. Mater. **26**, 272 (1997).

[68]A. Pavlovska, V. M. Torres, E. Bauer, R. B. Doak, I. S. T. Tsong, D. B. Thomson and R. F. Davis, Appl. Phys. Lett. **75**, 989 (1999).

[69]Z. Liliental-Weber, Y. Chen, S. Ruvimov and J. Washburn, Phys. Rev. Lett. **79**, 2835 (1997).

[70]B. Daudin, J. L. Rouviere and M. Arlery, Appl. Phys. Lett. **69**, 2480 (1996).

[71]Z. A. Munir, and A.W. Searcy, J. Chem. Phys. **42**, 4223 (1965).

[72]R. C. Schoonmaker, A. Buhl, and J. Lemley, Vap. Catal. **69**, 3455 (1965).

[73] E. Chen, Ph. D. Dissertation, North Carolina State University, Raleigh (1998).

[74]E. L. Knuth, in *Engine Emissions: Pollutant Formation and Measurement*, edited by G. S. Springer and D. J. Patterson (Plenum, New York, 1973), pp. 319-363.

[75]P. K. Sharma, E. L. Knuth, and W. S. Young, J. Chem. Phys. **64**, 4345 (1976).

[76]D. F. Patch, "Application of Free Jet Sources to Reactive Crossed Molecular Beam Experiments," PhD dissertation, University of California, San Diego.--??need a year???

[77]D. Eres, Mater. Res. Soc. Symp. Proc. **201**, 11 (1991).

[78]J. B. Anderson, R. P. Andres, J. B. Fenn, and G. Maise, Rar. Gas Dyn., edited by J. H. d. Leeuw (Academic, New York, 1966), p. 106.

[79]J. Fernandez de la Mora and J. Rosell-Llompart, J. Chem. Phys. **91**, 2603 (1989).

[80]H. Singh, J. W. Coburn, and D. B. Graves, J. Vac. Sci. Technol. A **18**, 299 (2000).

[81]A. Sellidj, B. A. Ferguson, T. J. Mattord, B. G. Streetman, and C. B. Mullins, Appl. Phys. Lett. **68**, 3314 (1996).

[82]J. E. Pollard, Rev. Sci. Instrum. **63**, 1771 (1992).

[83]A. Lebehot, S. Drawin, F. Aguillon, R. Campargue and X. Chapuisat, J. Chem. Phys. **92**, 7340 (1990).

[84]S. J. Sibener, R. J. Buss, C. Y. Ng and Y. T. Lee, Rev. Sci. Instr. **51**, 167 (1980).

[85]J. A. Silver, A. Freedman, and C.E. Kolb, Rev. Sci. Instr. **53**, 1714 (1982).

[86]D. Rapp, P. Englander-Golden, and D.D. Briglia, J. Chem. Phys. **42**, 4081 (1965).

[87]T. D. Mark, J. Chem. Phys. **63**, 3731 (1975).

[88]T. D. Mark, F. Egger, and M. Cheret, J. Chem. Phys. **67**, 3795 (1977).

[89]E. Brook, M. F. A. Harrison, and A. C. H. Smith, J. Phys. B **11**, 3115 (1978).

[90]R. W. B. Pearse, and A. G. Gaydon, *The Identification of Molecular Spectra*. 1963, New York: John Wiley & Sons Inc. 209-220.

2. Heavy Species Enrichment due to Aerodynamic Focusing in Seeded Supersonic Jets. Nicholas A. Smith, H. Henry Lamb. Manuscript will be sent to Journal of Chemical Physics.

Mass Separation due to Aerodynamic Focusing in Seeded Supersonic Jets

**Nicholas A. Smith**

**H. Henry Lamb***

Department of Chemical Engineering, North Carolina State University, Raleigh, NC 27695-7905, USA
*Corresponding author: Tel.: +1-919-515-6395; fax: +1-919-515-3465. E-mail address: lamb@eos.ncsu.edu (H. H. Lamb).

**ABSTRACT**

Seeded supersonic jets provide high-intensity, high-energy precursors when seeded in light carrier gases. Thermodynamics of seeded supersonic jets indicate ideal beam kinetic energy should be $E_i=RT_o\gamma/(\gamma-1)$. Non-ideal jet conditions ($T \neq 0$) affect the final kinetic energy, intensity, and energy resolution of the precursor. Aerodynamic focusing concentrates heavy gases along the axial centerline. Using time-of-flight (TOF) methods we determine the intensity, kinetic energy and parallel speed ratios of binary mixtures (combinations of He, $N_2$, Ar, Kr) of seeded supersonic jets. We determine that the ratio of parallel speed ratios of the seed and carrier gases squared approximates the enrichment ratio well at higher nozzle stagnation pressures. We correlate the mass weighted speed ratio of the seed gas with respect to a temperature slip parameter, $S_S(<m>/m_S)^{1/2} = 0.205(TSP)^{0.623}$. Carrier gas speed ratios are similar to the pure gas expansion speed ratios. All enrichment data scale to a common dimensionless parameter, the Stokes number, which is the ratio of the Fenn number (disparity of relaxation scales) to the Reynolds number (ratio of inertial to viscous forces), expressed as $\Phi=92(N_{Re}/N_F)^{-0.77}$.

## INTRODUCTION

Seeded supersonic free jets are used to produce beams of molecules with hyperthermal translational energies, narrow velocity distributions, and high centerline intensities. These unique properties of seeded supersonic free jets (and collimated supersonic molecular beams produced by skimming the isentropic core of the free jet) have been exploited in the study of elementary gas-phase reactions and as a tool to study surface reactions on metals and semiconductors. More recently, supersonic jets and molecular beams have been employed in thin film growth to increase growth rates. Xia, et al. used supersonic molecular beams of $SiH_4$ and $Si_2H_6$ to Si(100) and Si(111) surfaces to study thin film growth of Si.[1] Sellidj et al.[2] and Ferguson et al.[3] have grown GaN(0001) with RF $N_2$ supersonic beams on sapphire. In both of these situations, quantification of active species flux to the substrate was difficult to achieve. McGinnis, et al. grow GaN(0001) with $NH_3$-seeded supersonic molecular beams and does deal with the issue of focusing for $NH_3$ in different carrier gases.[4]

Characterization of supersonic molecular beams has been accomplished by many previous investigators.[5-8] Single-species supersonic molecular beams have been characterized in terms of centerline intensity[5], parallel speed ratio (parallel velocity distribution) and energy. Binary supersonic molecular beams are not as easy to characterize. Predictions have been made for energy and speed ratio of binary supersonic molecular beams,[6-8] but there has been little experimental verification of these predictions.

A seeded supersonic molecular beam yields species with hyperthermal translational energies. In an ideal beam (zero velocity slip), the terminal velocity is given by

$$V_\infty = \sqrt{\frac{2R}{\langle m \rangle}\langle C_p \rangle T_o} \tag{1}$$

where $<m>$ is the average molecular weight, $<C_p>$ is the average heat capacity, and $T_o$ is the stagnation temperature. The ideal kinetic energy, $E_i$, of species $i$ is given by

$$E_i = \frac{m_i}{\langle m \rangle}\langle C_p \rangle T_o \tag{2}$$

The energy of seeded beams can be accurately estimated [eq. (2)], if $P_{o,}d$, where $P_o$ is the stagnation pressure of the nozzle and $d$ is the orifice diameter, is on the order of 3 Torr-cm or greater. The flow structure of the jet is characterized by the Reynolds number (similar to $N_{Kno}^{-1}$, inverse of the Knudsen number), a ratio of inertial forces to viscous forces

$$N_{Re} = \gamma P_o d / \mu_o c_o \tag{3}$$

where $c_o = \sqrt{\gamma kT / m}$ is the speed of sound and $\mu_o$ is the viscosity coefficient (both evaluated at the stagnation conditions).

Beam energy resolution is described by the parallel speed ratio

$$S_{ll} = \frac{v_s}{\sqrt{\frac{2RT}{m}}} \tag{4}$$

where $v_s$ is the stream velocity of the species. Beam resolution is increased by increasing $P_{o,}d$ (or $N_{Re}$). The perpendicular speed ratio ($S_\perp$) is defined analogously and measures the thermal velocity spread perpendicular to the flow direction. In general, the two speed ratios are not equal.

Accurately determining the intensities (fluxes) of reactant molecules at the growth surface is essential in any thin film growth process. For seeded supersonic molecular beams, the enrichment of the beam with respect to the seed species is defined by an enrichment ratio,

$$\Phi = \frac{(J_S / J_C)_d}{(Q_S / Q_C)} \qquad (5)$$

where $Q_S$ and $Q_C$ are the flow rates of seed and carrier gas to the nozzle, respectively, and $J_{S,d}$ and $J_{C,d}$ are the fluxes of the seed and carrier gas at the detector (or thin film surface), respectively. Previous definitions of the enrichment ratio, $\Phi$, have been based on seed and carrier densities in the nozzle and at the detector. The density ratio and flux ratio at the detector are equivalent if $v_S = v_C$. Knowledge of the enrichment ratio of the seed gas is key information in supersonic molecular beam experiments and in growth of thin films. McGinnis, et al. demonstrated that significant mass separation can exist even for relatively light molecules, such as ammonia, in seeded supersonic molecular beams when He or $H_2$ is used as the diluent gas.[4] The same authors also noted that significant flux differences exist for beams of triethylgallium (TEG) seeded in He and $N_2$. Eres, et al. first noted focusing phenomena in growth of GaAs using seeded supersonic beams, where growth profiles had a $\cos^{22}\theta$ dependence,[9] as opposed to the standard $\cos^{4}\theta$ dependence found in single component supersonic jet expansions.[10] Pacheco, et al. also noted focusing phenomena in Si epitaxial growth using disilane seeded in $H_2$.[11] Since there is very little experimental information on the enrichment factor for binary systems, we decided to investigate this phenomena using TOF methods.

**EXPERIMENTAL METHODS**

Experiments are carried out in supersonic molecular beam apparatus (Fig. 1) with two stages of differential pumping. A pyrolytic-BN nozzle (stagnation pressure, 50-500 Torr) with a 150-µm laser-drilled orifice was installed in a source chamber. The source chamber is pumped by a VHS-6 diffusion pump (maximum pumping speed 2400 L/s) to maintain a background pressure of $<7\times10^{-4}$ Torr. The supersonic jet passes through a conical nickel skimmer (Beam Dynamics) with a 1-mm aperture, and an included angle of 25° at the top section and of 70° at the base. The nozzle-skimmer distance is approximately 1.9 cm. After the skimmer, the beam is modulated at 200 Hz using a rotating mechanical chopper. The 100-mm diameter chopper wheel has two 1-mm slotted teeth positioned approximately 180° apart. A 2-ns photocoupler indicates the beginning of the beam pulse, as the two slits are located at 180° opposite each other on the flywheel. The chopper is driven by a variable high-speed motor (Globe) controlled by a custom signal generator. The beam passes through a 3.3-mm collimation aperture before entering the detector chamber. The detector chamber houses a Hiden RC-301 quadrupole mass spectrometer (located approximately 48 cm from the nozzle) and is pumped by a 53-L/s turbomolecular pump (Pfeiffer). The nozzle stagnation pressure ($P_0$) is measured with a MKS Baratron gauge. Experiments were performed with research grade Ar, He, $N_2$ and Kr and flow rates were controlled by MKS mass flow controllers. Time-of-flight characterization takes place using a photocoupler, which is opposite the beam position to mark the beginning of the beam modulation. A Oxford/Tellenec multichannel scalar (MCS) card coordinates the trigger with the Hiden QMS to deliver time-of-flight spectra.

In order to calibrate the centerline intensity of the supersonic jet, the chopper is removed from beam modulation and a beam flag is placed (where the chopper was located) to separate the beam component from the effusive contribution in the final chamber. The QMS signal from a pure gas supersonic jet is measured along with the Bayard-Alpert ionization gauge measurement of $P_{dep}$. The effusive component of $P_{dep}$ from the second differential pumping stage is removed (by beam flag measurement) and using the pumping speed ($S_{pump}$ for the specific gas used) we get a beam flow rate entering the chamber, $Q = P_{dep}S_{pump}$. The QMS signal is compared to this flow rate and thus we get a calibration for this specific gas. This procedure was repeated for each gas. The calibration is valid for the gas at that velocity [given by eq. (1)], and consequently, careful consideration is taken for the velocity of each species entering the QMS ionizer. TOF signals are corrected for physical and electronic delays. The chopper is operated both directions (clockwise and counterclockwise) to determine the delay from the beam not passing exactly 180° opposite the photocoupler. Ion flight time delays are determined by compared our results versus the expect times from various pure gas beams. These ion flight time delays scale by $m^{1/2}$, as expected. Consideration of these delays give us an accurate flight time for all seeded beam experiments.

With a time resolution of 2-μs and defined by the MCS card, the response of the mass spectrometer can give a reasonable approximation of the beam's velocity distribution, $f(v)$. Knowledge of the time distribution and the actual flight path length allows the TOF spectra to be converted to the velocity domain

$$f(v) = v^3 \exp-\left(\frac{v - v_s}{\alpha}\right)^2 \qquad (6)$$

where $v$ is the parallel velocity, $v_s$ is the stream velocity and $\alpha$ is a fitting parameter

(similar to the thermal velocity of the beam after expansion) related to the temperature of the beam, $T$

$$\alpha = \sqrt{\frac{2kT}{m}} \tag{7}$$

and to $m$, mass of the species. Kinetic energy, $E_i$, is given by

$$E_i = \frac{1}{2} m v_s^2 \tag{8}$$

Eq. (6) only holds if the chopper gating function is ideal (a delta function pulse). In real systems, this is not the case. $g_{den}(t)$, the time domain response of $f(v)$, is related to the gating function, $A(\lambda)$,

$$g_{den}(t) = n \int_0^{2q} f(v) \frac{L}{(t-\lambda)^2} A(\lambda) d\lambda \tag{9}$$

Given by the geometry of our system, $A(\lambda)$ is trapezoidal and results in the following expression[12]

$$g_{den}(t) = nf(v) \left[ \frac{1}{0.8q} \left( \ln((t-0.8q)/t) + \ln((t-q)/(t-1.8q)) \right) \right] \tag{10}$$

where $q$ is the time the slit takes to pass by the beam (15.5 μs in our case). We do a least squares fit of the model $g_{den}(t)$ to the mass spectrometer signal, $I_{exp}(t)$,

$$\sum_{j=1}^{N} \left[ I_{\exp}(t_j) - g_{den}(t_j) \right]^2 \tag{11}$$

to get $\alpha$ (consequently $T_{ll}$ and $S_{ll}$) and $v_s$. TOF measurements produce spectra of QMS signal coordinated with time (photocoupler) averaged over many cycles (typically 100,000), as in Fig. 2. We get $S$, $v_s$ and $J_d$, the area under the curve, from this fit. All enrichment factor data ($\Phi_{exp}$) presented in this paper are in terms of flux.

**RESULTS AND DISCUSSION**

Typical $N_2$ TOF spectra of supersonic beams produced by seeding 5 sccm $N_2$ in 95 sccm He and in 95 sccm Ar (after background subtraction) are shown in Fig. 2. These examples were chosen as representative of typical high kinetic energy ("seeded") and low kinetic energy ("anti-seeded") molecular beams. The solid lines represent best fits of the data to Eq. (10). Random noise is magnified for short times because of the $1/t$ correction applied to the QMS signal. We have excluded the scattering tail [observed at long times in Fig. 2(a)] from the least squares fit. The $N_2$ peak appears at a shorter time in Fig. 2(a) than Fig. 2(b), consistent with the higher velocity predicted by eq. (1) for $N_2$/He beams. Clearly, the seeding case adds intensity to the $N_2$ beam whereas anti-seeding yields a far lower $N_2$ intensity.

Experimental enrichment ratios ($\Phi_{exp}$) were calculated from the measured beam intensities and the known gas flow rates using eq. (5). Fig. 3 shows the relationship between $\Phi_{exp}$ and $P_o$ on a semi-logarithmic scale. The data shown are for 5%/95% seed/carrier mixtures measured at different total flow rates, and consequently, nozzle pressures. There is a downward trend in $\Phi_{exp}$ with increasing $P_0$ (or equivalently with increasing $N_{Re}$) for all the binary gas mixtures including the "anti-seeded" 5% $N_2$/Ar case. The data for each binary mixture can be represented using a simple power law relationship $\Phi_{exp}= aP_o^{\,b}$, as illustrated by the curves in Fig. 3. The data also evidence that $\Phi_{exp}$ increases at constant $P_0$ with the seed-to-carrier gas mass ratio, $m_S/m_C$. The largest enhancement factors are observed for Kr/He and $N_2$/He mixtures. The anti-seeded $N_2$/Ar mixture exhibits enhancement factors of approximately unity or less. The Kr/$N_2$ and

Kr/Ar mixtures have similar mass ratios and exhibit similar $\Phi_{exp}$ values over most of the $P_0$ range.

Sharma, *et al*. have shown that for fully developed supersonic jet expansions ($v_{s,S} \approx v_{s,C}$ and $S >> 1$) that the enrichment factor is given by

$$\Phi = \left( \frac{S_{S,\perp}}{S_{C,\perp}} \right)^2 \tag{12}$$

where $S_{S,\perp}$ and $S_{C,\perp}$ are the perpendicular speed ratios of the seed and carrier species, respectively.[6] Assuming no velocity slip ($v_s = v_c$) and no temperature slip ($T_{S,\perp} = T_{C,\perp}$), and substituting eq. (4) into eq. (12), it reduces to the simple result that the enrichment ratio is given by the mass ratio of the seed and carrier species:[7]

$$\Phi = \frac{m_S}{m_C} \tag{13}$$

Thus, the mass ratio should be the dominant factor in determining $\Phi$ for fully expanded beams (provided that other non-ideal effects such as skimmer interference, pressure diffusion, and background scattering can be neglected). This ratio explains the observed trends in $\Phi_{exp}$ with gas mixture composition (i.e., Kr in He gives the largest $\Phi_{exp}$, while the $m_A/m_B$ ratio decreases, so do the $\Phi_{exp}$), but cannot explain the decrease in $\Phi_{exp}$ for a given mixture as $P_o$ is increased.

A second series of experiments was designed to investigate the effect of seed species mole fraction on the enrichment ratio for selected mixtures. Fig. 4 shows the relationship between $\Phi_{exp}$ and the molar flow ratio ($Q_{s,o}/Q_{c,o}$) for Kr/He, $N_2$/He, and $N_2$/Ar mixtures for total flow rates of 100, 100, and 50 sccm, respectively. Dilute mixtures appear to exhibit greater enrichment for all 3 sets of data, and the $\Phi_{exp}$ values

appear to saturate for mole ratios greater than approximately 0.1. The trend in $\Phi_{exp}$ at low mole ratios is most pronounced for Kr/He mixtures for which there is the largest increase in nozzle pressure with an increase in the seed mole fraction. Moreover, the enrichment ratio for this mixture only approaches that predicted by eq. (13) in the limit as the seed mole fraction approaches zero. The saturation values of $\Phi_{exp}$ follow the order predicted by eq. (13), with Kr in He being highest, then $N_2$/He and finally $N_2$/Ar, but the $\Phi_{exp}$ values for the latter two mixtures are closer to $m_S/m_C$ than that of the Kr/He.

A final series of experiments was conducted to investigate aerodynamic focusing of a seed species (at constant flow) by increasing the flow rate of a second gas (carrier) to the nozzle. The enrichment ratio ($\Phi_{exp}$) and the seed species flux (relative to the flux of the same gas at 10 sccm through the nozzle - $J_s / J_{s,r}$) are plotted versus carrier flow rate $Q_C$ in Fig. 5. For $N_2$/He mixtures, $J_s / J_{s,o_}$ increases to about 2 at $Q_{He}$ = 40 sccm and then decreases slowly with increasing $Q_{He}$ reaching approximately unity at 150 sccm. As $Q_{He}$ increases, $\Phi_{exp}$ increases to 10 at $Q_{He}$= 20 sccm and drops rapidly for higher $Q_{He}$, well below $m_{N2}/m_{He} = 7$. Fig. 5(a) shows the effects of anti-seeding $N_2$ in Ar. $J_s / J_{s,o}$ decreases as $Q_{Ar}$ increases, which is the expected result of anti-seeding. $\Phi_{exp}$ decreases with increased $Q_{Ar}$ as well, even though there is a slight enrichment at a 10/10 mixture. Kr/He mixtures produce lower $J_s / J_{s,o}$ (slight increase above unity) than $N_2$/He mixutres (almost 2). However, $\Phi_{exp}$ for Kr/He mixtures is higher than $\Phi_{exp}$ for $N_2$/He mixtures, following the general $m_S/m_C$ relationship [eq. (13)]. While seeding clearly produces a higher $\Phi_{exp}$ than anti-seeding, both cases exhibited decreasing $\Phi_{exp}$ with increased $Q_C$, similar to the decrease in $\Phi_{exp}$ with increased $P_o$ for 5% seeding and anti-seeding cases. The curves shown in Fig. 5(b) are power law fits of the data, demonstrating the same power law

dependence as found in Fig. 3 for the 5% seed data. Consequently, it would appear that there is little effect in changing the dilution ratio of the seed gas.

Since expermental data show a general trend of decreasing enrichment ratio with increasing $P_0$ that cannot be explained by the simple mass ratio expression (eq. 14), we decided to test the more general prediction of eq. (12) using our experimental speed ratios determined from the fit of TOF data using eq. (11). Fig. 6 shows the parallel speed ratios for the heavy and light components determined by TOF analysis of the 5% $N_2$/He and $N_2$/Ar beams as a function of nozzle stagnation pressure. In Fig. 6(a), it is evident that $S_{ll,N2}$ is much higher than $S_{ll,He}$ for all $P_o$. $S_{ll,He}$ actually drops to zero at the lowest $P_o$, which is characteristic of an effusive beam, even though the $N_2$ seed remains supersonic jet (although still not that well developed at low $P_o$). From this we can infer that the origin of the large enrichment values observed at low nozzle pressures results from the "decoupling" of the gases in the expanding binary mixture. Fig. 6(b) shows an example of $S_{ll,S}$ and $S_{ll,C}$ with respect to $P_o$ in an anti-seeding case. $S_{ll,S}$ very nearly approaches $S_{ll,C}$ for most $P_o$, while it is slightly lower for most cases, the opposite result of the seeding case in Fig. 6(a) where $S_{ll,S}$ is higher than $S_{ll,C}$. This result is expected as the masses of $N_2$ and Ar are fairly similar. 5% Kr in Ar mixtures (not shown) have similar speed ratio trends with Kr (the heavier seed) having a slightly higher speed ratio. The speed ratio data for both the 5% $N_2$ in Ar and the 5% Kr in Ar mixtures do criss-cross from data point to data point and it appears that the speed ratio measurement error is on the same order of magnitude as the difference between speed ratios of these heavy gases. This error is the speed ratio measurement is increased for heavy gases because of the scattering tail evident for heavy species (Fig. 2).

Fig. 7 shows the terminal $T_{ll}$ for seeding $N_2$ in He and anti-seeding $N_2$ in Ar (5% dilution). $T_{ll}$ data are transformed from $S_{ll}$ data using eq. (4). Fig. 7(a) shows that $T_{ll,N2} > T_{ll,He}$ for most $P_o$. There is a crossover at low $P_o$. This result is not surprising as the speed ratio measurements have higher error bars because of the loss in intensity and width of beam peak approaching thermal values for He. Since $T_{ll,N2} > T_{ll,He}$, this would violate assumptions leading to eq. (13) (where we assume $T_{ll} = T_{\perp}$ in the continuum region of the jet). Looking at Fig. 3 this is certainly the case, as $\Phi_{exp}$ is lower than 7 for high $P_o$. Other seeding cases (such as 5% Kr/Ar) all show that $T_{ll,S} > T_{ll,C}$ at high $P_o$ as well. Consistently, eq. (13) does not predict $\Phi_{exp}$ well for seeding cases. Fig. 7(b) shows the anti-seeding case and $T_{ll,N2} \approx T_{llAr}$. Accordingly, data in Fig. 3 for $N_2$/Ar at high $P_o$ show that eq. (13) is approximately correct.

In the continuum region of a supersonic jet, $T_{\perp}$ and $T_{ll}$ are equal [and consequently, using eq. (4), so are $S_{\perp}$ and $S_{ll}$]. The jet, after a short axial distance, $r$, away from the nozzle, enters free molecular flow at the "quitting surface," at a distance, $r_q$, where $T_{ll}$ is frozen and remains the same value downstream. $T_{\perp}$ decreases as $1/r^2$ in the free molecular flow regime due to "geometric cooling," so $T_{\perp}(r) = T_{\perp}(r_q) \Big/ \left(\frac{r}{r_q}\right)^2$. We can then use $S_{ll}$ data to get an approximation for eq. (12), where

$$\Phi = \left(\frac{m_S}{m_C}\right)\left(\frac{T_{ll,C}(r_q)}{T_{ll,S}(r_q)}\right)\left(\frac{v_{s,S}}{v_{s,C}}\right)^2 \tag{14}$$

Fig. 8 shows $\Phi_{exp}$ measured by the $J_{S,d}/J_{C,d}$ method and $\Phi_{S2}$ calculated by measured $S_{ll}$. The data correlate well for both $N_2$ in He and $N_2$ in Ar, including cases with very little dilution. The points showing the most deviation from the unity line are all

$N_2$ in Ar data. Most likely the error in the measurement of $S_{ll,N2}$ and $S_{ll,Ar}$ data [as shown in Fig. 6(b)] are responsible for this misapproximation using $\Phi_{S2}$. While $P_o$ is not shown on this plot, in general low $P_o$ corresponds to the high $\Phi$ data. Low $P_o$ data for especially $N_2$ in He data (and to a lesser extent $N_2$ in Ar data) show an overprediction of $\Phi_{exp}$ using $\Phi_{S2}$. This overprediction is a result of the expansion distribution no longer being supersonic ($S$<1) and hence rendering the assumptions for eq. (12) invalid.

In light of Fig. 8, it would appear that if accurate correlations for the terminal speed ratios of the heavy and light species were available, eq. (12) could be used to predict $\Phi$ (with good accuracy for reasonably high $P_o$ beams). Theoretical correlations exist for $T_{ll,S}$ and $T_{ll,C}$ by Patch in terms of the temperature slip parameter (TSP).[8] The TSP is a complex function of the molecular properties of the gases in a binary mixture:

$$TSP_i \equiv C_i n_o d\left(\frac{\langle m\rangle}{\mu_{ij}}\right)^{1/2} \tag{15}$$

where $C_i = B/A_i$, and

$$\begin{aligned} B \equiv\ & \frac{2x_i^2\mu_{ij}}{m_i+m_j}\left(\frac{m_i}{m_j}+5\right)\left(\frac{2\mu_{ij}}{m_i}\right)^{1/2}\sigma_{ij}^2\Omega_{ij}^{(2,2)^*}\sigma_{ii}^2\Omega_{ii}^{(2,2)^*} \\ & +\frac{2x_j^2\mu_{ij}}{m_i+m_j}\left(\frac{m_j}{m_i}+5\right)\left(\frac{2\mu_{ij}}{m_j}\right)^{1/2}\sigma_{ij}^2\Omega_{ij}^{(2,2)^*}\sigma_{jj}^2\Omega_{jj}^{(2,2)^*} \\ & +x_ix_j\left[\frac{10\mu_{ij}}{m_i+m_j}\sigma_{ij}^2\Omega_{ij}^{(2,2)^*}\sigma_{ij}^2\Omega_{ij}^{(1,1)^*}+\left(\frac{2\mu_{ij}}{m_i}\right)^{1/2}\left(\frac{2\mu_{ij}}{m_j}\right)^{1/2}\sigma_{ii}^2\Omega_{ii}^{(2,2)^*}\sigma_{jj}^2\Omega_{jj}^{(2,2)^*}\right] \end{aligned} \tag{16}$$

and

$$A_i \equiv \frac{2\mu_{ij} m_i}{m_i + m_j}\left(\frac{x_i}{m_j} - \frac{x_j}{m_i}\right)\sigma_{ij}^2 \Omega_{ij}^{(2,2)^*} + \frac{5\mu_{ij}}{m_i + m_j}\sigma_{ij}^2 \Omega_{ij}^{(1,1)^*} + x_j\left(\frac{2\mu_{ij}}{m_j}\right)^{1/2} \sigma_{jj}^2 \Omega_{jj}^{(2,2)^*} \tag{17}$$

where $x_i$ is the mole fraction of species $i$, $\mu_{ij}$ is the reduced mass, $\sigma_{ij}$ is the average collision cross section of species $i$ and $j$, and $\Omega_{ij}$ is the collision integral. Fig. 9 displays the relationship between the mass-weighted speed ratio $S_S(<m>/m_S)^{1/2}$ of the seed and TSP. This relationship is similar to the relationship that Xia, et al. had found for silane and disilane compounds seeded in $H_2$, He and Ar.[1] Our relationship includes both seeding and anti-seeding cases, where $N_2$ is seeded in He or Ar and Kr is seeded in He, $N_2$ or Ar. The empirical fit we arrive at for the mass-weighted speed ratio data is $S_S(<m>/m_S)^{1/2}=\beta(TSP)^{\alpha}$, where $\beta$=0.205 and $\alpha$=0.623. The $S_S(<m>/m_S)^{1/2}$ data for Kr in $N_2$ appear lower than the rest of the set. A possible explanation for this deviation is that rotational cooling of $N_2$ is much slower than translational cooling, yielding a higher $T_C$ than for a monoatomic carrier gas expansion (the rest of the data). Since the majority of collisions the seed gas involve the carrier gas, the excess thermal energy ($T_C$) would still transfer to the seed gas ($T_S$), yielding a lower $S_S$.

$S_{ll,C}$, the carrier gas speed ratio, follows a different trend. Fig. 10 shows $S_{ll}$ for (a) He (b) $N_2$ and (c) Ar. We include both data for both binary (closed circles) and single-component supersonic jets (open circles). There is very little difference between $S_C(<m>/m_C)^{1/2}$ for single-component and carrier beams versus *TSP* for $N_2$ and Ar. He as a carrier has a lower $S_C(<m>/m_C)^{1/2}$ than in a single-component beam. Essentially, the heavy seed gas in the $N_2$ or Ar expansions does not significantly affect $S_C$. Our speed

ratios for the monoatomic gases are significantly lower (about 2/3) of what Beijerinck, et al. determined experimentally that followed the relationship[5]

$$S_{ll,\infty} = A\left[\sqrt{2}n_o d\left(\frac{53C_6}{kT_o}\right)^{1/3}\right]^B \qquad (18)$$

where $n_o$ is the stagnation number density and $C_6$ is a Leonard Jones parameter. For monoatomic gases ($\gamma$=5/3), they determined $A$=0.778 and $B$=0.495. Our data shows pure He speed ratio relates as $S(<m>/m_C)^{1/2} = 0.046(TSP)^{0.94}$. $N_2$ speed ratios have the relationship of $S(<m>/m_C)^{1/2} = 0.29(TSP)^{0.49}$, while Ar speed ratios have the relationship of $S(<m>/m_C)^{1/2} = 0.14(TSP)^{0.73}$.

Using our data in Fig. 9 and 10, one can predict a beam's $S_{ll,S}$ and $S_{ll,C}$ from knowledge of beam composition and Lennard-Jones parameters. With $S_{ll,S}$ and $S_{ll,C}$ determined, one can use eq. (12) to estimate $\Phi$ at reasonably high $P_o$, and the viability of this approximation is shown in Fig. 8. For example, you want to determine the $\Phi$ of 5% $N_2$ in He at $P_o$=285 Torr. Using Lennard-Jones parameters and the given mole fraction, we get $TSP_S$=125 and $TSP_C$=235. This yields $S_{N2}$ = 9.63 using the seed gas relationship and $S_{He}$ = 5.68 for He from Fig. 10(a). In this case, we get $(S_{N2} /S_{He})^2$ = 2.9, which is in good agreement with $\Phi_{exp}$=3.2 in Fig. 3.

The difference between eq. (12) and eq. (13) are the assumptions of beam ideality, i.e. the lack of velocity and temperature slip [i.e., the second and third terms of the right hand side of eq. (15)]. Our data in Fig. 7 have already shown the difference between $T_{ll,S}$ and $T_{ll,C}$. We have also taken data on $v_{S,S}$ and $v_{S,C}$ of the binary expansions. Using the fit determined by minimizing eq. (11), we can get $f(v)$ of each constituent of the binary

expansion, which allows us to calculate the energy for each constituent. The energy correction factor, $\xi$, (fraction of ideal energy achieved) is expressed as

$$\xi = \frac{\frac{1}{2} m v_s^2}{\frac{1}{2} m v_\infty^2} \tag{19}$$

A fully expanded beam would yield $\xi$=1 and non-ideal beams yield $\xi$<1. Measurements of $\xi$ are correlated using the velocity slip parameter (VSP). The VSP[16] is defined as

$$VSP = \frac{(\mu \langle m \rangle)^{1/2}}{|m_S - m_C|} (n_o d) \sigma_{C,S}^2 \Omega_{C,S}^{(1,1)} \tag{20}$$

where $\mu = m_S m_C/(m_C + m_S)$ is the reduced mass, $m_C$ is the mass of the carrier gas, $n_o$ is the stagnation density, $d$ is the nozzle diameter, $\sigma_{S,C}^2$ is a mean Lennard-Jones $\sigma$ parameter, and $\Omega_{C,S}^{(1,1)}$ is the corresponding collision integral. An empirical relationship from Patch is used to get $\sigma_{S,C}^2 \Omega_{S,C}^{(1,1)} = 0.96(C_6 / k_B T_o)^{1/2}$, with $C_6 = (C_{6,S} C_{6,C})^{1/2}$ and $C_{6,i} = 4\sigma_i^6 \varepsilon_i$. Fig. 11 presents the relationship between the energy correction factor and the VSP, fitting the relationship

$$\xi = 1 - \frac{x_1}{(x_2 + VSP)^m} \tag{21}$$

where $x_1$ = 46.8, $x_2$=6.69 and $m$ = 2.02. Xia et.al. fit their data to eq. (212), but acquire different numbers, $x_1$ = 0.629, $x_2$=0.393 and $m$ = 0.529.[1] This difference may be attributed to the fact they used much heavier gases, such as $SiH_4$ and $Si_2H_6$, which are also polyatomic (more degrees of freedom to cool, such as rotational and vibrational) as opposed to being monatomic or diatomic as our gases are. The deviation at low pressures between $\Phi_{exp}$ and the $\Phi = (S_S/S_C)^2$ prediction also coincides with the velocity slip in Fig.

11. In addition, the ratio of sudden freeze surface positions for seed and carrier gas $\left(\frac{r_{q,C}}{r_{q,S}}\right)$ becomes less than unity as $P_o$ drops, making the equality in eq. (14) not valid.

While there has been some data published on the mass-weighted speed ratio and terminal energy of seeded supersonic beams,[1] that data had not been linked yet to the enrichment ratio of seeded supersonic beams.

Fernandez de la Mora, et al.[14] measured the degree of enrichment in a seeded supersonic beam for largely disparate mixtures ($m_S/m_C > 80$) by measuring the density of species transverse to the axial centerline at a short axial distances ($r/d \sim$ 1-5). They determined a correlation of $\Phi$ in terms of the full-width at half-maximum (FWHM) distribution of the seed gas $(d_p)$ and a parameter describing the carrier gas expansion. Their data, for a given $r/d$, correlated well to a dimensionless parameter, the Stokes number, $N_S$. $N_S$ is essentially a Knudsen number governing translational equilibrium between the two gases. Fernandez de la Mora, et al.[14] present data on the enrichment of heavy seed gases in light carrier gases of supersonic expansions, however in a different format than our data. Their data is presented in terms of $(d_p/d)$ at a given $r/d$ versus $N_S$.the data does consistently show the same relationship between enrichment and $1/N_S$. $N_S$ measures the ratio between the time $\tau$ required to stop a particle by friction with a quiescent suspending gas and a characteristic fluid deceleration time. We express $N_S$ as

$$N_S = \tau_o c_o / d \tag{22}$$

$c_o$ is the sound speed, $c = \sqrt{\gamma kT / m}$. If we consider Einstein's law to get $D$ diffusivity ($D = kT\tau/m_C$), $N_S$ can be rewritten as

$$N_S = N_F / N_{Re} \tag{23}$$

$N_{Re}$ (the Reynolds number) is expressed as

$$N_{Re} = \gamma P_o d/\mu_o c_o \quad (24)$$

where $\mu_o$ is the viscoscity coefficient. $N_F$ (Fenn number) is a property measuring the disparity of the relaxation scales for the two species in the gas mixture. $N_F$ may be expressed in terms of the mixture viscosity to the mass diffusivity ratio (the Schmidt number) $N_{Sc}=\mu/\rho D$ and the molecular mass ratio $m_S/m$ as

$$N_F = \gamma m_S/(mN_{Sc}) \quad (25)$$

$N_S$ is essentially a Knudsen number governing translational equilibrium between the two gases, which determines whether or not there is species separation. High $N_S$ indicates large translational nonequilbrium meaning there is significant aerodynamic decoupling of the species velocities. As $N_S \rightarrow 0$, translational equilibrium is reached and the streamlines of the two gases converge. $1/N_S \propto P_o d$, the typical supersonic jet nozzle parameter that measures the completeness of the expansion. Accordingly, in the limit of the ideal expansion, the expansion would be in equilibrium.

Our data are presented in Fig. 12 in terms of $\Phi_{exp}$ vs. $1/N_S$. $\Phi_{exp}$ decreases as $1/N_S$ increases, consistent with the approach towards the equilibrium limit. The 5% seeding data presented in Fig. 12(a) follow a trend with a slight downward concavity. Introduction of variable percentage data and 10 sccm constant seed flow rate with added $Q_C$ data [Fig. 12(b)] do appear to follow the same relationship as the 5% seeding data [Fig. 12(a)], however show a deviation towards high $\Phi_{exp}$ at low $N_{Re}/N_F$. In general, we find that the relationship $\Phi_{\mathrm{exp}} = 92(N_{Re}/N_F)^{-0.77}$ works well. Considering Fig. 11 and Fig. 12, the enrichment occurs precisely where there is significant velocity slip between the species (as $VSP$ and $N_{Re}/N_F$ are similar functions).

**CONCLUSIONS**

In summary, we use the TOF characterization of several mixtures of seeded supersonic beams to get information on $\Phi_{exp}$, $S$, $T$, $\xi$ and $v$. We measure these quantities for three different types of flow mixtures: 5% mole fraction seed gas with variable total flow rate, constant seed gas flow rate (10 sccm) with variable carrier gas flow rate, and variable percentage mole fraction seed gas with constant total flow rate. It has become clear that there is a minor dependence on the mole fraction seed gas used in the mixture. Instead, the controlling factors are primarily the disparity of masses $(m_S/m_C)$ and the pressure of the expansion. For high nozzle pressures, the square of the ratio of the seed and carrier gas parallel speed ratios does well to predict enrichment. For experimentalists who have the capability to measure speed ratio of the constituents of the expansion, this procedure can work. For seeding cases, the parallel temperature of the seed gas is always higher than the parallel temperature of the carrier gas. We present seed speed ratio data scaled by $(\langle m \rangle/m_S)^{1/2}$ versus *TSP* and carrier speed ratio data by $(\langle m \rangle/m_C)^{1/2}$ versus *TSP*. We present ideal energy fraction data, $\xi$, versus *VSP*. To conclude, we collapse all our enrichment data by relating $\Phi$ to $1/N_S = (N_{Re}/N_F)$, yielding $\Phi = 92(N_{Re}/N_F)^{-0.77}$. The experimentalist can use nozzle pressure and Lennard-Jones parameters to determine the dimensionless parameters $N_{Re}$ and $N_F$, consequently yielding $\Phi$.

## REFERENCES

[1]L.-Q. Xia, M. E. Jones, N. Maity, and J. R. Engstrom, J. Vac. Sci. Technol. A., **13**, 2651 (1995).

[2]A. Sellidj, B. A. Ferguson, T. J. Mattord, B. G. Streetman and C. B. Mullins, Appl. Phys. Lett., **68**, 3314 (1996).

[3]B. A. Ferguson, A. Sellidj, B. B. Doris and C. B. Mullins, J. Vac. Sci. Technol. A., **14**, 825 (1996).

[4]A. J. McGinnis, D. Thomson, R. F. Davis, E. Chen, A. Michel, and H. H. Lamb, Surf. Sci., **494**, 28 (2001).

[5]H. C. W. Beijerinck, N. F. Verster, Physica C, **111**, 327 (1981).

[6]E. L. Knuth, in *Engine Emissions: Pollutant Formation and Measurement*, edited by G. S. Springer and D. J. Patterson (Plenum, New York, 1973), pp. 319-363.

[7]P. K. Sharma, E. L. Knuth, and W. S. Young, J. Chem. Phys., **64**, 4345 (1976).

[8]D. F. Patch, “Application of Free Jet Sources to Reactive Crossed Molecular Beam Experiments,” PhD thesis, University of California, San Diego.??need year??

[9]D. Eres, Mater. Res. Soc. Symp. Proc. **201**, 11 (1991).

[10]J. B. Anderson, R. P. Andres, J. B. Fenn, and G. Maise, Rarified Gas Dynamics, edited by J. H. d. Leeuw (Academic, New York, 1966), p. 106.

[11]K. A. Pacheco, B. A. Ferguson, C. Li, S. John, S. Banerjee, and C. B. Mullins, Appl. Phys. Lett. **67**, 2951 (1995).

[12]N. A. Smith, “Time domain corrections,” PhD thesis, North Carolina State Univeristy, Raleigh (2003).

[13]S. DePaul, D. Pullman, and B. Friedrich, J. Phys. Chem., **97**, 2167 (1993).

[14]J. Fernandez de la Mora and J. Rosell-Llompart, J. Chem. Phys. **91**, 2603 (1989).

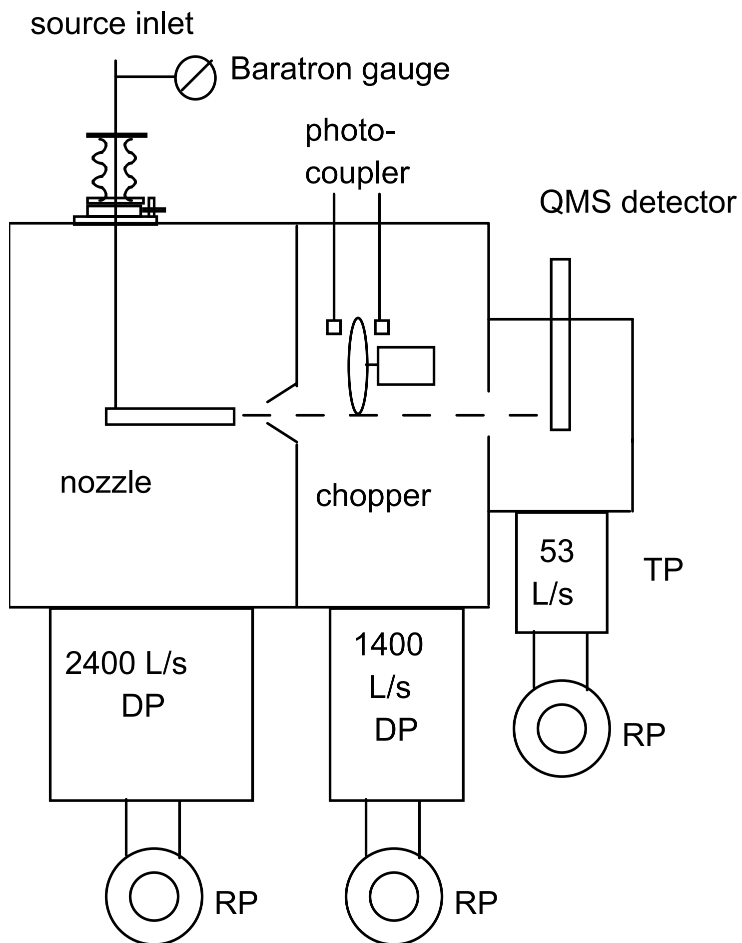


**Figure 1:** Schematic of two-stage TOF apparatus. DP - diffusion pump. TP - turbomolecular pump. RP - mechanical roughing pump.

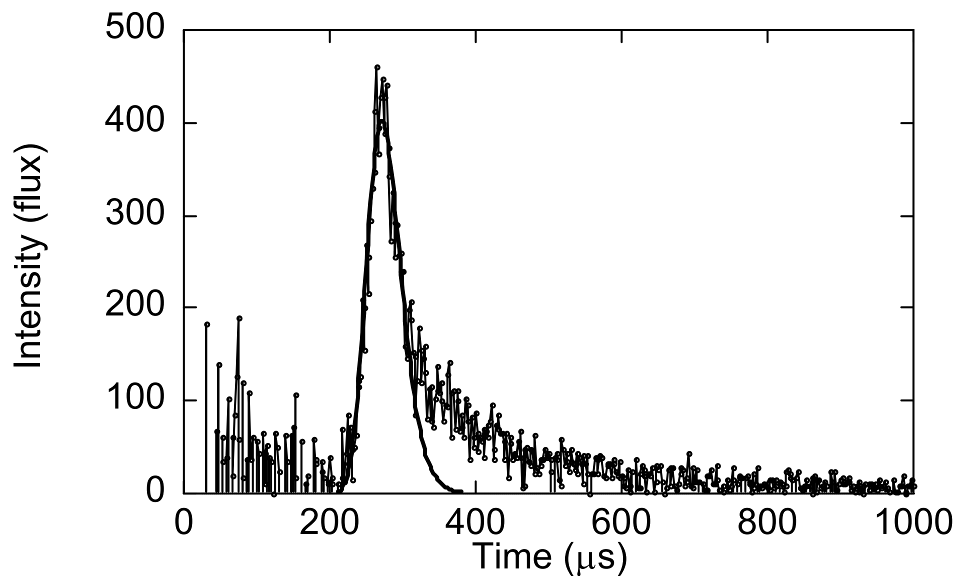


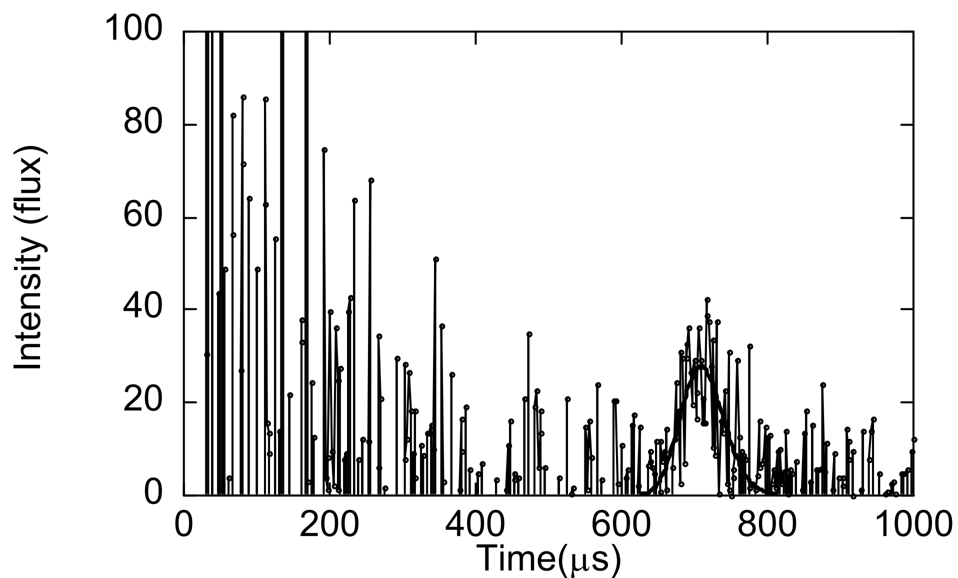


**Figure 2:** TOF spectra for 5 sccm $N_2$ in (a) 95 sccm He ($P_o$ = 240 Torr) and (b) 95 sccm Ar ($P_o$ = 429 Torr)

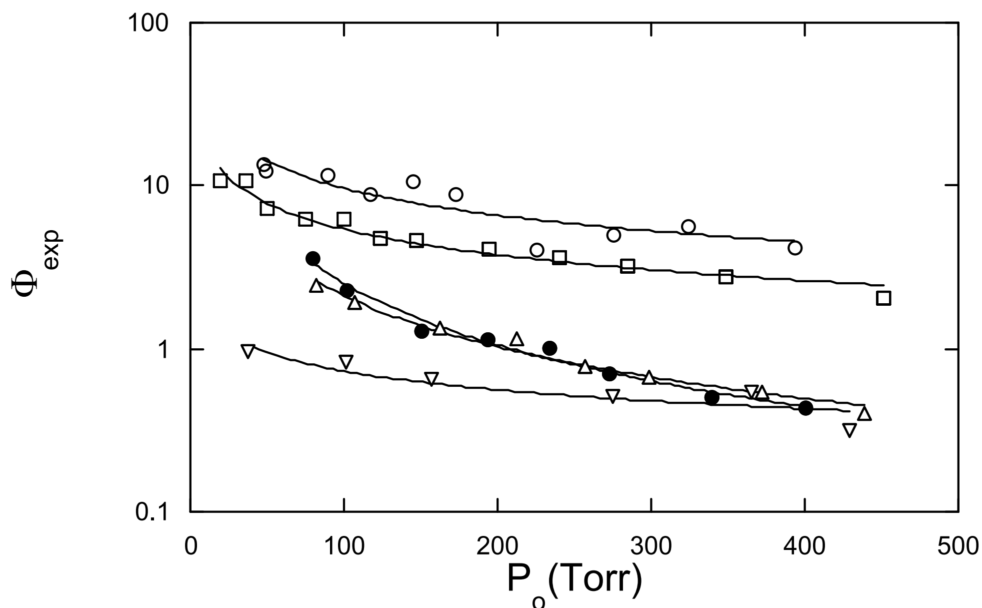


**Figure 3**: $\Phi_{exp}$ vs. $P_o$ (Torr). (a) ○ - 5% Kr in He; □ - 5% $N_2$ in He; △ - 5% Kr in Ar; ▽ - 5% $N_2$ in Ar; ●-5% Kr in $N_2$. Lines shown in figure are best fits to exponential relationship: $\Phi_{exp}= aP_o$

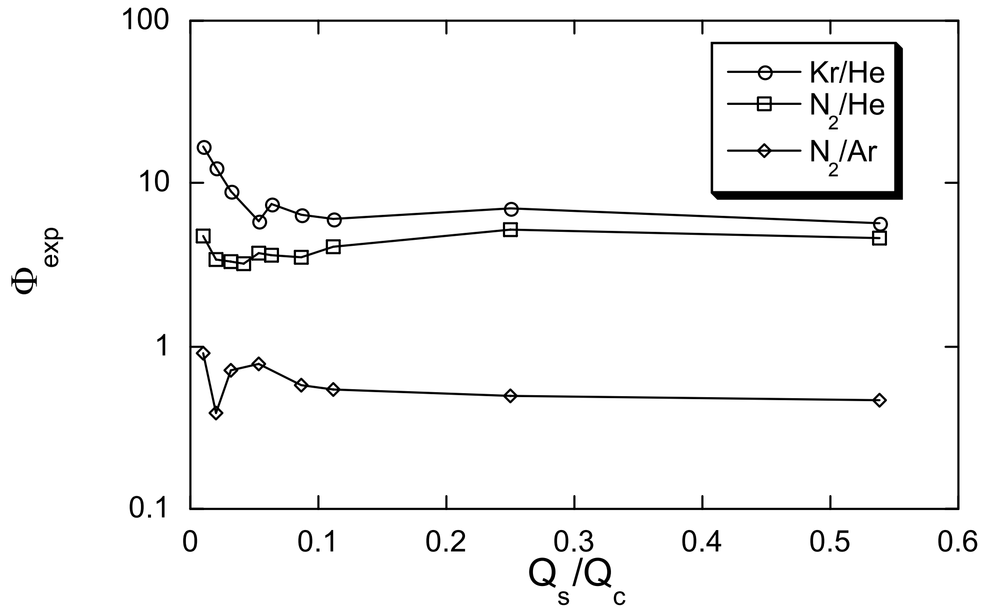


**Figure 4:** $\Phi_{exp}$ vs. molar flow ratio. ○ - 100 sccm total gas flow ($Q_C$ + $Q_S$), variable % Kr seeded in He; □-100 sccm total gas flow ($Q_C$ + $Q_S$), variable % $N_2$ seeded in He; ◇-50 sccm total gas flow ($Q_C$ + $Q_S$), variable % $N_2$ seeded in Ar.

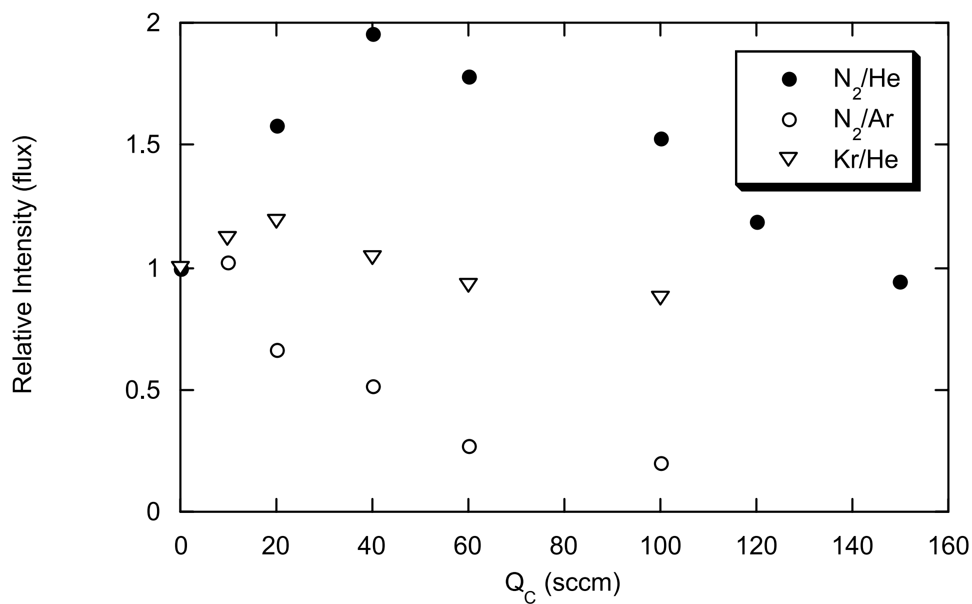


**Figure 5(a):** Relative intensity of seeded beam vs. carrier flow rate ($Q_C$) for constant $Q_S$ = 10 sccm.

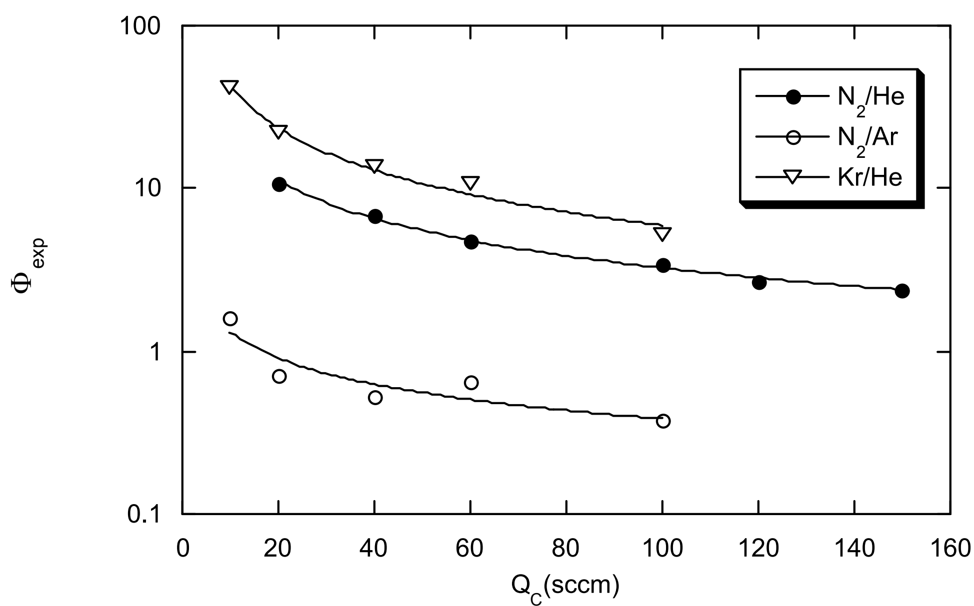


**Figure 5(b):** $\Phi_{exp}$ vs. carrier flow rate ($Q_C$) for constant $Q_S$ = 10 sccm.

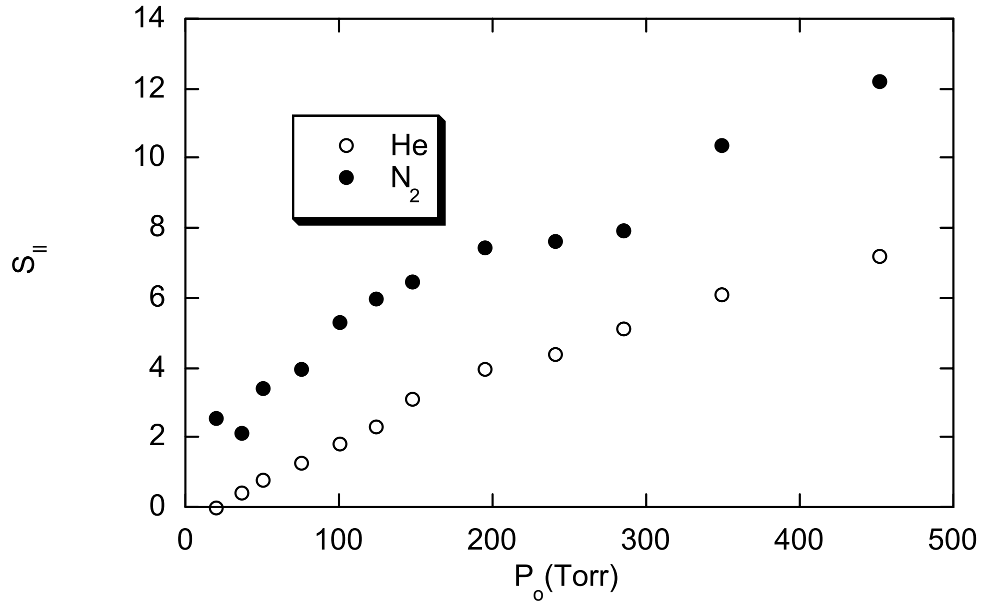


**Figure 6(a):** *S* vs. $P_o$, 5% $N_2$ in He.

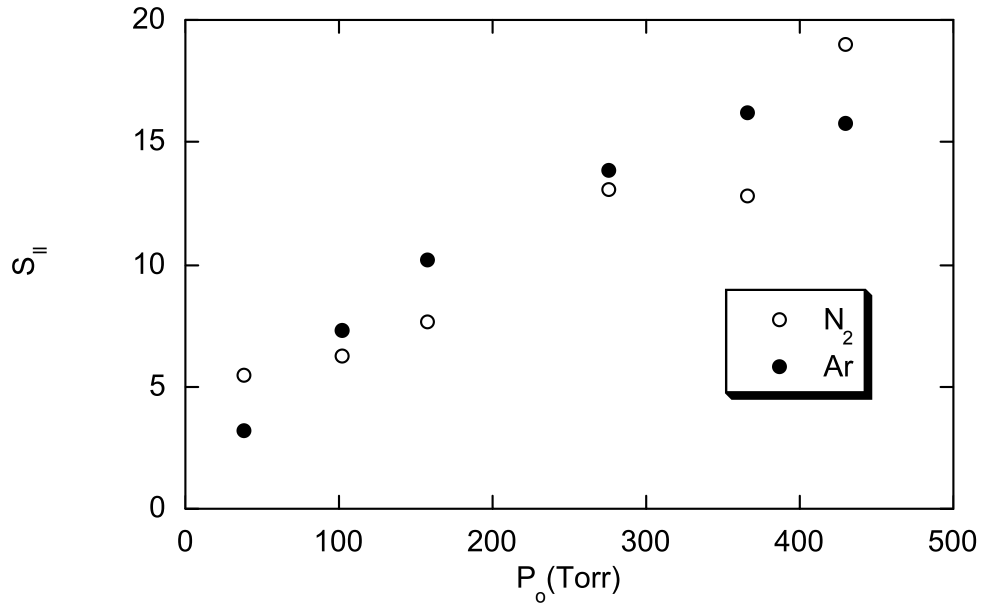


**Figure 6(b):** *S* vs. $P_o$, 5% $N_2$ in Ar.

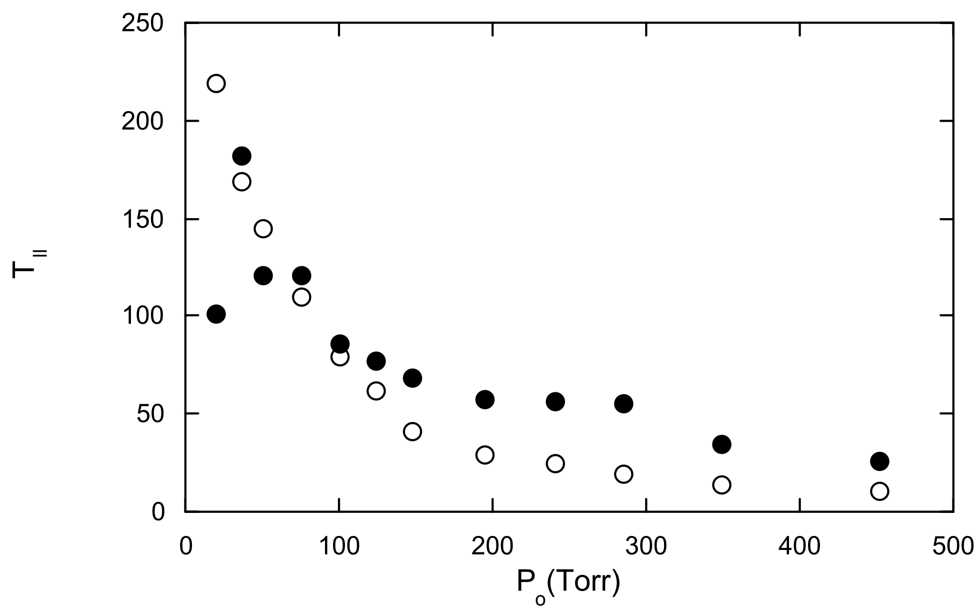


(a)
**Figure 7(a)**: $T_{ll}$ vs. $P_o$ for 5% $N_2$ in He. Closed symbols-$N_2$. Open symbols - He.

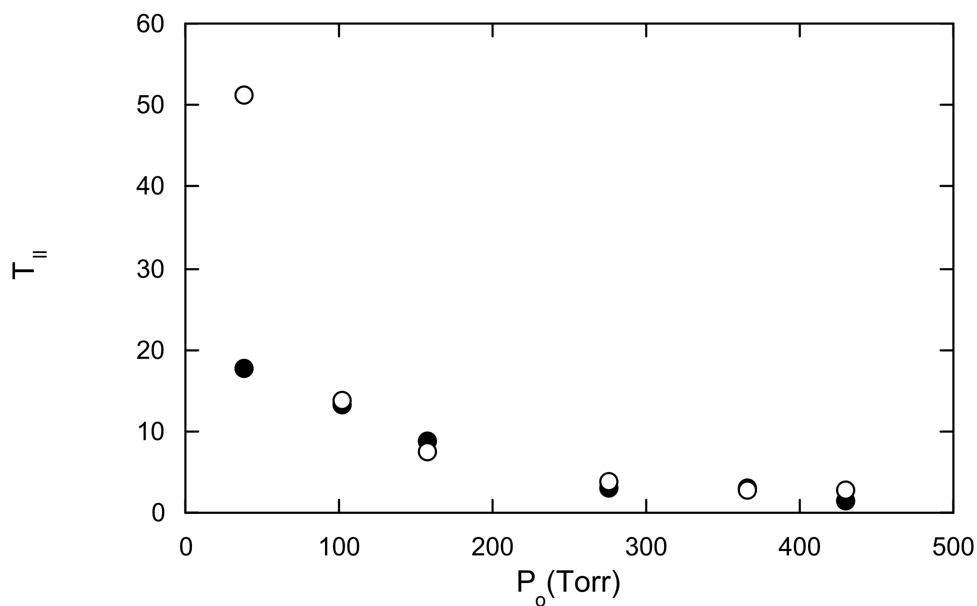


(b)
**Figure 7(b)**: $T_{ll}$ vs. $P_o$ for 5% $N_2$ in Ar. Closed symbols-$N_2$. Open symbols - Ar.

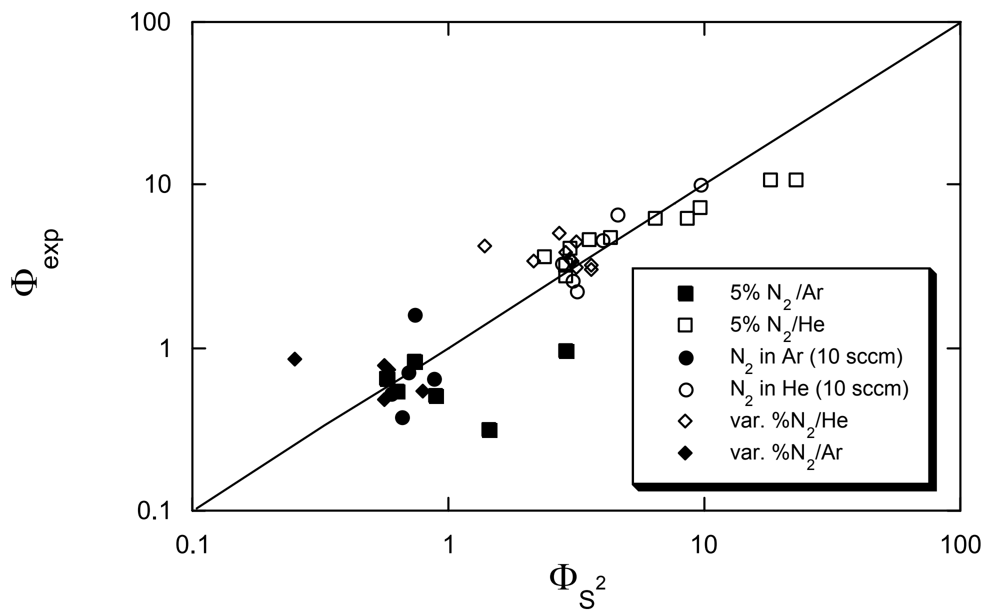


**Figure 8:** $\Phi_{exp}$ vs. $\Phi_{S2}$, a prediction based off of measured speed ratios.

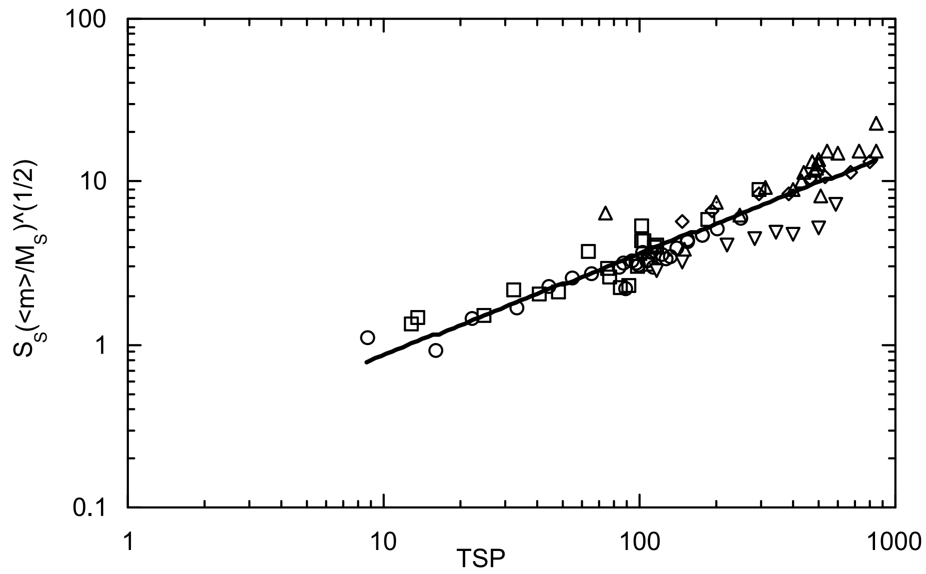


**Figure 9:** Mass-weighted speed ratio vs. TSP. ○ - $N_2$ in He; □ - Kr in He; ◇-Kr in Ar; △-$N_2$ in Ar; ▽-Kr in $N_2$; fit represents $S_S(<m>/m_S)^{(1/2)} = 0.205(TSP)^{0.623}$.

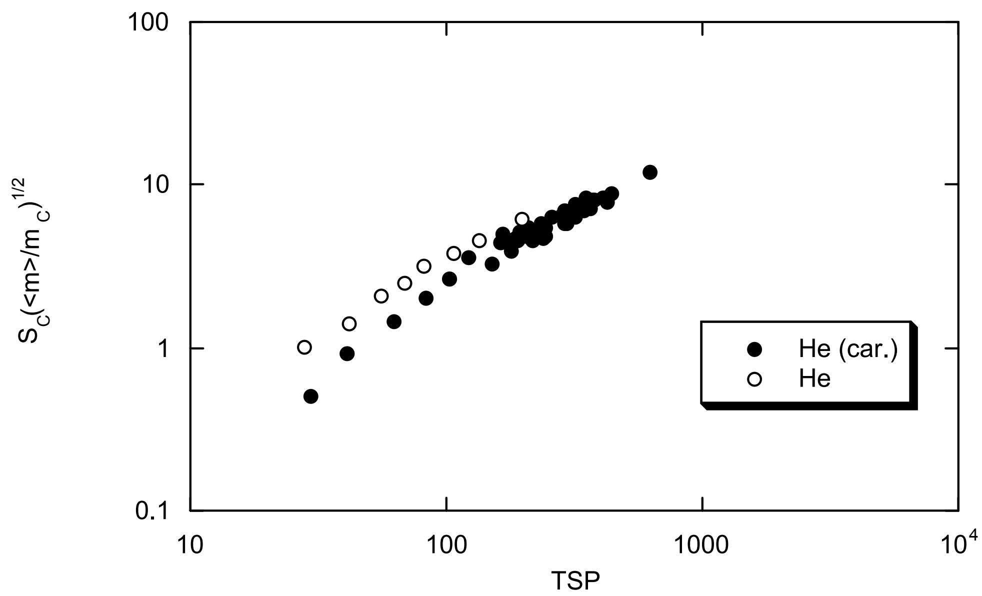


**(a)**

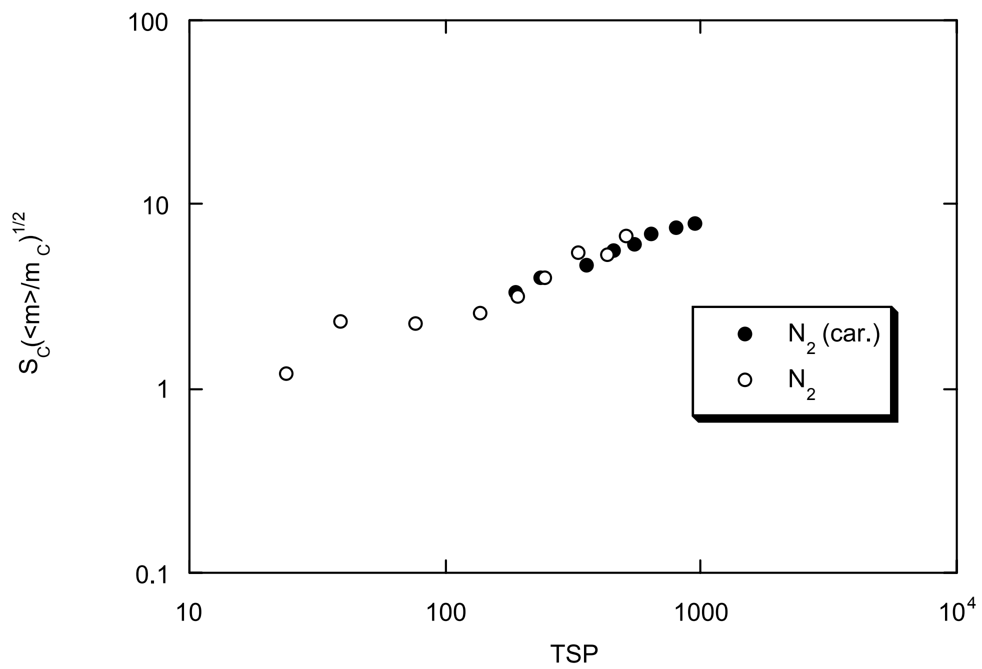


**(b)**

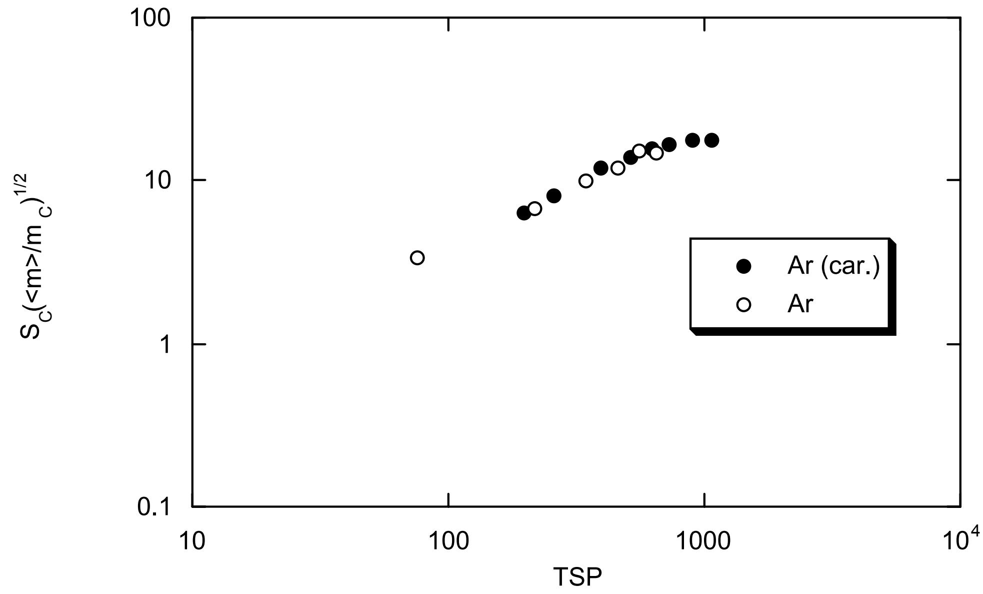


**(c)**

**Figure 10:** (a) He [$S(<m>/m_C)^{1/2} = 0.46(TSP)^{0.94}$]; (b) $N_2$ [$S(<m>/m_C)^{1/2} = 0.29(TSP)^{0.49}$] and (c) Ar [$S(<m>/m_C)^{1/2} = 0.14(TSP)^{0.73}$]. Carrier gas are closed circles, pure gas are open circles.

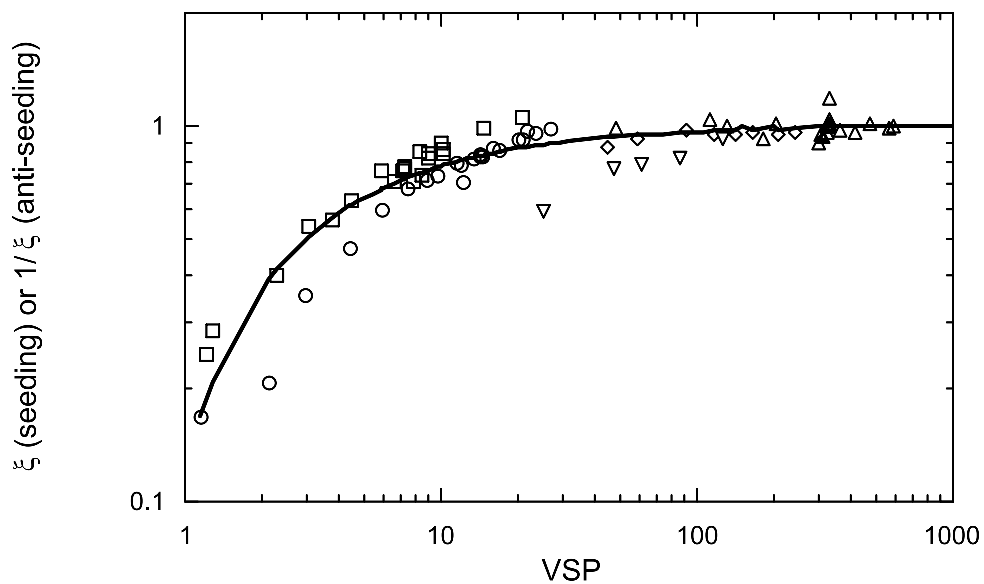


**Figure 11:** Energy correction factor ($\xi$) vs. VSP. ○ - $N_2$ in He; □ - Kr in He; ◇-Kr in Ar; △-$N_2$ in Ar; ▽-Kr in $N_2$. The solid line represents a fit of the data; $\xi = x_1/(x_2 + VSP)^m$, where $x_1$ = 46.8, $x_2$=6.69 and $m$ = 2.02.

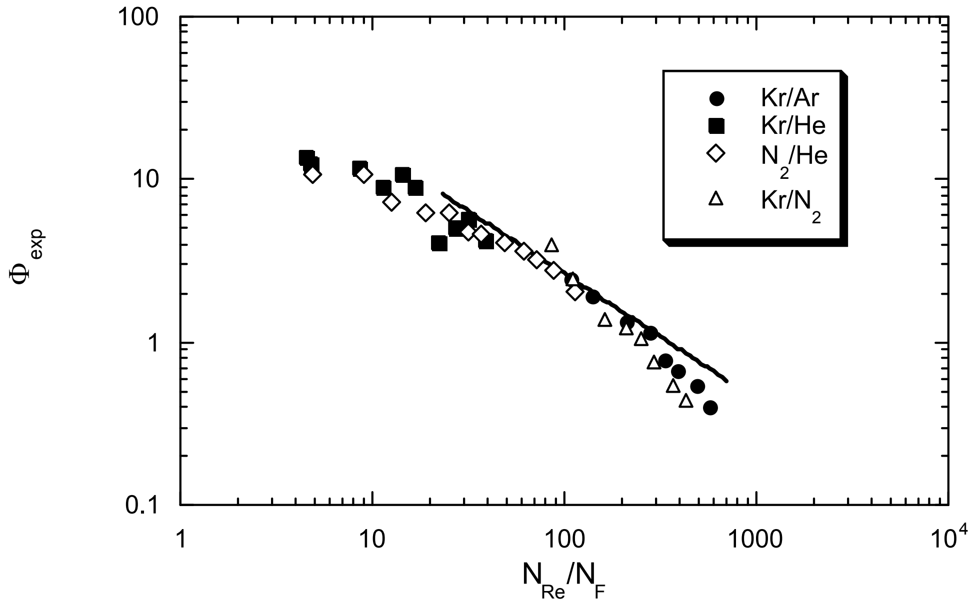


**(a)**

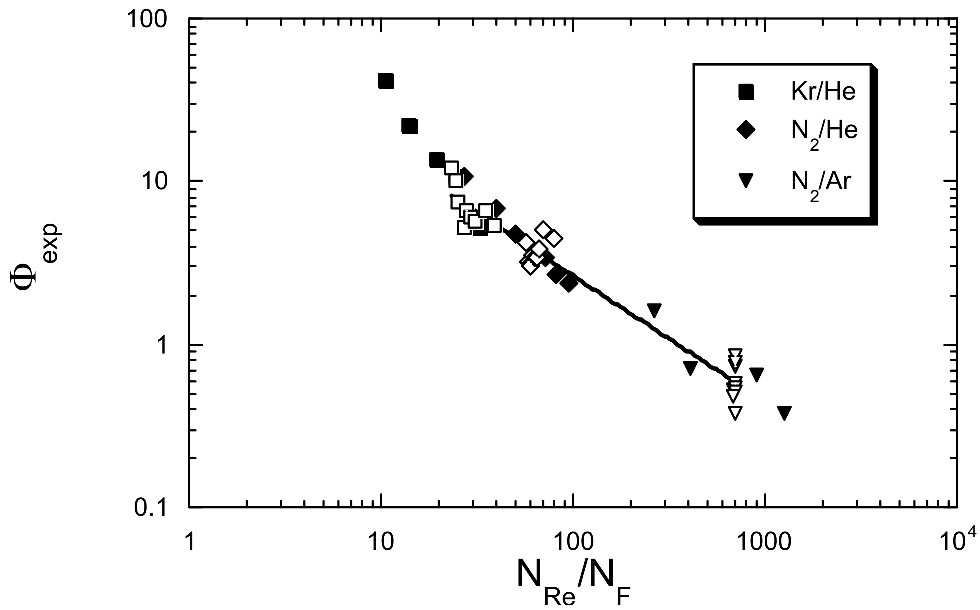


**(b)**

**Figure 12:** $\Phi_{exp}$ versus $N_{Re}/N_F$. (a) 5% seed in carrier gas (b) open symbols represents 10 sccm seed gas with added carrier gas flow; closed symbols represent var. % data. Fit of var. % data: $\Phi_{exp} = 92(N_{Re}/N_F)^{-0.77}$.

**Table 1:** Estimated values of $m_p/m$, $N_{Sc}$ and $N_F$ for several gas mixtures.

| Gas Mixture | $N_{Sc}$ | $N_F$ | $m_p/m$ |
|---|---|---|---|
| Kr/Ar | 0.783 | 4.47 | 2.1 |
| Kr/He | 0.920 | 38.06 | 21 |
| $N_2$/He | 0.792 | 14.73 | 7.0 |
| $N_2$/Ar | 0.562 | 2.08 | 0.7 |
| Kr/$N_2$ | 0.690 | 6.08 | 3.0 |

3. Surface roughness correlations in homoepitaxial growth of GaN(0001) films by $NH_3$ supersonic jet epitaxy. Nicholas A. Smith, Arthur J. McGinnis, Robert F. Davis and H. Henry Lamb. Manuscript will be sent to Journal of Applied Physics.

# Surface Roughness Correlations in Homoepitaxial Growth of GaN(0001) Films by $NH_3$ Supersonic Jet Epitaxy

Nicholas A. Smith[a], Arthur J. McGinnis[b], Robert F. Davis[b] and H. Henry Lamb[a,*]

[a]Department of Chemical Engineering, North Carolina State University, Raleigh, North Carolina 27695-7905, USA

[b]Department of Materials Science and Engineering, North Carolina State University, Raleigh, North Carolina 27695-7906, USA

[*]Corresponding author: Tel.: +1-919-515-6395; fax: +1-919-515-3465. E-mail address: lamb@eos.ncsu.edu.

**ABSTRACT**

The morphology of homoepitaxial growth of GaN(0001) thin films on metal-organic chemical vapor deposition (MOCVD)-grown GaN(0001)/6H-SiC substrates was probed using atomic force microscopy (AFM). $NH_3$-seeded supersonic molecular beams (0.3 eV - 1.8 eV) in He and $H_2$ were employed to provide an active source of nitrogen (flux > 2 x $10^{15}$ $cm^{-2}s^{-1}$ at the substrate). Substrate temperature was 750°C employing a Ga flux of 2.9 x $10^{14}$ $cm^{-2}s^{-1}$ for growth times ranging from 15 min to 6 h. Reflection high-energy electron diffraction (RHEED) patterns demonstrated quasi two-dimensional growth for $NH_3$-limited growth conditions and three-dimensional growth for Ga-limited growth conditions. AFM yielded non-faceted surfaces [root mean square (RMS) roughness ~ 1-3 nm] for $NH_3$-limited growth conditions and faceted surfaces (RMS roughness ~ 13-25 nm) for Ga-limited growth conditions. Scaling analysis of film surfaces determined that the primary surface transport mechanism is surface diffusion for all growth conditions employed.

## I. INTRODUCTION

Control of surface morphology is essential in the growth of semiconductor thin films for device applications. For example, smooth surfaces with minimal interfacial roughness are required in InGaN multiple quantum well structures for blue laser applications whether they are grown by molecular beam epitaxy (MBE) or metal-organic chemical vapor deposition (MOCVD). Substrate lattice match and orientation, temperature, growth rate, and reactant flux ratio are key experimental variables that affect surface morphology. Ideal layer-by-layer (Frank-van der Merwe) growth should result in atomically smooth films with low defect densities. The growth mode (Frank-van der Merwe, Volmer-Weber or Stranski-Krastanov) is determined in the thermodynamic limit by surface energy differences between the film and substrate.[1] Consequently, homoepitaxial films should always exhibit Frank-van der Merwe growth in the equilibrium thermodynamic limit. Thermodynamic models, however, often do not describe actual surfaces due to the low growth temperatures and high growth rates that are employed in many practical growth processes.[2]

Some information on GaN MBE growth modes is available. For example, King, *et al.* reported Stranski-Krastanov growth of GaN(0001) on AlN for low temperatures (<750°C) and Frank van der Merwe growth for high temperatures (>750°C).[3] Particular attention has been focused on the relationship between III/V flux ratio and the surface morphology of GaN films. Several investigators have reported that there is an abrupt transition in surface morphology from two-dimensional to three-dimensional surfaces for GaN growth when switching from Ga-rich conditions to N-rich conditions.[4,5,6,7] GaN($000\bar{1}$) grown heteroepitaxially on c-plane sapphire by MBE using elemental Ga

and either $NH_3$[4] or an RF N source[5] exhibited this morphological transition. Tarsa, *et al.* grew homoepitaxial GaN(0001) films by plasma-assisted MBE at 750°C and also observed similar behavior.[6] Pavloska, *et al.* grew homoepitaxial GaN(0001) by supersonic jet epitaxy (SJE) using $NH_3$-seeded beams at substrate temperatures of 655-710°C and reported a similar 3D to 2D transition.[7] Pavloska, *et al.* monitored the growth surface by in situ low energy electron microscopy (LEEM) and low energy electron diffraction (LEED) to gain insight into which growth mode prevails during $NH_3$-SJE of homoepitaxial GaN(0001) films.[7] High III/V flux ratios yielded films with non-faceted surfaces resulting from quasi-two-dimensional growth. LEEM studies monitored the growth in-situ and observed that the final surface morphology resembled the initial surface morphology. Initially, small islands nucleate on the substrate surface, grow laterally, and then coalesce. Featureless (less than LEEM resolution) basal plane growth occurred for the rest of the growth time. Low III/V flux ratios produced films with faceted surfaces. We infer from these observations that a III/V flux ratio-dependent faceted to non-faceted growth transition is a general phenomenon in GaN MBE regardless of the substrate, GaN polarity, choice of nitrogen precursor, and the substrate temperature.

Previous investigators[5,6] have ascribed faceted GaN growth to a stochastic (statistical) roughening mechanism. Tarsa, *et al.* hypothesized that the interfacial roughness arises from a restricted Ga diffusion length under N-rich growth conditions.[6] Stacking faults were also observed by cross-sectional transmission electron microscopy (XTEM) in homoepitaxial films grown under N-rich conditions. Myers, *et al.* attributed film roughening (faceting) for films grown under N-rich conditions to "quenched"

growth leading to stochastic roughening of the surface.[5] Their XTEM results showed inversion domain boundaries (IDBs) at the center of pyramidal hillocks. The XTEM results of Liliental-Weber, *et al.* suggest that pinholes (growth pits) and nanotube defects in GaN films arise from differences in growth rates for GaN(0001) and GaN($000\bar{1}$) (Ga- and N-polar surfaces, respectively).[8] Daudin, *et al.* determined by convergent beam electron diffraction (CBED) that non-faceted GaN films had Ga-termination whereas pyramidal hillock formations (faceted GaN) had tiny columnar inversion domains (with Ga polarity) imbedded in a matrix exhibiting an N polarity.[9]

The original motivation for $NH_3$-SJE growth of GaN(0001) was to promote $NH_3$ dissociative chemisorption at low growth temperatures and to provide an alternative to plasma-assisted MBE and its associated potential for ion damage. A supersonic jet can provide a high intensity source of $NH_3$ with well-defined kinetic energy. Assuming an ideal expansion and no slip, the kinetic energy of $NH_3$

$$E_{NH_3} = \left(\frac{W_{NH_3}}{\overline{W}}\right) R \left(\frac{\gamma}{\gamma - 1}\right) T_o \qquad (1)$$

is determined by the average molecular weight $\overline{W}$, the stagnation temperature $T_o$, and the specific heat ratio $\gamma$.[10] Seeding $NH_3$ in a light carrier gas (He or $H_2$) accelerates the precursor to hyperthermal energies (0.2~0.7 eV for $NH_3$ in He and 0.7 ~ 1.8 eV for $NH_3$ in $H_2$) and increases the precursor gas centerline intensity.[11] Antiseeding $NH_3$ in a heavy carrier gas (Ar) yields a lower centerline intensity and lower kinetic energy (0.05 eV for $NH_3$ in Ar). Increasing the kinetic energy of $NH_3$ could increase $NH_3$ dissociative chemisorption if the process was activated and direct by overcoming an activation barrier. Hyperthermal kinetic energy would lower $NH_3$ dissociation if the process were

precursor-mediated, as the additional kinetic energy would have to be accommodated for trapping to occur. McGinnis, *et al.* inferred from kinetics measurements using $NH_3$ seeded in He, $H_2$, $N_2$ and Ar that $NH_3$ dissociative chemisorption on the GaN(0001) growth surface was precursor mediated, and consequently, imparting hyperthermal kinetic energy to $NH_3$ did not increase growth rates.[12] Hyperthermal kinetic energy could also improve surface diffusion of the impinging precursor, hence improving surface morphology.

A post-deposition determination of the kinetic roughening and smoothening processes occurring on the surface during growth can be found through scaling analysis. Scaling analysis relates measurable quantities (e.g., interfacial roughness) to universality classes. In our scaling analysis of surface roughness, we first define the local interface height difference from the mean, $S(x,y) = H(x,y) - \langle H(x,y) \rangle_L$, where $\langle H(x,y) \rangle_L$ is the average interface height over a lateral (measurement) length scale, $L$. Self-similar surfaces scale such that $S(x,y)$ and $\kappa S(\kappa x, \kappa y)$ are indistinguishable. If the height dimension scales differently that the lateral dimension, *i.e.*, $S(x,y)$ and $\kappa' S(\kappa x, \kappa y)$ are indistinguishable, then the surface is said to be self-affine (many real surfaces are self-affine). Self-similar and self-affine surfaces exhibit characteristic scaling behavior up to a critical scaling length $L_c$ which is proportional to the lateral correlation length of self-affine surfaces and self-similar surfaces. Atomic force microscopy (AFM) measurements provide information on the height $H(x,y)$ of the surface relative to the mean $\langle H(x,y) \rangle_L$. The root-mean-square (RMS) variation (standard deviation) of $S(x,y)$ over a chosen lateral length scale can be calculated from AFM topographs:

$$\zeta = [\langle S(x,y)^2 \rangle_L]^{1/2} \qquad (2)$$

where $\zeta$ is a quantitative measure of surface roughness that depends on the lateral length scale $L$ from which it is derived. Scaling of the surface roughness can be expressed as

$$\zeta(L,t) = L^{\alpha} f\left(t / L^{z}\right) \tag{3}$$

where $t$ is time, $\alpha$ is the static scaling exponent, $z = \alpha/\beta$, and $\beta$ is the dynamic scaling exponent. The scaling function $f(t/L^z)$ behaves as $(t/L^z)^{\beta}$ for $x<<1$ and as a constant for $x>>1$,

$$\begin{aligned} \zeta(L,t) &\sim L^{\alpha} \text{ for } t / L^{z} >> 1 \\ \zeta(L,t) &\sim t^{\beta} \text{ for } t / L^{z} << 1 \end{aligned} \tag{4}$$

For $L<L_c$, $\zeta$ is dominated by static scaling, whereas for $L>L_c$, $\zeta$ is dominated by dynamic scaling. Static scaling of self-similar surfaces leads to $\alpha = 1$. The more general case of self-affine surfaces corresponds to $0 < \alpha < 1$.

The static and dynamic scaling exponents ($\alpha$ and $\beta$) provide evidence of which kinetic phenomenon dominates interface evolution during growth. Stochastic roughening describes the evolution of surface topography due to statistical variations in the incident flux with negligible lateral movement (diffusion) of adsorbed species. Stochastic roughening is characterized by $\alpha = 0$, $\beta = 0.5$, and a lateral correlation length, $L_c = 0$. Relaxation (smoothening) processes such as surface diffusion, viscous flow, evaporation-condensation and step flow compete with stochastic roughening and each leaves a fingerprint on the surface topography. Continuum models have been developed that ascribe values to $\alpha$ and $\beta$ for each relaxation process, and these are summarized in Table 1).[13] Surface diffusion as the dominant mechanism yields $\alpha = 1$ and $\beta = 0.25$. A continuum model of evaporation-condensation predicts $\alpha = 0$ and $\beta = 0$ meaning that the surface is completely featureless. Equivalent values are obtained for layer-by-layer

(Frank-van der Merwe) growth. Incorporating surface step motion in the layer-by-layer continuum model yields $\alpha = 0.67$ and $\beta = 0.20$. Atomically smooth semiconductor surfaces produced by MBE exhibit $\alpha \to 0$ and $\beta \to 0$, whereas many other vapor deposited films yield films with $\alpha$ values around 0.7.

In this work, homepitaxial GaN(0001) films grown on MOCVD GaN/6H-SiC substrates using $NH_3$-seeded supersonic beams and Ga from an effusion cell were characterized using AFM, reflection high-energy electron diffraction (RHEED), and scanning electron microscopy (SEM). Roughness scaling analysis using the AFM data was used to elucidate the dominant smoothening (or roughening) processes during growth.

## II. EXPERIMENT

The custom-fabricated SJE apparatus comprises a growth chamber and supersonic jet source with two stages of differential pumping.[12] A mixture of $NH_3$ and research-grade He (Ar, or $H_2$) is expanded through a 150-μm orifice into a source chamber pumped by an 8000 $ls^{-1}$ diffusion pump (Varian VHS-400). A seeded supersonic beam is extracted through a 1-mm conical skimmer into a second stage of differential pumping equipped with a 2000 $ls^{-1}$ diffusion pump (Varian VHS-6). The beam is collimated using a 5 × 5 $mm^2$ aperture before it enters the growth chamber. The growth chamber is equipped with a 350 $ls^{-1}$ turbomolecular pump, effusion cell sources, and a 15-keV electron gun and imaging system for RHEED. The substrate is introduced via a cryo-pumped (APD Cryogenics, APD-4) load-lock. A UHV chamber equipped with a

spherical capacitor analyzer and dual Mg/Al anode x-ray source for x-ray photoelectron spectroscopy (XPS) is also attached to the load-lock.

The substrates were 1 × 1 $cm^2$ pieces cut from 6H-SiC wafers on which a 1-2 μm GaN(0001) epitaxial layer had been grown by MOCVD.[14] Each substrate was cleaned ex-situ with trichloroethylene and inserted in the load-lock. Before GaN growth, the substrate was exposed to a supersonic beam containing either 10% $NH_3$ in He, 5% in $H_2$, 20% $NH_3$ in Ar, or 100% $NH_3$ for 30 min at 800°C depending on the desired beam conditions for growth.[15] GaN growth was performed at 750°C using an $NH_3$-seeded supersonic beam and Ga from a hot-lip effusion cell (SVT Associates).

RHEED patterns of the homoepitaxial films were acquired in situ after cooling under an $NH_3$ flux. Scanning electron microscopy (SEM) and atomic force microscopy (AFM) were performed ex-situ. AFM was performed using a Digital Instruments Dimension™ 3000 scanning probe microscope in tapping mode. Static scaling analysis was performed by determining the RMS roughness for different size regions, ranging from 4 × 4 pixel regions to 512 × 512 pixel regions (1 × 1 $\mu m^2$ image size). SEM images were acquired using a JEOL 6400FE SEM with a 5-kV cold field emission electron gun. SEM cross sections allowed us to measure film thickness since MOCVD-grown GaN and $NH_3$-seeded SJE GaN varied in image constrast.

## III. RESULTS AND DISCUSSION

Fig. 1 displays the experimental relationship between GaN growth rate and %$NH_3$ seeded in He when using a constant Ga flux of $2.94\times10^{14}$ $cm^{-2}s^{-1}$. Growth rate increases linearly up to about 5% $NH_3$ seeded in He. This kinetics regime is described as Ga-rich

(N-limited) growth, where the growth rate is directly proportional to the $NH_3$ flux. When the growth rate has saturated (>5% $NH_3$ seeded in He), the growth rate is limited by Ga flux, yielding a N-rich surface.

AFM images show that Ga-limited (N-rich) growth conditions correlate with highly faceted surfaces, whereas $NH_3$-limited (Ga-rich) conditions promote non-faceted basal plane growth, as previous investigators have observed.[4,5,6,7] The transition from non-faceted to faceted surface morphology is evident in films grown for 2 h using $2.94\times10^{14}$ $cm^{-2}s^{-1}$ Ga and $NH_3$ seeded in He as the $NH_3$ flux and hence the growth rate increase. Fig. 2a shows a $1 \times 1$ $\mu m^2$ AFM image of a GaN film grown using a beam of 1% $NH_3$ in He. A smooth, non-faceted surface morphology with a RMS roughness of 3.0 nm is observed. We infer that the spherical features in this image are Ga droplets. A film grown using a beam of 3% $NH_3$ in He displays a faceted surface with a RMS roughness of 19.7 nm (Fig. 2c). An AFM image of a film grown for 15 min using a beam of 3% $NH_3$ in He (Fig. 2d) indicates that faceting begins in the initial stages of growth. This film also exhibits a spotty transmission RHEED pattern in the $[2\bar{1}\bar{1}0]$ direction, as shown in Fig. 3a. The aspect ratios of the features remain the same among the 15 min and 2 h film growths (Fig. 2d and 2c, respectively), suggesting a self-similar behavior. Fig. 1 indicates that GaN growth using a 3% $NH_3$ in He beam is in the $NH_3$-limited kinetics regime. The transition from non-faceted to faceted growth occurs at a lower $NH_3$ flux than the saturation $NH_3$ flux (~5% $NH_3$ in He). The surface of a film grown using a beam of 2% $NH_3$ in He comprises faceted and non-faceted areas, as illustrated in Fig. 2b. The growth conditions for this film demarcate the transition point between non-faceted

and faceted basal plane growth. The growth rate (124 nm/h) is about one half of the maximum (Ga-limited) growth rate.

SEM images of two smooth (non-faceted) films grown using a seeded supersonic beam of 20% $NH_3$ in Ar for growth times of 2 and 6 h, respectively, are shown in Fig. 4. Anti-seeding of $NH_3$ in Ar yields a lower kinetic energy (~0.05 eV) and a lower flux due to the absence of aerodynamic focusing. The GaN growth rate under these conditions was 58 nm/h, which is in the $NH_3$-limited regime below the roughness transition. Feature size and aspect ratio do not change significantly with growth time (film thickness) and faceting is never observed. Although we do not have AFM images of these films, the SEM images closely resemble those of non-faceted films grown using higher energy $NH_3$ beams. We do not have data monitoring the evolution of the surface morphology with respect to time, our AFM and SEM images of our non-faceted films are consistent with growth via quasi-two-dimensional island coalescence.[6] AFM and SEM images of our faceted films represent island growth with faceted surfaces.

AFM images of GaN films grown using seeded supersonic beams of $NH_3$ seeded in $H_2$ are shown in Fig. 5. Seeding $NH_3$ in $H_2$ produces higher $NH_3$ kinetic energies and higher fluxes due to focusing. A film grown at 57 nm/h using a beam of 1% $NH_3$ in $H_2$ (1.8 eV) exhibits a smooth surface as shown in Fig. 5a with a RMS roughness of 1.6 nm. The streaky, one-fold RHEED pattern in the $[2\bar{1}\bar{1}0]$ direction (Fig. 3b) also indicates a smooth, non-faceted GaN(0001) surface. A film grown at 152 nm/h using a beam of 2% $NH_3$ in $H_2$ (0.74 eV) displays a faceted surface (Fig. 5c) with a RMS roughness of 22.8 nm. A film with a RMS roughness of 6.7 nm grown at 122 nm/h for 2 h using a beam of 1% $NH_3$ in $H_2$ (1.5 eV) displays a transitional surface morphology showing features

characteristic of non-faceted and faceted films as illustrated in Fig. 5b. Growth using the same beam conditions for 6 h yields a rough film with an RMS roughness of 23.6 nm (Fig. 5d) displaying facets similar to the film grown using 2% $NH_3$ in $H_2$ (0.74 eV) (Fig. 5c).

Fig. 6 shows the RMS roughness ($1 \times 1\ \mu m^2$ image size) as a function of GaN growth rate for SJE grown homoepitaxial films using a Ga flux of $2.94 \times 10^{14}$ $cm^{-2}s^{-1}$. There is an abrupt roughness transition at a growth rate ~120 nm/h, corresponding to about one half of the maximum (Ga-limited) growth rate. The transition from non-faceted to faceted growth for a given Ga flux occurs at the same growth rate regardless of the $NH_3$ beam energy. Growth rates lower than 120 nm/h yield smooth basal plane growth, whereas growth rates greater than 120 nm/h yield rough, faceted surfaces. Several investigators have ascribed the transition from non-faceted to faceted growth to differences in surface termination, with a Ga-terminated surface yielding non-faceted growth and a N-terminated surface yielding faceted growth. The steady-state Ga surface coverage can be estimated using a Ga balance:

$$\frac{d\theta_{Ga}}{dt} = F_{Ga} - k_{Ga}\theta_{Ga} - r_g(\theta_{Ga}, \theta_N, T) \tag{5}$$

where $F_{Ga}$ is the incident Ga flux and $r_g$ ($cm^{-2}s^{-1}$) is the GaN growth rate. Karpov, et al. provide the following expression for the first order rate constant for Ga desorption,

$$k_{Ga} = 2.45 \times 10^{13} e^{\left(\frac{-31450}{T}\right)} \tag{6}$$

where $T$ is the substrate temperature.[16] Assuming steady state growth $\left(\frac{d\theta_{Ga}}{dt} = 0\right)$, $\theta_{Ga}$ can be determined. The results shown in Fig. 6 indicate that the transition from non-

faceted to faceted basal plane growth occurs at $\theta_{Ga}$ ~1/8. This critical surface coverage demarcates the roughness transition for GaN growth by SJE using $NH_3$ seeded in $H_2$ and He and is also consistent for films grown using $NH_3$ in Ar and 100% $NH_3$. Pavloska, *et al.* (also using $NH_3$ seeded in a He supersonic beam) reported a similar transition from non-faceted to faceted growth at a critical III/V flux ratio of 2. Since their III/V flux ratio was defined as the ratio of Ga flux to reactive $NH_3$ flux, this III/V flux ratio also corresponds to ~1/2 $r_{g,max}$. We infer that the roughness transition is general for GaN(0001) as it occurs at a Ga incorporation efficiency of ~50% regardless of substrate temperature and incident Ga flux (~670°C and 750°C, for Pavloska et al. and our results, respectively).[7]

Fig. 7 illustrates the relationship between surface roughness ($\zeta$) and lateral length scale ($L$) for non-faceted and faceted homoepitaxial GaN films grown using supersonic beams of 1% $NH_3$ in He and 100% $NH_3$, respectively. The data in Fig. 7 were generated by applying Eq. (2) over different length scales (square regions) using 1×1 $\mu m^2$ AFM images. The corresponding $L_c$ values are given in Fig. 7. At length scales smaller than $L_c$, the roughness scales as $\zeta \sim L^{\alpha}$ where $\alpha$ is the static scaling coefficient, resulting in $\alpha$ = 0.90 for the non-faceted film and $\alpha$ = 1.08 for the faceted film. At length scales larger than $L_c$, $\zeta_{sat}$ = 1.58 nm for 1% $NH_3$ in He and $\zeta_{sat}$ = 22.7 nm for pure $NH_3$.

Fig. 8 illustrates the static scaling analysis for GaN films grown by SJE using $NH_3$ seeded in $H_2$ and He and a pure $NH_3$ beam. Table 2 summarizes the growth conditions, scaling parameters $L_c$ and $\alpha$, saturation roughness $\zeta_{sat}$ and growth rate $r_g$ for each film. Non-faceted films give $\alpha$ values of 0.86-0.90, whereas faceted films give $\alpha$ values of 1.06-1.13. At length scales much less than $L_c$, the data tend toward common

lines for non-faceted and faceted films. The in-situ cleaning process roughens the surface [from $\zeta_{sat}$=0.17 nm to $\zeta_{sat}$ =0.71 nm (1 x 1 μm$^2$ image size)] and this places on $\zeta_{sat}$ a lower limit of ~0.7 nm for non-faceted films. Moreover, the smooth films and the $NH_3$ beam cleaned surface have about the same roughness ($\zeta$~0.3 nm at $L$~10 nm) at small length scales ($L$<<$L_c$). The saturation roughness increases as the $L_c$ increases for the non-faceted and faceted films. The rough, faceted films all have about the same roughness ($\zeta$~1 nm at $L$~10 nm) at small length scales. The rough and smooth films grown with $NH_3$ in He have the same roughness characteristics as those grown with $NH_3$ in $H_2$. In order to discern the difference between non-faceted and faceted films, we made the static scaling analysis dimensionless by dividing length scale by $L_c$ and roughness by $\zeta_{sat}$ (Fig. 9). It is evident that there are two universality classes governing non-faceted and faceted films. The non-faceted films (Fig. 9a) all have an $\alpha \sim 0.9$, whereas the faceted films (Fig. 9b) have an $\alpha \sim 1.1$. The transitional film grown with 1% $NH_3$ in $H_2$ (1.48 eV) fits well with the dimensionless roughness analysis of the smooth films in Fig. 9a.

We performed a somewhat limited dynamic scaling analysis on GaN films grown by SJE using $NH_3$. As indicated by the data in Table 2 [using Eq. (2)], we have a $\beta \sim$ 0.25 for faceted films, using the 3% $NH_3$ in He (0.38 eV) beam for 0.25 h and 2 h. The SEM images (Fig. 4) of two non-faceted films make it appear that the saturation roughness of the films only change a small amount over the given time period, indicating that $\beta$ is low for these two $NH_3$ in Ar grown films. We did not determine a $\beta$ for the transitional film [1% $NH_3$ in $H_2$ (1.48 eV)] because the surface of the film changed dramatically between the 2 h and 6 h time periods. It has a similar roughness to the rough films at small length scales even though its saturation roughness ($\zeta_{sa} \sim$ 6.7 nm) is

lower than any of the rough films and it shares an $\alpha$ of the smooth films ($\alpha$=0.86). It might be that extended time is responsible for the roughening of the surface, however we believe that small variances or changes in the flux could be responsible for this change. Understanding the relationship between roughness and growth rate (Fig. 6) and that the growth rate of this transitional film is on a steep slope (growth rate = 116 nm/h), it is not surprising that the film may drastically change morphology.

Knowing that $\beta$~0.25 and $\alpha$=1.06-1.13 for faceted films grown and qualitatively that $\beta$ is low and $\alpha$~0.9 for non-faceted films (Fig. 4) indicates that our growth surface transport phenomena approximates the continuum model for surface diffusion (Table 1) for faceted and non-faceted films. Continuum models describing surface diffusion growth from an initially flat surface indicate $\alpha$=1. Our growth process does not begin from an initial flat surface as the cleaning process does leave some finite roughness. One would expect this to have an effect on both $\alpha$ and $\beta$. The static scaling coefficient can be thought as a general description of the ratio of vertical transport versus lateral transport. Non-faceted films have an $\alpha$~0.9 and growth rates less than 120 nm/h. Faceted films have an $\alpha$~1.1 and growth rates between 120 and 240 nm/h. We would expect faceted surfaces to have more vertical growth than non-faceted surfaces, explaining the increase in $\alpha$ for faceted surfaces. The non-faceted surfaces having an $\alpha$~0.9 suggests this growth process would be similar to a combination of surface diffusion and step flow growth as the surface growth mechanism (step flow growth $\alpha$~0.67, Table 1). There is no continuum model yielding scaling coefficients for two-dimensional island coalescence, but one would expect a model to be qualitatively a combination of the surface diffusion and step-flow growth models. Therefore, the $NH_3$ SJE GaN growth

process is dominated by a surface diffusion process, not stochastic roughening, as suggested by previous investigators for PAMBE GaN growth.[5,6]

Plotting $L_c^{\alpha}$ versus $\zeta_{sat}$ (Fig. 10) demonstrates a linear relationship between these variables including both non-faceted and facted films. This implies that surface diffusion of the same species controls morphology of both Ga-rich and N-rich surfaces. There is no significant deviation in the $L_c^{\alpha}$-$\zeta_{sat}$ relationship for faceted films (N-rich) among films grown using a beam of $NH_3$ seeded in either He or $H_2$. However, non-faceted (Ga-rich) films grown using a beam of $NH_3$ seeded in $H_2$ yield a smaller $L_c^{\alpha}$ for a given $\zeta_{sat}$ than non-faceted films grown using a beam of $NH_3$ seeded in He. A beam of high-energy $NH_3$ reduces feature size on Ga-rich surfaces. Ga diffusion on Ga-terminated surfaces is the surface diffusion process with the lowest activation barrier according to density functional theory (DFT) calculations.[17] Our surface is GaN(0001) unlike Held's GaN($000\bar{1}$), so one must consider the possibility that both surfaces (non-faceted and faceted) are Ga-terminated. Our and Pavloska et al.[7] GaN(0001) films undergo a roughness transition at a Ga incorporation efficiency of ~50% regardless of substrate temperature and incident Ga flux whereas Held, *et al.* reported that the transition from non-faceted to faceted for $NH_3$-MBE grown GaN($000\bar{1}$) films occurred at a Ga incorporation efficiency of ~100%.[4] DFT calculations indicate an activation barrier of 0.2 eV for Ga surface diffusion on Ga-terminated GaN($000\bar{1}$) and 0.4 eV for Ga surface diffusion on Ga-terminated GaN(0001).[17] It is possible that from 120 to 240 nm/h growth rates for SJE with $NH_3$ seeded beams, the surface is Ga-terminated GaN($000\bar{1}$) and that the surface from 0 to 120 nm/h growth rates for our conditions is Ga-terminated GaN(0001). A decrease in the activation barrier for Ga diffusion on Ga-terminated

surfaces for GaN($000\bar{1}$) surfaces would support our increase in $L_c$ for faceted surfaces (Table 2 and Fig. 10). Films grown in low III/V ratios and high III/V ratios both exhibited surface diffusion as the primary surface mechanism as opposed to stochastic roughening. If stochastic roughening were the growth mechanism for SJE with $NH_3$ seeded beams grown GaN films, the scaling analysis would have yielded $\alpha \rightarrow 0$ and $\beta \rightarrow 0.5$. The fundamental transition to faceted GaN films grown by SJE with $NH_3$ seeded beams does not arise from stochastic roughening as surface diffusion is always the dominate growth process. Instead, the fundamental transition from non-faceted to faceted for SJE-$NH_3$ grown GaN(0001) films arises as the Ga incorporation efficiency >50%.

**ACKNOWLEDGMENTS**

This work was supported by the Office of Naval Research (N00014-01-1-0003). The authors would like to thank Kevin Bray for introducing us to topological scaling analysis of surface roughness and for his help with some of the AFM measurements.

## REFERENCES


[1]D. L. Smith, *Thin-Film Deposition* (McGraw-Hill, New York, 1995), p. 119.

[2]A.-L. Barabasi and H. E. Stanley, *Fractal Concepts in Surface Growth* (Cambridge University Press). (need year and location)

[3]S. W. King, E. P. Carlson, R. J. Therrien, J. A. Christman, R. J. Nemanich and R. F. Davis, J. Appl. Phys. **86**, 5584 (1999).

[4]R. Held, D. E. Crawford, A. M. Johnston, A. M. Dabiran and P. I. Cohen, Surf. Rev. Lett. **5**, 913 (1998).

[5]T. H. Myers, L. S. Hirsch, L. T. Romano and M. R. Richards-Babb, J. Vac. Sci. Technol. B **16**, 2261 (1998).

[6]E. J. Tarsa, B. Heying, X. H. Wu, P. Fini, S. P. DenBaars and J. S. Speck, J. Appl. Phys. **82**, 5472 (1997).

[7]A. Pavlovska, V. M. Torres, E. Bauer, R. B. Doak, I. S. T. Tsong, D. B. Thomson and R. F. Davis, Appl. Phys. Lett. **75**, 989 (1999).

[8]Z. Liliental-Weber, Y. Chen, S. Ruvimov and J. Washburn, Phys. Rev. Lett. **79**, 2835 (1997).

[9]B. Daudin, J. L. Rouviere and M. Arlery, Appl. Phys. Lett. **69**, 2480 (1996).

[10]David R. Miller, in *Atomic and Molecular Beam Methods*, edited by Giacinto Scoles (Oxford, New York, 1988), Vol. 1., pp. 14-53.

[11]P. K. Sharma, E. L. Knuth and W. S. Young, J. Chem. Phys. **64**, 4345 (1976).

[12]A. J. McGinnis, D. Thomson, R. F. Davis, E. Chen, A. Michel and H. H. Lamb, Surf. Sci. **494**, 28 (2001).

[13]W. M. Tong and R. S. Williams, Annu. Rev. Phys. Chem. **45**, 401 (1994).

[14]T. W. Weeks, Jr., M. D. Bremser, K. S. Ailey, E. Carlson, W. G. Perry, and R. F. Davis, Appl. Phys. Lett. 67, 401 (1995).

[15]A. J. McGinnis, D. Thomson, R. F. Davis, E. Chen, A. Michel and H. H. Lamb, J. Crys. Grow. **222**, 452 (2001).

[16]S. Yu. Karpov, R. A. Talalaev, Yu. N. Makarov, N. Grandjaen, J. Massies and B. Damilano, Surf. Sci. **450**, 191 (2000).

[17]T. Zyweitz, J. Neugebauer and M. Scheffler, App. Phys. Lett. **73**, 487 (1998).

**Table 1.** Theoretically predicted values of static scaling exponent α and dynamic scaling exponent β[9]

| Continuum Models | | |
|---|---|---|
| | α | β |
| Stochastic roughening | 0 | $\frac{1}{2}$ |
| Evaporation-condensation (layer by layer growth) | 0 | 0 |
| Surface diffusion | 1 | $\frac{1}{4}$ |
| Surface diffusion plus steps | $\frac{2}{3}$ | $\frac{1}{5}$ |

**Table 2**: Conditions and roughness parameters for GaN(0001) growth.

| $NH_3$ | $L_c$ | $\alpha$ | $\zeta_{sat}$ | growth rate | $NH_3$ flux |
|---|---|---|---|---|---|
| | (nm) | | (nm) | (nm/h) | ($cm^{-2}s^{-1}$) |
| 1% in $H_2$ (300°C) 6 hrs. | 134 | 1.12 | 23.6 | 114 | 1.13E+15 |
| 2%in $H_2$ (RT) | 126 | 1.13 | 22.8 | 152 | 1.99E+15 |
| 100% (200°C) | 162 | 1.08 | 22.7 | 144 | 1.10E+15 |
| 3% in He (200°C) | 133 | 1.09 | 19.7 | 172 | 1.50E+15 |
| 2% in He (200°C) | 140 | 1.11 | 18.2 | 132 | 9.92E+14 |
| 3% in He (200°C) 15 min | 80 | 1.13 | 13.3 | 160 | 1.50E+15 |
| 2% in He (RT) | 108 | 1.06 | 12.3 | 124 | 9.92E+14 |
| 1% in $H_2$ (300°C) | 98 | 0.86 | 6.7 | 122 | 1.13E+15 |
| 1% in He (180°C) | 115 | 0.90 | 3.03 | 29 | 5.01E+14 |
| 1% in $H_2$ (400°C) | 57 | 0.87 | 1.58 | 62 | 1.13E+15 |
| 10% in He, Cleaning @800°C | 28 | 0.89 | 0.71 | - | 3.78E+15 |

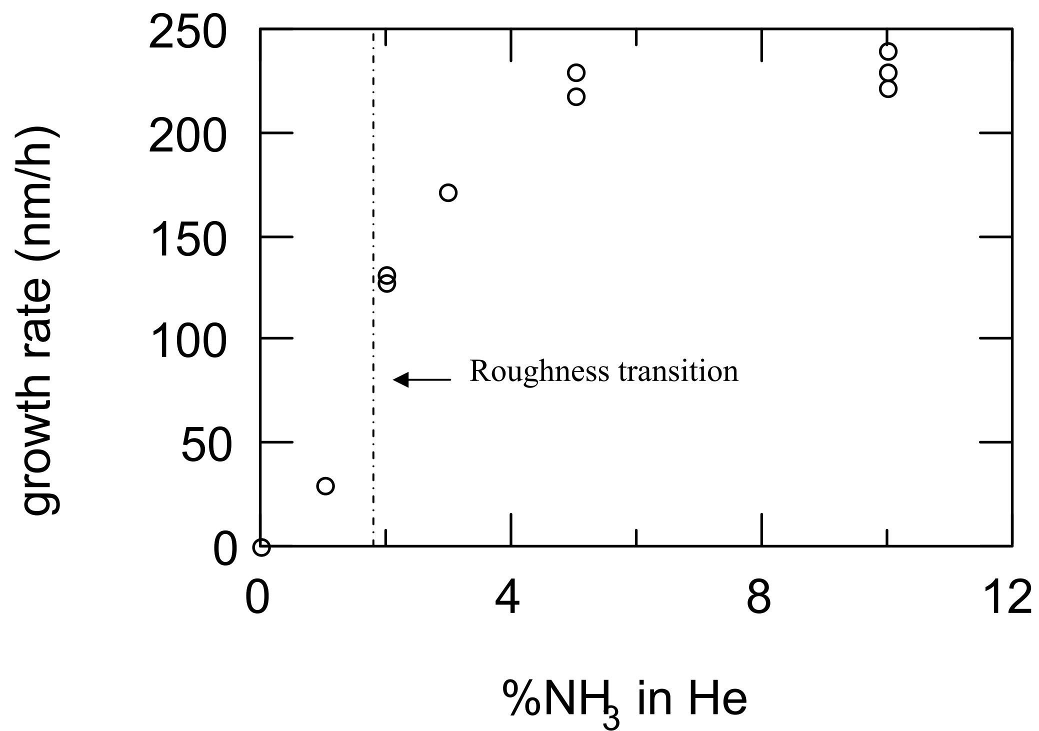


**Figure 1**: Growth rate of GaN with $NH_3$ (0.2 eV to 0.4 eV) in He, vs. %$NH_3$ in He.

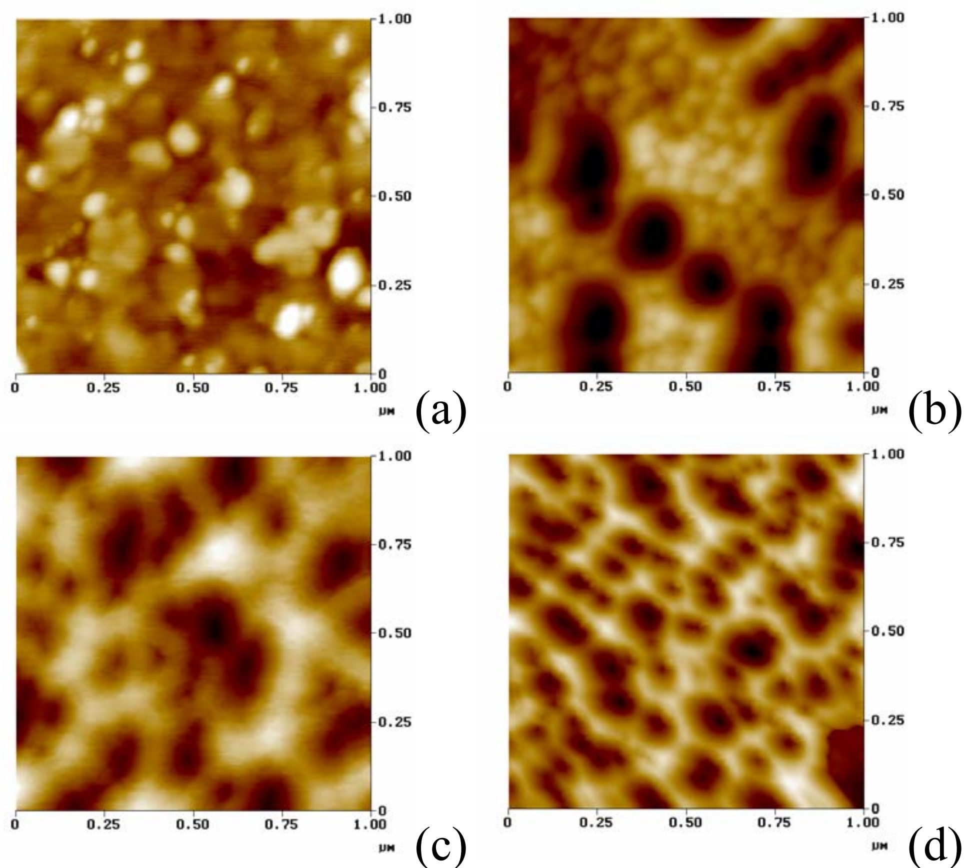


**Figure 2:** (a) 1% $NH_3$ in He (180°C), RMS roughness of 3.0 nm, grayscale 25 nm; (b) 2% $NH_3$ in He (200°C), RMS roughness of 18.2 nm, grayscale 100 nm; (c) 3% $NH_3$ in He (200°C), RMS roughness of 19.7 nm, grayscale 120 nm; (d) 3% $NH_3$ in He (200°C), RMS roughness of 13.3 nm (grown for 15 min), grayscale 85 nm.

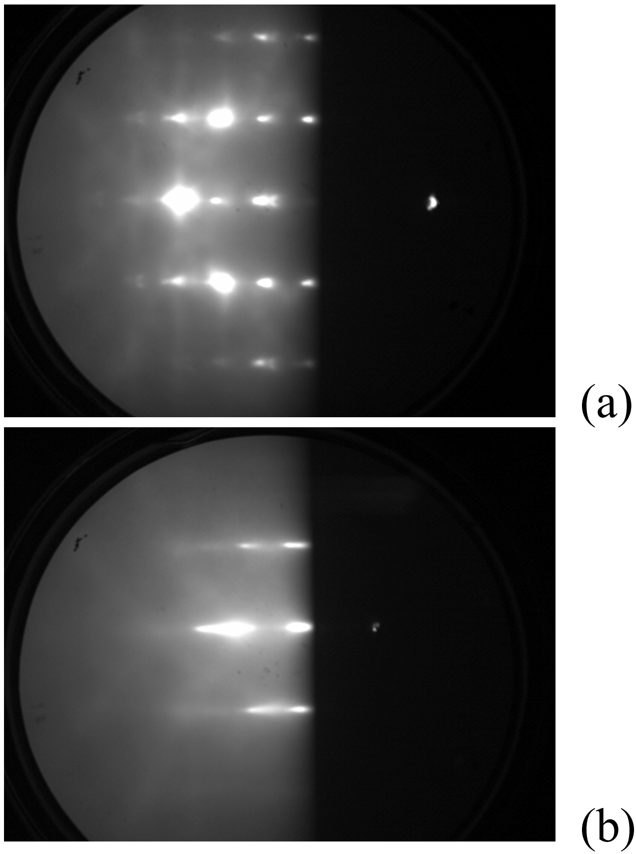


**Figure 3**: RHEED patterns of GaN(0001). (a) RHEED pattern of GaN(0001) grown homoepitaxially with 3% $NH_3$ in He (200°C) for 15 minutes. (b) RHEED pattern of GaN(0001) grown homoepitaxially with 1% $NH_3$ in $H_2$ (400°C) for 2 hours.

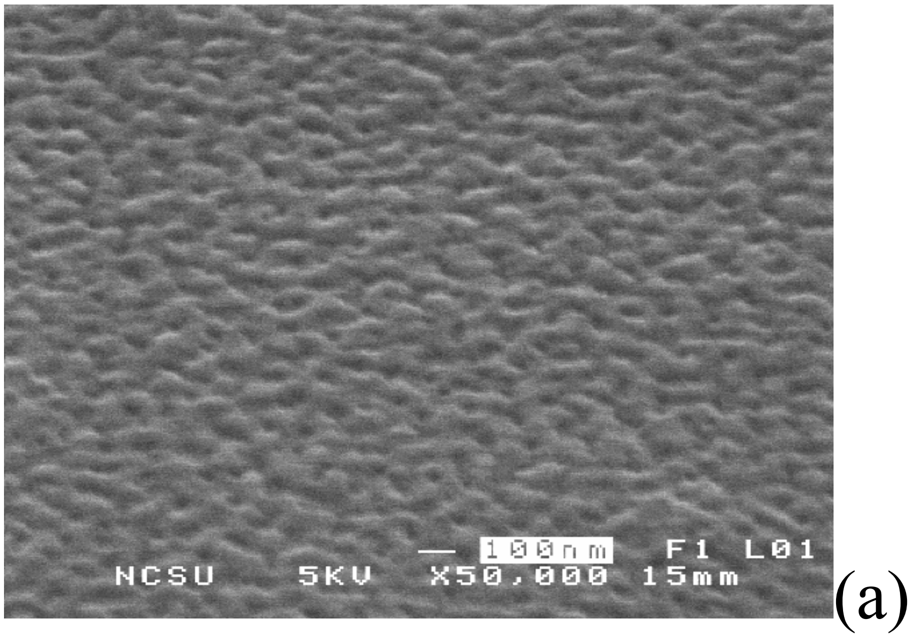


(a)

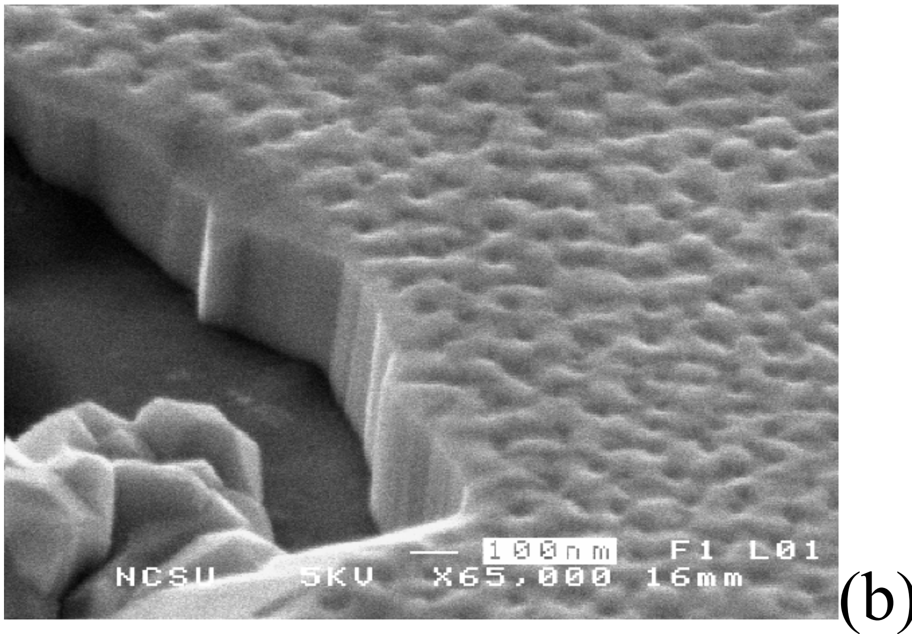


(b)

**Figure 4**: GaN grown with 20% $NH_3$ seeded in Ar ($NH_3$ kinetic energy of 0.05 eV at $3.38\times10^{14}$ $cm^{-2}s^{-1}$) grown for (a) 2 hours and (b) 6 hours. The total film thicknesses are (a) 126 nm and (b) 336 nm.

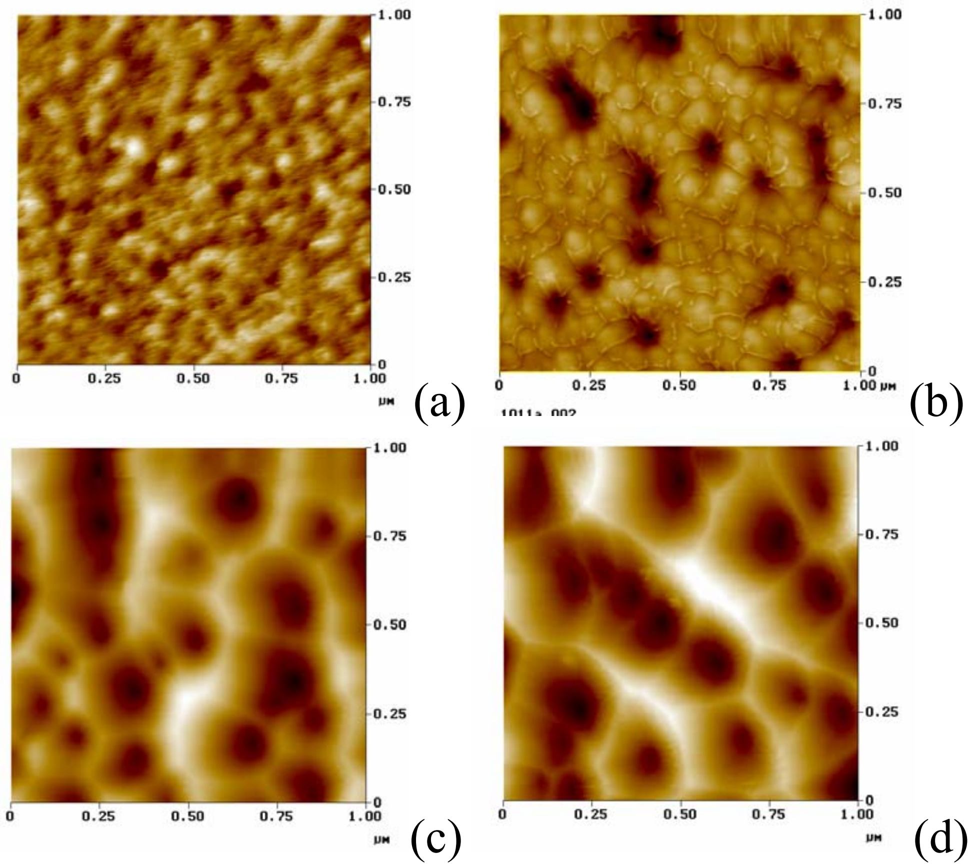


**Figure 5:** (a) 1% $NH_3$ in $H_2$ (400°C), RMS roughness of 1.6 nm, grayscale 15 nm; (b) 1% $NH_3$ in $H_2$ (300°C), RMS roughness of 6.7 nm, grayscale 60 nm; (c) 2% $NH_3$ in $H_2$(RT), RMS roughness of 22.8 nm, 2 hr. growth, grayscale 150nm; (d) 1% $NH_3$ in $H_2$ (300°C), RMS roughness of 23.6 nm (grown for 6 hrs), grayscale 135 nm.

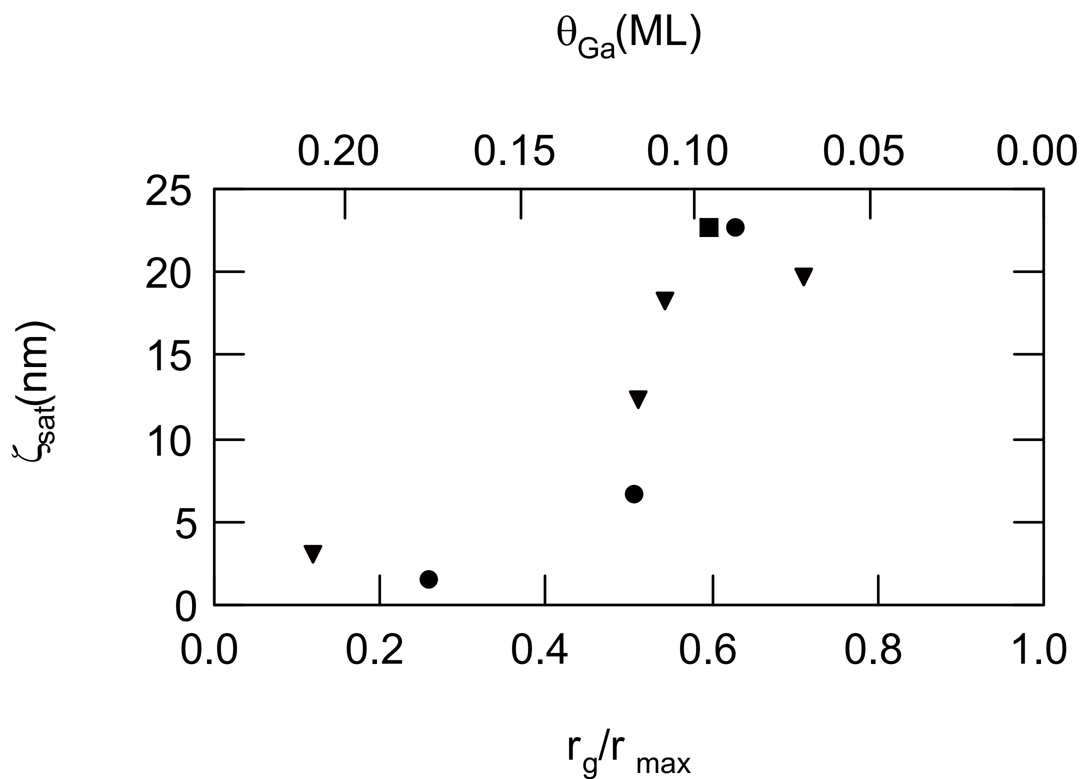


**Figure 6**: Roughness vs. Surface coverage of Ga and growth rate. ■ Pure $NH_3$; ▼ $NH_3$ in He; ● $NH_3$ in $H_2$.

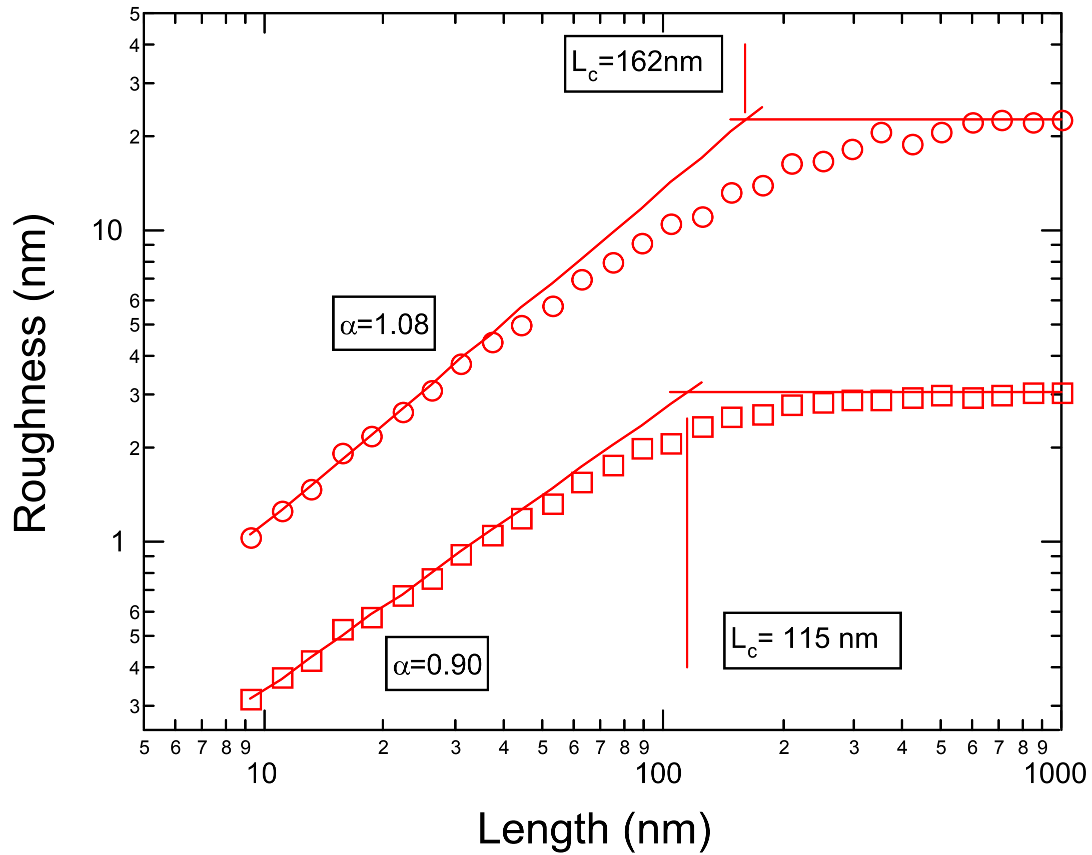


**Figure 7**: A log-log plot of Roughness versus length scale. The slope of the roughness versus length in the log scale yields the static scaling coefficient $\alpha$. Intersection of this line and the saturation roughness yields the critical length, $L_c$. The film having $L_c$=162 nm and $\alpha$=1.08 is grown with 100% $NH_3$. The film having $L_c$=115 nm and $\alpha$=0.90 is grown with 1% $NH_3$ in He.

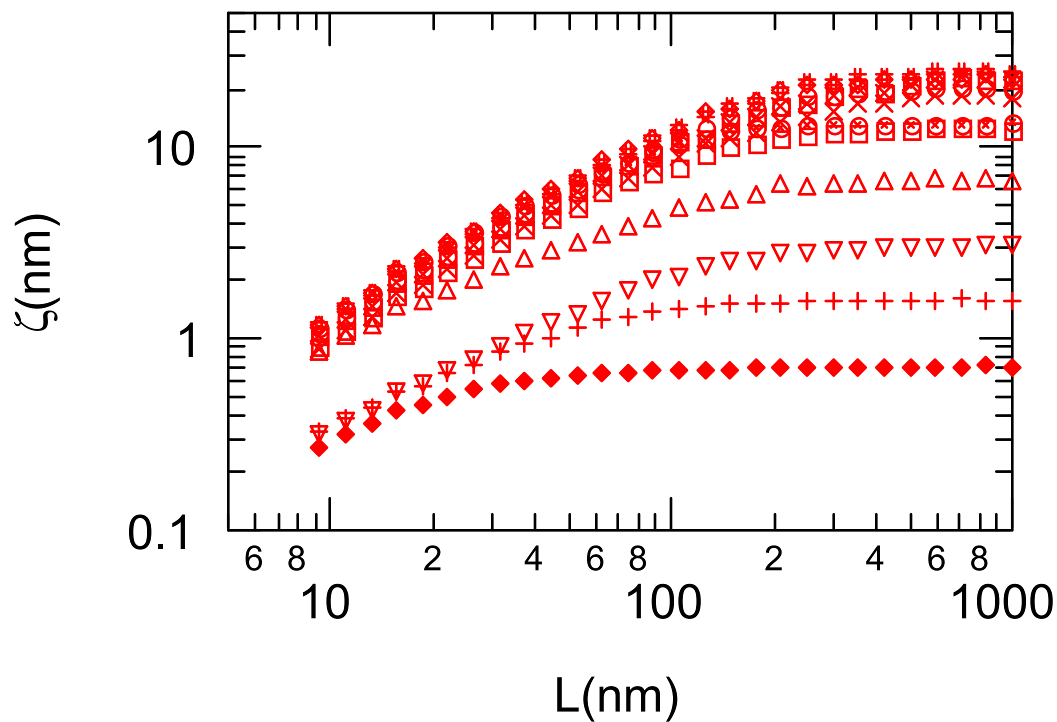


**Figure 8**: ◆10% $NH_3$ in He, cleaning at 800°C; + 1% $NH_3$ in $H_2$ (400°C); ▽ 1% $NH_3$ in He (180°C); △ 1% $NH_3$ in $H_2$ (300°C); □ 2% $NH_3$ in He (RT); ⊗ 3% $NH_3$ in He (200°C); ○ 3% in He (200°C); × 2% $NH_3$ in He (200°C); 100% $NH_3$; # 1%$NH_3$ in $H_2$ (300°C); 2% $NH_3$ in $H_2$ (RT).

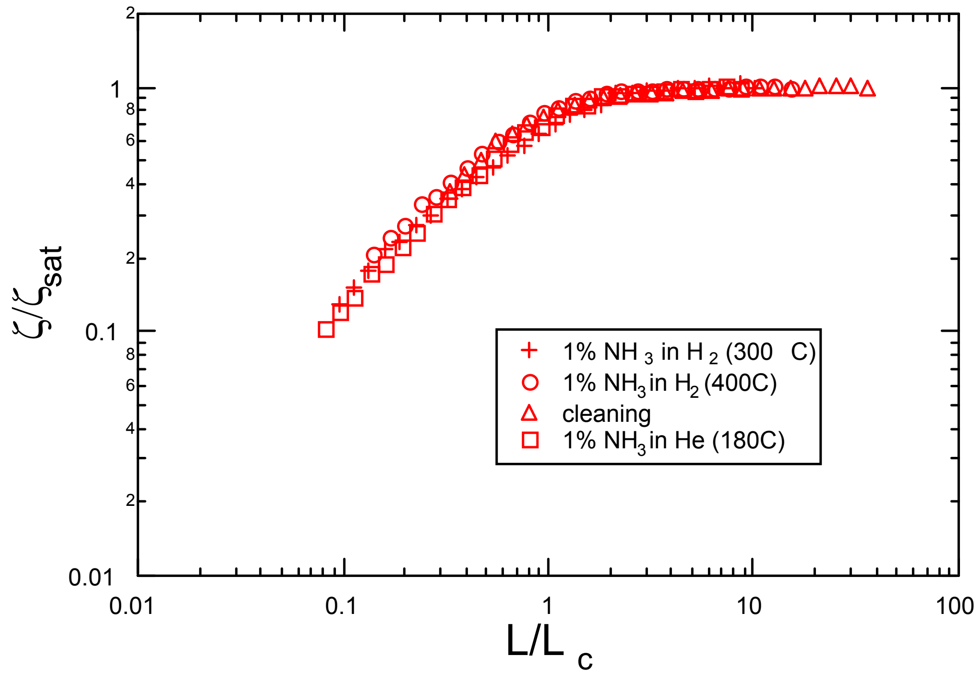

(a)

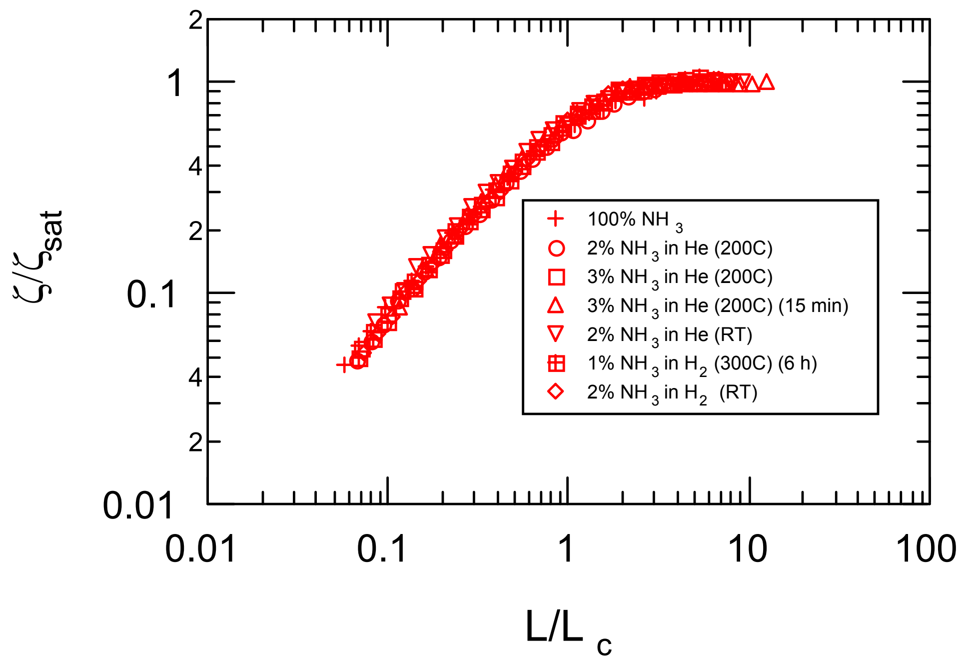

(b)

**Figure 9:** (a) Scaling Analysis of non-faceted GaN(0001) (b) Scaling Analysis of faceted GaN(0001).

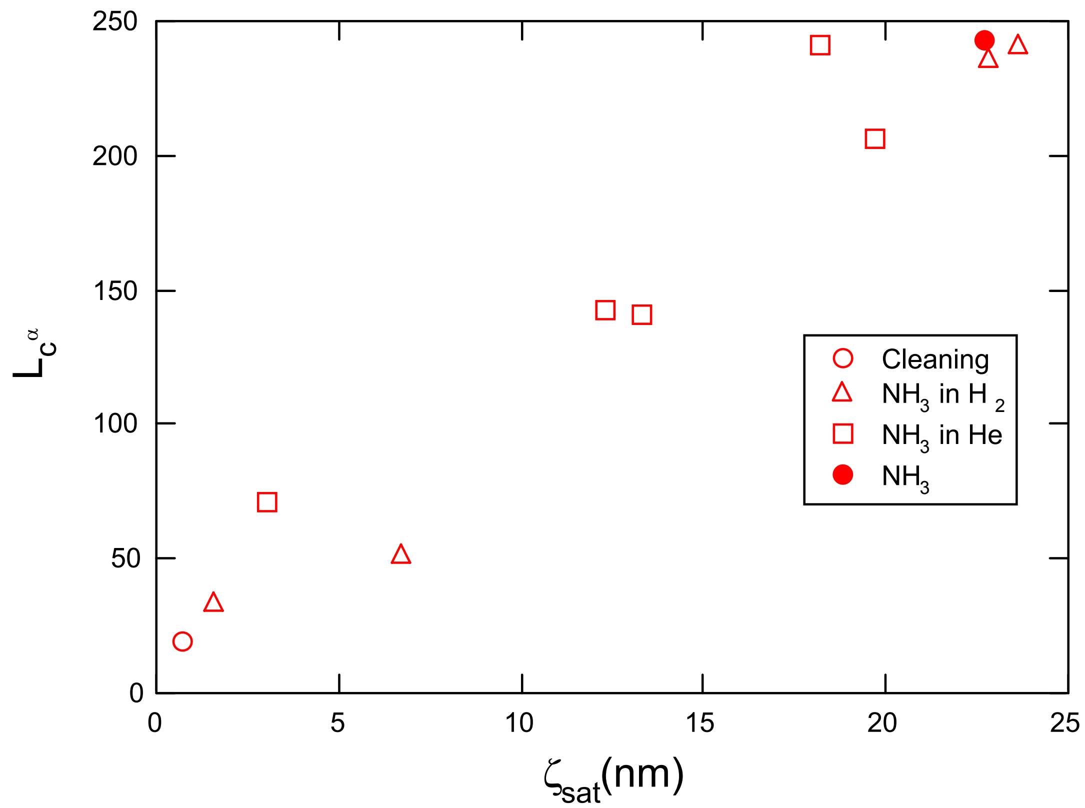


**Figure 10:** Critical length to the scaling exponent vs. saturation roughness value.

4. GaN growth using seeded supersonic jets: Effects of aerodynamic focusing on triethylgallium flux and surface morphology. Nicholas A. Smith, Arthur J. McGinnis, Robert F. Davis and H. Henry Lamb. Manuscript to be submitted to Journal of Crystal Growth.

GaN growth using seeded supersonic jets: Effects of aerodynamic focusing on triethylgallium flux and surface morphology

Nicholas A. Smith[a], Arthur J. McGinnis[b], Robert F. Davis[b] and H. Henry Lamb[a,*]

[a]Department of Chemical Engineering, North Carolina State University, Raleigh, North Carolina 27695-7905, USA

[b]Department of Materials Science and Engineering, North Carolina State University, Raleigh, North Carolina 27695-7906, USA

[*]Corresponding author: Tel.: +1-919-515-6395; fax: +1-919-515-3465. E-mail address: lamb@eos.ncsu.edu.

## ABSTRACT

Triethylgallium (TEG)-seeded supersonic molecular beams (0.5 eV - 2.1 eV) in $N_2$ and He employed in homoepitaxial growth of GaN(0001) thin films on metal-organic chemical vapor deposition (MOCVD)-grown GaN(0001)/6H-SiC substrates were chosen to provide a high intensity and high energy Ga source that would fulfill the requirement of high III/V flux ratios (morphological benefits) and perhaps provide additional or alternate surface reaction pathways, respectively. Substrate temperature were 750°C employing $NH_3$ through a leak valve at pressures from 0.77 to $1.53 \times 10^{-5}$ Torr for growth times ranging from 2 h to 4 h. A correlation of enrichment factors helped determine the relative flux of TEG in seeded supersonic molecular beams due to aerodynamic focusing. Reflection high-energy electron diffraction (RHEED) patterns demonstrated quasi two-dimensional growth for $NH_3$-limited growth conditions achieved with relatively higher fluxes of TEG seeded in He and three-dimensional growth for Ga-limited growth conditions achieved with relatively lower fluxes of TEG seeded in $N_2$. The morphology was probed using atomic force microscopy (AFM). AFM yielded non-faceted surfaces [root mean square (RMS) roughness ~ 1-3 nm] for $NH_3$-limited growth conditions and faceted surfaces (RMS roughness ~ 19-30 nm) for Ga-limited growth conditions. Scaling analysis of film surfaces determined that the primary surface transport mechanism is surface diffusion for all growth conditions employed.

## I. INTRODUCTION

GaN(0001) thin films for optoelectronics applications are grown primarily by metal-organic chemical vapor deposition (MOCVD).[1-7] Molecular beam epitaxy (MBE) is a technique that has potential advantages for GaN growth by lower substrate temperature, precise control of layer thickness as well as *in situ* doping. Chemical beam epitaxy (CBE) involves a group III metal-organic compound and a group V hydride to grow III-V semiconductor films (ex. GaN, GaAs, InP) in a high-vacuum environment.[8] Typically, the growth precursors are delivered to the substrate via an effusive molecular beam in which kinetic energy is controlled by the temperature of the source. There have been a few studies of III-nitride growth.[9-12] Substrate temperature is found to affect GaN film quality [measured by x-ray diffraction (XRD)] and the CBE optimum temperature is 800°C. The best GaN crystal quality has been obtained by using 6H-SiC as a substrate in CBE.

Supersonic molecular beams have been used as high-intensity sources of precursor molecules with hyperthermal kinetic energies for thin film growth.[13] A seeded supersonic molecular beam yields species with hyperthermal translational energies. In an ideal beam (zero velocity slip), the terminal velocity (and consequently energy, $E = \frac{1}{2} m V_\infty^2$) is given by

$$V_\infty = \sqrt{\frac{2R}{\langle m \rangle} \langle C_p \rangle T_o} \qquad (1)$$

where $m$ is the average molecular weight, $\langle C_p \rangle$ is the average heat capacity, and $T_o$ is the stagnation temperature. The ideal energy, $E_i$, would be

$$E_i = \frac{m_i}{\langle m \rangle}\langle C_p \rangle T_o \qquad (2)$$

Prediction of the energy of seeded beams can be closely estimated [eq. (2)] if $P_{o,}d$ is on the order of 3 Torr-cm or greater, where $P_o$ is the stagnation pressure of the nozzle and $d$ is the orifice diameter.

A potential advantage for thin film growth with seeded SJE arises from the production of a hyperthermal reactant beam. This hyperthermal reactant would improve the sticking coefficient for dissociative chemisorption if the process is direct and activated (requiring no absorbed precursor). Thin film growth taking advantage of direct chemisorption has been demonstrated for group IV compounds on metal, such as $CH_4$ on Ni(111).[14] By employing hyperthermal kinetic energy to $Si_2H_6$, its dissociative chemisorption probability has increased on Si(100).[15] Consequently, higher Si epitaxial growth rates result under low hydrogen coverage conditions.[16,17] SJE has been used to grow epitaxial SiC in order to lower the substrate temperature.[18] Group III-N have also been grown with SJE in order to lower the growth temperature.[19,20] Growth rates of AlN by Brown et al.[19] were reported to increase greatly when TEA was seeded in either He or $H_2$. They concluded hyperthermal kinetic energy of AlN allowed an activation barrier for dissociative chemisorption to be surmounted. However, previous studies of group III metal-organic compounds on semiconductor surfaces is unactivated, thus going through a precursor-mediated reaction pathway.[21] Excess kinetic energy would decrease the sticking coefficient of a precursor-mediated reaction pathway. McGinnis et al. grew GaN(0001) with high energy (~2.1 eV) and low energy (~0.5 eV) TEG - seeded supersonic molecular beams, formed by using He and $N_2$, respectively.[22] $NH_3$ pressure was controlled via a variable leak valve. A quadrupole mass spectrometer (QMS)

determined the relative flux intensities of TEG seeded in He and $N_2$. By measuring GaN(0001) growth rates at 750°C under $NH_3$-rich conditions and using the QMS data, they determined Ga incorporation efficiencies to be higher for TEG seeded in $N_2$. Consequently, TEG on GaN(0001) is a precursor-mediated process. This previous work by McGinnis et al. takes into account another seeded SJE property, aerodynamic focusing.[23,24] In general, aerodynamic focusing is not as well quantified as the energetic effects of seeded SJE in the thin film growth literature. Eres, et al. first noted focusing phenomena in growth of GaAs using seeded supersonic beams, where growth profiles had a $cos^{22}\ \theta$ dependence,[25] as opposed to the standard $cos^{4}\ \theta$ dependence found in single component supersonic jet expansions.[26] Also, Pacheco et al. noted focusing phenomena in Si epitaxial growth using $Si_2H_6$ seeded in $H_2$.[16]

In this work, we have grown GaN(0001) homoepitaxially on MOCVD-grown GaN(0001) substrates by supersonic jet epitaxy (SJE) using TEG seeded in $N_2$ and He. Scanning electron microscopy (SEM) was used for surface analysis and growth rate measurements (cross section). Atomic force microscopy (AFM) was used for surface roughness analysis.

## II. EXPERIMENT

The custom-fabricated SJE apparatus comprises a growth chamber and supersonic jet source with two stages of differential pumping.[27] The growth chamber is equipped with a 350 $ls^{-1}$ turbomolecular pump, leak valve, a QMS (UTI 100C) and a 15-keV electron gun and imaging system for RHEED. Connected to the SJE chamber is a cryo-pumped (APD Cryogenics, APD-4) load-lock. The TEG was provided by flowing a

controlled flow rate of the carrier gas (He or $N_2$) through a commercial bubbler (Epichem, electronic grade) that was immersed in a temperature-controlled water-ethylene glycol bath. Two streams of the carrier gas are controlled by a 50 sccm and a 500 sccm mass flow controller, respectively. The first stream passes through the TEG bubbler and is regulated by the 50 sccm mass flow controller while the second stream bypasses the bubbler and is regulated by the 500 sccm mass flow controller. The streams are recombined before entering the TEG nozzle. Careful attention is paid to keep the TEG gas lines free of air and water with extensive leak checking and they are baked periodically. Pressure at the bubbler and at the nozzle ($P_o$) are monitored separately by capacitance manometers (MKS Baratron). By varying the TEG bubbler temperature and the carrier gas flow rate into the bubbler, we can controlled the flow rate of TEG, $Q_{TEG}$. Fine tuning of the mole fraction of TEG in the nozzle can be accomplished by changing the carrier gas flow rate through the bypass line. Two TEG nozzles are employed in this work. Both TEG nozzles are constructed of stainless steel and have laser-drilled Pt orifices. By flowing various flow rates of the carrier gases and measuring $P_o$, we use the nozzle flow equation to determine the hydrodynamic nozzle diameter ($d$) of each TEG nozzle, getting $d_1$ = 82 μm and $d_2$ = 140 μm respectively (using He). The TEG-seeded supersonic beam is extracted through a 1-mm conical skimmer into a second stage of differential pumping. The beam is collimated using a 5 x 5 mm$^2$ aperture before it enters the growth chamber and is incident on the substrate at a 6° angle with respect to the surface normal, and the deposition area is 15 × 15 mm$^2$.

While the $Q_{TEG}$ out of the bubbler can be controlled straightforwardly, the flux at the substrate, $J_{TEG,d}$, is not as simple to control. Aerodynamic focusing and the carrier gas

flow field play a significant role in the intensity ($I_{TEG}$) of the beam.[24] The enrichment ratio, $\Phi$, is defined as

$$\Phi = \frac{I_S / I_C}{Q_S / Q_C} \tag{3}$$

where $I_S$ and $I_C$ are the intensities (in mc/sr•s) for the seed and the carrier, respectively. Rearranging eq. (3), we get

$$I_s = \Phi \bullet I_C \bullet \frac{Q_S}{Q_C} \tag{4}$$

For pure gas expansions, Beijerinck et al. determine

$$I_o = \kappa Q_o / \pi \tag{5}$$

where $\kappa$ is a peaking factor, dependent on heat capacity ratio, $\gamma$. If we assume the carrier gas behaves as a pure gas, which is a good assumption according to Smith et al.,[24] we can assume $I_C = \kappa Q_C / \pi$. Substituting this expression into eq. (4), we get

$$I_S = \Phi_s \bullet \frac{\kappa_C}{\pi} \bullet Q_S \tag{6}$$

For simplicity, we expression $I_s$ with respect to a reference condition, yielding

$$\frac{I_S}{I_{S,ref}} = \frac{\Phi_S}{\Phi_{ref}} \bullet \frac{\kappa_C}{\kappa_{C,ref}} \bullet \frac{Q_S}{Q_{S,ref}} \tag{7}$$

where the subscript *ref* is a reference condition. Our previous work[24] shows a correlation for $\Phi$ is

$$\Phi = 92\left(N_{\mathrm{Re}} / N_F\right)^{-0.77} \tag{8}$$

where $N_{Re}$ and $N_F$ are the Reynolds number and Fenn number, dimensionless quantities that describe the ratio of inertial to viscous forces and the disparity of relaxation scales for the two species. $N_{Re}$ is expressed as

$$N_{Re} = \gamma P_o d/\mu_o c_o \tag{9}$$

where $\mu_o$ is the viscosity coefficient, $c_o$ is the speed of sound, and $\gamma$ is the heat capacity ratio for stagnation conditions. $N_F$ may be expressed in terms of the mixture viscosity to the mass diffusivity ratio (the Schmidt number) $N_{Sc}=\mu/\rho D$ and the molecular mass ratio $m_S/m$ as

$$N_F = \gamma m_S/(m N_{Sc}) \tag{10}$$

Fig. 1 shows our calculation of eq. (7) as two lines (choosing 0.44 sccm TEG in He as a reference condition) using $P_o$ and $Q_{TEG}$ used to get the QMS intensity data points shown on Fig. 1. There is fairly good agreement in the data, although our prediction for TEG seeded in $N_2$ is a little lower than the QMS data. Our experimental growth conditions are shown in Table 1. Viscosity is calculated using the Chapman-Enskog relation and $D$ by Fuller and experimental data (for TEG-$H_2$ mixtures)[28] in order to get $N_{Re}$ and $N_F$ for $\Phi$. Our reference case is the first growth condition listed in Table 1. The effect of $\Phi$ is clear for the first two cases, as these two conditions have the same $Q_{TEG}$ and $P_o$, but $I_s/I_{s,ref}$ is a factor of 0.67 different due to the effect that $d$ has on $N_{Re}$ and consequently $\Phi$. TEG beam energy can be approximated with a correlation by Smith et al.,[24] yielding $E_{TEG}$ in $N_2$ = 0.5 eV and $E_{TEG}$ in He = 2.1 eV.

The substrates were 1 × 1 cm$^2$ pieces cut from 6H-SiC wafers on which a 1-2 μm GaN(0001) epitaxial layer had been grown by MOCVD.[11] The MOCVD-grown GaN surface was atomically smooth with a roughness of 0.17 nm rms (1× 1 mm$^2$ image

size).[29] Metallized tungsten on the back of the substrate absorbs radiation from the pyrolytic boron nitride-coated graphite heater. An infrared optical pyrometer measured the substrate temperature, $T_s$.

Each substrate was ultra-sonically cleaned *ex situ* with trichloroethylene for 20 min and inserted in the load-lock. Before GaN growth, the substrate was exposed to a $1.0\times10^{-5}$ Torr $NH_3$ flux from the leak valve for 30 min at 800°C.[29] GaN growth was performed at 750°C using the TEG-seeded supersonic beam in either He or $N_2$ and $NH_3$ from a variable leak valve (Varian: $P_{NH3} = 5.0\times10^{-6} – 1.0\times10^{-5}$ Torr). RHEED patterns of the homoepitaxial films were acquired *in situ* before and after growth using a charge-coupled-device (CCD) camera and software from kSpace Associates.

Scanning electron microscopy (SEM) and atomic force microscopy (AFM) were performed *ex situ*. AFM was performed using a Digital Instruments Dimension™ 3000 scanning probe microscope in tapping mode. Static scaling analysis was performed by determining the RMS roughness for different size regions, ranging from 4 × 4 pixel regions to 512 × 512 pixel regions (1 × 1 $\mu m^2$ image size). SEM images were acquired using a JEOL 6400FE SEM with a 5-kV cold field emission electron gun. SEM cross sections allowed us to measure film thickness since MOCVD-grown GaN and $NH_3$-seeded SJE GaN varied in image constrast. A UHV chamber equipped with a spherical capacitor analyzer and dual Mg/Al anode x-ray source for x-ray photoelectron spectroscopy (XPS) is also attached to the load-lock.

## III. RESULTS AND DISCUSSION

The original motivation for SJE-TEG growth of GaN(0001) was to increase TEG kinetic energy to perhaps allow direct chemisorption at lower temperatures and increase intensity for higher growth rates. McGinnis et al. has shown that the latter is not a benefit, as it was determined that TEG chemisorption on GaN(0001) is precursor mediated, i.e. excess kinetic energy should decrease the sticking coefficient since the additional kinetic energy would have to be accommodated for trapping to occur.[27] Hyperthermal kinetic energy could also improve surface diffusion of the impinging precursor, hence improving surface morphology.

Fig. 2(a) shows the RHEED patterns for a leak-valve $NH_3$ cleaned substrate at 800°C for 30 min. These streaky patterns evidence the smooth two-dimensional surface morphology of the cleaned film. The film grown with 0.70 sccm TEG in $N_2$ beam and $1.0\times10^{-5}$ Torr $NH_3$ is spotty and indicative of 3D surface structure [Fig. 2(b)]. The RHEED pattern in the $[2\bar{1}\bar{1}0]$ direction shown in Fig. 2(c) appears to be qualitatively between the streaky RHEED pattern in Fig. 2(a) and the spotty RHEED pattern in Fig. 2(b). The film grown in Fig. 2(c) used a 0.78 sccm TEG seeded in He growth condition with $1.0\times10^{-5}$ Torr $NH_3$. It would first appear that the beam intensity is similar for the two cases looking at $Q_{TEG}$ for each growth condition, but Table 1 clearly shows that $I_s/I_{s,ref}$ 0.78 sccm TEG in He beam is an order of magnitude higher in intensity than 0.70 sccm TEG in $N_2$ beam. The difference in surface structure is mostly like a function of the difference in III/V ratio for the two cases presented. Previous investigators have found that there is a morphological transition from 2D to 3D surfaces for GaN(0001) as the III/V ratio decreases in MBE.[30-33]

Fig. 3 displays SEM images of selected GaN(0001) films at 50,000× magnification. The films in Fig. 3(a)-(b) were grown with low-energy TEG ($N_2$ seeded) at 0.70 sccm. These films clearly have faceted structures with deep pits and trenches throughout the film. Interestingly, feature size seems to decrease with an increase in $P_{NH3}$ ($1.0\times10^{-5}$ Torr $NH_3$ compared to $5.0\times10^{-6}$ Torr $NH_3$). The growth rates ($r_g$) measured by cross-sectional SEM are fairly similar for each film (99 nm/h compared to 104 nm/h). There is most likely great uncertainty in these $r_g$ measurements due to the high void density apparent from top view SEM in Fig. 3. Examples of smooth films grown with high-energy TEG (He seeded) are shown in the Fig. 3(c)-(d). The order of magnitude increase in $I_s$ (as shown in Table 1) is most likely responsible for improved film quality from TEG seeded in $N_2$ to He beam because of the increased III/V ratio, not necessarily the increase in $E_{TEG}$. Unless relative enrichment ratios are considered when planning experimentation, the relative effects of precursor flux and kinetic energy are difficult to decouple in SJE. Noting the conditions on Table 1, it would appear that there is a roughness / surface transition occurring when $I_s/I_{s,ref} \sim 0.85$ for films grown with TEG seeded in He. All intensities lower than $I_s/I_{s,ref} \sim 0.85$ yield rough films [yielding surfaces similar to those shown in Fig. 3(a)-(b)]. For conditions leading to $I_s/I_{s,ref} > 0.85$, smooth films are grown. All films grown with supersonic beams of TEG seeded in $N_2$ exhibit rough surfaces.

The AFM images shown in Fig. 4 demonstrate the effects of flux (and hence III/V ratio) on surface morphology. Fig. 4(a) is the GaN(0001) substrate after the $NH_3$ cleaning process, which leaves a smooth surface with a faint atomic step structure; the RMS roughness of the 1×1 μm image is 0.27 nm. Fig. 4(b) shows a faceted surface that

resulted from a 0.70 sccm TEG in $N_2$ beam, where there are many pits and crevices evident. This film grown with a low intensity TEG beam is consistent with what previous investigators have observed[30-33] for low III/V ratio GaN(0001) growth, in that Ga-limited (N-rich) growth conditions correlate with highly faceted surfaces. Films grown with high intensity TEG beams (seeded in He) are shown in Fig. 4(c)-(d). These surfaces are consistent with those surfaces produced by $NH_3$-limited (Ga-rich) conditions that promote non-faceted basal plane growth. Neither of the images produced by growth using high intensity TEG beams (seeded in He) show evidence of faceting. The surface in Fig. 4(d) appears to be constructed of sheets growing over the top of one another, i.e. layer-by-layer growth. Fig. 4(c) shows a film grown with a lower TEG intensity ($I_s/I_{s,ref}$ = 1.00; 0.42 sccm TEG in He) than the film grown in Fig. 4(d) ($I_s/I_{s,ref}$ = 1.41; 0.80 sccm TEG in He). The film in Fig. 4(c) has a smaller feature size than what is found in Fig. 4(d), while their 1×1 μm RMS roughness values are comparable [1.69 for Fig.4(c) and 1.94 for Fig. 4(d)]. In addition, the film in Fig. 4(d) is about 40% thicker than the film in Fig. 4(c).

In order to monitor how the GaN(0001) surface evolves with time, we grew two films with 0.78 sccm TEG in He and $1.0\times10^{-5}$ Torr $NH_3$ for a period of 2 h and 4 h. The AFM images of these two films are shown in Fig. 5. The 2 h [Fig. 5(a)] film growth has larger island features whereas the 4 h [Fig. 5(b)] film growth has small island features. The 2 h film is rougher than the 4 h film. It is likely that the 2 h film is before the islands filled in their initial crevices. Consequently, the 4 h growth could be after the initial island coalescence, yielding a 2D smooth film. This same phenomena was observed by Pavloska et al. when they monitored $NH_3$ SJE-GaN(0001) growth with low energy

electron diffraction (LEEM). Initially, the surface appeared as islands and converted to planar growth after a period of time.

A post-deposition determination of the kinetic roughening and smoothening processes occurring on the surface during growth can be found through scaling analysis. Scaling analysis relates measurable quantities (e.g., interfacial roughness) to universality classes. Fig. 6 illustrates the relationship between surface roughness ($\zeta$) and lateral length scale ($L$) for a faceted homoepitaxial GaN films grown using a supersonic beams of 0.55 sccm TEG in He. The data in Fig. 6 were generated by applying eq. (11) over different length scales (square regions) using a 1×1 μm$^2$ AFM image, 0.5×0.5 μm$^2$ AFM image and a 0.25×0.25 μm$^2$ AFM image. The sample size (in this instance) has little effect of the measurement of $\xi$ vs. $L$, as each of the three sample sizes are above the critical length, $L_c$. $\zeta$ is a quantitative measure of surface (interfacial) roughness that depends on the length scale $L$ over which it is measured. Scaling of the surface roughness can be expressed as

$$\zeta(L,t) = L^{\alpha} f\left(t / L^{z}\right) \tag{12}$$

where $t$ is time, $\alpha$ is the static scaling exponent, $z = \alpha/\beta$, and $\beta$ is the dynamic scaling exponent. The scaling function $f(t/L^z)$ behaves as $(t/L^z)^\beta$ for $x$<<1 and as a constant for $x$>>1,

$$\zeta(L,t) \sim L^{\alpha} \text{ for } t / L^{z} >> 1 \tag{13}$$

$$\zeta(L,t) \sim t^{\beta} \text{ for } t / L^{z} << 1 \tag{14}$$

Following the relationship in eq. (13), $L_c$ and $\alpha$ values are determined for each data set in Fig. 5. At length scales smaller than $L_c$(~55 nm), the roughness scales as $\zeta \sim L^{\alpha}$ where $\alpha$

is the static scaling coefficient, resulting in $\alpha \approx 0.91$ for this non-faceted film. At length scales larger than $L_{c,}$ $\zeta_{sat}$ = 1.20 nm. Static scaling of self-similar surfaces leads to $\alpha = 1$. The more general case of self-affine surfaces corresponds to $0 < \alpha < 1$.

Fig. 6 illustrates the static scaling analysis for GaN films grown by SJE using TEG seeded in $N_2$ and He. Table 2 summarizes the growth conditions, scaling parameters $L_c$ and $\alpha$, saturation roughness $\zeta_{sat}$, thickness, and growth time for each film. Non-faceted films (grown with TEG seeded in He) give $\alpha$ values of 0.87-1.07, $L_c$ ~ 55-70 nm and $\xi_{max}$ ~1-2 nm, whereas faceted films (grown with TEG seeded in $N_2$) give an $\alpha$ value of 1.07, a $L_c$ ~ 110 nm, and a $\xi_{max}$ ~ 19-30 nm. In between these two regimes appear to be the shorter time growth of 2 h with TEG seeded in He. It has a larger $L_c$~115 nm and a larger $\alpha$~0.96 than most of the other films grown with TEG seeded in He. As discussed earlier in the paper, this could be the result of islands that have not coalesced, apparently from the deep crevices shown in Fig. 5. At length scales much less than $L_c$, the data tend toward common lines for non-faceted and faceted films. The *in situ* cleaning process roughens the surface [from $\zeta_{sat}$=0.17 nm to $\zeta_{sat}$ =0.27 nm (1 x 1 $\mu m^2$ image size)] and this places a lower limit on $\zeta_{sat}$ for non-faceted films of ~0.27 nm. Saturation roughness increases as the $L_c$ increases for the non-faceted and faceted films, except for the film exhibiting a growth surface prior to island coalescence. It is evident that there are two universality classes governing non-faceted and faceted films. The non-faceted films (Fig. 6) all have an $\alpha$ ~ 0.9, whereas the faceted films (Fig. 6) have an $\alpha$ ~ 1.1. The TEG seeded in He film grown for 4 h with $I_s/I_{s,ref}$ = 1.41 does not fit in the above classification, as it has an $\alpha$=1.07, similar to the $\alpha$ for faceted films.

In general, knowing that $\alpha$ =1.06-1.13 for faceted films grown and $\alpha$~0.9 for non-faceted films (Fig. 7) indicates that our growth surface transport phenomena approximates the continuum model for surface diffusion for faceted and non-faceted films.[34] Continuum models describing surface diffusion growth from an initially flat surface indicate $\alpha$=1. Our growth process does not begin from an initial flat surface as the cleaning process does leave some finite roughness. One would expect this to have an effect on both $\alpha$ and $\beta$. $\alpha$ can be thought as a general description of the ratio of vertical transport versus lateral transport. In general, non-faceted films have an $\alpha$~0.9 and growth rates less than 95 nm/h. In general, faceted films have an $\alpha$~1.1 and growth rates greater than 99 nm/h. We would expect faceted surfaces to have more vertical growth than non-faceted surfaces, explaining the rise in $\alpha$ for faceted surfaces. The non-faceted surfaces having an $\alpha$ ~0.9 suggests this growth process would be similar to a combination of surface diffusion and step flow growth as the surface growth mechanism (step flow growth $\alpha$ ~0.67).[34] There is no continuum model yielding scaling coefficients for two-dimensional island coalescence, but one would expect a model to be qualitatively a combination of the surface diffusion and step-flow growth models. Therefore, the TEG SJE GaN growth process is dominated by a surface diffusion process, similar to $NH_3$ SJE GaN growth,(Smith et al.) not stochastic roughening as suggested by previous investigators for PAMBE GaN growth.[31,32]

It is difficult to discern the effects of $E_{TEG}$ on the quality of GaN(0001) surface grown since the flux was not kept constant from seeding TEG in He to seeding TEG in $N_2$. It was demonstrated previously that TEG follows a precursor mediated pathway for GaN(0001) growth since there is an enhanced growth rate comparatively for lower

energy TEG. A beam of high-energy TEG reduces feature size on Ga-rich surfaces. Ga diffusion on Ga-terminated surfaces is the surface diffusion process with the lowest activation barrier according to density functional theory (DFT) calculations.[35] Our surface is GaN(0001) unlike Held's GaN($000\bar{1}$), so one must consider the possibility that both surfaces (non-faceted and faceted) are Ga-terminated. DFT calculations indicate an activation barrier of 0.2 eV for Ga surface diffusion on Ga-terminated GaN($000\bar{1}$) and 0.4 eV for Ga surface diffusion on Ga-terminated GaN(0001).[35] It is possible that for 95 nm/h and greater growth rates for SJE with TEG seeded beams, the surface is Ga-terminated GaN($000\bar{1}$) and that the surface from 0 to 95 nm/h growth rates for our conditions is Ga-terminated GaN(0001). A decrease in the activation barrier for Ga diffusion on Ga-terminated surfaces for GaN($000\bar{1}$) surfaces would support our increase in $L_c$ for faceted surfaces (Table 2 and Fig. 7). Films grown in low III/V ratios and high III/V ratios both exhibited surface diffusion as the primary surface mechanism as opposed to stochastic roughening. If stochastic roughening were the growth mechanism for SJE with TEG seeded beams grown GaN films, the scaling analysis would have yielded $\alpha \rightarrow 0$ and $\beta \rightarrow 0.5$. The fundamental transition to faceted GaN films grown by SJE with TEG seeded beams does not arise from stochastic roughening as surface diffusion is always the dominate growth process. Instead, the fundamental transition from non-faceted to faceted for SJE-$NH_3$ grown GaN(0001) films arises as the surface changes from Ga-rich to N-rich.

**ACKNOWLEDGEMENTS**

This work was supported by the Office of Naval Research (N00014-01-1-0003). The authors would like to thank Kevin Bray for introducing us to topological scaling analysis of surface roughness and for his help with some of the AFM measurements.

# REFERENCES

[1]H. Morkoc, S. Strite, G. B. Gao, M. E. Lin, B. Sverdlov, and M. Burns, J. Appl. Phys. **76**, 1363 (1994).

[2]R. F. Davis, Proc. IEEE **79**, 702 (1991).

[3]J. W. Orton and C. T. Foxton, Rep. Prog. Phys. **61**, 1 (1998).

[4]H. Amano, I. Akasaki, T. Kozowa, K. Hiamatsu, N. Sawak, K. Ikeda, and Y. Ishii, J. Lumin. **40-41**, 121 (1988).

[5]S. Nakamura, M. Senoh, S. Nagahama, N. Iwasa, T. Yamada, T. Matsushita, H. Kyoku, and Y. Sugimoto, Jpn. J. Appl. Phys., Part 2 **35**, L74 (1995).

[6]S. Nakamura, Y. Harada, and M. Seno, Appl. Phys. Lett. **58**, 2021 (1991).

[7]T. W. Weeks, Jr., M. D. Bremser, K. S. Ailey, E. Carlson, W. G. Perry, and R. F. Davis, Appl. Phys. Lett. **67**, 401 (1995).

[8]W. T. Tsang, J. Cryst. Growth **111**, 529 (1991).

[9]S. Bharatan, K. S. Jones, C. R. Abernathy, S. J. Pearton, F. Ren, P. Wisk, and J. R. Lothian, J. Vac. Sci. Technol. A **12**, 1094 (1994).

[10]C. R. Kingsley, T. J. Whitaker, A. T. S. Wee, R. B. Jackman, and J. S. Foord, Mater. Sci. Eng., B **29**, 78 (1995).

[11]E. Kim, I. Berishev, A. Bensaoula, S. Lee, S. S. Perry, K. Waters, and J. A. Schultz, J. Vac. Sci. Technol. B **16**, 1270 (1998).

[12]X. Q. Shen, S. Tanaka, S. Iwai, and Y. Aoyagi, J. Cryst. Growth **188**, 86 (1998).

[13]B. A. Ferguson and C. B. Mullins, J. Cryst. Growth **178**, 134 (1997).

[14]S. T. Ceyer, J. D. Beckerle, M. B. Lee, S. L. Tang, Q. Y. Yang, and M. A. Hines, J. Vac. Sci. Technol. A **5**, 501 (1987).

[15]L.-Q. Xia, M. E. Jones, N. Maity, and J. R. Engstrom, J. Vac. Sci. Technol. A., **13**, 2651 (1995).

[16]K. A. Pacheco, B. A. Ferguson, C. Li, S. John, S. Banerjee, and C. B. Mullins, Appl. Phys. Lett. **67**, 2951 (1995).

[17]K. A. Pacheco, B. A. Ferguson, and C. B. Mullins, J. Vac. Sci. Technol. A **14**, 2190 (1997).

[18]S. A. Ustin, K. A. Brown, and W. Ho, Rev. Sci. Instrum. **71**, 1479 (2000).

[19]K. A. Brown, S. A. Ustin, L. Lauhon, and W. Ho, J. Appl. Phys. **79**, 7667 (1996).

[20]J. J. Sumakeris, R. K. Chilukuri, R. F. Davis, and H. H. Lamb, Mater. Res. Soc. Symp. Proc. **395**, 331 (1996).

[21]M. L. Yu and L. A. Delouise, Surf. Sci. Rep. **19**, 286 (1994).

[22]A. J. McGinnis, D. Thomson, A. Banks, E. Preble, R. F. Davis, and H. Henry Lamb, J. Vac. Sci. Technol. A **21**, 294 (2003).

[23]J. Fernandez de la Mora and J. Rosell-Llompart, J. Chem. Phys. **91**, 2603 (1989).

[24]N. Smith, H. H. Lamb, to be submitted for publication (Ch. 2 - Focusing).

[25]D. Eres, Mater. Res. Soc. Symp. Proc. **201**, 11 (1991).

[26]J. B. Anderson, R. P. Andres, J. B. Fenn, and G. Maise, Rarified Gas Dynamics, edited by J. H. d. Leeuw (Academic, New York, 1966), p. 106.

[27]A. J. McGinnis, D. Thomson, R. F. Davis, E. Chen, A. Michel and H. H. Lamb, Surf. Sci. **494**, 28 (2001).

[28]M. Suzuki and M. Sato, J. Elec. Soc., **132**, 1684 (1985).

[29]A. J. McGinnis, D. Thomson, R. F. Davis, E. Chen, A. Michel and H. H. Lamb, J. Crys. Grow. **222**, 452 (2001).

[30]R. Held, D. E. Crawford, A. M. Johnston, A. M. Dabiran and P. I. Cohen, Surf. Rev. Lett. **5**, 913 (1998).

[31]T. H. Myers, L. S. Hirsch, L. T. Romano and M. R. Richards-Babb, J. Vac. Sci. Technol. B **16**, 2261 (1998).

[32]E. J. Tarsa, B. Heying, X. H. Wu, P. Fini, S. P. DenBaars and J. S. Speck, J. Appl. Phys. **82**, 5472 (1997).

[33]A. Pavlovska, V. M. Torres, E. Bauer, R. B. Doak, I. S. T. Tsong, D. B. Thomson and R. F. Davis, Appl. Phys. Lett. **75**, 989 (1999).

[34]W. M. Tong and R. S. Williams, Annu. Rev. Phys. Chem. **45**, 401 (1994).

[35]T. Zyweitz, J. Neugebauer and M. Scheffler, App. Phys. Lett. **73**, 487 (1998).

**Table 1: Growth conditions for GaN and TEG beam**

| Diluent gas | $Q_{TEG}$ (sccm) | $Q_C$ (sccm) | $P_o$ (Torr) | $P_{NH3}$ (Torr) | $r_g$ (nm/h) | film quality | $N_F$ | $N_{Re}$ | $\Phi$ | $I_s/I_{s,ref}$ |
|---|---|---|---|---|---|---|---|---|---|---|
| He | 0.44 | 100 | 426.5[a] | 1.00E-05 | 61[a] | smooth | 31.9 | 872 | 7.209 | 1.000 |
| He | 0.45 | 290 | 435 | 1.00E-05 | - | rough | 31.9 | 1515 | 4.712 | 0.670 |
| He | 0.59 | 290 | 453 | 1.00E-05 | - | rough | 31.9 | 1579 | 4.565 | 0.849 |
| He | 0.80 | 215 | 348.4 | 1.00E-05 | 79 | smooth | 31.9 | 1214 | 5.590 | 1.410 |
| He | 0.78 | 215 | 357.8 | 1.00E-05 | 70[c] | smooth | 31.9 | 1246 | 5.476 | 1.347 |
| He | 0.78 | 215 | 330 | 1.00E-05 | 95[b] | smooth | 31.9 | 1150 | 5.828 | 1.433 |
| He | 0.78 | 215 | 324 | 1.00E-05 | 89 | smooth | 31.9 | 1129 | 5.911 | 1.454 |
| $N_2$ | 0.63 | 90 | 327 | 1.00E-05 | 72 | rough | 5.6 | 2419 | 0.863 | 0.126 |
| $N_2$ | 0.63 | 90 | 330 | 5.00E-06 | 75 | rough | 5.6 | 2441 | 0.857 | 0.125 |
| $N_2$ | 0.70 | 80 | 287 | 5.00E-06 | 104 | rough | 5.6 | 2123 | 0.954 | 0.155 |
| $N_2$ | 0.70 | 80 | 294 | 1.00E-05 | 99 | rough | 5.6 | 2175 | 0.936 | 0.152 |
| $N_2$ | 0.78 | 71 | 256 | 1.00E-05 | - | rough | 5.6 | 1894 | 1.042 | 0.188 |
| $N_2$ | 0.78 | 71 | 251 | 5.00E-06 | 66 | rough | 5.6 | 1857 | 1.058 | 0.191 |
| $N_2$ | 0.90 | 62 | 224 | 5.00E-06 | - | rough | 5.6 | 1657 | 1.154 | 0.241 |

a- 82 μm nozzle instead of 140 μm nozzle.
b - 2:00 growth instead of 4:00.
c - $T_s$ = 730°C. All other growths at 750°C.

**Table 2**: TEG beam conditions and corresponding roughness parameters determined by AFM images.

| $Q_{TEG}$ (sccm) | *car.* gas | $P_{NH3}$ (Torr) | *d* (μm) | $L_c$ (nm) | $\alpha$ | $\xi_{max}$ (nm) | *thickness* (nm) | *Growth time* (h) |
|---|---|---|---|---|---|---|---|---|
| 0.55 | He | $1.0\times10^{-5}$ | 82 | 59 | 0.87 | 1.20 | 256 | 4 |
| 0.42 | He | $1.0\times10^{-5}$ | 82 | 55 | 0.98 | 1.69 | 236 | 4 |
| 0.80 | He | $1.0\times10^{-5}$ | 140 | 70 | 1.07 | 1.94 | 317 | 4 |
| 0.70 | $N_2$ | $5.0\times10^{-6}$ | 140 | 110 | 1.07 | 29.9 | 416 | 4 |
| 0.70 | $N_2$ | $1.0\times10^{-5}$ | 140 | 112 | 1.07 | 19.3 | 396 | 4 |
| 0.78 | He | $1.0\times10^{-5}$ | 140 | 115 | 0.96 | 2.47 | 190 | 2 |
| 0.78 | He | $1.0\times10^{-5}$ | 140 | 64 | 0.94 | 1.18 | 357 | 4 |
| Substrate | - | $1.0\times10^{-5}$ | - | 107 | 0.37 | 0.27 | - | - |

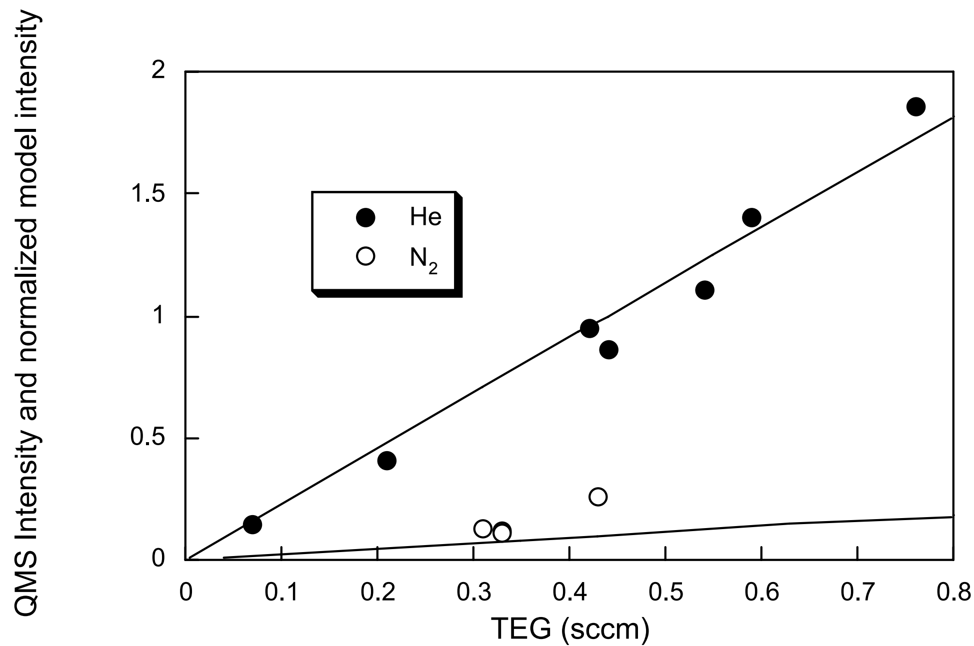


**Figure 1:** QMS intensity of TEG seeded in 100 sccm He and 50 sccm $N_2$. Lines represent model intensity (given experiment conditions) with respect to $I_{s,ref}$ (0.44 sccm TEG, 82-μm hydrodynamic nozzle).

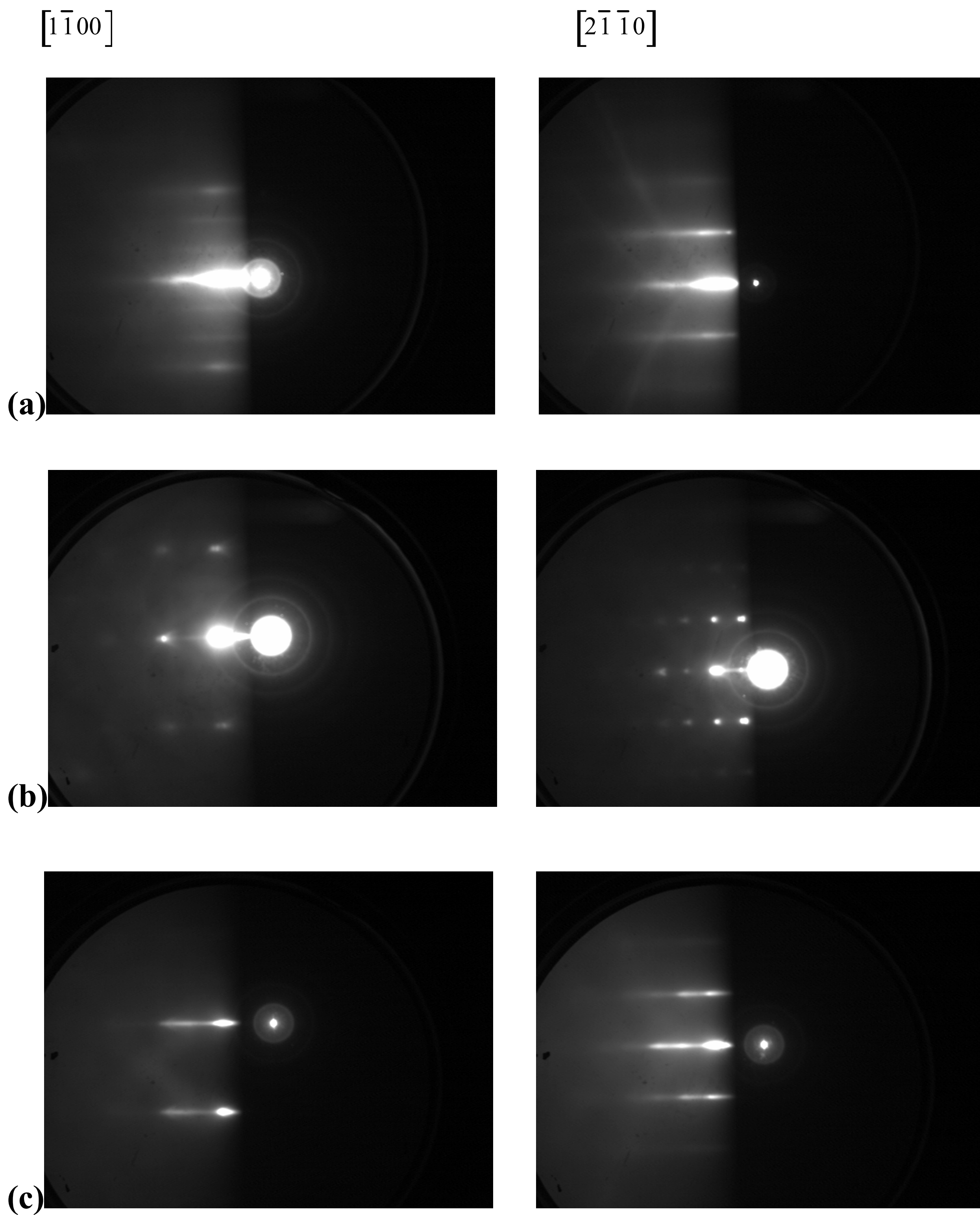


**Figure 2:** RHEED Patterns for clean substrate (top), 0.70 sccm TEG in $N_2$ beam (middle), 0.78 sccm TEG in He beam (bottom).

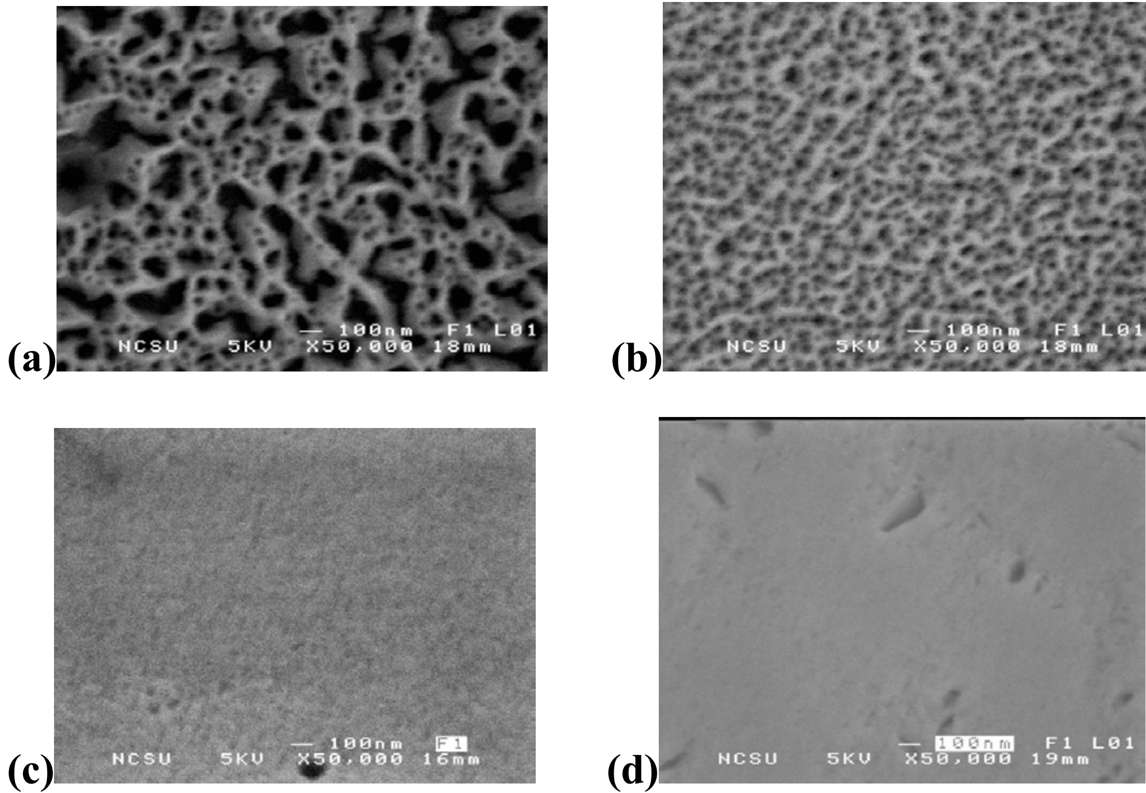


**Figure 3:** 750°C growth runs, low-energy ($N_2$ seeded) growth runs. (a) $5.0\times10^{-6}$ Torr $NH_3$, 0.70 sccm TEG, $N_2$; (b)$1.0\times10^{-5}$ $NH_3$, 0.70 sccm TEG, $N_2$. (c) $1.0\times10^{-5}$ Torr $NH_3$, 0.44 sccm TEG, He. (d) $1.0\times10^{-5}$ $NH_3$, 0.78 sccm TEG, He, 2 h.

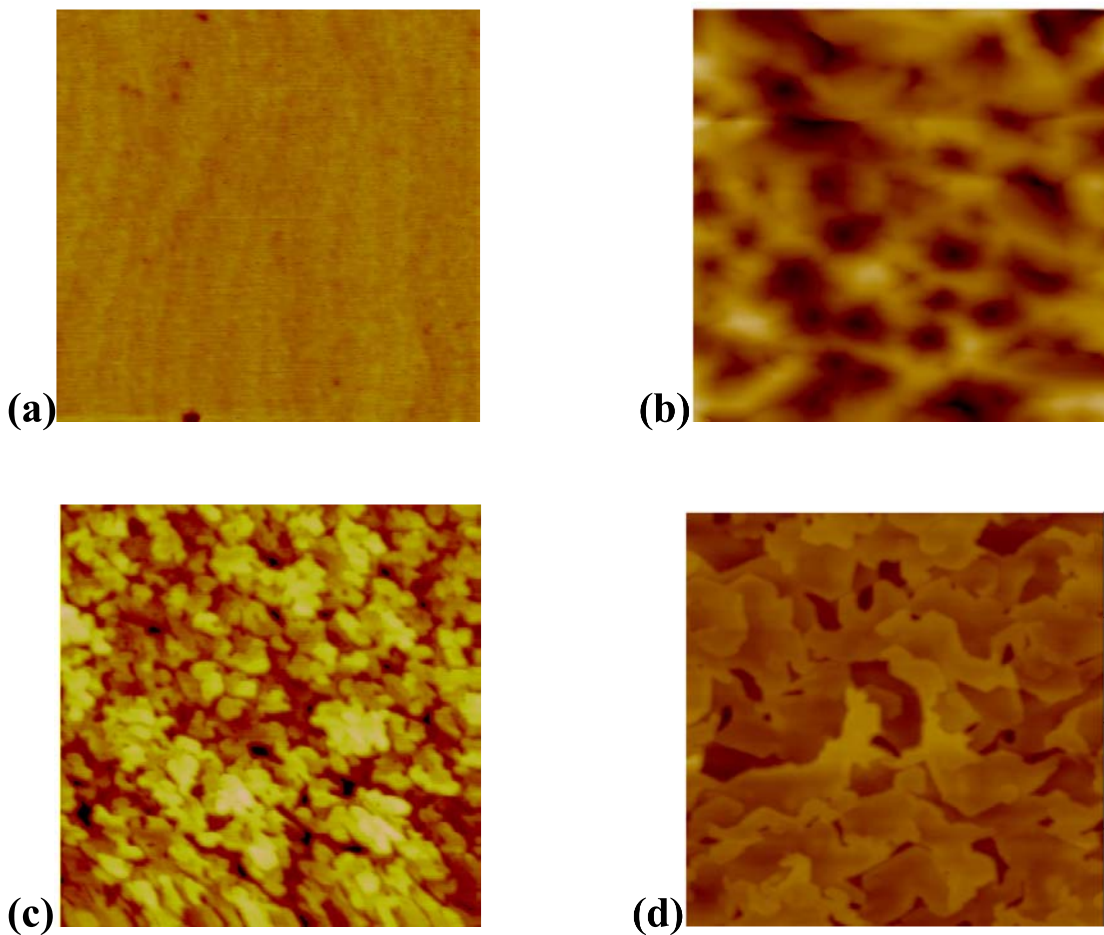


**Figure 4:** (a) 10 nm grayscale: substrate, cleaned by leak valve; (b) 200 nm grayscale: 0.70 sccm TEG in $N_2$, $1.0\times10^{-5}$ $NH_3$; (c) 15 nm grayscale: 0.42 sccm TEG in He, $1.0\times10^{-5}$ $NH_3$; (d) 40 nm grayscale: 0.78 sccm TEG in He, $1.0\times10^{-5}$ $NH_3$.

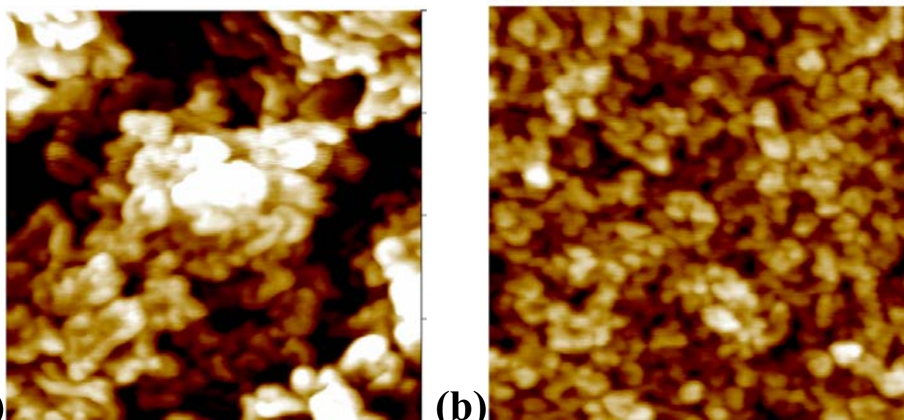


**Figure 5:** AFM: 20nm grayscale, $1.0\times10^{-5}$ $NH_3$, 0.78 sccm TEG in He, 2 h; 20 nm grayscale, $1.0\times10^{-5}$ $NH_3$, 0.78 sccm TEG in He, 4 h.

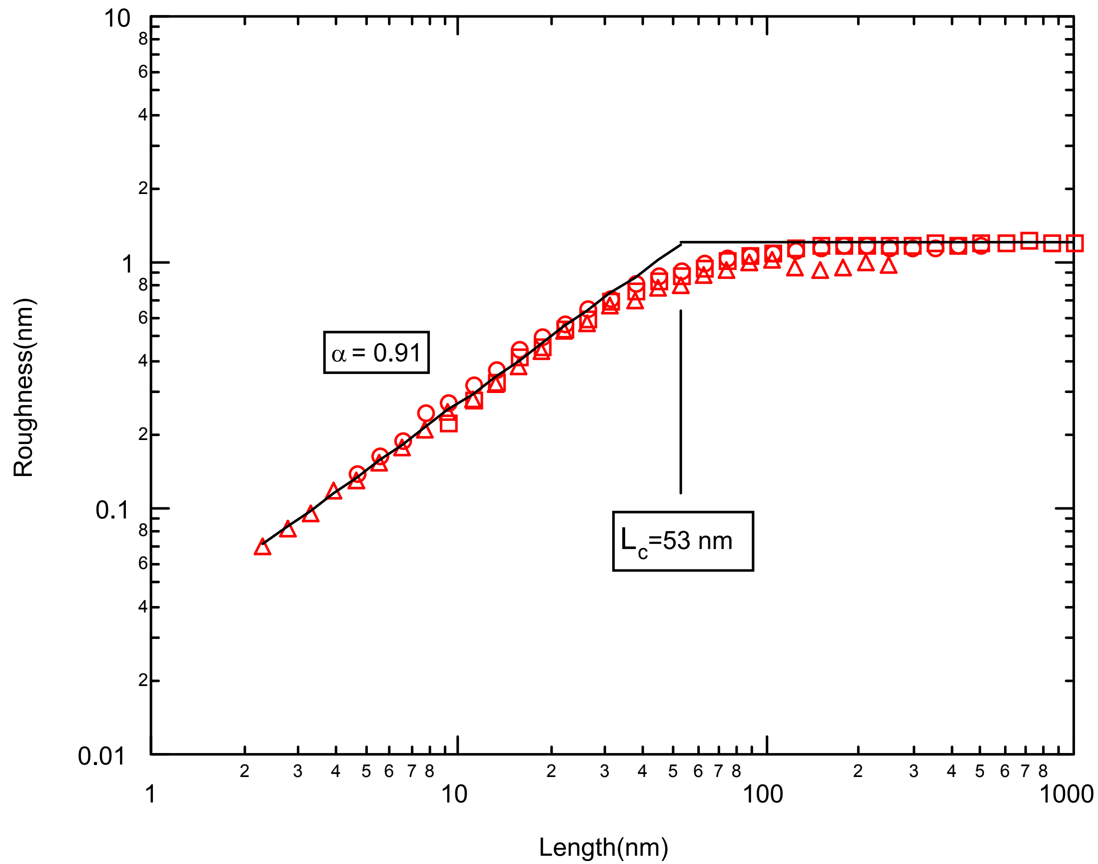


**Figure 6:** Roughness plot of 0.55 sccm TEG in He, 1.0×10-5 $NH_3$. □ - AFM data for image size of 1000 nm, yielding $\alpha$=0.91 and $L_c$= 53 nm. ○ - AFM data for image size of 500 nm, yielding $\alpha$=0.87 and $L_c$= 53 nm. △ - AFM data for image size of 250 nm, yielding $\alpha$=0.87 and $L_c$= 59 nm.

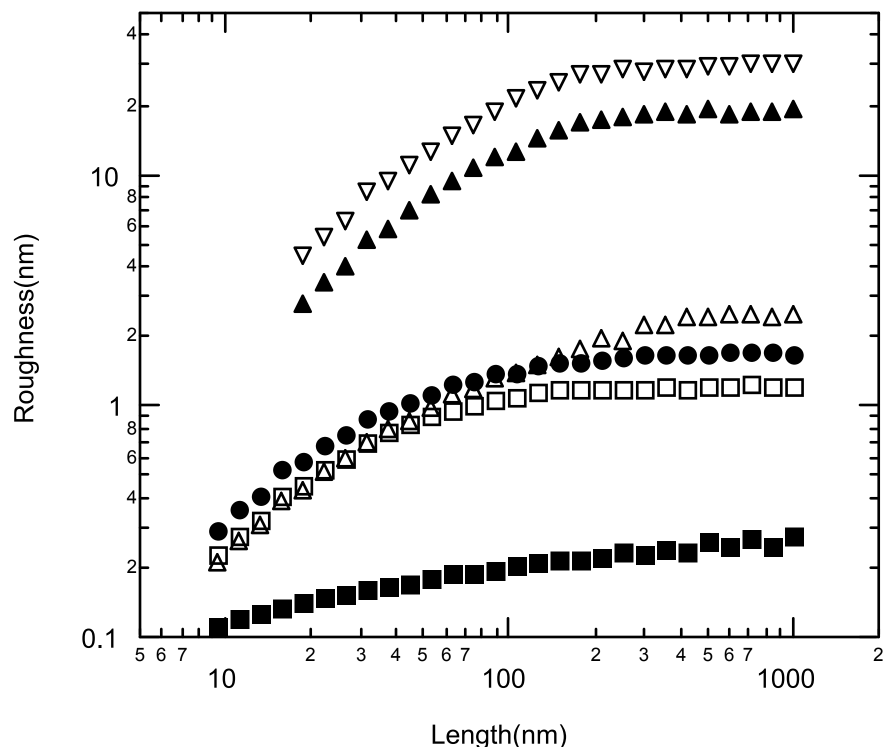


**Figure 7:** Plot of Roughness vs. Length. ▽ - 0.70 sccm TEG in $N_2$, $5.0\times10^{-6}$ Torr $NH_3$; ▲ - 0.70 smm TEG in $N_2$, $1.0\times10^{-5}$ Torr $NH_3$; △ - 0.78 sccm TEG in He, $1.0\times10^{-5}$ Torr $NH_3$ 2 h; ●- 0.42 sccm TEG in He, $1.0\times10^{-5}$ Torr $NH_3$; ■ - clean substrate □ - 0.78 sccm TEG in He, $1.0\times10^{-5}$ Torr $NH_3$ 4 h.

5. Time-of-flight appearance potential mass spectrometry of a radio-frequency -discharge supersonic jet nitrogen source. Nicholas A. Smith and H. Henry Lamb. Manuscript will be sent to Journal of Applied Physics.

Time-of-Flight Appearance Potential Mass Spectrometry of an Radio-Frequency - Discharge Supersonic Jet Nitrogen Source

Nicholas A. Smith and H. Henry Lamb*

Department of Chemical Engineering, North Carolina State University, Raleigh, North Carolina 27695-7905, USA

*Corresponding author: Tel.: +1-919-515-6395; fax: +1-919-515-3465. E-mail address: lamb@eos.ncsu.edu.

## ABSTRACT

A combination of appearance potential mass spectrometry (APMS) and time-time-of-flight (TOF) techniques was employed to achieve precise measurements on reactive species emitted from a 13.56 MHz radio-frequency discharge (RFD) supersonic jet (SSJ) nitrogen source. TOF methods were used to discriminate between background and beam signals in the analysis chamber and also to determine the directed kinetic energies and thermal energies of the beam components. APMS yields the relative concentrations of various reactive species (such as $N_2^+$ ions,$N_2$ metastables, and ground-state N) by varying the electron impact energy used for ionization. By the TOF-APMS method, we demonstrate that our RFD-SSJ nitrogen source produces primarily ground-state N atoms ($^4S^0$), with only minor concentrations of metastable molecular nitrogen ($A^3\Sigma_u^+$) and molecular ions. Energy analysis using the TOF-APMS data indicate neutral plasma temperatures are from 1200 K - 1650 K. Optical emission spectra (OES) show small broad emission bands from 570 nm to 900 nm representing the $N_2$ first positive (1+) series, which arises from $N_2(B^3\Pi_g)\rightarrow N_2(A^3\Sigma_u^+)$ transitions.

# I. INTRODUCTION

Determining the concentrations of reactive species emitted from plasma sources has long been an issue of interest and debate. Indirect methods have frequently been employed, such as measuring growth rates of thin films subject to fluxes of reactive species. One can then infer the reactive species flux if it is the kinetically limiting species in thin film growth. The reactive species flux may, however, be higher than the equivalent growth rate if there is a significant de-excitation pathway. For simple systems, this method can be effective, although the identities of the actual reactive intermediates may remain unknown. For binary and tertiary material systems, surface kinetics can become more complicated (perhaps non-linear). This empirical method has been employed in chemical vapor deposition (CVD) systems and molecular beam epitaxy (MBE) systems.

An alternative to this indirect approach is to employ a quadrupole mass spectrometer (QMS) to measure the fluxes of reactive species emitted by the plasma source. Typically, the QMS would be placed in line-of-sight of where the materials processing would occur, as there are usually geometric variations in species concentrations due to flow and excitation conditions. For CVD, the QMS would not be placed directly in the processing chamber, as the pressure is too high; instead it would be placed in a separate chamber with its own pumping system. This extra distance decreases the signal received by the QMS. With the low operating pressure found in MBE systems one can insert a QMS directly in the growth chamber. Signal-to-background ratio has always been an issue for QMS sampling. It is not simple to discriminate between source and background signals. In many cases, the non-reactive beam species may only be 1%

or less of the total QMS signal (beam + background). The active species may not be completely condensable on the detection chamber walls either, so an appreciable background of active species may remain. The noise of the background signal can greatly interfere with the QMS beam signal resolution. To increase the beam to background ratio, the QMS can be placed in a separate differential pumping chamber or further downstream in one of a number of differential pumping chambers.[1] Modulated beam mass spectrometry (MBMS) offers a solution to increase beam-to-background ratio by alternatively blocking and allowing the beam to pass to the mass spectrometer.[2,3,4] The difference in mass spectrometer signals (off and on signals) is then proportional to the concentrations of the beam species, as long as the duty of the beam admitted is small enough so that it does not affect the background pressure in the detection chamber. The devices used to modulate the beam in MBMS vary from simple beam flags to mechanical choppers. Simple beam flags can accomplish a base level of beam concentration determination. The combination of a chopper with a lock-in amplifier greatly improves the extraction of beam data from beam + background data.[3]

QMS can only determine the mass-to-charge ratio of the detected species. Thus, difficulty arises when species with the same mass to charge ratio are ionized (i.e., $C_2H_4$ vs. $N_2$ vs. $N_2^*$ or $N_2^{++}$ vs. $N^+$.) For example, $N_2(A)$ and $N_2(X)$ both contribute to the 28 m/e QMS signal, and thus, discrimination between the two species signals is not trivial. Appearance potential mass spectrometry (APMS) is a technique that overcomes this interference by varying the electron impact energy ($E$) used for ionization.[2,5,6] Each species has a minimum required energy for ionization, called the threshold voltage or appearance potential ($E_i$). Singh, *et al.* employed a combination of MBMS and APMS to

characterize a parallel-plate inductively-coupled $O_2$ plasma using a triply differentially pumped system.[2] They were able to detect O atom ionization for the “plasma on” condition. Jordan, *et al.* employed APMS on a corona discharge supersonic free jet of $N_2$ and determined that the primary reactive species in the plume was $N_2$ ($A_3\Sigma_u^+$) metastables.[5]

Time-of-flight (TOF) methods allow discrimination between the beam and background signals from a QMS, and consequently, is a type of MBMS. In TOF analysis, the beam modulation frequency is high enough so gas is admitted to the QMS as a short pulse and the flight path is long enough to measure the dispersion in velocity. In conventional low-frequency MBMS, the signal difference between the beam on and beam off states may also include an additional contribution to the background. This residual contribution required previous investigators to include "wall-loss" coefficients, to account for reactivity or adsorption of reactive species on stainless steel.[6,7,8] TOF methods effectively obviate the need for such approximations since the beam duty cycle is much smaller.

In this paper, we describe a TOF-APMS technique to accurately assess the fluxes of reactive species emanating from a radio-frequency discharge (RFD) supersonic jet (SSJ) nitrogen source. The experimental apparatus is similar to that employed by Singh, *et al.* for MBMS;[2] however, our chopper is placed further away from the source, and it continuously modulates the beam at a high frequency (200 Hz). The RFD-SSJ plasma plume was also characterized by optical emission spectroscopy (OES).

## II. EXPERIMENT

The RFD-SSJ source was constructed after those built by Pollard and Sellidj et al.;[6,7] our source closely resembles Sellidj's source since we both use the same RF power (13.56 MHz) for the helical resonator (Fig. 1). The 7"-long nozzle was constructed of a 3/8" diameter pyrolytic boron nitride (PBN) tube with a nominal laser-drilled 150-μm orifice. Antenna design for the helical resonator was based of work done by Macalpine.[8] The Ta antenna was wrapped around a 1.1" BN insulator with 70 turns, spaced at 0.025" per turn. Surrounded by a copper shield, the antenna was free at the nozzle end of the resonator and grounded on the gas supply side of the resonator. The RF is generated by a commerical ACG-6 RF generator. Power is matched via a homemade matching network before arriving at a tap positioned at turn 20 (from the gas supply side). A thicker second Cu coil wrapped coaxially around the back 4" of the 7" PBN tube together with a tesla coil was used to ignite the plasma when the cold nozzle pressure was 100 Torr - 150 Torr. The orifice is placed 3/4" from the tip of a nickel 1-mm diameter skimmer in the source chamber (Fig. 2). Successful operation of the plasma source requires a hot mode plasma, where there is a plasma ignited in the tube and a plasma plume extends from the nozzle and seems to couple with the skimmer. Cold mode operation (tube only plasma and subsequently lower $T$ as measured by $P_o$) was not desirable (no detectable excited species by APMS). Hot mode operation (1200 K to 1550 K by pressure rise at 80 W forward power) and ignition of our source required Ar gas flow. He gas flow could be admitted, but a minimum of some Ar gas flow must be maintained to keep the hot mode operational (typical flow rates of 41.2 sccm He, 1.5 sccm $N_2$ and 2.5 sccm Ar). $N_2$ could be admitted as well at low flow rates (0.5 – 2 sccm $N_2$); higher flow rates of $N_2$ would switch the

source to the cold mode operation. Hot mode operation requires proper matching (reflected power <1%) and also the proper pressure ranges. Stagnation nozzle pressure ranged from 100 Torr to 250 Torr for successful plasma operation. If background pressure in the source chamber was too high, the source would ground at places other than the skimmer. If background pressure were too low, the plasma would not maintain its coupling with the skimmer, leading to cold mode operation. After a period of successful hot mode operation, there was visible erosion of the Ni skimmer.

The custom-fabricated TOF-APMS apparatus comprises a growth chamber and the supersonic jet source (detailed above) with three stages of differential pumping (Fig. 2).

The source chamber is pumped by a 2000 $ls^{-1}$ diffusion pump (Varian VHS-6). A seeded supersonic plasma beam is extracted through a 1-mm skimmer into a second stage of differential pumping with a 2000 $ls^{-1}$ diffusion pump (Varian VHS-6). In the second stage, a variable-speed mechanical chopper modulates the beam via a dual 1-mm wide slit. Beam admittance is timed via a (2-ns) photocoupler positioned opposite the beam admittance position. The beam is collimated before it enters the third stage of differential pumping (53 $ls^{-1}$ via a Pfeiffer TMU-064) via a 3.33-mm diameter aperture. The beam finally enters the growth chamber via a 6-mm diameter aperture. The growth chamber is equipped with a 350 $ls^{-1}$ turbomolecular pump, effusion cell sources, and a 15-keV electron gun and imaging system for RHEED. A Hiden 300PIC quadrapole mass spectrometer (QMS) is used to analyze the beam composition. A microcomputer equipped with an Oxford-Tellenec multichannel scalar (MCS) II card acquires trigger information (photocoupler) and signals the beginning of a new pass, recording cumulative QMS data into 2-μs wide channels. With a data resolution of 2-μs, the

response of the mass spectrometer can give a reasonable approximation of the beam's velocity distribution, *f(v)*. Knowledge of the time distribution and the actual flight path length allows the TOF spectra to be converted to the velocity domain

$$f(v) = v^3 \exp\left(-\left(\frac{v - v_s}{\alpha}\right)^2\right) \tag{1}$$

where $v$ is the parallel velocity, $v_s$ is the stream velocity and $\alpha$ is a fitting parameter related to the temperature of the beam, T

$$\alpha = \sqrt{\frac{2kT}{m}} \tag{2}$$

and to $m$, mass of the species. Kinetic energy, $E_i$, is given by

$$E_i = \frac{1}{2} m v_s^2 \tag{3}$$

The TOF method allows us to determine the velocity distribution and hence acquire $S$ (speed ratio), $T_{ll}$ and $v_s$.

Fig. 3(a) shows a typical TOF curve taken at m/e=28 for the 41.2 sccm He/ 2.5 sccm Ar/ 1.5 sccm $N_2$ case. The relative signal to background ratio is even smaller for the 28 amu curve than the ratio for m/e=14. The shaded area represents the background signal. Fig. 3(b) shows a typical TOF spectrum taken over 100,000 cycles at m/e=14 for a 41.2 sccm He/ 2.5 sccm Ar/ 1.5 sccm $N_2$ supersonic plasma. This background signal arises from dissociative ionization of ground state $N_2$. (Table 1) The peak above the background represents the modulated plasma beam on its first entry in the chamber before wall scattering. In conventional mass spectrometry, where the signal is directly representative of the pressure in the analysis chamber, the beam would only contribute ~5% of the total signal compared to the background for the data in Fig. 3(b). In

determining the true intensity of the excited species by MBMS, some approximations must be made. The mass spectrometer is a density sensitive device, so faster moving molecules will get sampled for less time, producing a smaller signal. One must approximate the speed at which the active species are moving, which can be done by measuring the temperature of the plasma source, which is often not a trivial measurement. Assuming one has measured the temperature accurately, an effusive beam source should have a Boltzmann velocity distribution. If the plasma cools any beyond the temperature sampling region or if the supersonic jet source is not ideal (not all species velocities exactly the same), then MBMS will not accurately assess the true intensity of the active species. TOF measurements yield $v_s$, hence the necessary information to correctly assess beam intensity. The mass spectrometer signal intensity is not directly proportional to the flux intensity data (i.e., the flux intensity does not represent the area underneath the curves as shown in Figs. 6-7). The flux intensity data is acquired by first subtracting the background, then transforming the mass spectrometer signal intensity with a 1/t correction due to the density sensitive nature of the mass spectrometer. The resulting area under this curve would be the flux intensity.

## III. RESULTS AND DISCUSSION

OE spectra from a 80 W Ar/$N_2$ supersonic jet plasma plume are shown in Fig. 4(a). The lower spectrum represents a plume when only Ar is admitted to the nozzle. Emission lines at 697, 738, 750, 763, 772, 795, 800, 811, 826 and 840 nm are due to Ar. Addition of 1.5 sccm $N_2$ in 23 sccm Ar for plasma plume operation does not affect the Ar emission lines significantly. Small broad emission bands from 570 nm to 900 nm

representing the $N_2$ first positive (1+) series, which arises from $N_2(B^3\Pi_g) \rightarrow N_2(A^3\Sigma_u^+)$ transitions, are evident in the top spectrum. OE spectra from a 80 W He/Ar/$N_2$ supersonic jet plasma plume are shown in Fig. 4(b). The lower spectrum represents a plume where only He and Ar are admitted to the nozzle. Emission lines at 502, 587, 668, 707 and 728 nm are indicative of He. Emission lines at 697, 738, 750, 763, 772, 795, 800, 811, 826 and 840 nm are indicative of Ar. Addition of 1.5 sccm $N_2$ in the 41.2 sccm He and 2.5 sccm Ar gas mixture for plasma plume operation does not affect the He and Ar emission lines significantly. Broad emission bands from 570 nm to 900 nm representing the $N_2$ (1+) series are more prominent than in the $N_2$/Ar plume. The OES results demonstrate the presence of $N_2$(A) metastables in the plasma plumes and that the He/Ar plume contains a higher concentration of $N_2$(A) than the $N_2$/Ar plume. Emissions arising from the $N_2$ second positive series [$N_2(C^3\Pi_u) \rightarrow N_2(B^3\Pi_g)$] and the $N_2^+$ first negative series [$N_2^+(B^2\Sigma_u^+) \rightarrow N_2^+(X^2\Sigma_g^+)$] are negligible in both OE spectra [Fig. 4(a)-(b)]. If excited nitrogen atoms (N*) were present, an emission line at 821.6 nm would be observed. This peak is not detected; other emission peaks associated with N* overlap the 1+ series emission bands. Ground-state N atoms ($^4S$) may be present, but selection rules disallow any direct evidence via OES. Ground-state N atoms can recombine into $N_2(B)$, which transition to $N_2(A)$ emitting 1+ series peaks. Whereas OE spectra indicate $N_2(A)$ metastables are present in the plasma plume, the spectra cannot give direct evidence of ground-state N atoms.

The TOF method allows us to discriminate between beam and background contributions but does not allow us to directly determine which species [$N_2$(A), $N_2^+$ or $N_2$] contribute to the m/e=28 signal or which species [$N_2$(A), N, $N_2$, $N^+$ or N*] contribute

to the m/e=14 signal. APMS allows us to determine which species contribute to the m/e=4, 14, 28 and 40 signals in the mass spectrometer. Fig. 5 shows the TOF-APMS curves for m/e=40 and m/e=4 for the plasma off and on for 1.5 sccm $N_2$ in 2.5 sccm Ar and 41.2 sccm He. The intensities (fluxes) in Fig. 5 (Fig. 6, Fig. 7) are both corrected for the density sensitive nature of the detector. There is little difference between the plasma off and on conditions for 40 amu beyond the threshold for ground-state Ar ionization (15.8 eV, Table 1), except a slight increase in flux for the plasma on condition. Even though the signal drops off-scale for the plasma off condition below the threshold, there is a small but consistent signal down to 0 eV electron impact energy for the plasma on condition. This would indicate that there is a small concentration (~0.01%) of $Ar^+$ in the plasma beam. The lack of any shoulder in the data from the Ar ionization threshold energy down to the threshold energy of $Ar\left({}^2P^*_{3/2}\right)$( 4.2 eV) indicates there is not a significant contribution from Ar metastables. Fig. 5(b) shows the APMS curve for m/e=4 for the plasma off and on for 1.5 sccm $N_2$ in 2.5 sccm Ar and 41.2 sccm He. There is a small increase in the flux for the plasma on condition above the He ionization threshold (24.6 eV), just as there was for Ar. The small flux of ions detected below the He ionization threshold down to 0 eV electron impact energy result from $He^+$ ions in the beam. The lack of any shoulder in the data between the He ionization threshold (24.6 eV) down to the He($^3$S) ionization threshold (4.8 eV) indicates there is not a significant He($^3$S) density in the beam.

Table 1 indicates that there are three possible candidates [N, $N_2$(A) and $N_2$] for N atom signal generation in the mass spectrometer with threshold voltages of 14.5, 18.1 and 24.3 eV respectively. In addition, the beam portion of the m/e=28 signal would include

both $N_2$(A) and ground-state ionization products if the electron impact energy is 70 eV (Table 1), since these processes have threshold energies of 10.5 and 15.6 eV respectively. Fig. 6 is composed of flux intensity data for the plasma off and on states for 1.5 sccm $N_2$ seeded in 23 sccm Ar for electron impact energies of 0-70 eV. Flux intensities for m/e=28 over a range of 0 to 70 eV electron impact energy are displayed in Fig. 6(a). The TOF-APMS of the plasma discharge off and on appear similar, except for magnitude. There appears to be a small shift in electron energy (on the linear scale) which may indicate a small presence of $N_2(A)$ ionization contribution as the plasma on signal appears to go to 14 eV, slightly below the $N_2(X)$ dissociative ionization threshold energy. Fig. 6(b) shows that there is no detectable signal above the background for m/e=14 for electron energies less than 30 eV for the plasma off condition. There is a small signal from 26 eV to 28 eV (down to the dissociation ionization threshold) although it is (almost) indiscernible from the background. With the plasma discharge on, the m/e=14 signal begins at 16 eV, just above the ionization potential for a ground-state N atom. This is strong evidence of ground-state N atoms in the plasma, as this energy is below the thresholds for $N_2(A)$ and ground-state $N_2(X)$ dissociative ionization. $N_2(A)$ dissociative ionization is not ruled out as a contributing species (threshold at 18.1 eV) to the TOF-APMS curve for m/e=14, however it cannot be the primary component.

Fig. 7 shows the TOF-APMS flux intensity data for the plasma discharge off and on of a RFD-SSJ produced using 1.5 sccm $N_2$, 2.5 sccm Ar, and 41.2 sccm He. Flux intensities for 28 amu over a range of 0 to 70 eV electron impact energy are displayed in Fig. 7(a) for the $N_2$ seeded in the He/Ar beam. The TOF-APMS of the plasma discharge off and on appear similar, except for magnitude. There appears to be a small shift in

electron energy (from 11 eV to 16 eV) which likely indicates a small presence of $N_2$(A) ionization contribution. In addition, the nonzero signal at 0 eV indicates a detection of $N_2^+$. The overall flux intensity change for the m/e=28 signal is due to the change in $T_o$, which affects the beam dynamics and number of collisions in the supersonic jet, thus affecting the intensity. In addition, the number of collisions in a binary expansion will affect the degree of focusing/anti-focusing of molecules (focusing is the effect that describes the difference in downstream intensity due to radial spread of beam species due to mass difference in binary/tertiary expansions).[11] Fig. 7(b) shows that there is no detectable signal above the background for m/e=14 for electron energies less than 28 eV for the plasma off condition. There is a small signal at 26 eV [down to the $N_2$(X) dissociation ionization threshold], but it is indiscernible from the background as demonstrated by the TOF spectrum. With the plasma discharge on, the m/e=14 signal begins at 15 eV, just above the ionization threshold for ground-state N atoms. This is strong evidence for ground-state N atoms in the plasma, as this energy is below the thresholds for $N_2(A)$ and $N_2(X)$ dissociative ionization. $N_2(A)$ dissociative ionization is not ruled out as a contributing species (threshold at 18.1 eV) to the TOF-APMS curve for m/e=14, however it cannot be the primary component and substantial m/e=14 signals are produced at 15 and 16 eV.

The TOF-APMS curves in Figs. 6 and 7 demonstrate the presence of ground-state N atoms in the $N_2$/Ar and $N_2$/He/Ar RFD-SSJ for the plasma on condition. Determining a quantitative composition of the beam [N, $N_2^+$, $N_2$, and $N_2$(A)] requires knowledge of the cross sections of $\sigma_i$(E), electron impact ionization, of the processes in Table 1. The mass spectrometer count rate $\dot{N}(E)$ at electron impact energy $E$ is the sum of the count rates

for each process due to density $n_i$ of each species $I$ with electron ionization cross section $\sigma_i(E)$,

$$\dot{N}(E) = \sum_i C_i j_e n_i \sigma_i(E) \tag{4}$$

where $C_i$ is an instrumental constant, $j_e$ is the ionization current of the mass spectrometer, and $V_d$ is the volume of the ionization region. Ascribe $\beta = C_i j_e V_d n_i$ as a fitting constant yields

$$\dot{N}(E) = \sum_i \beta_i \sigma_i(E) \tag{5}$$

If each species dominates as the largest signal for a portion of the APM spectra, an accurate determination of $\beta_i$ can be achieved, hence yielding $n_I$ (proportional to $\beta_i$). In Fig. 6 and Fig. 7 it would appear the majority excited species in Ar/ $N_2$ and He/Ar/$N_2$ plasma beams would be ground state N atoms, with a minor contribution of $N_2^+$ and $N_2(A)$. Fig. 8 shows a fit for the m/e=28 TOF-APMS of a $N_2$ in He/Ar plasma beam. In logarithmic format, the TOF-APMS clearly shows at electron impact energies less than the threshold for ionization of $N_2$(A) (less than 10.5 eV), the signal arises from $N_2^+$ ions, in that with the plasma discharge on, there is a small but detectable signal at 0, 8, 9 and 10 eV. There is a small shoulder in the data at energies from 10 eV to 15 eV. This region is above the threshold for ionization of $N_2(A)$ (and includes the signal from $N_2^+$) but remains below the threshold for ionization of ground state $N_2$. This data from 11 to 14 eV can only include counts from $N_2^+$ or ionized $N_2$(A) as other excited species [such as $N_2$(B) and $N_2$(C)] possess radiative lifetimes much less than the flight time it takes to get to the mass spectrometer. Counts due to ions are subtracted (using 0 eV signal) from the count rate and consequently fit with electron impact ionization data for $N_2(A)$

$\rightarrow N_2^+$.[12] Data from 20 eV to 45 eV are used to fit to ground-state $\sigma_i(E)$, yielding an $\beta_{N_2(X)}$.[13,14] These fits produce an $N_2(A)$ contribution of 0.062% and an ion contribution of 0.016%. The $N_2(A)$ $\sigma_i(E)$ do not fit the data precisely as the TOF-APMS data has a steeper slope than that of the published cross section data.

Determining the dissociation fraction $\alpha$ of $N_2$ requires knowledge of cross sections of electron-impact ionization for $N \rightarrow N^+$ ($\sigma_1$), $N_2 \rightarrow N_2^+$ ($\sigma_2$) and $N_2 \rightarrow N^+ + N$ ($\sigma_3$).[15-19] The dissociation fraction

$$\alpha = R/(R+2) \tag{6}$$

where $R \equiv [N]/[N_2]$, the ratio of concentrations of species in the detector. Measuring the intensity of $N^+$ and $N_2^+$ with the plasma off ($\eta \equiv N^+/N_2^+$) and plasma on ($\rho \equiv N^+/N_2^+$), we get

$$R = (C_2/C_1)(\sigma_2/\sigma_1)(\rho - \eta) \tag{7}$$

where $C$ is the mass spectrometer transmission probability. $C_2/C_1$ is approximated as $C_2/C_{NH_3} \sim 1.14$,[8] since N and $NH_3$ are similar in mass. Fig. 9 illustrates $\eta$ and $\alpha$ as functions of E for both a $N_2$ in Ar supersonic plasma beam and a $N_2$ in He/Ar supersonic plasma beam. $\eta$ was determined by averaging a number of APMS curves including $N_2$ in He/Ar, $N_2$ in Ar, and background $N_2$ (which all agreed well). $\eta$ drops to zero around 28 eV since the threshold voltage for ground state dissociation ionization is 24.3 eV, and it saturates to ~3.57% at 70 eV. $\alpha$ remains at ~5.6% for $N_2$ in Ar and at 2% for $N_2$ in He/Ar, both measurements independent of electron impact energy, giving confidence in the use of cross sections for electron-impact ionization.

We measured $\alpha$ for $N_2$ in He/Ar supersonic plasma beams and $N_2$ in Ar supersonic plasma beams as a function of %$N_2$ seeded in the beam.(Fig. 10) Addition of

$N_2$ in the beam decreases α (concurrently for $N_2$ in Ar and $N_2$ in He/Ar) likely resulting from a decrease in plasma temperature. Additional measurements were made at electron impact energies below the $N_2(X)$ dissociative ionization threshold (at 23 eV) to establish confidence in the data. $N_2$ seeded in Ar beams yielded higher α than $N_2$ seeded in He/Ar. Whether the molecular dynamics of the expansion of $N_2$/Ar versus $N_2$ in He/Ar (probability of N atom recombination), He acting as a high energy electron sink in the plasma expansion, or the resonance time of N species in the continuum region of the expansion [N has a longer resonance time in Ar than He/Ar (Figs. 11 and 12)] is the primary reason for the difference in $\alpha$ for the two types of plasma beams is unknown.

Figs. 11 and 12 shows experimental TOF curves (after background subtraction) for $N_2$/Ar and $N_2$/Ar/He RFD-SS jets along with the fit of the data to eq. (1). Fig. 11(a) shows the TOF spectrum of m/e=40 at 70 eV electron impact energy for a $N_2$/Ar plasma expansion. The fit is applied to the short-time side of the peak and about the top third of the long-time side of the peak, yielding $S$=3.5 and $v_s$=965 m/s. The long tail of the peak is believed to be due to scattering in the QMS ionizer.[20] Fig. 11(b) shows the TOF spectrum of m/e=28 at 23 eV for a $N_2$/Ar plasma expansion. A fit of this data yields $S$=3.2 and $v_s$=981 m/s, quantities similar to Ar. Fig. 11(c) shows the TOF spectrum of m/e=14 at 23 eV for a $N_2$/Ar plasma expansion. This spectrum cannot include $N_2(X)$ dissociation ionization products as it is below the threshold of that process. It is a combination of ionization of N atoms and dissociative ionization of $N_2(A)$. In order to get an accurate understanding of which species directly contribute to this TOF spectrum we would need to know $\sigma_i$ of both processes $N_2(A) \rightarrow N^+$ and $N \rightarrow N^+$. Unfortunately, there is no cross section data available for $N_2(A) \rightarrow N^+$. The fit in Fig. 8, however, gives

a good approximation of the $N_2(A)$ concentration. Fig. 9 demonstrated the percentage of N atoms present in the beam. Thus, the TOF spectrum in Fig. 11(c) should be primarily N atoms. A fit of the data shows that N atoms from the expansion have $S$=3.6 and $v_s$=1138 m/s. The speed ratio is similar to that of $N_2$ and Ar, but the velocity is about 20% greater. $T_{ll}$ of this $N_2$/Ar plasma expansion are low ($T_{ll}$ =84-188 K) but not quite ideal ($T_{ll}$~0).

Fig. 12(a) shows the TOF data for a $N_2$/Ar/He RFD-SS jet taken at 70 eV electron impact energy (m/e=28) and the fit ascribed to the data. With 70 eV electron impact energy, this data would include contributions from $N_2(X)$ ionization, $N_2(A)$ ionization, and $N_2^+$. The fit to eq. (1) minimizes the error from the left side of the peak (low time-of-flight, high velocity) to about halfway down the right side of the peak. The low-energy (high time-of-flight) tail of the peak is not included in the fit, as it is attributed to scattering in the ionization volume.[17] The speed ratio and stream velocity of the $N_2$ molecules are 1.39 and 1230 m/s, respectively. Using eq. (2), $T_{ll}$ = 1326 K, which is similar to $T_o$ = 1376 K measured by pressure rise. Consequently, there appears to very little cooling of the $N_2$ molecule in the supersonic jet (normally $T_{ll} \sim 0$ in a supersonic beam).

Fig. 12(b) shows the data for m/e=14 and the fit applied to the data. This data was taken at 23 eV impact energy, where only ground-state N atom ionization and excited state dissociative molecular nitrogen ionization can occur. We concluded from Figs. 6-9 that the majority species contribution is N atoms at 23 eV. Consequently, the data shown in Fig. 12(b) only show N atoms and thus do not include the $N_2(X)$ ionization products. Fitting this data yields an $S$=2.08 and $v_s$=1924 m/s for the N atoms. The entire

peak was employed for minimization of eq. (1) as there appears to be minimal scattering (N atoms are active enough to react with wall surfaces.)[3,4,5] Using eq. (2), $T_N$ = 720 K, which is significantly cooler than $T_o$ or $T_{N2}$. The fact that the N atom has a tighter velocity distribution than $N_2$ is not surprising. A major factor in the breadth of the velocity distribution is the last collisions that each species undergoes before entering the free molecular region of the supersonic jet. The fact that the N atoms are faster than the $N_2$ molecules in a supersonic jet by a significant factor points to two different explanations. One possibility is that both N atoms and $N_2$ molecules do reach about the same velocity; however, because $N_2$ molecules have a larger cross section, they are more likely to experience collisions and thus obtain a lower energy. Another possibility is that N atoms are energized in the free jet region of the expansion by high energy ions or electrons and consequently include a higher energy from that impact. This brings about the most interesting question about the RF-discharge source. Are the N atoms produced in the high-pressure region of the nozzle and can only remain energized in the expansion of the supersonic free jet by the energetic collision by ions / electrons? This would seem to be a likely possibility as the cold mode does produce a discharge within the nozzle tube, but not a plume in the supersonic jet expansion. The cold mode shows no production of N atoms. (Table 3)

Fig. 12(c) shows the data and fit for the m/e=4 signal at 70 eV. The fit yields an $S$=0 and $v_s$=0 m/s, demonstrating the He species is mostly similar to an effusive source. The fit minimized the error for whole peak. We could not get an $S$ low enough to make the fit wide enough to incorporate the data. TOF measurements of other sources have shown effusive sources that cannot incorporate the full width of the data, i. e. the velocity

distribution is wider than that predicted by a Boltzmann distribution. In fact, high-temperature source data taken by Shimada et al.[18] has the same skewed fit as we do in Fig. 12(c), where the data is wider than the fit and the tail is over-predicted. One may consider that the gating function of the chopper might provide this distortion in the data; however, the gating function had been taken care of properly in pure beam measurements and fit well with that TOF data.

Fig. 12(d) shows the TOF data and fit for the m/e=40 signal at 70 eV. The fit minimizes the data from the left side of the peak to about a quarter of the way down on the right side of the peak. The long time scattering tail is ignored for this fit just as it was for the m/e=28 signal. The fit yielded an $S = 1.70$ and a $v_s = 1251$ m/s. Using eq. (2), we get a $T_{Ar} = 1305$ K, which is not that much cooler than the initial condition, $T_o = 1376$ K. $T_{Ar}$ and $T_{N2}$ as well as $v_{s,Ar}$ and $v_{s,N2}$ are both very similar in value, which could be expected as their cross sections are fairly similar,[9] so there final conditions should not be that different.

Table 2 summarizes the TOF-APMS data for four different $N_2$ flow rate conditions in 41.2 sccm He and 2.5 sccm Ar along with a room temperature (plasma-off) supersonic jet. As seen in Figs. 11-12, the TOF-APMS data is fit to eq. (1) minimizing the error of the fit to the peaks to get $S$ and $v_s$ for each component. Scattering tails are truncated from the fit (as in Figs. 11-12) and N atoms measurements are acquired at 23 eV so that only N atoms are measured, not a combination of N atoms and ground state dissociative ionization products. Pressure rise calculations yield $T_o$ (first column). $T_o$ is converted to energy by

$$E = C_{p,avg} T_o \qquad (8)$$

This energy should describe the full energy of the beam. An ideal supersonic jet attains hyperthermal energies, which is governed by

$$E_{N_2} = \left(\frac{W_{N_2}}{\overline{W}}\right) R \left(\frac{\gamma}{\gamma - 1}\right) T_o \qquad (9)$$

where the energy is determined by the average molecular weight $\overline{W}$, the stagnation temperature $T_o$, and the specific heat ratio $\gamma$.[9] In an ideal supersonic jet, all enthalpy is converted to kinetic energy, with $T_i \rightarrow 0$, thus leaving no thermal energy in the beam. In real systems, there is going to be a velocity spread in the beam, resulting in a non-infinite $S$. The energy balance should be[22]

$$C_{p,avg} T_o = \sum_i \frac{1}{2} x_i m_i v_s^2 + \sum_i x_i C_{p,i} T_i \qquad (10)$$

We can get $v_s$ from the fit of the TOF-APMS data. $T_i$ arises from eq. (1)-(2) ($x_i$ is the mole fraction). Table 2 displays the results of the fits and converts them into kinetic and thermal energy [respectively, the 1st and 2nd terms in right hand side of eq. (10)]. To be more specific, the thermal energy term in eq. (10) is broken down into translational and rotational (which only pertains to $N_2$) energies. We can assume translational temperature is the parallel temperature that is measured by TOF-APMS. The rotational temperature does not necessarily equal the parallel temperature. Typically, in free jet expansions, the rotational temperature does not cool as fast as the translational temperature.[9] Our approximation of rotational temperature is to assume that there is no rotational cooling in the expansion, thus we assume $T_o = T_R$. Taking into account the rotational energy, thermal energy and kinetic energy, as measured by TOF-APMS, we calculate the energy on the right hand side of eq. (10). Most data points agree fairly well between the left-hand side and right-hand side calculations.

Table 3 summarizes the TOF-APMS data for $N_2$/Ar expansions. There are a few differences between $N_2$/Ar and $N_2$/He/Ar expansions. The speed ratios are much higher for $N_2$/Ar expansions ($S$=3-4) than $N_2$/He/Ar expansions. There is less of a difference between velocities of N atoms and the rest of the species in expansion for $N_2$/Ar expansions. Fig. 13 shows the relationship between the measured temperature of the plasma discharge source and the flow rate of $N_2$ in the source, $Q_{N2}$. Independent of flow rate, the energy balance does not close well for the $N_2$/Ar plasma expansion [Fig. 13(a)]. Using TOF spectrum, the temperature is measured to be about 300 K lower than it is measured by the pressure drop method. There is not much trend in temperature vs. $Q_{N2}$ for $N_2$/Ar plasma expansions. In general, the temperature of the plasma source decreases as $Q_{N2}$ increases for $N_2$/He/Ar plasma expansions. [Fig. 13(b)] Both the temperatures measured by pressure rise in the nozzle and by TOF-APMS fall with $Q_{N2}$. One explanation for this cooling could be that the higher $Q_{N2}$ provides a larger energy sink (breaking $N_2$ into N) of energy, reducing the temperature of the plasma. In Table 2, the cooling trend occurs for all species, N, $N_2$, Ar and He with increasing $Q_{N2}$. All species in the expansion experience an increase in $S$ with increasing $Q_{N2}$. This increase in $S$ could occur because the decrease in temperature of the source allows more collisions before entering the free molecular region of the jet (molecular dynamics) or that the cross section of $N_2$ increases the number of collisions a fraction enough to change the speed ratios.

## IV. CONCLUSIONS

Use of the combination of TOF and APMS guarantees direct detection of excited species from a molecular beam source by eliminating background contributions from the detection chamber and also selectively detecting specific ionization processes. In our $N_2$ in He/Ar supersonic RF plasma source, we choose an electron impact energy that can only ionization ground state N atoms and cannot dissociatively ionize ground state $N_2$. By using the TOF-APMS method, we provide a unique method of filtering and characterizing a plasma supersonic jet source to prove that the source primarily emits N atoms as the active species.

## REFERENCES


[1]D. C. Jordan, I. S. T. Tsong, David J. Smith, B. J. Wilkens, and R. B. Doak, Appl. Phys. Lett. **77**, 3030 (2000).

[2]H. Singh, J. W. Coburn, and D. B. Graves, J. Vac. Sci. Technol. A **18**, 299 (2000).

[3]W. M. M. Kessels, M. C. M. van de Sanden, and D. C. Schram, J. Vac. Sci. Technol. A **18**, 2153 (2000).

[4]S. F. Adams and T. A. Miller, Plasma Sources Sci. Technol. **9**, 248 (2000).

[5]H. Singh, J. W. Coburn, And D. B. Graves, J. Appl. Phys. **88**, 3748 (2000).

[6]A. Sellidj, B. A. Ferguson, T. J. Mattord, B. G. Streetman, and C. B. Mullins, Appl. Phys. Lett. **68**, 3314 (1996).

[7]J. E. Pollard, Rev. Sci. Instrum. **63**, 1771 (1992).

[8]W. W. Macalpine and R. O. Schildknecht, Proc. Inst. Rad. Eng. **47**, 2099 (1959).

[9]D. R. Miller, in *Atomic and Molecular Beam Methods*, edited by G. Scoles (Oxford, New York, 1988), Vol. 1., pp. 14-53.

[10]D. Rapp, P. Englander-Golden, and D. D. Briglia, J. Chem. Phys. **42**, 4081 (1965).

[11]P. K. Sharma, E. L. Knuth and W. S. Young, J. Chem. Phys. **64**, 4345 (1976).

[12]P. B. Armentrout, S. M. Tarr, A. Dori, and R. S. Freund, J. Chem. Phys. **75**, 2786 (1981).

[13]T. D. Mark, J. Chem. Phys. **63**, 3731 (1975).

[14]Y. Itikawa, M. Hayashi, A. Ichimura, K. Onda, K. Sakimoto, K. Takayanagi, M. Nakamura, H. Nishimura, and T. Takayanagi, J. Phys. Chem. Ref. Data, **15**, 985 (1986).

[15]D. Rapp, P. Englander-Golden, and D. D. Briglia, J. Chem. Phys. **42**, 4081 (1965).

[16]A. Crowe and J. W. McConkey, J. Phys. B: Atom. Molec. Phys. **6**, 2108 (1973).

[17]E. Brook, M. F. A. Harrison, and A. C. H. Smith, J. Phys. B: Atom. Molec. Phys. **11**, 3115 (1978).

[18]P. C. Cosby, J. Chem. Phys. **98**, 9544 (1993).

[19]B. Van Zyl and T. M. Stephen, Phys. Rev. A **50**, 3164 (1994).

[20]L. Q. Xia, M. E. Jones, N. Maity, and J. R. Engstrom, J. Vac. Sci. Technol. A **13**, 2651 (1995).

[21]T. Shimada, J. Koide, K. A. Cho, and A. Koma, J. Vac. Sci. Technol. A **17**, 615 (1999).

[22]D. R. Miller and D. F. Patch, Rev. Sci. Instrum. **40**, 1566 (1969).

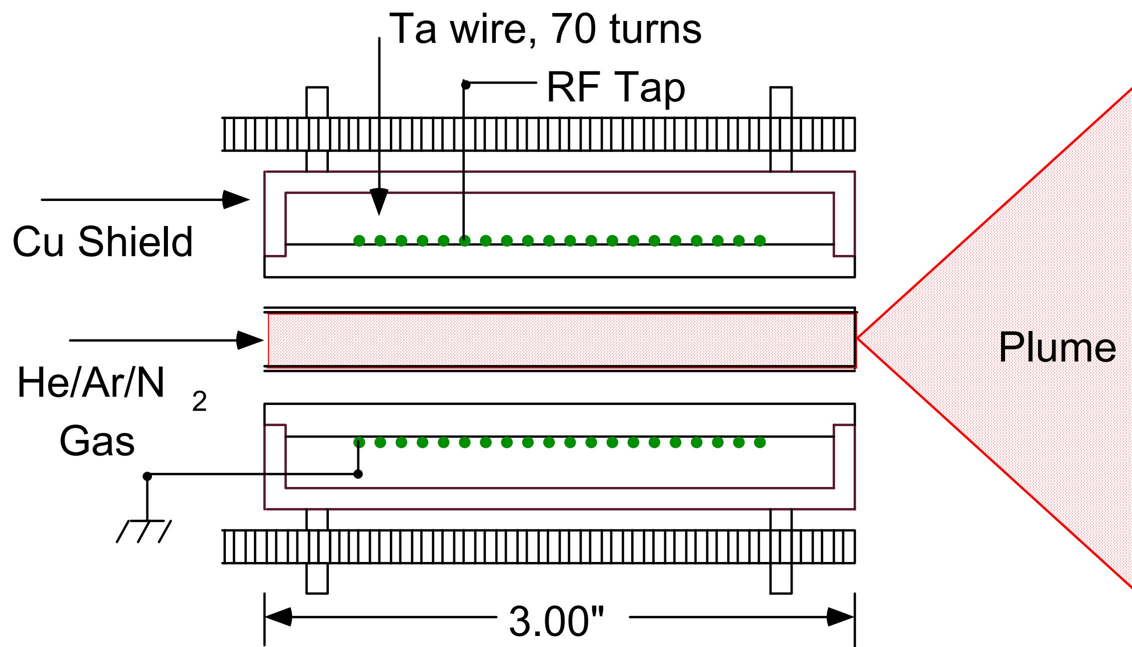


**Figure 1:** Schematic diagram of supersonic plasma jet nozzle.

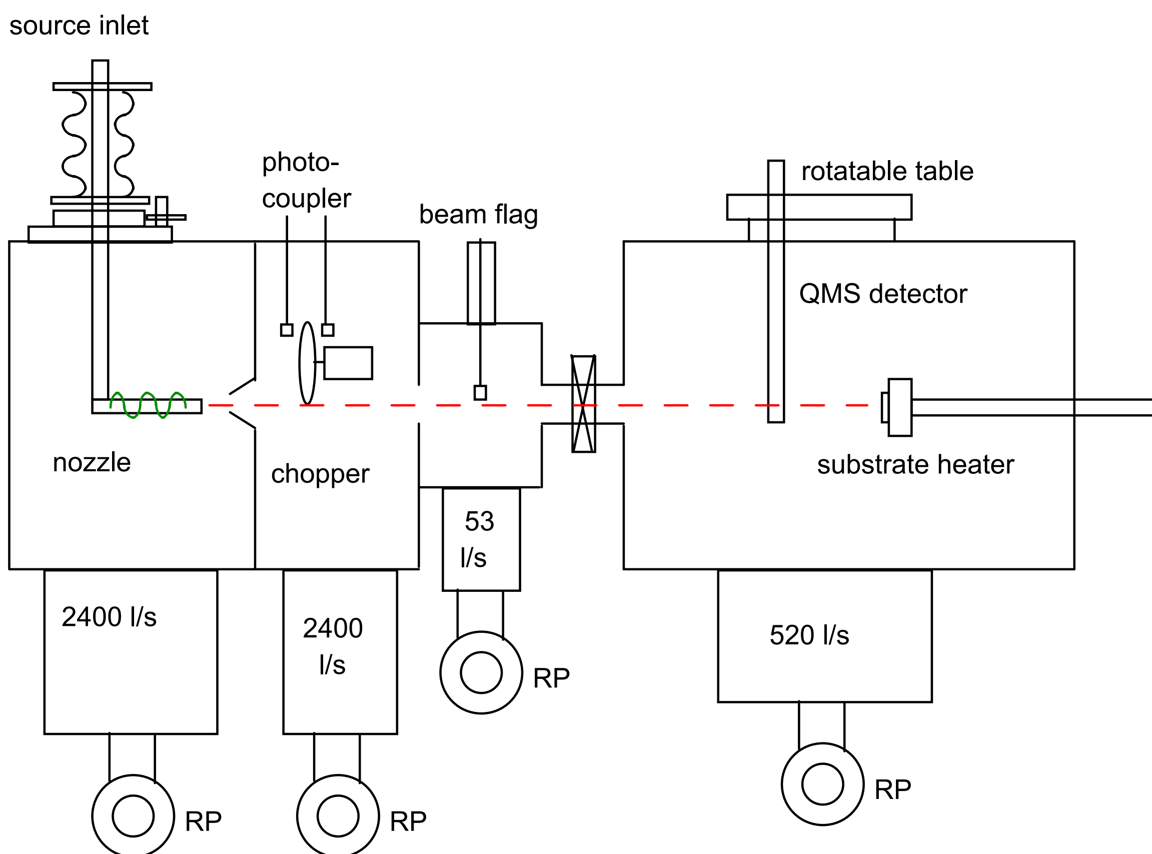


**Figure 2:** TOF-APMS system with attached supersonic jet RF plasma source.

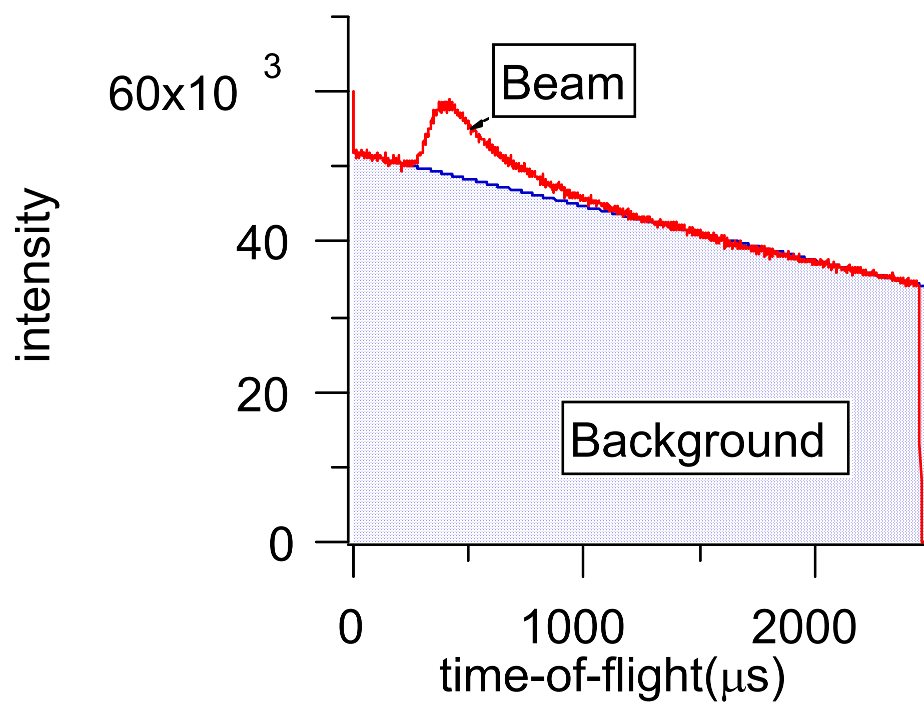


**Figure 3(a):** TOF spectrum for m/e = 28; 1.5 sccm $N_2$ in 2.5 sccm Ar and 41.2 sccm He.

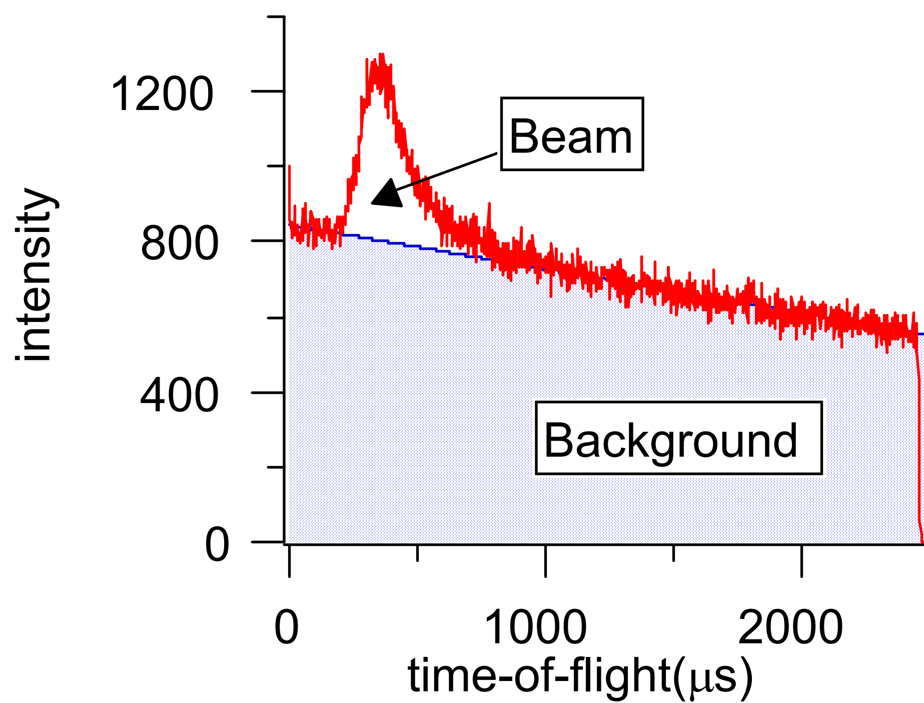


**Figure 3(b):** TOF spectrum for m/e= 14; 1.5 sccm $N_2$ in 2.5 sccm Ar and 41.2 sccm He.

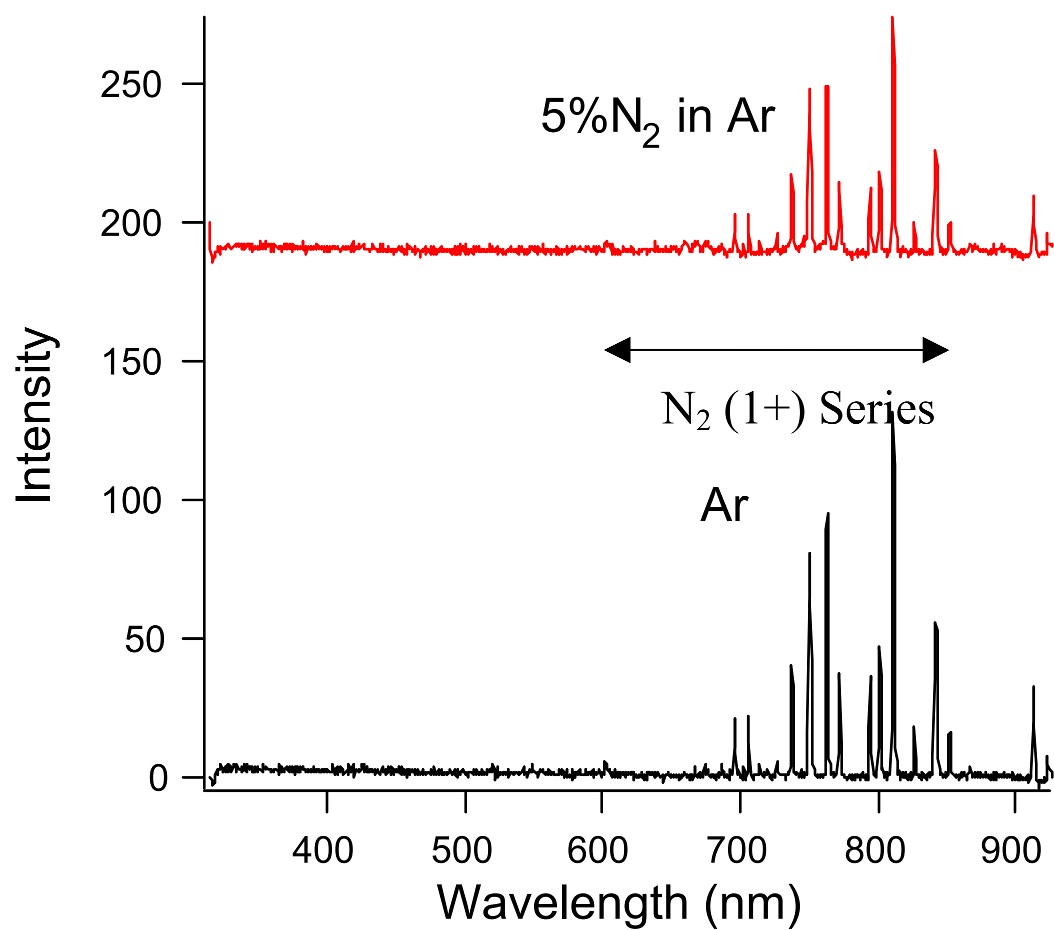


**Figure 4(a):** OES spectra of 1.5 sccm $N_2$ in 23 sccm Ar and Ar only gas flow (~150 Torr).

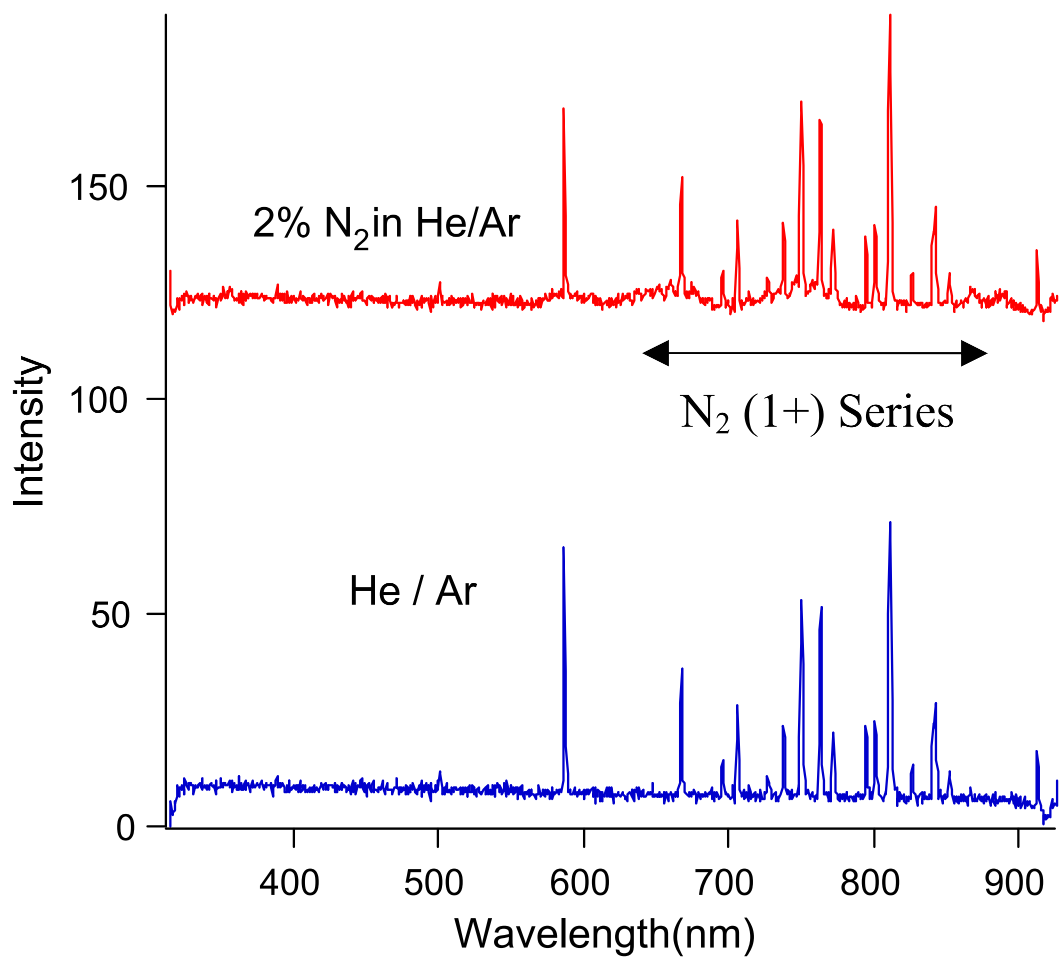


**Figure 4(b):** OES spectra of 1.5 sccm $N_2$ in He/Ar and He/Ar only gas flow (~150 Torr).

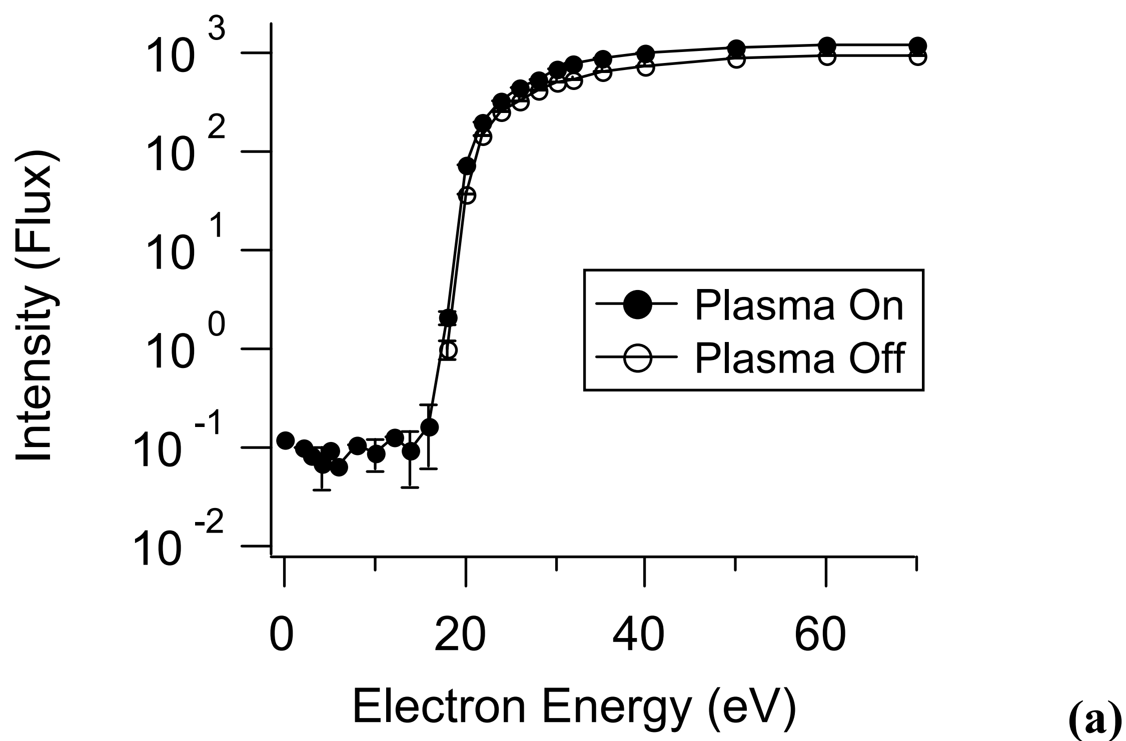


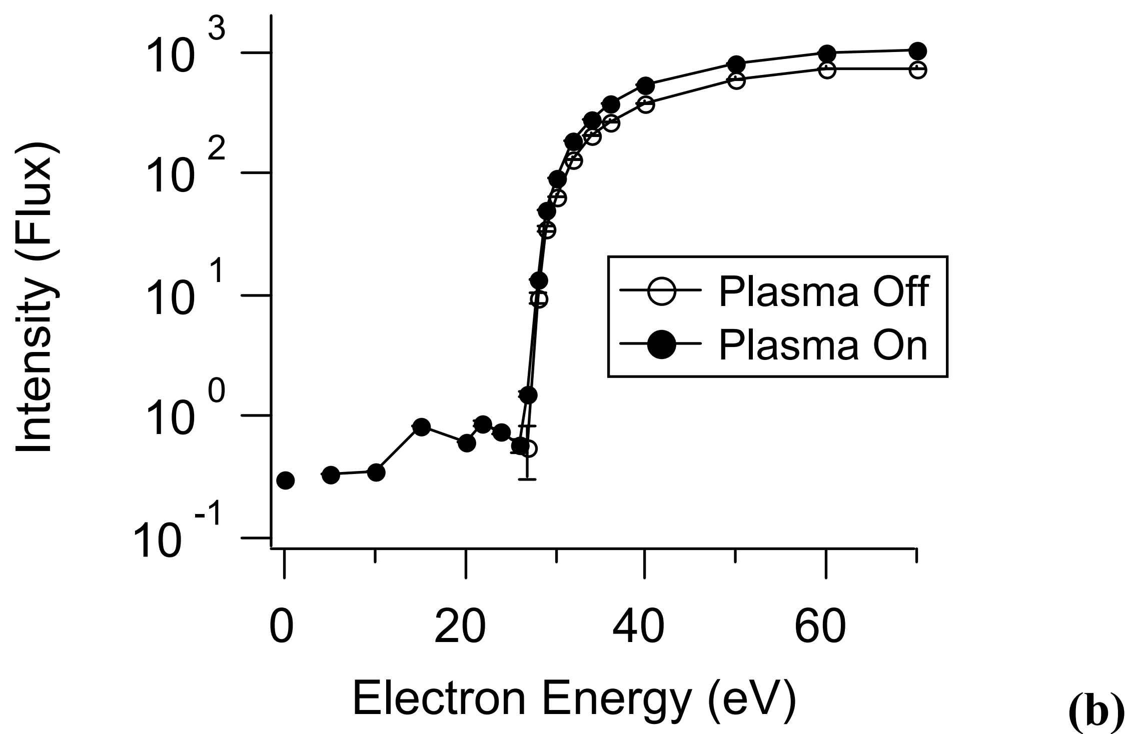


**Figure 5**: TOF-APMS curves for (a) m/e = 40 and (b) m/e = 4 for 1.5 sccm $N_2$ in 2.5 sccm Ar and 41.2 sccm He.

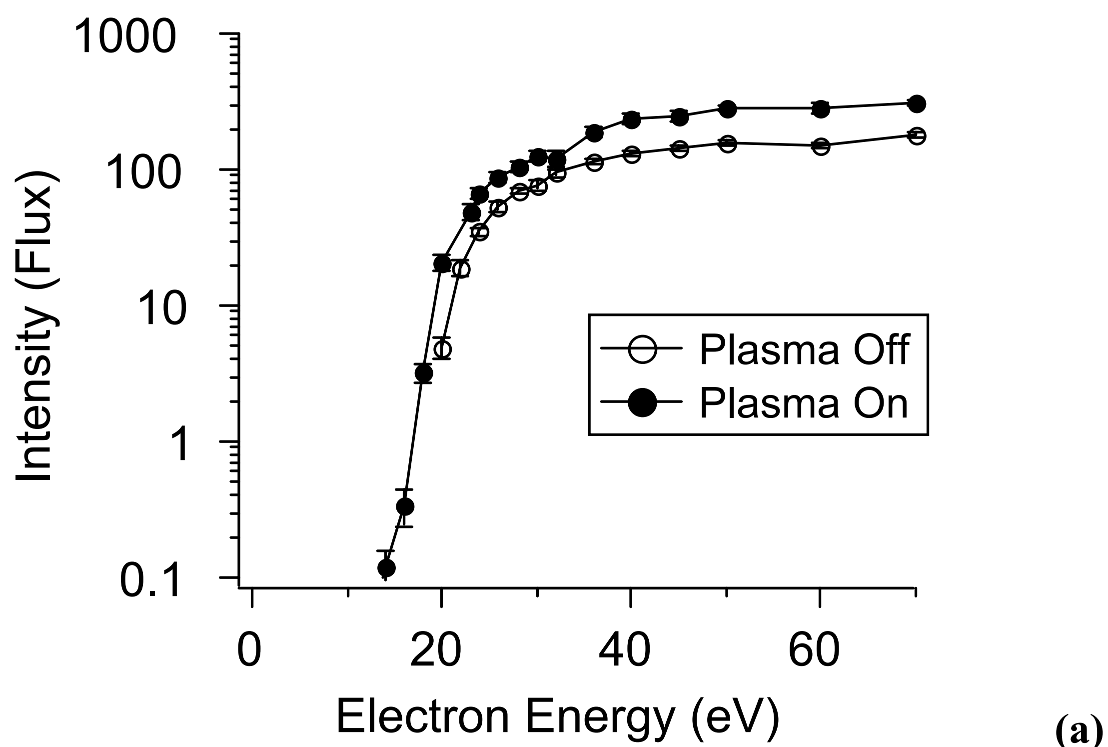


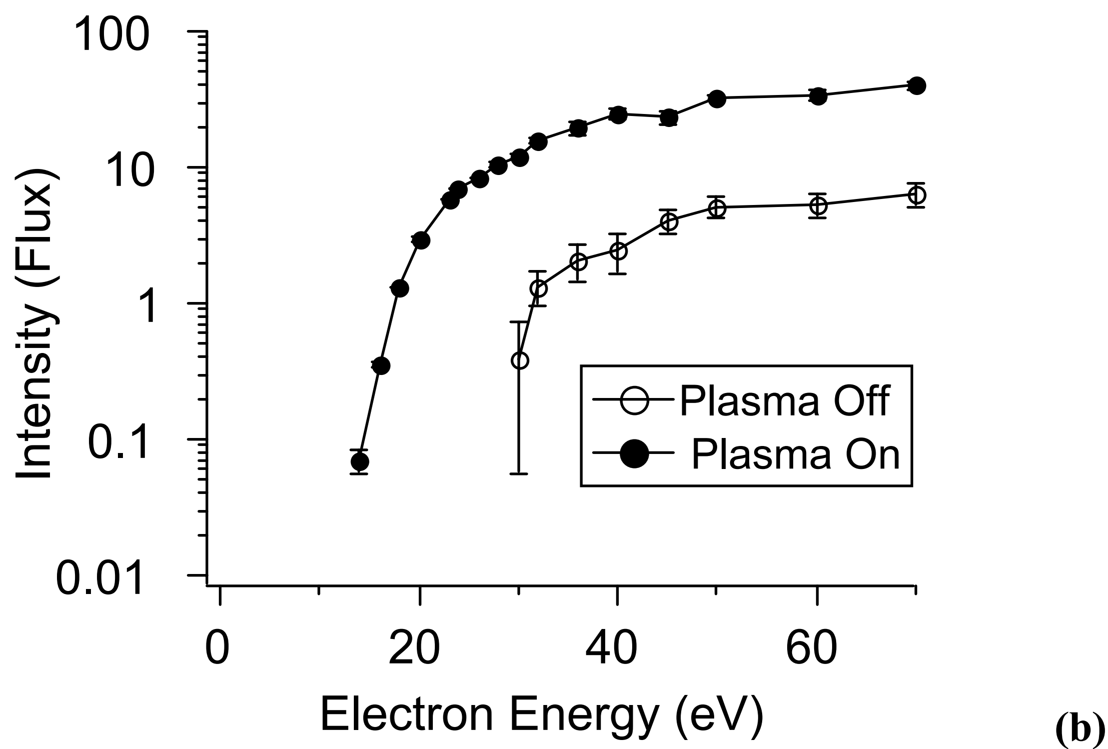


**Figure 6: (a)** TOF-APMS of 1.5 sccm $N_2$ in 23 sccm Ar, m/e=28. **(b)** TOF-APMS of 1.5 sccm $N_2$ in 23 sccm Ar, m/e=14.

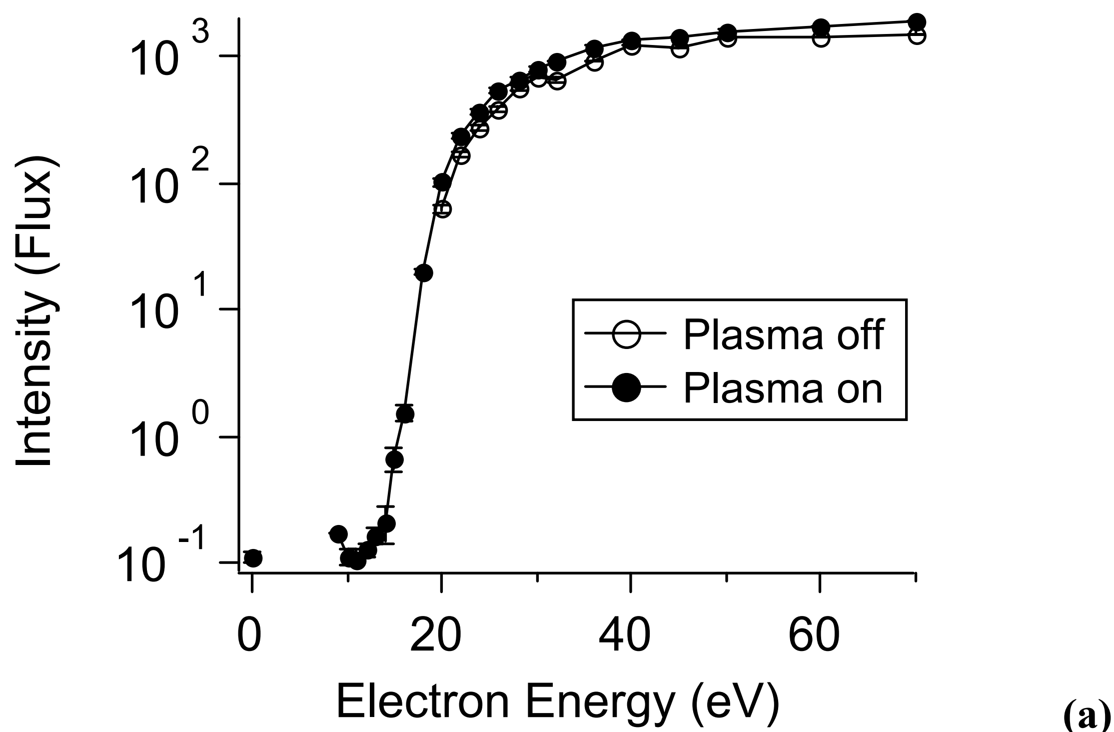


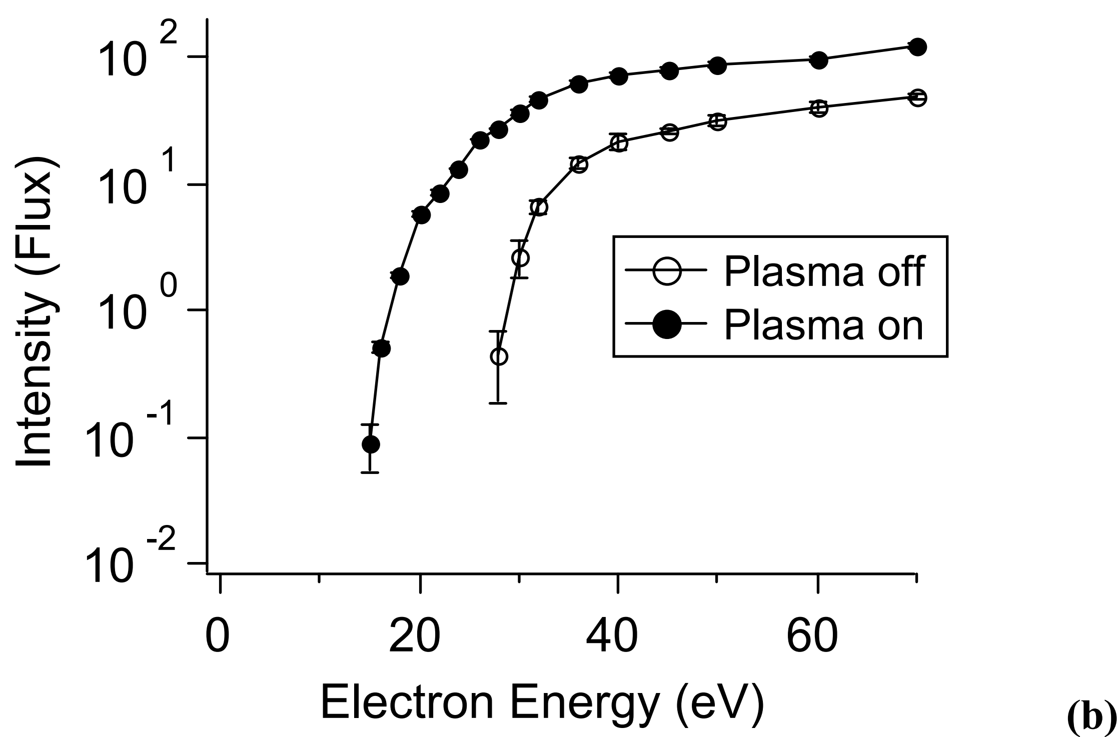


**Figure 7**: **(a)** TOF-APMS of 1.5 sccm $N_2$ in 2.5 sccm Ar and 41.2 sccm He, m/e=28. **(b)** TOF-APMS of 1.5 sccm $N_2$ in He/Ar, m/e=14.

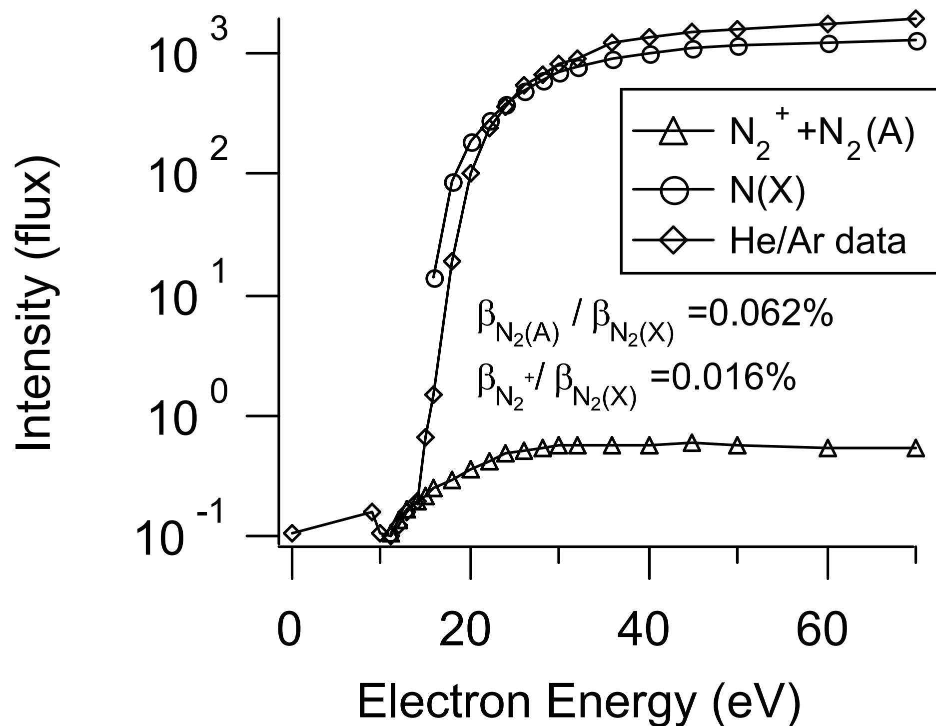


**Figure 8:** TOF-APMS of 1.5 sccm $N_2$ in He/Ar, m/e= 28. Data is fit to cross sections for $N_2$(A) to determine the percentage concentration.

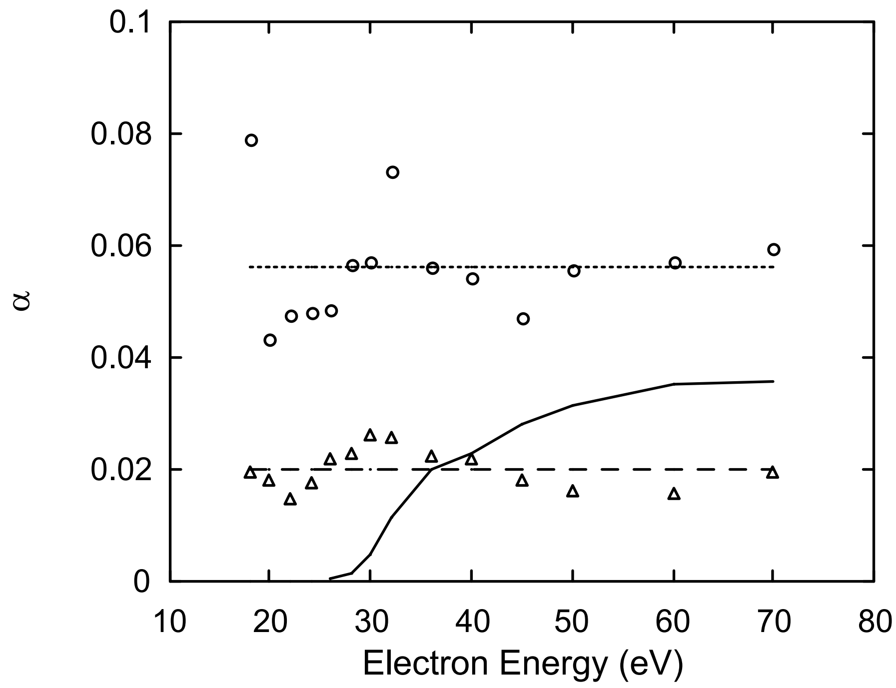


**Figure 9:** Calculation of η and α for ○ 6.7% $N_2$ in Ar and △ 4% $N_2$ in He/Ar vs. electron energy (eV). Dashed lines represent average values over the range of electron energies.

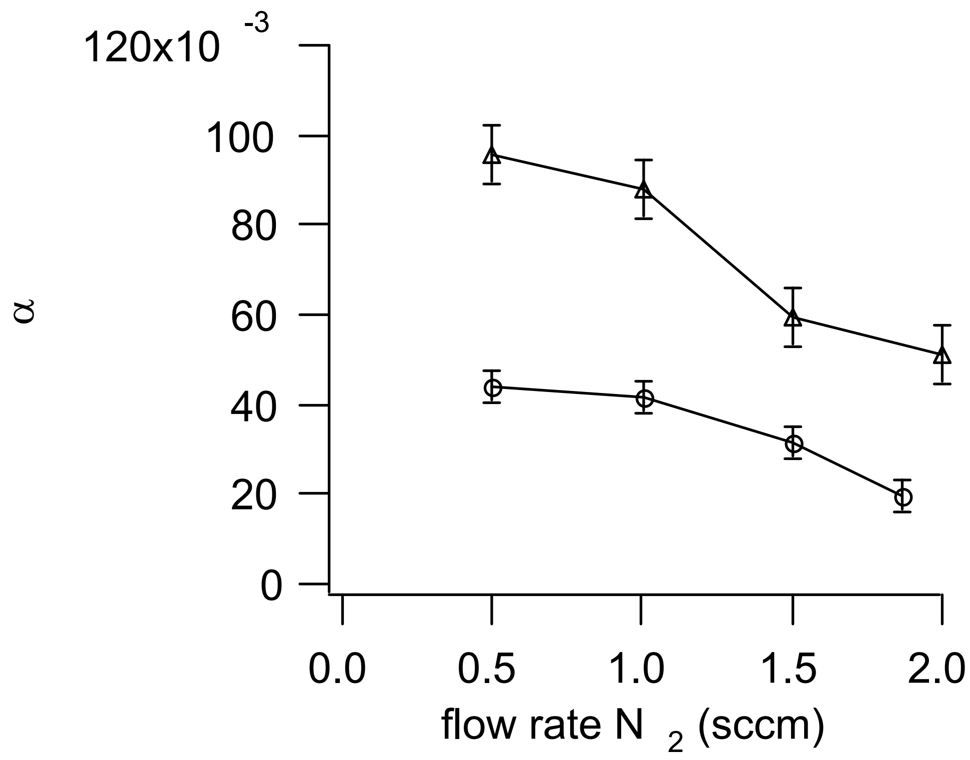


**Figure 10:** Dissociation fraction vs. %$N_2$. ○ $N_2$ in 41.2 He/2.5 Ar @ 70 eV; △ $N_2$ in Ar @ 70 eV.

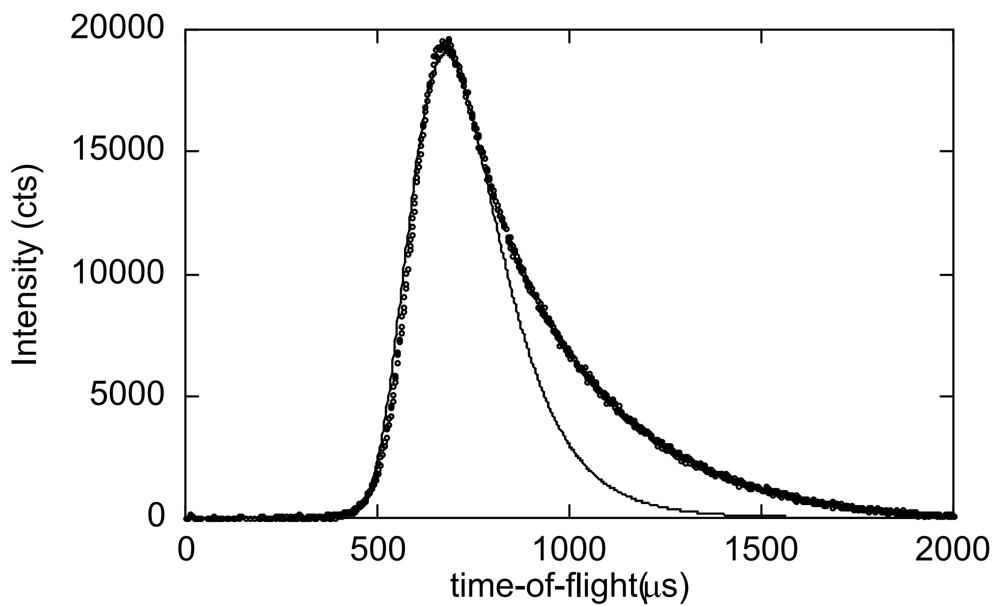


**Figure 11(a)**: TOF of an 80 W, 1.5 sccm $N_2$ in 23 sccm Ar expanision; m/e=40 signal at 70 eV.

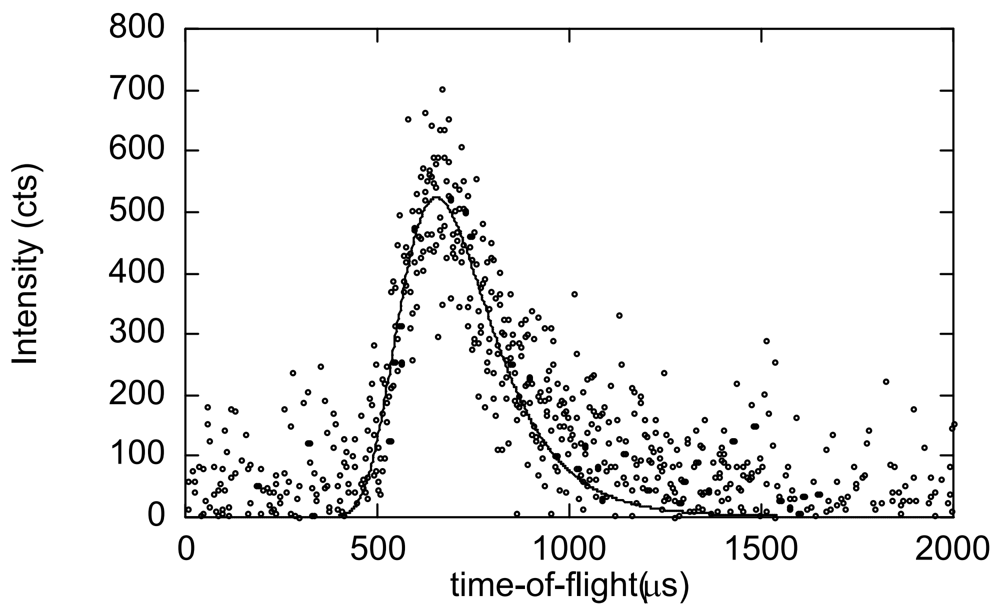


**Figure 11(b)**: TOF of an 80 W, 1.5 sccm $N_2$ in 23 sccm Ar expanision; m/e=28 signal at 23 eV.

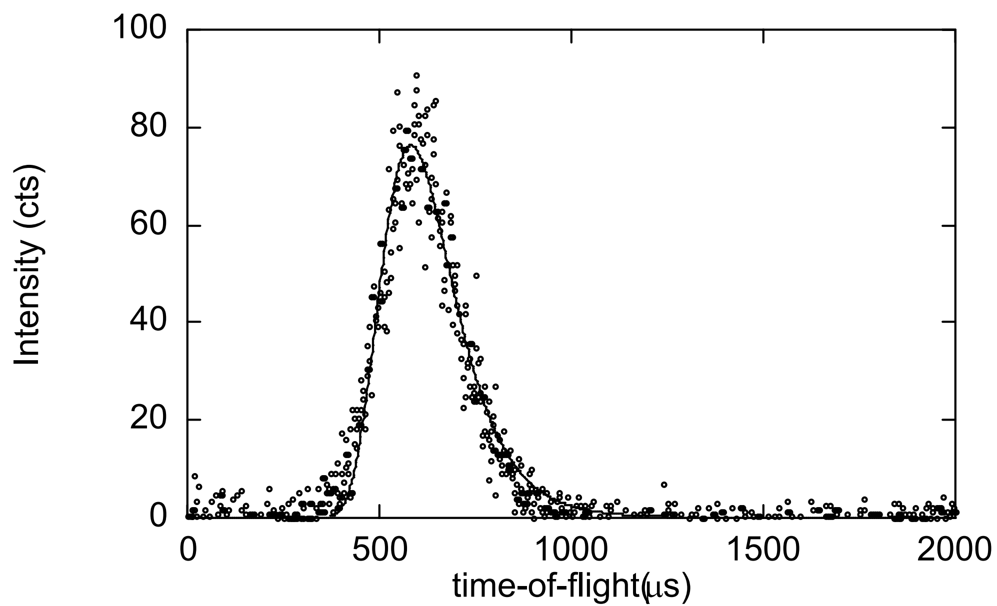


**Figure 11(c)**: TOF of an 80 W, 1.5 sccm $N_2$ in 23 sccm Ar expanision; m/e=14 signal at 23 eV.

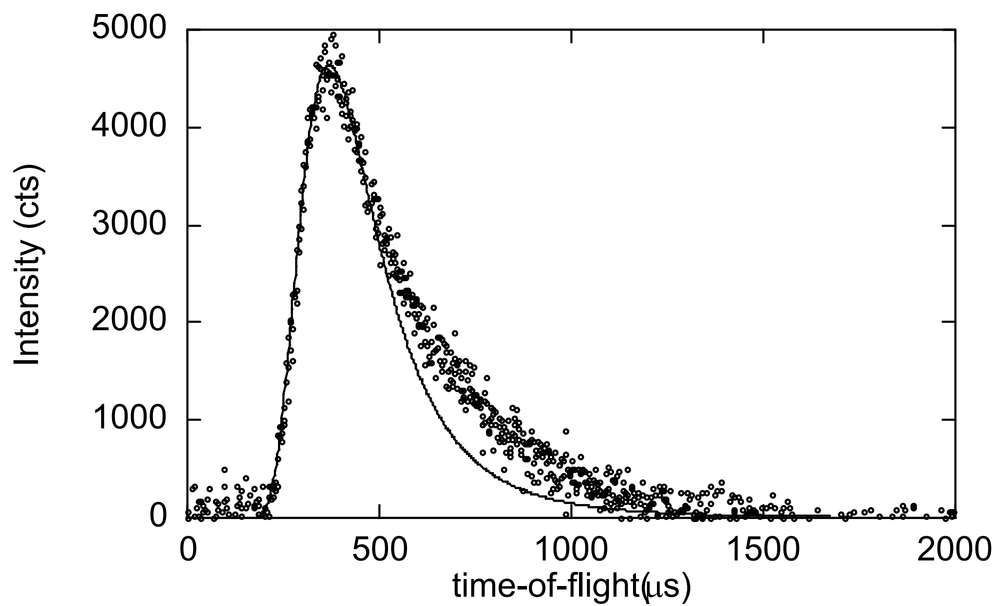


**Figure 12(a):** TOF data from a 80-W, 1.5 sccm $N_2$ in 2.5 sccm Ar and 41.2 sccm He plasma supersonic jet. m/e=28 and at 70 eV electron impact energy.

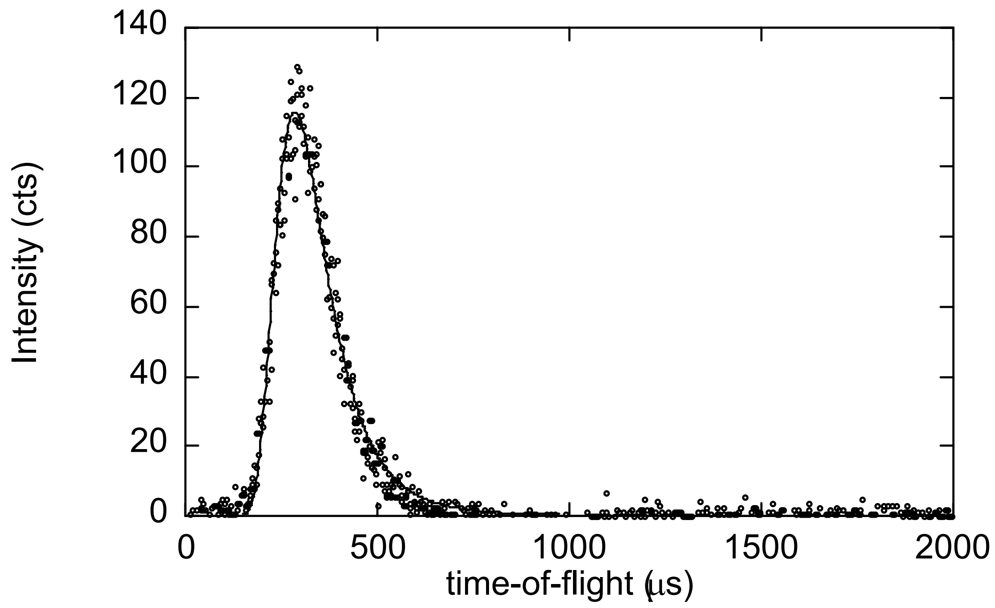


**Figure 12(b)**: TOF data from a 80-W, 1.5 sccm $N_2$ in 2.5 sccm Ar and 41.2 sccm He plasma supersonic jet. m/e=14 and at 23 eV electron impact energy.

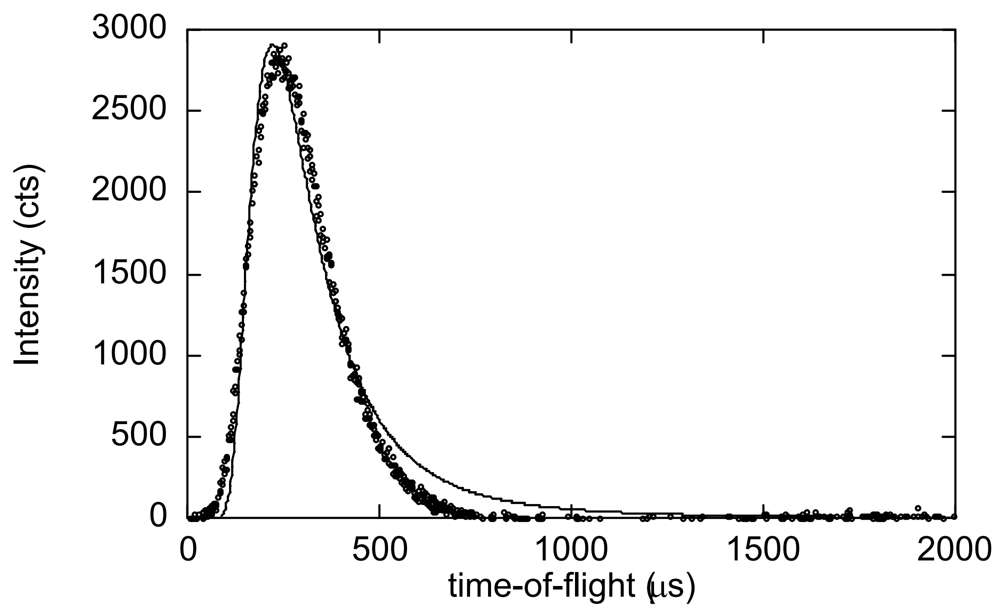


**Figure 12(c)**: TOF data from a 80-W, 1.5 sccm $N_2$ in 2.5 sccm Ar and 41.2 sccm He plasma supersonic jet. m/e=4 and at 70 eV electron impact energy.

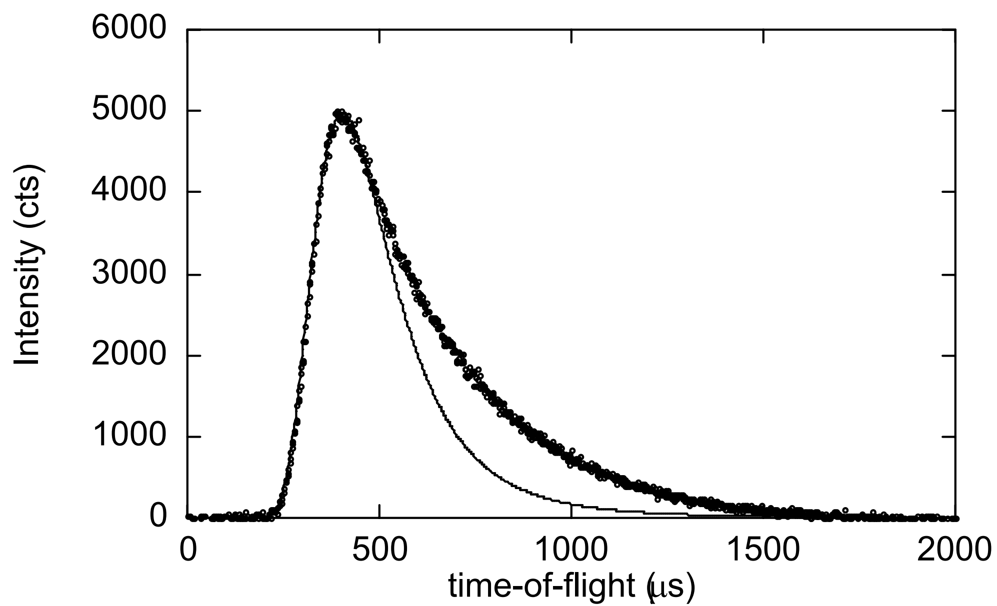


**Figure 12(d)**: TOF data from a 80-W, 1.5 sccm $N_2$ in 2.5 sccm Ar and 41.2 sccm He plasma supersonic jet. m/e=40 and at 70 eV electron impact energy.

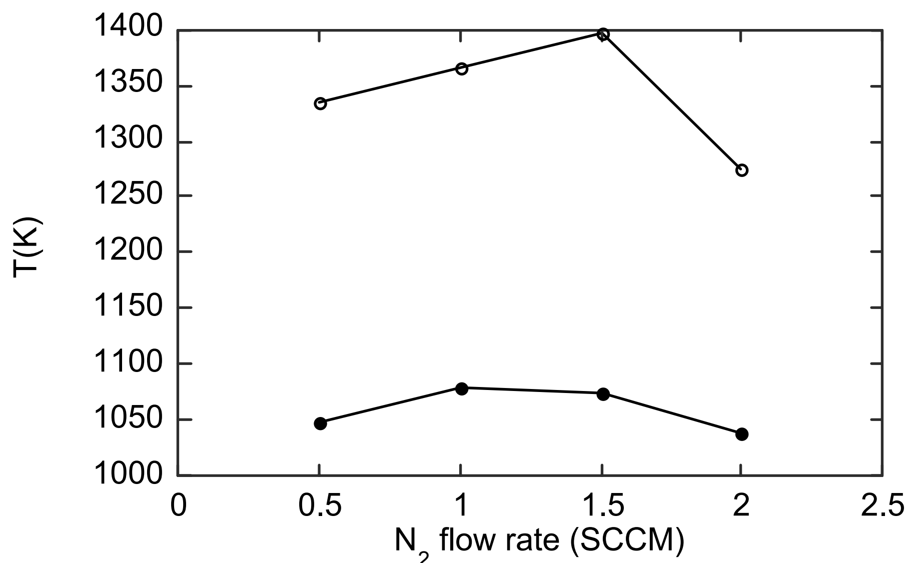


**(a)**

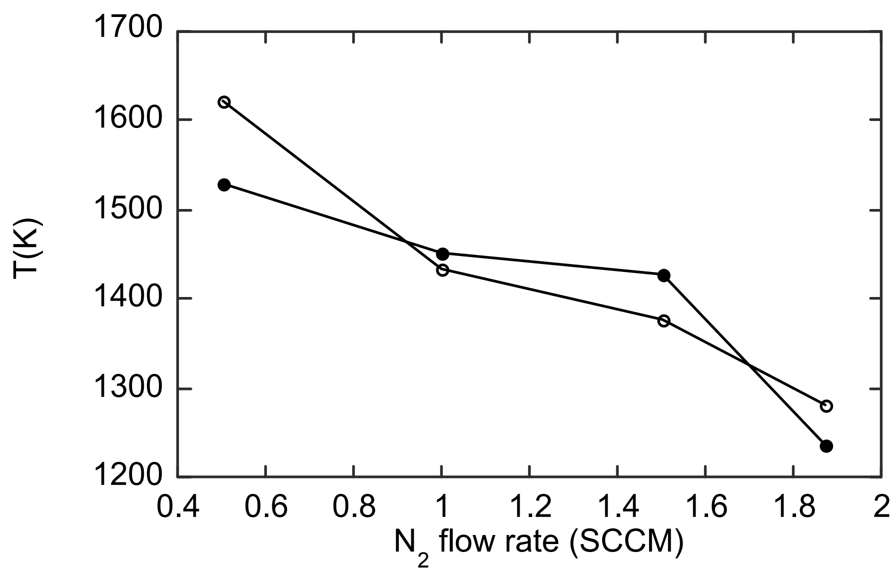


**(b)**

**Figure 13:** $T_o$ vs. $N_2$ flow rate. (a) $N_2$ in 23 sccm Ar. (b) $N_2$ in 2.5 sccm Ar / 41.2 sccm He. Open symbol represent $T_o$ calculated from pressure rise. Closed symbols represent $T_o$ calculated from energy balance.

**Table 1:** Appearance potential mass spectrometry

| Transition | Threshold Potential (eV) |
|---|---|
| $N(^4S^0) \rightarrow N^+$ | 14.5 |
| $N_2(A^3\Sigma_u^+) \rightarrow N^+$ | 18.1 |
| $N_2(X^1\Sigma_g^+) \rightarrow N^+$ | 24.3 |
| $N_2(A^3\Sigma_u^+) \rightarrow N_2^+(A^2\Pi_u)$ | 10.5 |
| $N_2(X^1\Sigma_g^+) \rightarrow N_2^+(X^2\Sigma_g^+)$ | 15.6 |
| $Ar(^1S) \rightarrow Ar^+$ | 15.8 |
| $Ar\left(^2P^*_{3/2}\right) \rightarrow Ar^+$ | 4.2 |
| $He(^1S) \rightarrow He^+$ | 24.6 |
| $He(^3S) \rightarrow He^+$ | 4.8 |

K. S. E. Eikema, W. Ubachs, W. Vassen, and H. Horgorvorst, Phys. Rev. A 55, 1866-1884 (1997).
S. D. Bergeson, A. Balakrishnan, K. G. H. Baldwin, T. B. Lucatorto, J. P. Marango, T. J. McIlrath, T. R. O'Brian, S. L. Rolston, C. J. Sansonetti, J.
Wen, and N. Westbrook, Phys. Rev. Lett. 80, 3475 (1998).
L. Minnhagen, J. Opt. Soc. Am. 63, 1185-1198 (1973).

**Table 2:** Energy balance table.

| $N_2$ | Gas | $T_o$ | Stag. En. | S | $v_s$ | T | K.E. | T. E. | R.E. | TOF En. |
|---|---|---|---|---|---|---|---|---|---|---|
| [sccm] | | [K] | [kJ/mol] | | [m/s] | [K] | [kJ/mol] | [kJ/mol] | [kJ/mol] | [kJ/mol] |
| 0.5 | He | | | 0.000 | 0 | 1432 | 0.000 | 27.743 | | |
| | N | | | 2.026 | 1963 | 791 | 0.015 | 0.009 | | |
| | $N_2$ | | | 1.200 | 1174 | 1612 | 0.218 | 0.379 | 0.152 | |
| | Ar | | | 1.514 | 1201 | 1512 | 1.630 | 1.778 | | |
| | | 1620 | 33.826 | | | | 1.864 | 29.908 | 0.152 | 31.925 |
| 1 | He | | | 0.000 | 0 | 1337 | 0.000 | 25.625 | | |
| | N | | | 1.996 | 1927 | 785 | 0.029 | 0.018 | | |
| | $N_2$ | | | 1.190 | 1141 | 1547 | 0.407 | 0.719 | 0.267 | |
| | Ar | | | 1.576 | 1215 | 1431 | 1.652 | 1.663 | | |
| | | 1435 | 30.095 | | | | 2.088 | 28.026 | 0.267 | 30.381 |
| 1.5 | He | | | 0.000 | 0 | 1307 | 0.000 | 24.767 | | |
| | N | | | 2.081 | 1924 | 720 | 0.043 | 0.025 | | |
| | $N_2$ | | | 1.387 | 1230 | 1326 | 0.703 | 0.915 | 0.380 | |
| | Ar | | | 1.698 | 1251 | 1305 | 1.730 | 1.500 | | |
| | | 1376 | 28.982 | | | | 2.476 | 27.206 | 0.380 | 30.062 |
| 1.87 | He | | | 0.176 | 372 | 1079 | 0.251 | 20.269 | | |
| | N | | | 2.165 | 1931 | 670 | 0.054 | 0.029 | | |
| | $N_2$ | | | 1.487 | 1270 | 1228 | 0.926 | 1.048 | 0.437 | |
| | Ar | | | 1.829 | 1282 | 1182 | 1.804 | 1.347 | | |
| | | 1280 | 27.043 | | | | 3.035 | 22.693 | 0.437 | 26.164 |
| 0.5[a] | $N_2$ | | | 3.123 | 1069 | 197 | 0.225 | 0.058 | 0.035 | |
| | Ar | | | 3.382 | 1026 | 221 | 1.186 | 0.259 | | |
| | He | | | 1.530 | 1073 | 118 | 2.142 | 2.286 | | |
| | | 300 | 6.271 | | | | 3.553 | 2.603 | 0.035 | 6.191 |

[a]Room temperature with 2 sccm Ar and 33 sccm He. All other data sets have 2.5 sccm Ar and 41.2 sccm He with 80 W.

**Table 3:** Energy analysis of $N_2$/Ar beam expansions.

| $N_2$ | Gas | $T_o$ | Stag. En. | S | $v_s$ | T | K.E. | T. E. | R.E. | TOF En. |
|---|---|---|---|---|---|---|---|---|---|---|
| [sccm] | | [K] | [kJ/mol] | | [m/s] | [K] | [kJ/mol] | [kJ/mol] | [kJ/mol] | [kJ/mol] |
| 0.5 | N | | | 3.985 | 1107 | 65 | 0.017 | 0.003 | | |
| | $N_2$ | | | 4.242 | 1005 | 95 | 0.263 | 0.037 | 0.207 | |
| | Ar | | | 3.9 | 969 | 148 | 18.404 | 3.019 | | |
| | | 1334 | 27.946 | | | | 18.684 | 3.058 | 0.207 | 21.949 |
| 1 | N | | | 3.904 | 1139 | 71.7 | 0.035 | 0.006 | | |
| | $N_2$ | | | 3.500 | 999 | 137 | 0.511 | 0.104 | 0.415 | |
| | Ar | | | 3.740 | 978 | 165 | 18.411 | 3.298 | | |
| | | 1365 | 28.810 | | | | 18.958 | 3.409 | 0.415 | 22.782 |
| 1.5 | N | | | 3.593 | 1138 | 84 | 0.057 | 0.011 | | |
| | $N_2$ | | | 3.170 | 981 | 161 | 0.783 | 0.195 | 0.675 | |
| | Ar | | | 3.450 | 965 | 188 | 17.479 | 3.673 | | |
| | | 1396 | 29.728 | | | | 18.319 | 3.879 | 0.675 | 22.872 |
| 2 | N | | | 2.990 | 1059 | 106 | 0.059 | 0.017 | | |
| | $N_2$ | | | 3.100 | 957 | 161 | 0.951 | 0.247 | 0.785 | |
| | Ar | | | 3.150 | 933 | 210 | 16.115 | 4.051 | | |
| | | 1275 | 27.288 | | | | 17.125 | 4.315 | 0.785 | 22.225 |
| 2[a] | $N_2$ | | | 9.12 | 563 | 6.42 | 0.222 | 0.007 | 0.125 | |
| | Ar | | | 10.10 | 562 | 7.44 | 5.992 | 0.147 | | |
| | | 300 | 6.361 | | | | 6.214 | 0.154 | 0.125 | 6.493 |
| 1.5[b] | N | | | 4.680 | 942 | 34 | 0.000 | | | |
| | $N_2$ | | | 4.960 | 870 | 52 | 0.539 | 0.055 | 0.417 | |
| | Ar | | | 4.600 | 904 | 93 | 16.057 | 1.829 | 17.829 | |
| | | 987 | 20.933 | | | | 16.596 | 1.884 | 0.417 | 18.897 |

[a]Room temperature with 2 sccm $N_2$ and 38 sccm Ar. All other data sets have 25 sccm Ar with 80 W.
[b]Cool plasma expansion - only tube is lit, no plume extending from nozzle; 28 sccm Ar with 80 W.

# 6. Appendices

# CHEMICAL BEAM EPITAXY OF INDIUM NITRIDE USING SEEDED SUPERSONIC BEAMS OF AMMONIA AND TRIMETHYL-INDIUM

**Nicholas A. Smith**[a]

**Arthur J. McGinnis**[b]

**H. Henry Lamb**[a,*]

[a]Department of Chemical Engineering, North Carolina State University, Raleigh, NC 27695-7905, USA
[a]Department of Materials Science and Engineering, North Carolina State University, Raleigh, NC 27695-7907, USA

***Corresponding author: Tel.: +1-919-515-6395; fax: +1-919-515-3465. E-mail address: lamb@eos.ncsu.edu (H. H. Lamb).**

(a version of a report sent to the Office of Naval Research, contract # N00014-01-1-0003)

### *Introduction*

The III-nitride semiconductors (AlN, GaN and InN) continue to be the focus of intensive research and development activity due to their applications in blue light-emitting devices and high-temperature, high-frequency microelectronic devices.[1] Most of the recent emphasis has been on the development of GaN ($E_g$ = 3.45 eV) materials for blue light-emitting diodes (LEDs) and laser diodes.[2] Successful development of InN ($E_g$ = 1.9 eV) materials will allow fabrication of orange and red light-emitting devices, an important step in the evolution of nitride-based optoelectronics. Moreover, InN is a candidate for use in microelectronic devices, such as high electron mobility transistors (HEMTs). InN films have been grown by a variety of methods including rf sputtering,[3] plasma-assisted metal-organic vapor phase epitaxy (plasma-MOVPE),[4] plasma-assisted molecular beam epitaxy (plasma-MBE),[5] atomic layer epitaxy (ALE),[6] and, more recently, MOVPE using ammonia ($NH_3$).[7] The typical substrate has been sapphire, despite the poor lattice match; however, InN films with superior electrical properties have been grown recently on MOVPE GaN substrates.[8] The indium sources used in these studies include elemental In, trimethyl-indium (TMIn), triethyl-indium (TEIn), and ethyldimethyl-indium (EDMIn). $NH_3$ and plasma-excited molecular nitrogen have been used as nitrogen sources. Progress in the epitaxial growth of InN films for device applications has been hindered by the low thermal stability of InN. The equilibrium $N_2$ pressure over InN is much higher that over AlN and GaN,[9] and this restricts typical epitaxial growth temperatures to less than 500°C.

Growth temperatures less than 500°C limit the nitrogen incorporation efficiency of $NH_3$ and necessitate the use of very large V/III flux ratios in InN MOVPE. A very low reaction efficiency is also observed for $NH_3$ nitridation of elemental Ga temperatures at less than 500°C;[10] however, $NH_3$ is known to undergo dissociative chemisorption on the GaN(0001) Ga-polar surface at room temperature to produce adsorbed $NH_x$ and H moieties.[11,12] Temperature-programmed desorption experiments on GaN films indicate that most of the adsorbed $NH_3$ desorbs by recombination of $NH_x$ and H at approximately 300°C.[12] A small amount of irreversible chemisorption (e.g., nitridation) occurs, as

evidenced by a $H_2$ desorption peak at a slightly higher temperature. A previous study on polycrystalline GaN films indicated that $H_2$ desorption from N sites (e.g., $NH_x$ moieties) required higher temperatures (~500°C) than $H_2$ desorption from Ga sites (~250°C).[13] These observations suggest that $H_2$ desorption from $NH_x$ moieties limits the nitridation efficiency of $NH_3$ at low temperatures. A similar situation is expected for $NH_3$ nitridation of elemental In. There is some ambiguity in the literature regarding the crystalline quality of InN films deposited at low temperatures. Bedair and coworkers[6] reported that a very narrow temperature window near 480°C exists for ALE growth of monocrystalline InN films on sapphire using EDMIn and $NH_3$. Films grown at lower temperatures were polycrystalline, and the ALE growth rate was suppressed markedly by InN decomposition at higher substrate temperatures. In contrast, InN films with the best reported crystalline quality, as measured by a 96-arcsec FWHM of the InN(0001) x-ray rocking curve, were grown on sapphire by MOVPE at 375°C using TMI and $NH_3$.[7] Unfortunately, electrical characterization data were not reported for these films; however, InN films grown by MOVPE at 450°C on GaN substrates had a Hall mobility of approximately 700 $cm^2s^{-1}V^{-1}$ at an electron concentration of $5 \times 10^{19}$ $cm^{-3}$.[8]

**Research Issues**

1) High *n*-type conductivity of InN films due to nitrogen vacancies and/or electrically active impurities.
2) Low nitrogen incorporation efficiency of $NH_3$ at substrate temperatures typically employed for InN growth.
3) Poor crystalline quality of InN films deposited at low temperatures due to restricted surface adatom mobility.

### Suppositions

- Low reaction efficiency of $NH_3$ with elemental Ga (and by extension In) at temperatures less than 500°C is due to slow $H_2$ desorption kinetics.
- Hydrogen transfer between adsorbed In alkyl and $NH_x$ moieties may provide a reaction pathway for low-temperature InN growth.

- Hyperthermal kinetic energy of In precursor can be used to improve crystalline quality of InN films grown at low temperatures by enhancing surface adatom mobility.

**Approach**

This research project explored low-temperature growth of InN films by supersonic jet epitaxy (SJE), a novel chemical beam epitaxy (CBE) technique that employs intense, monoenergetic beams of precursor molecules.[14] The supersonic molecular beams used for growth are generated by expanding a gas mixture through a small orifice into vacuum. The precursor fluxes achievable with supersonic molecular beams are higher than can be obtained using conventional effusive sources. By seeding the growth precursors in a light carrier gas (e.g., He or $H_2$) beams of precursor molecules with hyperthermal velocities and narrow (non-Boltzmann) kinetic energy distributions are obtained. Heavier precursor molecules seeded in He supersonic beams attain kinetic energies of 0.2 eV to greater than 5 eV, depending on their molecular weight and the pre-expansion (stagnation) temperature. The directed kinetic energy of molecules in seeded supersonic beams can be used to overcome activation barriers to (i) precursor decomposition and (ii) adatom surface migration, resulting in higher incorporation efficiencies and better crystalline quality in epitaxial growth.

The remarkable intensities achievable with seeded supersonic beams are illustrated by the peak growth rate of 0.25 μm *per second* obtained by Eres, *et al.* for the heteroepitaxial growth of Ge using a supersonic free jet of 5% digermane in He.[15] Mullins and coworkers[16] demonstrated that imparting hyperthermal kinetic energy to disilane by seeding in $H_2$ increases its reaction probability in Si homoepitaxial growth. Ho and coworkers[17] have demonstrated that the growth temperature of β-SiC on Si(111) can be lowered to 560°C by using methylsilane seeded in He or $H_2$. Moreover, the growth rate and crystalline quality of the epitaxial SiC films are enhanced. We employed hyperthermal TEGa beams and $NH_3$ from a UHV leak valve to grow homoepitaxial GaN films on MOVPE GaN(0001) substrates at 700-750°C.[18] The surface morphology of these films was superior to homoepitaxial GaN films grown by gas-source MBE using

$NH_3$ and elemental Ga. These achievements provided a scientific rationale for developing a low-temperature InN SJE process using TMIn and $NH_3$ as precursors.

## Experiment

The SJE experiments were performed using a custom-built apparatus equipped with dual supersonic jet sources, a UHV leak value for back-filling the growth chamber with $NH_3$, and a Knudsen cell for elemental In.[19] The SJE chamber is equipped with reflection high-energy electron diffraction (RHEED), desorption mass spectroscopy (DMS),[20] and optical reflectivity tools for in situ growth monitoring. Two quadrupole mass spectrometers (QMS) are available: a UTI-100C interfaced to LabView for DMS and a cross-beam Hiden HAL-301 triple mass filter mounted on a rotatable table for time-of-flight (TOF) measurements of the seeded supersonic beams. X-ray photoelectron spectroscopy (XPS) is available on-line in an adjacent surface analysis chamber. The surface analysis chamber is equipped with a PHI 3057 XPS system comprising a 10-360 spherical capacitor analyzer (SCA), Omni Focus III fixed-aperture lens, 16-element multichannel detector, and 257 DR11 PC interface card. A 400 W dual Al/Mg anode x-ray source is used.

TMIn was supplied from a commercial stainless steel bubbler (Epichem "Solution Trimethyl-indium"). Anhydrous $NH_3$ (electronics grade) was supplied by Air Products and further purified by passage through a Nanochem unit (Matheson). The substrates were 1.5-2 μm thick GaN(0001) films grown by MOCVD on on-axis 6H-SiC using a 0.1-μm AlN buffer layer. The substrates are coated on the backside (SiC face) with tungsten and cut into $1 \times 1$ $cm^2$ pieces. *Ex situ* cleaning was effected by ultrasonic degreasing in

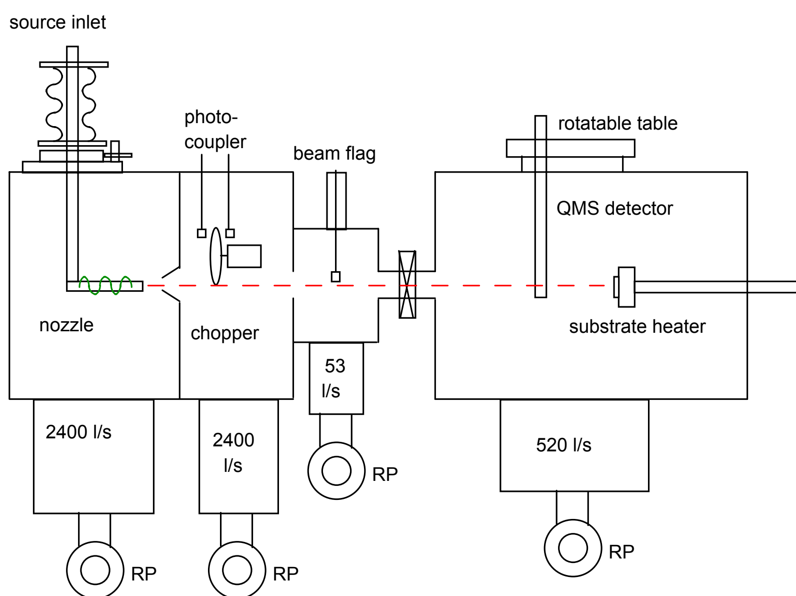


**Figure 1: Schematic of supersonic molecular beam scattering apparatus.**

trichloroethylene for 20 min. The substrates were initially atomically smooth with a roughness of 0.17 nm RMS, as determined from $1 \times 1$ $\mu m^2$ atomic force microscopy (AFM) images. *In situ* cleaning at 800°C by annealing in an $NH_3$ ambient ($1.5 \times 10^{-5}$ Torr) removed oxygen and carbon contamination from the surface. The resultant growth surface exhibited a $\sqrt{3} \times \sqrt{3}$ R30° reconstruction but was rougher (0.28 nm RMS) than the surface before cleaning.[21]

## Results and Discussion

InN growth experiments were performed using elemental In from a Knudsen cell and a seeded supersonic beam of 10% $NH_3$ in $H_2$. MOVPE-grown GaN(0001) on AlN-buffered 6H-SiC substrates were used to provide a chemically compatible surface for InN nucleation. InN growth was attempted at substrate temperatures of 480-600°C. The $NH_3$ flux at the substrate position was approximately $5 \times 10^{15}$ $cm^{-2}$ $s^{-1}$, and the In flux was varied from $7.5 \times 10^{11}$ to $1.9 \times 10^{14}$ $cm^{-2}$ $s^{-1}$ to provide V/III flux ratios ranging from 26 to 6,670 (Table 1). The average kinetic energy of $NH_3$ molecules in these experiments was estimated to be 0.3 eV, assuming an ideal supersonic expansion with zero velocity slip. The InN growth rates were very low for all experimental conditions. Metallic In accumulation was detected by XPS if the incident In flux exceeded the theoretical In desorption flux at the substrate temperature, *i.e.*, the substrate temperature was less than the In condensation temperature. InN growth was suppressed at substrate temperatures greater than 500°C due to thermal decomposition. An SEM image of an InN film grown at 480°C using an In flux of $7.5 \times 10^{11}$ $cm^{-2}$ $s^{-1}$ is shown in Fig. 2. The InN film was patchy with a maximum thickness of 100 nm after 30 h of growth. The rough surface morphology is suggestive of Volmer-Weber growth.

**Table 1. Experimental conditions for InN growth on GaN(0001) using $NH_3$ seeded in $H_2$**

| Substrate temp. | In K-cell temp. | $NH_3$ flow rate | $NH_3$ flux | In flux | In cond. temp. | Growth time |
|---|---|---|---|---|---|---|
| (°C) | (°C) | (sccm) | ($cm^{-2}s^{-1}$) | ($cm^{-2}s^{-1}$) | (°C) | (hr) |
| 480 | 757 | 30 | 5.0E+15 | 4.0E+13 | 573 | 5 |
| 555 | 757 | 30 | 5.0E+15 | 4.0E+13 | 573 | 2 |
| 600 | 757 | 30 | 5.0E+15 | 4.0E+13 | 573 | 3.3 |
| 480 | 605 | 30 | 5.0E+15 | 7.5E+11 | 469 | 30 |

Heteroepitaxial growth of InN on MOCVD-grown GaN(0001) substrates was attempted using seeded supersonic molecular beams of TMIn in He and $NH_3$ background pressures of $1.0 \times 10^{-5}$ to $1.0 \times 10^{-4}$ Torr. The average kinetic energy of TMIn molecules in these experiments was estimated to be ~2 eV, assuming an ideal supersonic expansion with zero velocity slip. The maximum $NH_3$ pressure was limited by the need to maintain molecular flow conditions within SJE growth chamber. The substrate temperature (320-520°C) and TMIn flow rate (0.06 – 0.37 sccm) were varied to provide a wide range of potential growth conditions, as summarized in Table 2. The nominal V/III flux ratios in these experiments ranged from 80 to 5300. The In condensation temperature was

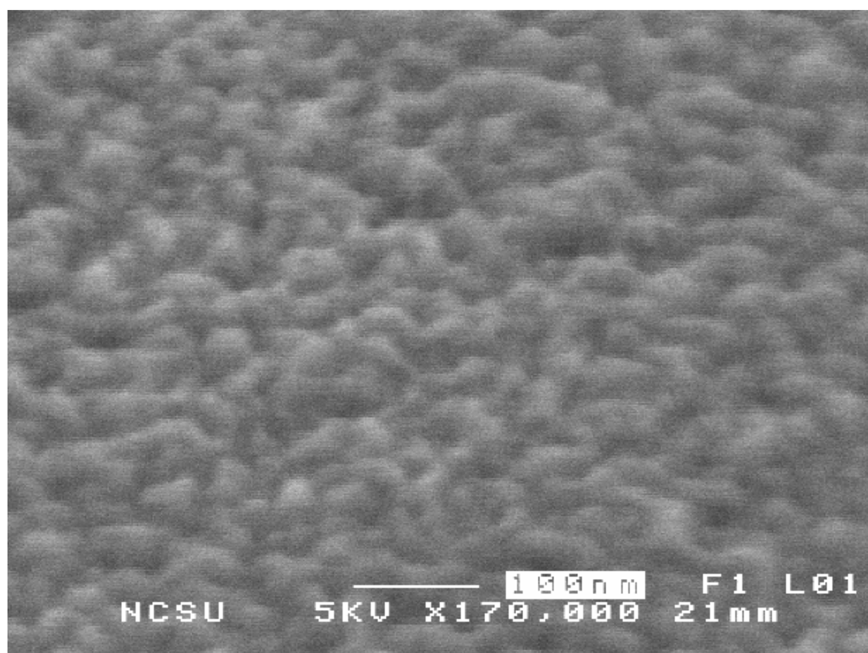


**Figure 2: Top-view SEM image of an InN film on GaN grown at 480°C using an In flux of 7.5 $\times 10^{11}$ $cm^{-2}$ $s^{-1}$ and an $NH_3$ flux of approximately 5 $\times 10^{15}$ $cm^{-2}$ $s^{-1}$.**

calculated from the In flux by assuming a sticking coefficient of unity for TMIn. The condensation temperature represents the minimum substrate temperature required to prevent accumulation of metallic In on the substrate in the *absence* of reaction with $NH_3$ to form InN.

XP spectra and SEM images indicated the deposition of metallic In under the chosen growth conditions. The amount of deposited In was limited at the lower substrate temperatures (<400°C) by the decomposition rate of TMIn. XPS evidenced the amount

of In on the substrate increased in direct proportion to the incident TMIn flux for substrate temperatures greater than 400°C. SEM images of films grown under the most promising conditions (Fig. 3) revealed the presence of spherical In droplets on the substrate after the growth experiments. Energy-dispersive x-ray (EDX) analysis (resolution: 0.5 μm) verified that the droplets contained In. The surface regions between the droplets in Fig. 3(a) have a roughened appearance similar to that of the InN film shown in Fig. 2, and growth pits are evident between the droplets in Fig. 3(b). We infer from these observations and the close similarity of the growth temperatures to that required to achieve InN growth on GaN(0001) using elemental In and $NH_3$ (*vide supra*) that the substrates are covered by very thin InN layers. We estimate that the InN growth rates under these conditions are extremely low (less than 3 nm/h).

Indium accumulation can be avoided by reducing the TMIn flux and/or increasing the substrate temperature, but either choice will result in unrealistically low growth rates. Unfortunately, there is no evidence of a reaction pathway involving TMIn and $NH_3$ that results in InN growth at temperatures less than approximately 500°C. We infer that $NH_3$ decomposition is the rate-limiting step in InN growth using $NH_3$ and elemental In or TMIn.

**Table 2: Experimental conditions for InN growth on GaN(0001) using TMIn seeded in He.**

| Substrate temp. | TMIn flow rate | $NH_3$ pressure | $NH_3$ flux | TMIn flux | In cond. temp. | Growth time |
|---|---|---|---|---|---|---|
| (°C) | (sccm) | (torr) | ($cm^{-2}s^{-1}$) | ($cm^{-2}s^{-1}$) | (°C) | (hr) |
| 320 | 0.24 | 1.00E-05 | 4.9E+15 | 3.9E+13 | 570 | 4 |
| 380 | 0.37 | 1.00E-05 | 4.9E+15 | 6.1E+13 | 581 | 4 |
| 380 | 0.24 | 1.00E-05 | 4.9E+15 | 4.0E+13 | 570 | 4 |
| 480 | 0.22 | 1.00E-05 | 4.9E+15 | 3.7E+13 | 570 | 4 |
| 480 | 0.06 | 1.00E-05 | 4.9E+15 | 9.4E+12 | 530 | 4 |
| 520 | 0.24 | 1.00E-05 | 4.9E+15 | 4.0E+13 | 570 | 4 |
| 500 | 0.24 | 1.00E-05 | 4.9E+15 | 4.0E+13 | 570 | 4 |
| 500 | 0.24 | 1.00E-04 | 4.9E+16 | 4.0E+13 | 570 | 4 |
| 480 | 0.24 | 1.00E-04 | 4.9E+16 | 4.0E+13 | 570 | 4 |
| 520 | 0.06 | 1.00E-04 | 4.9E+16 | 9.3E+12 | 530 | 8 |
| 500 | 0.12 | 1.00E-04 | 4.9E+16 | 2.0E+13 | 552 | 8 |

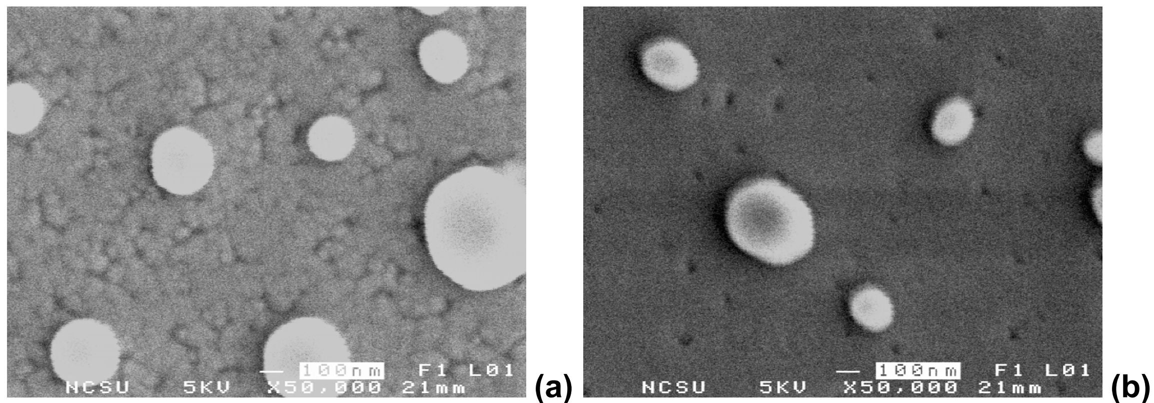


**Figure 3: Top-view SEM images of InN films grown on GaN(0001) using a TMIn flux of 4.0 × $10^{13}$ $cm^{-2}$ $s^{-1}$ and an $NH_3$ flux of 4.9 × $10^{16}$ $cm^{-2}$ $s^{-1}$ at substrate temperatures of (a) 500 and (b) 480°C.**

## References

[1]S. N. Mohammed and H. Morkoç, Prog. Quant. Electr., **20,** 361 (1996).

[2]S. Nakamura and G. Fasol, "The Blue Laser Diode: GaN Based Light Emitters and Lasers," Springer, Berlin (1997).

[3]B. R. Natarajan, *et al*., Thin Solid Films, **69**, 201 (1980).

[4]A. Wakahara, T. Tsuchiya, and A. Yoshida, J. Crystal Growth, **99**, 385 (1990).

[5]W. E. Hoke, P. J. Lemonias and D. G. Weir, J. Crystal Growth, **111**, 1024 (1991). C. R. Abernathy, *et al.*, J. Vac. Sci. Technol. B, 11 (1993) 179. L. C. Jenkins, *et al. ibid*., **13,** 1585 (1995).

[6]F. G. McIntosh, *et al.*, Appl. Surf. Sci., **112,** 98 (1997).

[7]W. K. Chen, *et al.*, Jpn. J. Appl. Phys. **36**, L1625 (1997).

[8]S. Yamaguchi, *et al.*, J. Appl. Phys., **85**, 7682 (1999).

[9]O. Ambacher, *et al.*, J. Vac. Sci. Technol. B, **14**, 3532 (1996).

[10]M. Mesrine, N. Grandjean, and J. Massies, Appl. Phys. Lett., **72**, 350 (1998).

[11]V. M. Bermudez, Chem. Phys. Lett., **317**, 290 (2000).

[12]R. Shekhar and K. F. Jensen, Surf. Sci., **381**, L581 (1997).

[13]Chiang, C. –M., *et al*., Chem. Phys. Lett., **246**, 275 (1995).

[14]B. A. Ferguson and C. B. Mullins, J. Crystal Growth, **178**, 134 (1997).

[15]D. Eres, D. H. Lowndes, and J. Z. Tischler, Appl. Phys. Lett., **55**, 1008 (1989).

[16]K. A. Pacheco, et al., Appl. Phys. Lett., **67**, 2951 (1995).

[17]S. A. Ustin, C. Long, and W. Ho, Solid-State Electronics, **42**, 2321 (1998).

[18]A. J. McGinnis, D. Thomson, A. Banks, E. Preble, R. F. Davis, and H. H. Lamb, J. Vac. Sci. Technol. A, **21**, 294 (2003).

[19]A. J. McGinnis, D. Thomson, R. F. Davis, E. Chen, A. Michel, and H. H. Lamb, Surf. Sci., **494**, 28 (2001).

[20]R. Held, *et al.*, J. Electron. Mater., **26**, 272 (1997).

[21]A. J. McGinnis, *et al.*, J. Cryst. Growth, **222**, 452 (2001).

## 6.2 Si-H (100) nitridation via an Atomic N RF-discharge supersonic molecular beam

As device dimensions are reduced, the reliability and performance of gate materials have become a great concern. Thin silicon oxide can develop leakage currents decreasing device performance and reliability. Nitrogen incorporation into the gate dieletric has several benefits. Nitrogen near the top surface of oxide prevents boron penetration. Nitrogen placed throughout the gate oxide increases the dielectric constant, allowing a thinner gate oxide dimension. Nitrogen at the Si-$SiO_2$ interface improves device reliability and performance.[1-8]

Reduced device scaling of metal-oxide-semiconductor field-effect-transistors (MOSFETs) has placed concerns on $SiO_2$ films as gate dielectrics. These device density increases require ultra-thin $SiO_2$ films (~ 1nm) or other high-κ dielectrics to meet requirements to maintain device performance and reliability.[9] The limiting factors with ultra-thin film gate oxides are controlled by interfacial properties. $SiO_2$ has problems with direct tunneling currents for thicknesses <1.5 nm which increases power consumption for for low standby power MOSFETs. The introduction of nitrogen in ultra-thin gate dielectrics has shown to improve reliability in MOS devices. Nitrogen has also been shown to prevent indiffusion of B from $p^+$ doped poly-Si in p-MOSFET devices.[8] Silicon nitride films offer a moderately high dielectric constant of 7. In addition to applications with MOSFETs, silicon nitride has advantageous properties for use as a surface (and bulk) passivating anti-reflective coating for c-Si solar cells.[10]

Ultra-thin oxides benefit from nitrogen incorporation at the Si-$SiO_2$ interface by improving reliability of the device as measured by time-to-breakdown and charge-to-

breakdown.[11] Stress-induced changes in peak transconductance, threshhold voltage and leak current are reduced by monolayer nitrogen incorporation.[12]

Si-$SO_2$-interfacial nitrogen incorporation can be accomplished by several different techniques, including thermal annealing in $NH_3$, $N_2O$ or NO ambient, ion implantation of $N_2$ into Si substrate, chemical vapor deposition of $Si_3N_4$ on to the Si substrate, thermal oxidation-nitridation of the Si substrate in $N_2O$ or NO, or low-temperature plasma-assisted nitridation. Low-temperature plasma-assisted nitridation is beneficial because low temperatures do not reduce the overall thermal budget and also allow a regime where process control (ultra-thin film deposition) is more optimal.

Low-temperature plasma-assisted nitridation can be accomplished by a parallel plate (direct) discharge $N_2$ plasma, remote $N_2O$/He plasma, remote $N_2$/He plasma, remote expanding thermal plasma (Ar-$H_2$-$N_2$-$SiH_4$), electron cyclotron resonance $N_2$ plasma or supersonic jet $N_2$/He/Ar-plasma source. A supersonic jet plasma source would allow fine-controlled nitridation under molecular beam epitaxy (MBE) conditions, where direct kinetic results can be obtained.

Remote $N_2$/He and $N_2O$/He plasmas generate either $N_2^+$ (~0.1 Torr) or N atoms and $N_2$(A) (~0.3 Torr) for nitridation.[13] While there is much speculation as to which species are responsible for the best quality $Si_xN_y$ deposition, studies done at ~0.1-1.0 Torr involve many species interactions due to short mean free path. SJE has the benefit of having mean free path greater than system dimensions, allowing direct analysis of plasma species. Supersonic jet epitaxy (SJE) provides a high intensity with well-controlled kinetic energy and conditions conducive for direct methods of characterization. Sellidj et al. have employed a SJE $N_2$/He RF-plasma source for the purpose of GaN deposition.[14]

Results from Pollard indicate that the SJE $N_2$/He RF-plasma source primarily produces atomic N as the active species.[15] Jordan et al. constructed a SJE $N_2$/Ar corona discharge source, employed appearance potential mass spectrometry (APMS) to determine the active species was $N_2A\Sigma_u^+$ and consequently grew GaN.[16,17]

$N_2$ plasmas are contained a wide variety of species, including $N_2^*$, N, $N_2$ and $N_2^+$ (each of allowed vibrational, rotational and electronic energies). Many species are short lived, and they typically de-excite to certain energy levels. $N_2^*$ (metastables) rapidly radiate to the $N_2$(A) state. Atomic N can be found in the ground state, however typically there is a high rate of recombination to $N_2^*$, which de-excites to $N_2$(A). We have constructed and characterized an RF $N_2$ supersonic jet source as a source of N atoms by OES and TOF-APMS.[18] Using this source of N atoms, we will nitride Si-H (100). Surface composition and bonding information will be acquired via x-ray photoelectron spectroscopy (XPS) ex-situ.

Details of the SJE system employed for Si-H (100) nitridation have been published elsewhere.[18] For Si-H (100) nitridation, the QMS is rotated out of beam alignment and a Si-H(100) substrate is placed in the beam's path. The chopper is also removed to increase active N intensity. The same nominal conditions of the hot mode $N_2$/Ar/He plasma (1.5 sccm $N_2$ / 2.5 sccm Ar / 41.2 sccm He, 80 W forward power, $P_o \sim$ 150 Torr, ~ 1300 K) are used in the nitridation of Si-H (100) as the condition characterized in the previous work.[18]

The substrates were $1 \times 1$ cm$^2$ pieces cut from a Si(100) wafer. Each substrate was cleaned ex-situ with ultra-violet ozone (UVO) for 5 minutes. A HF dip follows the UVO process along with a DI-water rinse, and then blown dry with dry $N_2$. This process

was repeated. The substrate enters the chamber via a drytel-pumped (Alcatel 31) load-lock and then is exposed to the supersonic jet plasma beam while heating up to 300°C (4 min). Exposure to the N atom source ranged from 5 min to 2 h, ending with a 4 min plasma exposure cool down. After the substrate has been nitrided, is it removed from the SJE system and then consequently reloaded into another load-lock chamber, which is connected to a separate x-ray photoelectron spectroscopy (XPS) chamber. This UHV chamber is equipped with a spherical capacitor analyzer and dual Mg/Al anode x-ray source. This chamber has a base pressure of $\sim 1.0 \times 10^{-10}$ Torr.

Fig. 1(a) shows the peaks for the N(1s) binding energy resulting from XPS for different plasma exposure times, ranging from 0 min to 120 min. No significant N is present on the surface of the bare, clean substrate (0 min). N incorporation appears to increase with exposure time, and then saturates at 17 at. % after 1 h of exposure time (Table 1). The binding energy (~398.4 eV) is indicative of N-$Si_3$ bonding, i.e., silicon nitride ($Si_3N_4$).

Fig. 1(b) shows the peaks for the O(2p) binding energy resulting from XPS for different plasma exposure times, ranging from 0 min to 120 min. Even for the bare Si-H(100) surface (0 min), there is O present, 3.4% (Table 1). This peak is located at 533 eV, consistent with the binding energy indicative of $SiO_2$ bonding. Exposure to the plasma increase the O content of the thin film; it appears to reach ~10% for exposures from 30 min to 120 min. This peak is very close to the same position as the bare peak at 533 eV. At first glance, one might assume this to be $SiO_2$ bonding; however, nitrate bonding has the almost the same binding energy (slightly higher) and the peak does appear to be slightly weighted to higher binding energies. From Fig. 1(b) alone, it is

unclear whether the O is bonded to Si or N. If you consider Fig. 1(a), however, it appears that the bonding is $SiO_2$ for O, as there is no significant nitrate bonding peak (~408 eV) present in the N(1s) binding energy scan.

Fig. 1(c) shows the binding energy scan of Si (2p) with respect to exposure time, ranging from 0 min to 120 min. The bare Si-H(100) substrate (0 min) shows the largest peak, located at 100.2 eV, fairly close to pure Si. This peak decreases with exposure time and also appears to saturate to a minimum (~61%, Table 1) at 77 min, just as the N(1s) appeared to saturate to a maximum. There is a shoulder from 101.8 to 103.8 eV for plasma exposures (not present for the bare substrate). Because of the size of the substrate peak at 100.2 eV, it is difficult to determine whether there is a peak for SiN bonding at ~102 eV. It would probably be safe to assume there is a peak at ~103 eV representing $SiO_2$ bonding, but it would not be easy to conclude that it is dominating the SiN peak. It might be more accurate to say those peaks are similar in magnitude. This conclusion would be consistent with the SiN and $SiO_2$ bonding represented in Figs. 1(a) and 1(b), and also the relative at. % determined (Table 1).

Fig. 2 shows the relative intensity of the atomic constituents of the Si-H(100) film exposed to the plasma for 77 min with respect to escape depth angle, $\theta$, i.e. angle resolved XPS (ARXPS). The Si intensity decreases as $\theta$ decreases. This is expected as the pure Si signal would decrease since it would be below any film produced. C intensity strongly increases as $\theta$ decreases, indicating the C is on the top surface of the film. N and O intensities tend to follow each other over the range of $\theta$, implicating they have the same profile and are located in the same location, depth-wise, in the film. Both N and O intensity increase to a maximum around $\sin(\theta) \sim 0.6$, and then decrease as $\theta$ goes to zero.

Certainly, both N and O are in the film, however C would be on top of both N and O. Most certainly the origin of C would be ex-situ exposure to the atmosphere ($CO_2$, etc.) after plasma exposure and before XPS analysis. It would appear that because the N and O profiles follow each other closely, it is likely that O is introduced during the plasma processing, as a small leak in the depostion chamber or even outgassing. However, it remains possible that dangling Si bonds remain after being exposed to N atom incorporation. The lattice may be incomplete, so the dangling bonds would immediately bond in atmosphere to either $H_2O$ or $O_2$. If the SiN layer were thin enough (2-3 layers), it is possible that this atmosphere O incorporation may be complete enough to yield the same depth profile on ARXPS as N.

It is clear that a thin film of SiN can be grown with a supersonic N atom source at 300°C from Si-H(100), and that there appears to be a maximum amount of N incorporation that can be achieved (~17%). Whether O from the process inhibits further N incorporation or that the N incorporation reaction is likely to be diffusion limited (i.e. direct) at 300°C (no or little N migration during the reaction) cannot be concluded for sure. XPS binding energy spectra indicate there is significant N-Si bonding [from N(1s)] and significant O-Si bonding [from O(2p)], but no N-O bonding. In order to determine where the O contamination is originating from, the XPS will be conjoined to the SJE deposition chamber for in-situ analysis. This would likely eliminate any C contamination and also remove the chance of O incorporation from the atmosphere.

**REFERENCES**

[1]H. Fukuda, M. Yasuda, T. Iwabuchi, and S. Ohno, Appl. Surf. Sci. **60**, 359 (1992).

[2]H. Fukuda, T. Arakawa, and S. Ohno, Jpn. J. Appl. Phys., Part 2 **29**, L2333 (1990).

[3]H. Hwang, W. Ting, B. Maiti, D. Kwong, and J. Lee, Appl. Phys. Lett. **57**, 1010 (1990).

[4]E. C. Carr and R. A. Buhrman, Appl. Phys. Lett. **63**, 54 (1993).

[5]P. J. Tobin, Y. Okada, S. A. Ajuria, V. Lakhoita, W. A. Feil, and R. I. Hedge, J. Appl. Phys. **75**, 1811 (1994).

[6]Z. Q. Yao, H. B. Harrison, S. Dimitrijev, Y. T. Yeow, and D. Sweatman, Appl. Phys. Lett. **64**, 3584 (1994).

[7]S. V. Hattangady, H. Niimi, and G. Lucovsky, Appl. Phys. Lett. 6**6**, 3495 (1995).

[8]K. A. Ellis and R. A. Buhrman, Appl. Phys. Lett. 68, 1696 (1996).

[9]The National Technology Roadmap for Semiconductors (Semiconductor Industry Association, San Jose, CA 2001).

[10]A. G. Aberle, Sol. Energy Meter. Sol. Cells **65**, 239 (2001).

[11]Z. Liu, H. J. Wann, P. K. Ko, C. Hu, and Y. C. Cheng, IEEE Electron Device Lett. **EDL-13**, 519 (1992).

[12]H. S. Momose, T. Morimoto, Y. Ozawa, K. Yamabe, and H. Iwai, IEEE Trans. Electron Devices **41**, 546 (1994).

[13]A. Khandelwal, B. C. Smith, and H. H. Lamb, J. Appl. Phys. **90** 3100 (2001).

[14]A. Sellidj, B. A. Ferguson, T. J. Mattord, B. G. Streetman, and C. B. Mullins, Appl. Phys. Lett. **68**, 3314 (1996).

[15]J. E. Pollard, Rev. Sci. Instrum. **63**, 1771 (1992).

[16]D. C. Jordan, I. S. T. Tsong, David J. Smith, B. J. Wilkens, and R. B. Doak, Appl. Phys. Lett. **77**, 3030 (2000).

[17]D. C. Jordan, C. T. Burns, and R. B. Doak, J. Appl. Phys. **89**, 883 (2000).

[18]N. A. Smith, Ph. D. dissertation, North Carolina State University, 2003.

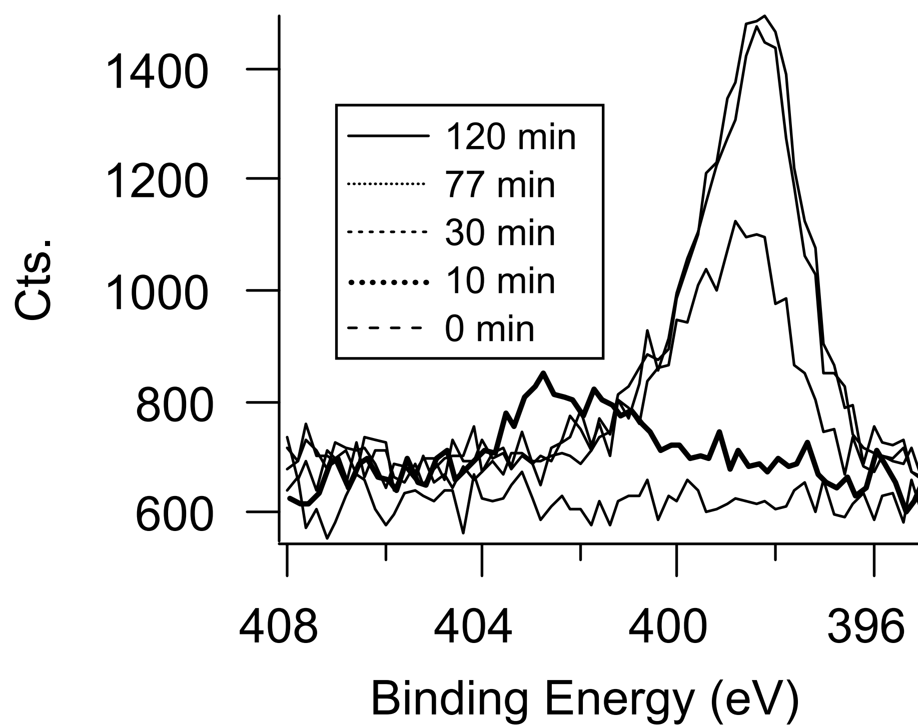


(a)

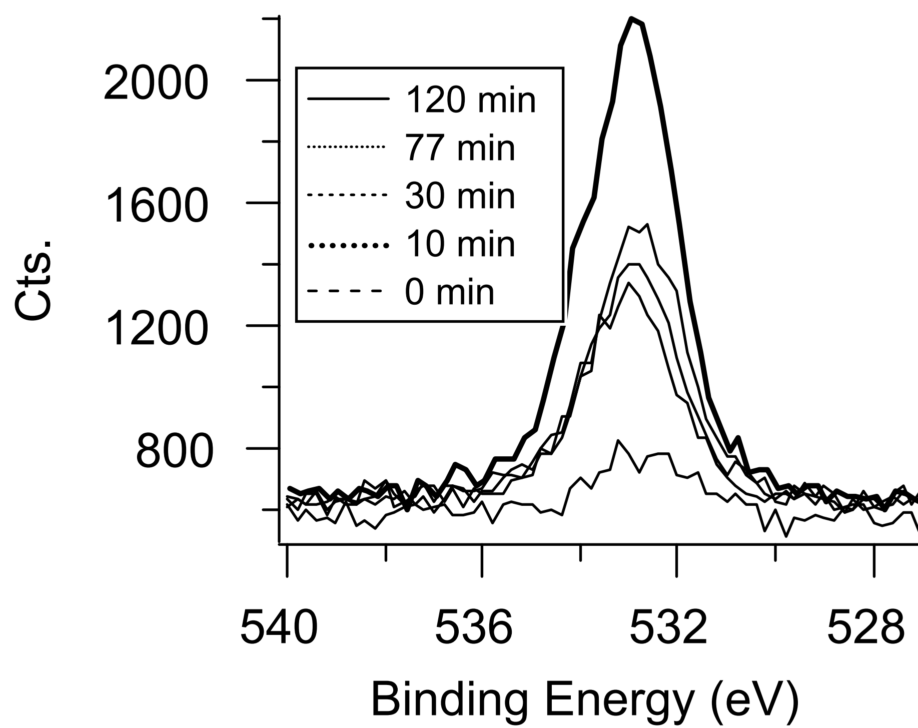


(b)

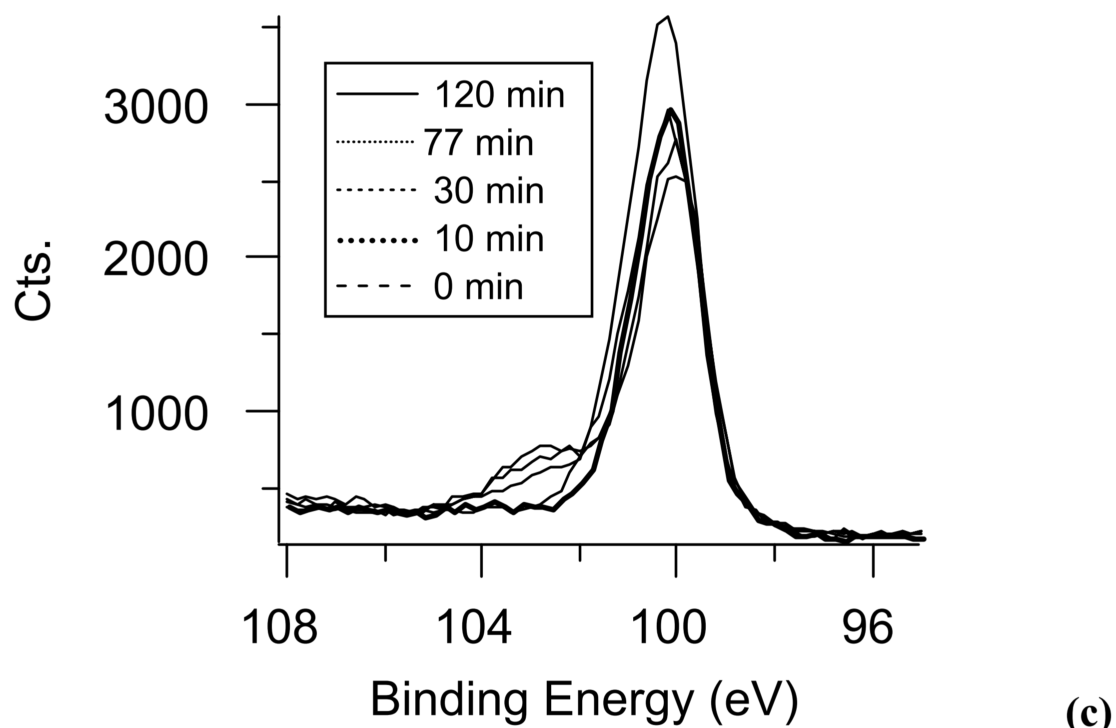


**(c)**

**Figure 1:** XPS spectra of binding energy for (a) N(1s) (b) O(2p) and (c) Si(2p).

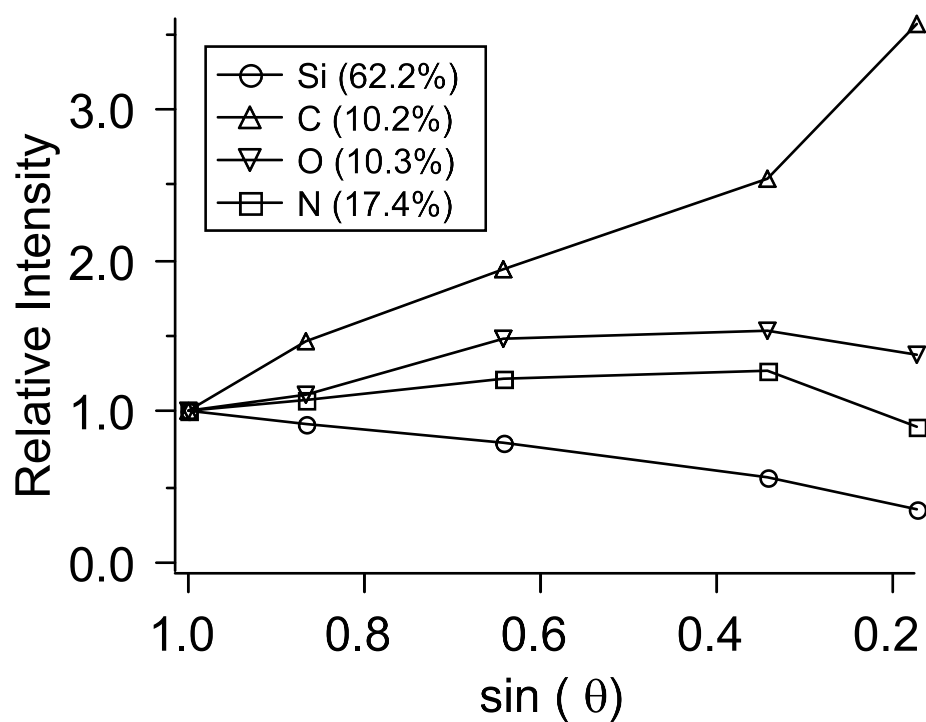


**Figure 2:** ARXPS of N atom plasma treated Si. Exposure time of 77 min.

**Table 1:** Thin film composition of surface by XPS after plasma exposure.

| Time (min) | Si at. % | C at. % | O at. % | N at. % |
|---|---|---|---|---|
| 0 | 91.9 | 4.7 | 3.4 | 0.0 |
| 10 | 57.9 | 17.1 | 21.8 | 3.1 |
| 30 | 67.9 | 11.6 | 9.0 | 11.5 |
| 77 | 62.2 | 10.2 | 10.3 | 17.4 |
| 120 | 61.0 | 10.8 | 10.9 | 17.4 |

## 6.3 Converting time-of-flight spectra to velocity distributions

Coordinating the mass spectrometer with the chopper photocoupler yields a time-of-flight sprectrum of a supersonic molecular beam. This time-of-flight spectrum does not directly relate to a velocity distribution of the supersonic molecular beam, as detection non-idealities do exist. The mass spectrometer signal $N_x(t)$, is density sensitive, and must be taken into consideration. In addition, the chopper admits the beam signal with a gating function, $A\omega l)$, which causes some loss of beam resolution. The gating function is defined by the geometry of the system, including collimation, chopper slit size and the detector's sample size and position. Our chopper slit is 1 mm wide and the chopper rotates at 202 Hz. See Fig. 1 below for geometry of the molecular beam time-of-flight.

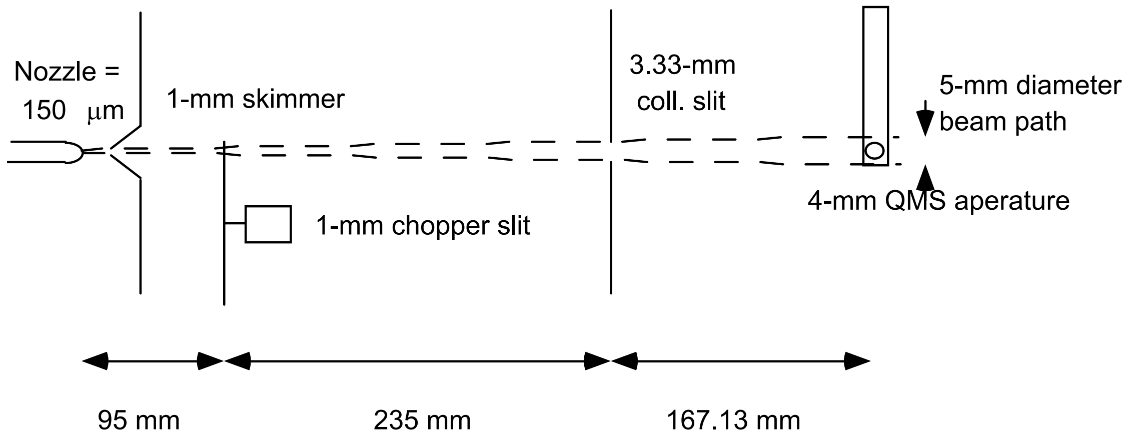


**Figure 1:** Set-up of the time-of-flight molecular beam characterization.

The beam begins by expanding through the 150-µm orifice. It is first defined by the 1-mm skimmer opening. Each subsequent opening that the beam must pass through reduces the solid angle of the beam admitted to the detector. The solid angle $\phi$ is defined by the distance from the source to the restricting aperture $l$ and the width of the slit $w$.

For small $\phi$, $\phi \approx (1/2)tan(w/l)$. The limiting $\phi$ defined by the collimation slit is similar to the $\phi$ defined by the skimmer ($\phi$~0.01). Assuming full intensity of the beam passing through the skimmer and using $\phi$~0.01 results in a 5-mm diameter beam swath at the QMS aperture distance. As the slit rotates pass the "open" position, the 4-mm QMS aperture receives the following approximately trapezoidal gating function (neglecting transforms from circular to rectangular to circular slits),

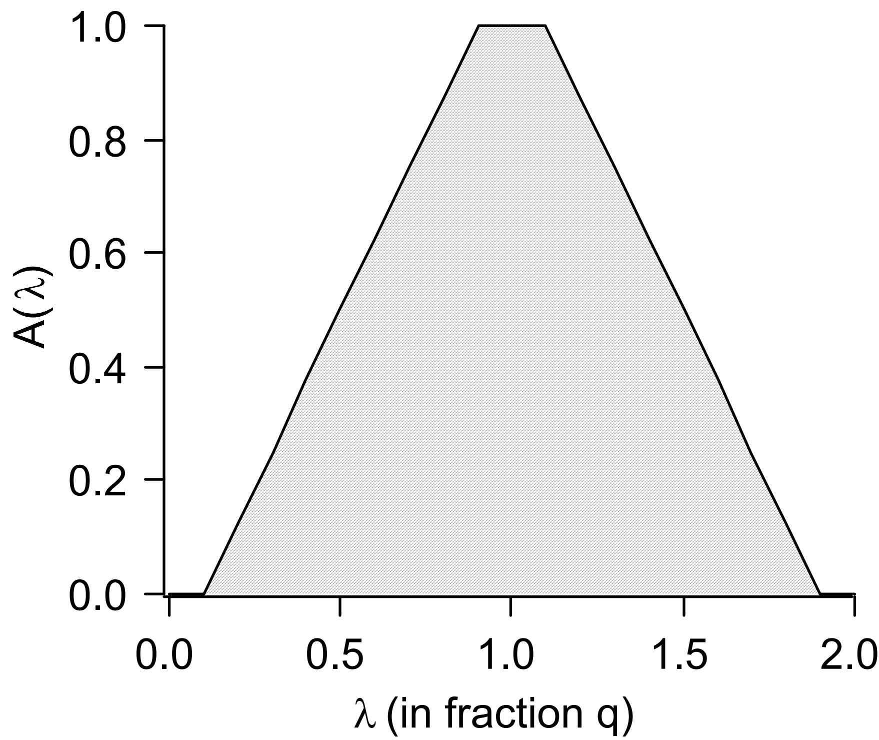


**Figure 2:** Gating function, $A(\lambda)$ of the beam with respect to the QMS, for 2-stage set-up.

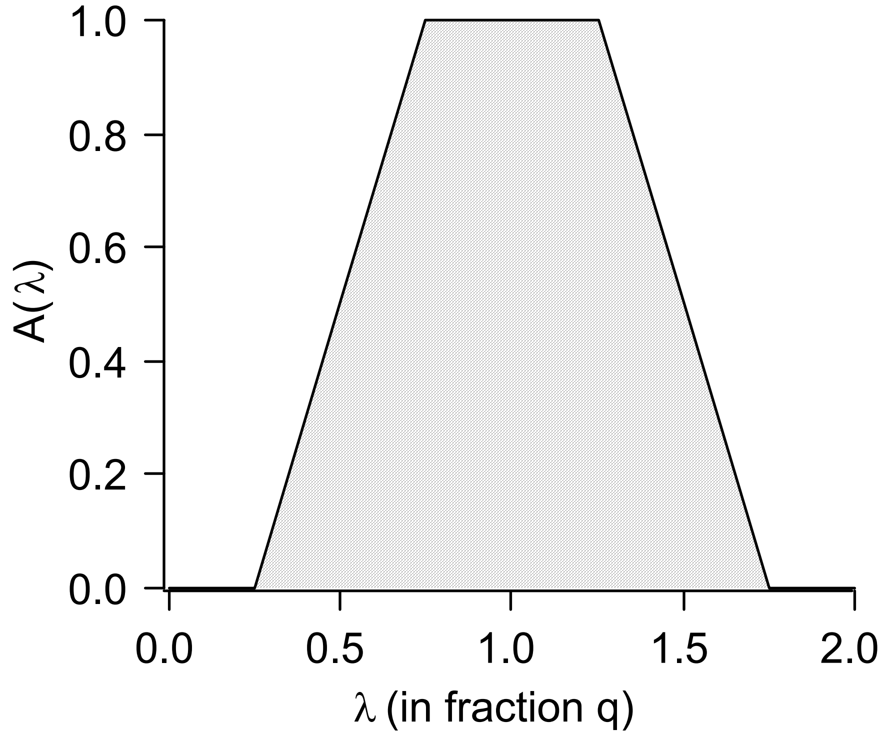


**Figure 3**: Gating function, *A(λ)* of the beam with respect to the QMS, for 3-stage set-up.

$\lambda$ represents the admittance time of the beam where $\lambda$=0 for beginning of beam admittance. $q$ represents the time it takes for the slit to pass through a given point, i.e., $q$=(1 mm) / (101.6$\pi$ mm) * 202 Hz ~ 15.5 μs. Eq. 1 represents the relationship between time $t$ and velocity $v$,

$$v = L/(t-\lambda) \tag{1}$$

The Jacobian transformation of Eq. (1) yields

$$dv = -\frac{L}{t^2}dt \tag{2}$$

The flight-time distribution will be

$$g(t)dt = f\left(\frac{L}{t}\right)dv(t) = -\frac{L}{t^2}f\left(\frac{L}{t}\right)dt \tag{3}$$

where $f(v)$ is the velocity distribution. A density-sensitive detector (such as a QMS) requires division by $v=L/t$, leaving

$$g_{den}(t) \sim \frac{1}{t} f\left(\frac{L}{t}\right) \tag{4}$$

Transforming $dv$ into $dl$, we get

$$ds = \left(\frac{\partial s}{\partial \lambda}\right)_t d\lambda = \frac{L}{(t-\lambda)^2} d\lambda \tag{5}$$

Integrating $g_{den}(t)$ from $\lambda$=0 to 2$q$, we get

$$g_{den}(t) = n \int_0^{2q} f(v) \frac{L}{(t-\lambda)^2} A(\lambda) d\lambda \tag{6}$$

Even though $f(v)$ does vary with $\lambda$, since we only integrating over ~30 μs we will assume $f(v)$ to act as a constant over that short range (as the thinnest peak width appears to be ~100 μs in our data), and hence pull it outside the integral.

$$g_{den}(t) = nf(v) \int_0^{2q} \frac{L}{(t-\lambda)^2} A(\lambda) d\lambda \tag{7}$$

Using the $A(\lambda)$ from the 2-stage system, we get

$$g_{den}(t) = nf(v) \left[ \frac{1}{0.8q} \left( \ln\left((t-0.8q)/t\right) + \ln\left((t-q)/(t-1.8q)\right) \right) \right] \tag{8}$$

or

$$g_{den}(t) = nf(v) \left[ \frac{1}{0.44q} \left( \ln\left((t-0.44q)/t\right) + \ln\left((t-0.88q)/(t-1.32q)\right) \right) \right] \tag{9}$$

for the 3-stage system. Molecular beam velocity distributions can be modeled as a Maxwellian distribution,

$$f(v) = v^3 \exp\left(-\left(\frac{v - v_o}{\alpha}\right)^2\right) \tag{10}$$

where $v_o$ is the stream velocity. The experimental time-of-flight distribution $I_{exp}(t)$ is compared with $g_{den}(t)$ by minimizing the sum of the squares of the deviation

$$\sum_{j=1}^{N} \left[I_{\exp}(t_j) - g_{den}(t_j)\right]^2 \tag{11}$$

to get parameters $v_o$, $\alpha$, and $n$. The speed ratio S of the beam is related directly to $\alpha$ and $v_o$ as

$$S = \frac{v_o}{\alpha} \tag{12}$$

Knuth et al. and Auberbach provide further details of these transformations.

7. Future work

As it is with most academic endeavors, one answer will provide many more questions. Growth of GaN(0001) with supersonic jet epitaxy and analysis of AFM topogrphs has yielded a surface diffusion mechanism as the dominant surface transport mechanism, regardless of the faceted or non-faceted surface that results. Considering the flux ratio (2:1) at which GaN(0001) has a roughness transition and that GaN() appears to have a roughness transistion at a (1:1) flux ratio, it would be intersting to confirm this fact experimentally by operating the same system with both surfaces.

Application of the RFD-SSJ source (now proven primarily to be a N atom source) towards growing GaN(0001) homoepitaxially would be desirable. This application has been attempted; however, because of low intensity we were not able to grow any GaN(0001) of measurable thickness. Modifications to the growth/characterization system could be made to increase intensity, including reattaching a larger pump as well as reduce source to substrate distance. It is a likely assumption that N atom chemisorption is a direct chemisorption process considering the energy the N atom possesses over the kinetic barrier, likely implying 100% incorporation. Now, with a viable technique for active species concentration detection (TOF-APMS) and combining that measurement with our enrichment correlation, we can verify this assumption (by measuring the growth rate). Consequently, angular dependence and energetic dependence (available via RFD-SSJ) of the N atom precursor can be monitored for changes in GaN(0001) surface morphology using AFM.

The RFD-SSJ source can also be applied to grow InN(0001) films, removing any dependence on use of $NH_3$, which has a low nitrogen incorporation efficicency at 500°C.

Investigation into nitridation of Si-H (100) can also be studied with this source. Most imporantly, the oxygen contanimation issue would need to be obviated. This can be accomplished by doing XPS *in situ*, removing any exposure to atmospheric $O_2$ or $H_2O$.

We can apply the TOF-APMS method to characterize other active sources, such as remote plasmas. Clear determinations can be made as to which species are emitted from these sources.